Discovery of the Higgs Boson with the Diphoton Decay Channel and First Differential Cross-Section Measurements with ATLAS

by

Amanda Kruse

A dissertation submitted in partial fulfillment of

the requirements for the degree of

Doctor of Philosophy

(Physics)

at the

University of Wisconsin – Madison

2014

Defended on 13 Aug 2014

Dissertation approved by the following members of the Final Oral Committee:

Yibin Pan · Professor of Physics

Wesley Smith · Professor of Physics

Lisa Everett · Professor of Physics

Terry Millar · Professor of Mathematics

Bruce Mellado · Professor of Physics

Abstract

In July 2012, a Higgs boson was discovered by both the ATLAS and CMS experiments. This thesis presents the most recent version of the $H \to \gamma\gamma$ analysis that was used in the discovery. Since the discovery, focus has shifted to measure the properties of the Higgs boson. The analysis presented here is the analysis of the Higgs couplings, where events are divided into twelve categories defined to isolate the various production processes. Specific focus is given to the vector boson fusion (VBF) process where the Higgs boson is produced in association with two foward/backward jets. Due to its small theory errors, the VBF process can allow for very precise measurements of the Higgs boson's properties. Also presented are the first differential cross section measurements for the Higgs boson as measured in the diphoton decay channel. Distributions in data are unfolded to particle level and compared with the latest Monte Carlo event generators for gluon-gluon fusion. Many distributions concentrate on the kinematics of the Higgs boson produced in association with jets. Finally, a proposal for a 1-jet VBF region for the high-luminosity LHC is proposed based on the difference in rapidity between the Higgs boson and the leading jet. This region shows good discrimination power against gluon-gluon fusion events and has been shown to discriminate against beyond the Standard Model couplings.

Acknowledgements

I would like to say a few words of thank you to the many people who have helped me towards the completion of my doctorate.

First and foremost, I thank my family. My parents, Dave and Sue Kruse and Patty and Bob Jensen, have been a constant source of support not just for my five years of graduate school, but for my entire life. They never doubted my possibilities, and have always encouraged me to be the greatest version of myself. I'd like to also thank my siblings, Megan, Jason, and Kelly who always keep my spirits up and have been a great source of energy. Furthermore, I must also thank my extended family. I have gotten a large amount of support from them, especially in the final stretch of my dissertation and defense.

In addition, I would like to say a few words of thank you to my fantastic friends. A very special thank you goes to my fellow graduate students, Guilhem Ribeill, Zack DeLand, and Walter Pettus. We had many nights of working on homework and not-so-much working on homework. They were a great source of support in the times of doubt, and a great group to enjoy the happier times with. They ensured I got out, enjoyed life, and maintained my sanity. A special thank you to the friends I hung out with at CERN: Scarlet Norberg, Austin Belknap, Ashley WennersHerron, Nicola Black, and Hasib Ahmed. Without them, I would not have been brave enough to explore France and Switzerland.

I would also like to thank my husband, Stephen Cole, for cooking many meals and pushing me out the door for ballroom. Thank you for getting through a move, a wedding, and my defense all within two weeks.

Finally, I would like to thank all those who helped me professionally. My advisor Bruce Mellado for introducing me to the ATLAS experiment and setting me on a

ground-breaking analysis. Thank you for my final advisor Yibin Pan for agreeing to be advisor at Wisconsin and supporting me at the end. I would also like to thank my committee members, Wesley Smith, Lisa Everett, Yibin Pan, Bruce Mellado, and Terry Millar. They provided very nice feedback and words of encouragement for the future. A special thank you to Larry Nodulman, and his delightful dinners, drinks, and fun. Finally, I would like to thank Jimmy Proudfoot for his continuing encouragement and advise.

Contents

Chapter 1

Introduction

1.1 Standard Model

The Standard Model of particle physics is a well established theory describing three of the four fundamental forces of nature: the electromagnetic, weak, and strong forces. It is based on the symmetry group $SU(3)_C \times SU(2)_L \times U(1)_Y$.

1.1.1 Elementary Particles

There are two different types of fundamental particles in the Standard Model: fermions, which constitute all the observed matter, and bosons, which mediate the interactions between particles. Fermions are spin $\frac{1}{2}$ particles which have three generations of particles, each more massive than the previous. They can be further broken down into particles that feel the strong force, quarks, and those which do not, leptons. The charged leptons are the electron (e), the muon (μ), and the tau (τ) each with an electric charge of -1. Each of these generations also has a corresponding neutral lepton called a neutrino: $(\nu_e, \nu_\mu, \nu_\tau)$. Quarks also have two particles per generation, called the 'up-type' and 'down-type' quarks. The up-type quarks consist of the up, charm,

and top quark, each of which has an electric charge of $+\frac{2}{3}$. Down-type quarks consist of the down, strange, and bottom quarks, each with an electric charge of $-\frac{1}{3}$. All fermions are summarized in their respective generations in Fig. 1.1.

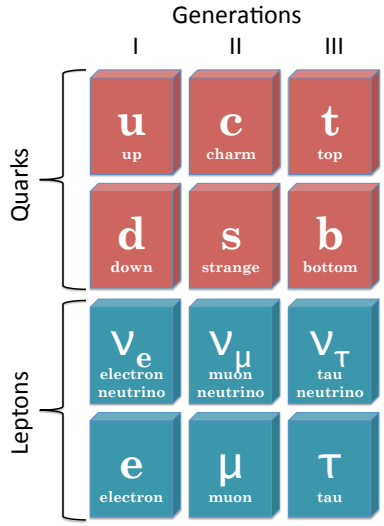

Figure 1.1: The three generations of fermions divided into quarks and leptons.

Bosons are particles of integer spin that mediate the electromagnetic, weak, and strong forces. The massless photon is the boson associated with the electromagnetic force and therefore couples to particles with electric charge. The weak force is mediated by three massive vector bosons, the $W^{\pm}$ and the Z bosons.

Another massless boson, the gluon, is the mediator of the strong force. The gluon couples to particles with non-zero color quantum numbers, or color charge. Of the fermions, only the quarks carry color charge, which can be R (red), G (green), or B (blue). The gluons themselves also carry color charge and can therefore interact with each other. There are eight gluons, each with a different combination of color and anti-color ($\bar{R}$, $\bar{G}$, or $\bar{B}$).

1.1.2 Quantum Chromodynamics

Quantum ChromoDynamics (QCD) is the theory of the strong force and is described by the $SU(3)_C$ group, where C is color charge. The strong force is quantified by the coupling constant α_S, which is a running coupling constant, meaning that the strength of the strong force coupling depends on the energy of the interaction. At high energies, the strong force weakens until it reaches asymptotic freedom. This is the ultra high energy regime where the strong coupling becomes so small that particles become essentially non-interacting via the strong force. At the other end of the spectrum, at low energies, the coupling becomes very strong and QCD can no longer be perturbatively calculated. This leads to the phenomenon known as confinement. Confinement describes the behavior of quarks in the presence of the strong force, and explains why quarks are never directly detected. At this low energy regime, the quarks begin forming bound states called hadrons, and they combine in such a way that the hadron is colorless, meaning there is no residual color charge associated with the hadron. Hadrons can be mesons which contain two quarks, one with color charge and one with anti-color charge. An example would be the π^+ which consists of an up quark and an anti-down quark and can have the color combinations of $R\bar{R}$, $G\bar{G}$, or $B\bar{B}$. Hadrons can also be baryons which are made up of three quarks. A common example is the proton which consists of two up quarks and a down quark. A baryon will have all three colors: RBG or $\bar{R}\bar{B}\bar{G}$ so that the resultant baryon is then colorless.

1.1.3 ElectroWeak Theory

Electroweak theory is the theory of the unified electromagnetic and weak interactions as described by the $SU(2)_L \times U(1)_Y$ symmetry. Y is the hypercharge of a particle

and is calculated by

$$Y = 2(Q - I_3) \tag{1.1}$$

where Q is the electric charge and I^3 is the third component of weak isospin of the particle. The L denotes the fact that the weak force only interacts with left handed (negative chirality) particles. Chirality is defined using the γ^5 operator:

$$\begin{aligned} \psi_L &= \frac{1}{2}(1 - \gamma^5)\psi \\ \psi_R &= \frac{1}{2}(1 + \gamma^5)\psi \end{aligned} \tag{1.2}$$

Fermions can be either left handed or right handed where left handed fermions are weak isospin doublets and interact with the weak force, and right handed fermions are singlets which do not interact with the weak force.

While the photon, the mediator of the electromagnetic force, is known to be massless, the W and Z bosons, mediators of the weak force, are known to be massive. However, introducing mass terms into the Standard Model Lagrangian destroys the $SU(2)_L \times U(1)_Y$ gauge invariance, thus electroweak symmetry must be broken in a way to allow the W and Z boson to have mass while keeping the photon massless. This is the subject of the next section where the Higgs mechanism is introduced as the method for electroweak symmetry breaking.

1.2 ElectroWeak Symmetry Breaking

The theory of spontaneous symmetry breaking comes originally from the field of condensed matter physics, Refs [1, 2], where it was shown that a non-zero ground state is possible. Because the ground-state is no longer at zero, the symmetry is said to be spontaneously broken.

The idea of spontaneous symmetry breaking was applied to quantum field theory by Nambu and Goldstone in the 1960's [3, 4, 5].

As a simple example of spontaneous symmetry breaking, a scalar field, ϕ, in a simple potential, V is considered. The Lagrangian for such a case is

$$\mathcal{L} = \frac{1}{2}\partial_\mu\phi\partial^\mu\phi - V(\phi) \tag{1.3}$$

where the potential V is defined as

$$V(\phi) = \frac{1}{2}\mu^2\phi^2 + \frac{1}{4}\lambda\phi^4. \tag{1.4}$$

The self-coupling term, λ, must be positive, but the mass term, μ^2, can be chosen as positive or negative. For the case where $\mu^2 > 0$, the minimum of the potential will be at 0. However, if the mass term is chosen to be negative, $\mu^2 < 0$, then the minimum is no longer located at 0. Two minima are now present, as shown in Fig. 1.2, and the field develops a vacuum expectation value: $\phi_0^2 = -\frac{\mu^2}{\lambda} \equiv v^2$, where $\pm v$ is the vacuum expectation value, or vev.

Now the Lagrangian should be rewritten to reflect that the minimum is no longer at 0. To do this, the field is expanded around the minima:

$$\phi = v + \phi'. \tag{1.5}$$

The Lagrangian is now written as

$$\mathcal{L} = \frac{1}{2}\partial_\mu\phi'\partial^\mu\phi' - (-\mu^2)\phi'^2 - \sqrt{-\mu^2\lambda}\phi'^3 - \frac{\lambda}{4}\phi'^4 + \text{const.} \tag{1.6}$$

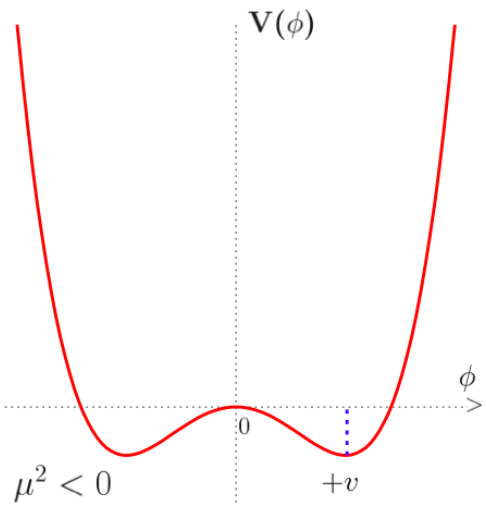

Figure 1.2: Potential of the scalar field, ϕ, for the case where μ^2 <0. In this case, the field develops two minima centered around the vacuum expectation value, $\pm v$. Figure is from Ref. [6].

where the scalar field ϕ' now has mass $M_{\phi'} = \sqrt{-2\mu^2}$.

It was proposed by Nambu and Goldstone [4, 7, 8, 5, 9], that the breaking of a continuous symmetry will lead to the introduction of massless scalar bosons: one boson for each symmetry broken. Further work done by Brout and Englert [10], Higgs [11, 12], and Guralnik, Hagen, and Kibble [13] showed that in theories which also require local gauge invariance, a gauge transformation can be done where three of the massless Goldstone bosons are no longer present in the Lagrangian, but instead get absorbed into the gauge bosons as a third degree of freedom, a longitudinal polarization, giving them mass. The fourth massless Goldstone boson becomes a real massive scalar particle, known today as the Higgs boson. In this gauge, only physical particles are present, and one new particle, the Higgs boson, has been introduced as a consequence of spontaneous symmetry breaking.

In the Standard Model, electroweak symmetry breaking is a spontaneous symmetry breaking, where the Goldstone bosons become the longitudinal polarizations

of the $W^{\pm}$ and Z gauge bosons. The same formalism presented previously can now be applied to electroweak symmetry breaking; however, three degrees of freedom are needed to form the longitudinal polarizations of the vector gauge bosons, so the scalar field is now a complex scalar doublet

$$\Phi = \begin{pmatrix} \phi^+ \\ \phi_0 \end{pmatrix} = \frac{1}{\sqrt{2}} \begin{pmatrix} \phi_1 - i\phi_2 \\ \phi_3 - i\phi_4 \end{pmatrix} \tag{1.7}$$

and the Lagrangian becomes

$$\mathcal{L} = (D^\mu \Phi)^\dagger (D_\mu \Phi) - V(\Phi) \tag{1.8}$$

where the potential, $V(\Phi)$, now has the form

$$\mu^2 \Phi^\dagger \Phi + \lambda (\Phi^\dagger \Phi)^2. \tag{1.9}$$

As before, μ^2 is taken to be less than 0 and λ is positive. With electroweak symmetry breaking, the vector bosons need to be massive while keeping the photon massless. In order to maintain the $U(1)_{QED}$ symmetry, only the neutral component, ϕ_3 should receive a vacuum expectation value (vev). The potential then has minima at $\phi_{3,0} = \sqrt{\frac{-\mu^2}{2\lambda}}$, or $\Phi_0 = \frac{1}{\sqrt{2}}\binom{0}{v}$. The corresponding vev is then $v = \pm\sqrt{\frac{-\mu^2}{\lambda}}$. As before, the field is now rewritten to take into account the vacuum expectation value of the neutral component.

$$\Phi = \frac{1}{\sqrt{2}} \begin{pmatrix} \phi_1 - i\phi_2 \\ (\phi_3' + v) - i\phi_4 \end{pmatrix}. \tag{1.10}$$

It is possible to apply a Gauge transformation to this scalar field, so that it is written in the unitary gauge,

$$\Phi = \frac{1}{\sqrt{2}} \begin{pmatrix} 0 \\ v + \phi_3' \end{pmatrix}. \tag{1.11}$$

With the introduction of the complex scalar doublet, four new degrees of freedom were introduced. In the unitary gauge, only one degree of freedom, ϕ_3', which is recognized as the Higgs field, is associated with the scalar field. With the transformation, the physical $W^{\pm}$ and Z bosons each acquire a new degree of freedom, which is the longitudinal polarization. The three massless fields that were previously introduced, (ϕ_1, ϕ_2, ϕ_4), were non-physical Goldstone bosons, and they are said to be 'eaten' by the $W^{\pm}$ and Z bosons.

In order for this new scalar field to be compatible with observations and the Standard Model, the vacuum expectation value must be fixed by the Fermi constant, G_F, which gives the scale of electroweak symmetry breaking,

$$v = (\sqrt{2} G_F)^{-1/2} = 246\text{GeV}. \tag{1.12}$$

The Higgs boson mass can then be related to both the vev and the self-coupling parameter λ,

$$M_H^2 = 2\lambda v^2. \tag{1.13}$$

Because the Higgs field couples to massive particles, the particle masses enter directly

into the coupling strengths, as does the vev. Table 1.1 shows the couplings of the Higgs boson to Standard Model particles as well as the self-couplings of the Higgs boson. No fermion mass terms enter directly into the Standard Model Lagrangian due to gauge invariance requirements. Instead, fermions are expected to acquire mass through the Yukawa interactions with the Higgs field,

$$-\lambda_\ell(\bar{\nu}_\ell\bar{\ell})_L\Phi\ell_R. \tag{1.14}$$

Here Φ is the same Φ from Eq. 1.11.

Couplings to fermions are proportional to the fermion mass, and couplings to vector bosons are proportional to the square of the boson mass. This implies that the more massive a particle, the greater its coupling to the Higgs boson.

Interaction	Coupling
Hff	$\frac{m_f}{v}$
HVV	$\frac{2m_V^2}{v}$
$HHVV$	$\frac{2m_V^2}{v^2}$
HHH	$\frac{3m_H^2}{v}$
$HHHH$	$\frac{2m_H^2}{v^2}$

Table 1.1: Higgs boson couplings to Standard Model particles and Higgs boson self-couplings. v is the vacuum expectation value, f are fermions, and V are the vector bosons $W^\pm$ and Z.

1.3 The Higgs Boson

This section summarizes the main processes that produce the Higgs boson at the LHC as well as the many decay channels that are available to a Higgs boson depending on

its mass. The final portion of this section is dedicated to the history of the searches for the Higgs boson and the July 2012 discovery of the Higgs boson at the LHC.

1.3.1 Higgs Boson Production

At the LHC, the Higgs boson can be produced through five main production processes: gluon-gluon fusion (ggF), vector boson fusion (VBF), associated production with a weak boson (WH and ZH), and associated production with two top quarks ($t\bar{t}H$). The cross sections for the different production processes as a function of the Higgs boson mass are shown in Fig. 1.3.

The dominant production process is the ggF process, where the interaction is initiated by two gluons and the Higgs boson is produced via a heavy quark loop. The leading order (LO) Feynman diagram for this process is shown in Fig. 1.4. Higgs boson production via ggF accounts for the majority of the Higgs boson production at the LHC, and therefore, an observation of a Standard Model-like Higgs boson is proof of the ggF process, and also indirect proof of the Higgs boson coupling to fermions. The diagrams shown in Fig. 1.4 are at LO, but in the case of the ggF production, this is not an accurate description. The perturbative series of the production cross section does not nicely converge, and the contributions from the NLO and higher diagrams are needed. Contributions from the NLO in QCD corrections were calculated in Refs. [14, 15, 16, 17] and shown to increase the cross section by $\sim$60% while NNLO contributions are still on the order of $\sim$20-30% [18, 19, 20]. This leads to large theoretical uncertainties for the ggF process, especially when selecting on jet multiplicities, which require higher order calculations.

The second largest contribution to the Higgs boson production is the VBF process. This process is initiated by a quark-quark interaction, which produce weak bosons. These bosons then interact to create the Higgs boson. The VBF topology includes the

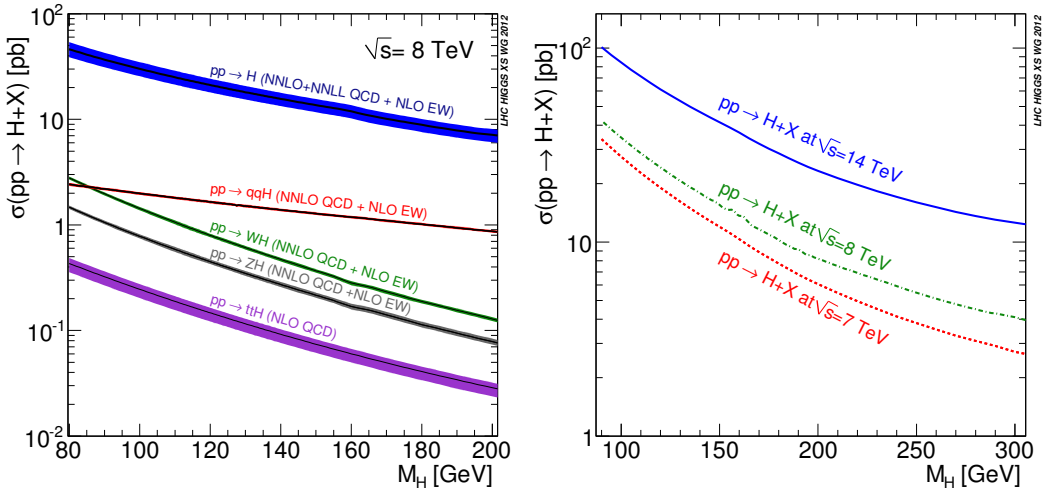

Figure 1.3: Higgs boson production process cross sections as a function of the Higgs boson mass [21]. Individual cross sections (left) are calculated at 8 TeV. Total cross sections (right) are for different center of mass energies.

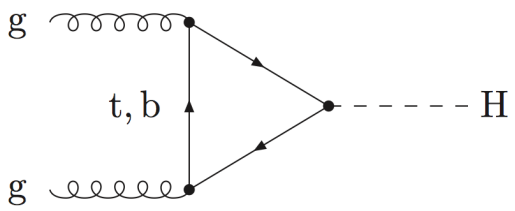

Figure 1.4: Feynman diagram for the ggF production mechanism of the Higgs boson [21].

production of a Higgs boson along with two jets in the forward/backward directions, and a lack of QCD activity between the two jets. Observing the VBF production provides information as to the couplings of the Higgs boson to the electro-weak bosons, W and Z. The diagrams for the VBF production process are shown in Fig. 1.5. Unlike the ggF production, the size of the QCD and EW corrections to the VBF process are small.

The next largest contributions are from the production of a Higgs boson in association with a weak boson: the WH and ZH production processes. The VH processes

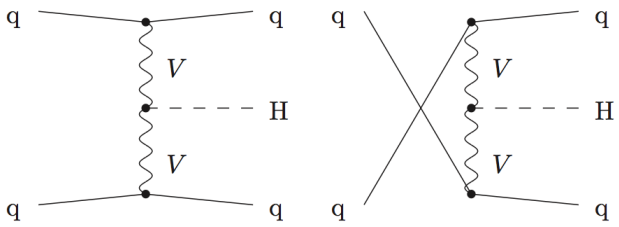

Figure 1.5: Feynman diagrams for the VBF production mechanism of the Higgs boson [21].

are mostly initiated by quark-antiquark pairs, where the W or Z radiates a Higgs boson. Diagrams for these processes and the case where a Z boson and a Higgs boson are produced via a heavy quark loop are shown in Fig. 1.6. These processes will result in events with either two jets in the final state with an invariant mass consistent with either a W or Z boson, or at least one lepton. These types of topologies are easily identified in detectors, and in particular, the ZH process where the Z decays leptonically is especially important for observing the cases where the Higgs boson decays into $b\bar{b}$ pairs.

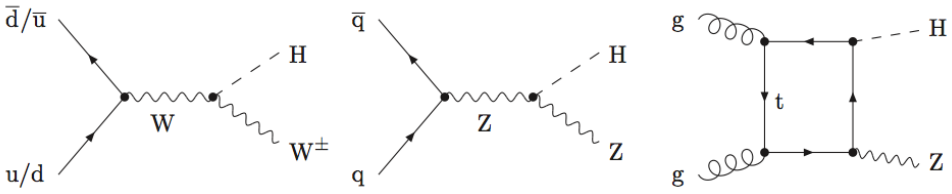

Figure 1.6: Feynman diagrams for the WH and ZH production mechanisms of the Higgs boson [21].

The smallest contribution of the five main production processes is that of the $t\bar{t}H$ process. Here the Higgs boson is produced in association with a top-antitop quark pair. These events are characterized by the decay products of the top quarks and will be seen in detectors as Higgs boson events with large jet multiplicities. Feynman

diagrams for this process are shown in Fig. 1.7.

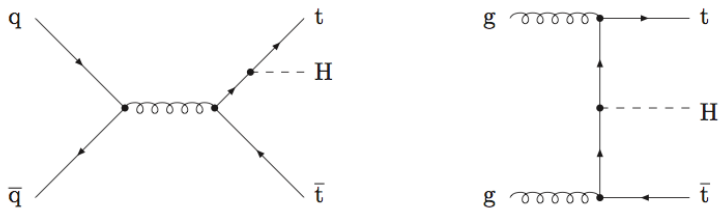

Figure 1.7: Feynman diagrams for the $t\bar{t}H$ production mechanism of the Higgs boson [21].

1.3.2 Decay of the Higgs Boson

The probability that a particle will decay into a particular set of final-state particles is called the partial decay width (Γ_i) and is dependent on the couplings between the initial and final state particles. Branching ratios are the fraction of times a particle decays into a specific set of particles and are defined as

$$B_i = \frac{\Gamma_i}{\Gamma_H} \tag{1.15}$$

where Γ_H is the full decay width of the Higgs boson.

The Higgs boson has many decay channels whose partial widths depend on the Higgs boson mass. Fig. 1.8 shows these branching ratios as a function of the Higgs boson mass.

The partial width for decays into WW and ZZ can be written as [22, 23, 24]

$$\Gamma_V = \frac{N_C G_F m_H^3}{8\sqrt{2}\pi}\beta(m_V)\left([\beta(m_V)]^2 + \frac{12m_V^4}{m_H^4}\right) \tag{1.16}$$

where

$$\beta(m_V) = \left(1 - \frac{4m_V^2}{m_H^2}\right)^{\frac{1}{2}} \tag{1.17}$$

and the factor $N_C = 2$ for WW and $N_C = 1$ for ZZ on account of the W boson being charged.

For fermions, the partial width can be written as [25, 26]

$$\Gamma_f = N_c \frac{G_F m_H}{4\sqrt{2}\pi} m_f^2 [\beta(m_f)]^3, \tag{1.18}$$

where the QCD color factor $N_c = 3$ for quarks and $N_c = 1$ for leptons.

For lower mass Higgs bosons (m_H <130 GeV), the $b\bar{b}$ decay channel is the dominant decay. This is due to both the heavy mass of the b quark and the color factor (C_n =3) from the possible color quantum numbers. For higher mass Higgs bosons, the WW and ZZ decay channels are favored. This is due to the VV partial decay width being proportional to m_H^3 while the ff partial decay width has a m_H dependence.

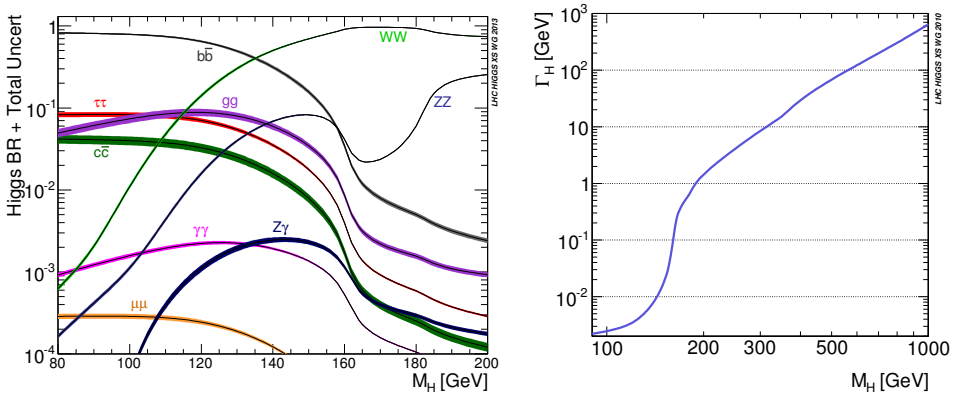

Figure 1.8: Higgs boson branching ratios (left) and total decay width (right) as a function of the Higgs boson mass [21].

The diphoton decay has a very small branching ratio ($\sim 2\times10^{-3}$) within the Higgs boson mass range of 110< m_H <160 GeV. This is one of three decays (gg, $\gamma\gamma$, $Z\gamma$) which proceed through a loop, due to the decay products being massless and therefore not coupling directly to the Higgs boson. For the diphoton decay channel, the loop particles must be massive charged particles. Therefore, the loop proceeds through W bosons and top quarks. The Feynman diagram for the diphoton decay is shown in Fig. 1.9. Despite the small branching ratio, the diphoton decay channel is particularly important for the discovery of the Higgs boson. The diphoton system will create a narrow resonance on top of a smooth background distribution, which allows for very good signal to background ratios.

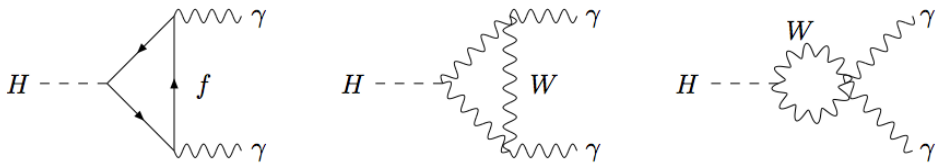

Figure 1.9: Feynman diagram for the Higgs boson decay to diphotons [27]. The decay is a loop induced process of W bosons and top quarks.

1.3.3 History and Discovery

As was shown in Secs. 1.3.1 and 1.3.2, the production and decay of the Higgs boson is known as a function of the Higgs mass. This is because all of the couplings of the Higgs boson to Standard Model particles are completely determined by fermion masses and coupling constants. The one unknown parameter from theory is the Higgs boson mass.

Before experiments were able to directly search for the Higgs boson, precision electro-weak measurements pointed to preferred mass ranges of a Higgs boson. Here

the Higgs boson contributes to the radiative corrections to weak bosons as shown in Fig. 1.10. By fitting to EW High-Q^2 observables such as the mass of the W and Z bosons, the mass of the top quark, the width of the W boson, the Fermi coupling constant, and the weak mixing angle, constraints can be placed on the Higgs boson mass. A fit to the precision electro-weak measurements showed a favored Higgs boson mass of 94^{+29}_{-24} GeV with a 95% confidence level (C.L.) upper bound of $m_H \leq$ 152 GeV as shown in Fig. 1.10. While this fitted Higgs boson mass is in the region later excluded by direct searches, it does motivate the direct searches to look for a lighter mass Higgs boson.

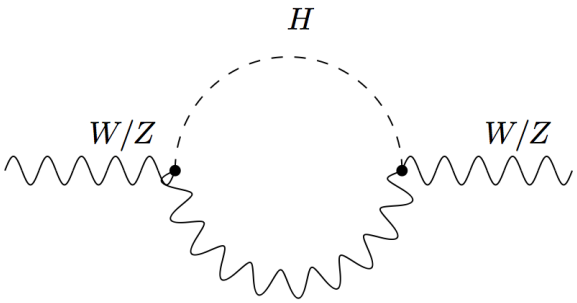

Figure 1.10: The Higgs contribution to the radiative corrections of the W or Z bosons.

Prior to the LHC, an experiment called the Large Electron Positron collider (LEP) [29, 30] was searching for the Higgs boson. This experiment, per its name, collided electrons and positrons at center of mass energies between 189 and 209 GeV. In this collider, the production of a Higgs boson in association with a Z boson was the primary process. LEP ran from 1989 until 2000 and set an experimental lower bound on the mass of the Higgs boson at 114.4 GeV at 95% C.L. as shown in Fig. 1.12.

The search was then carried out at the Tevatron Collider [31], where protons and antiprotons were collided at a center of mass energy of 1.96 TeV. At the Tevatron, the most important production modes are the ggF and the Higgs boson production in association with a weak boson. The greatest sensitivity is from the $H \to b\bar{b}$

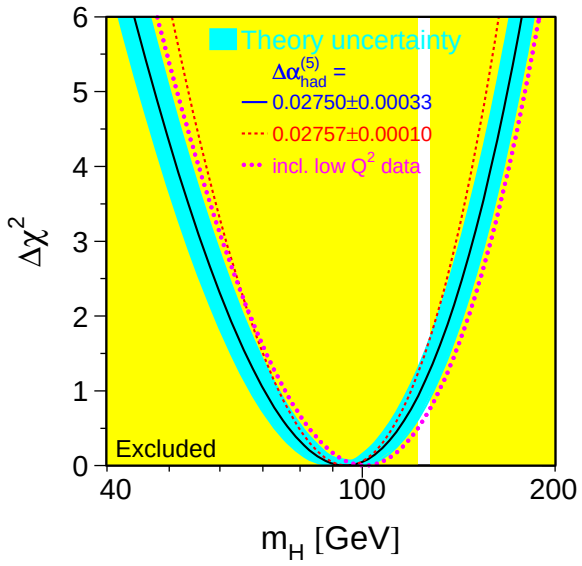

Figure 1.11: The $\Delta\chi^2$ vs. m_H curve from LEP [28]. The solid line is from the fit of all high-Q^2 data while the band is the theoretical error. The shaded regions show the exclusion limits from all direct searches (LEP+Tevatron+LHC).

and $H \rightarrow WW$ decay channels. Previous to the start of the LHC, the Tevatron experiments were able to exclude a Higgs mass with 162 GeV$< m_H <$166 GeV [32]. With the most recent results shown in Fig. 1.13, the Tevatron was able to exclude a Higgs boson in two mass regions: 100$< m_H <$103 GeV and 147$< m_H <$180 GeV at 95% C.L.

Beginning in 2010, the LHC began running collisions at a center of mass energy of 3.5 TeV. This was then increased to 7 TeV in 2011 and to 8 TeV in 2012. On July 4 of 2012, both multipurpose experiments at the LHC (ATLAS and CMS) announced independent discoveries of a Higgs-like boson at a mass around 125 GeV [33, 34] using data from 2011 (7 TeV) and 2012 (8 TeV). Figure 1.14 shows the p_0-values, the probability for the results to be generated by background-only processes, for each experiment; the ATLAS signal had local and global significances, the level of rejection

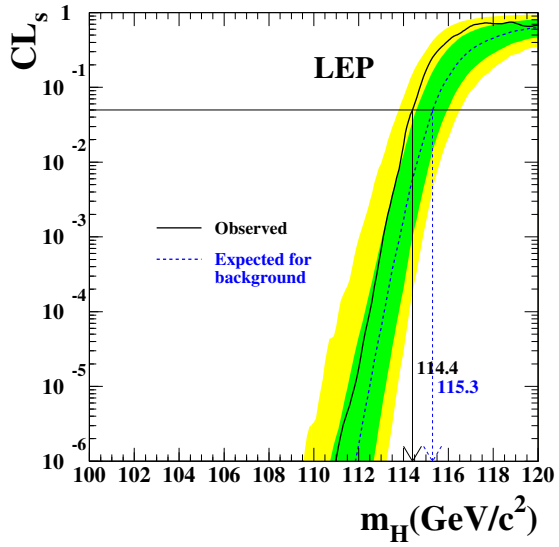

Figure 1.12: The final combined exclusion results of all experiments at LEP. The dashed line represents the expected results for a Standard Model Higgs boson, and the solid black line represents the observed limit. The limit at 95% C.L. is 114.4 GeV while the 68% C.L. limit is 115.3 GeV [29].

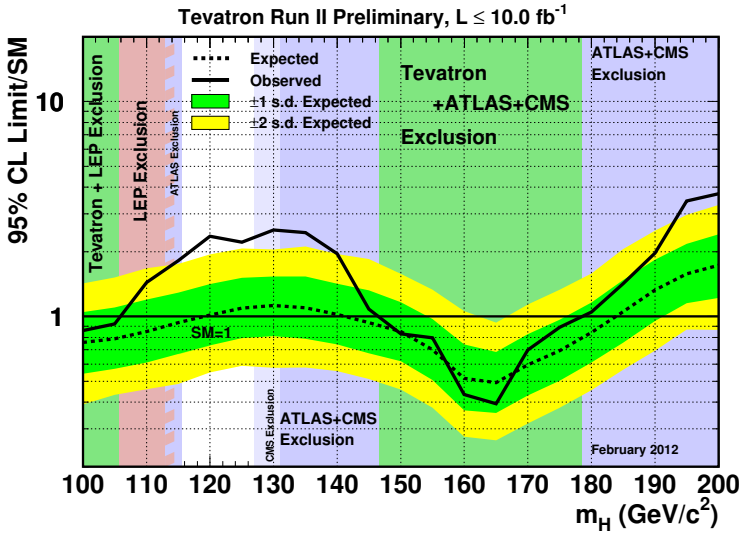

Figure 1.13: The final combined exclusion results of experiments at the Tevatron. The dashed line represents the expected results for a Standard Model Higgs boson, and the solid black line represents the observed limit [31].

of the background-only hypothesis, of 5.9 σ and 5.1 σ respectively, while the CMS signal had local and global significances of 5.0 σ and 4.6 σ respectively. Five decay channels were analyzed, $\gamma\gamma$, ZZ, WW, $b\bar{b}$, and $\tau\tau$, but most of the sensitivity came from the $\gamma\gamma$ and ZZ channels. At the time, while the overall signal strength was compatible with the expected Standard Model rates, both experiments observed an excess rate ($\mu \equiv \frac{N_{obs}}{N_{SM}} > 1$) over the Standard Model in the $\gamma\gamma$ decay channel as can be seen in Fig. 1.15. Now that the Higgs boson has been discovered, analyses are underway to accurately measure its properties such as its mass and couplings to determine whether the newly discovered Higgs boson is the Higgs boson of the Standard Model.

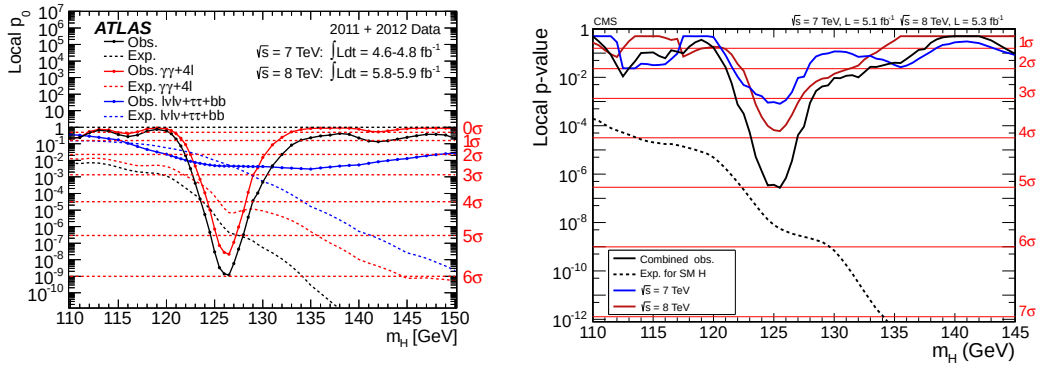

Figure 1.14: p_0-values for the discovery of the Higgs boson using the ATLAS (left) and CMS (right) detectors. Both experiments measured a significance of $\geq$5 σ. Results shown here are from the discovery papers published in 2012 [33, 34].

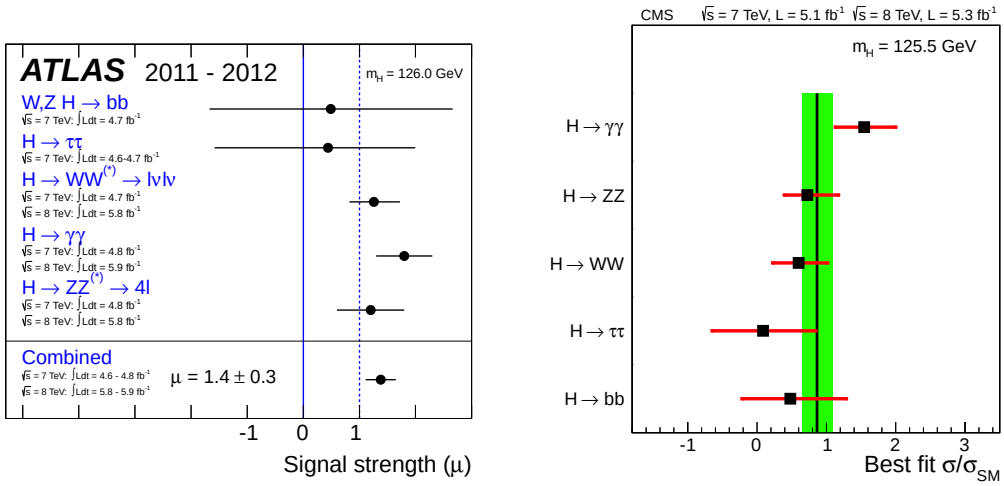

Figure 1.15: Measured signal strengths (μ) for individual decay channels with the ATLAS (left) and CMS (right) detectors. Both experiments measured an excess of events (μ >1) in the $\gamma\gamma$ decay channel. Results shown here are from the discovery papers published in 2012 [33, 34].

Chapter 2

ATLAS Detector

2.1 LHC Machine

2.1.1 LHC Overview

The Large Hadron Collider (LHC) [35] is mainly a proton-proton collider located at the border of France and Switzerland. It is housed in a circular tunnel, previously used for LEP, which is 26.7 km in circumference and sits 45-170 m below the surface of the earth. The LHC has an initial design center-of-mass energy, or $\sqrt{s}$, of 14 TeV and a design luminosity of 10^{34} cm^{-2}s^{-1}. It has also been designed to accelerate heavy ions of lead with $\sqrt{s}$ =5.5 TeV at a peak luminosity of 10^{27} cm^{-2}s^{-1}. Because it accelerates particles with the same charge in both beams, the LHC has two separate beam pipes contained within a single magnet, which only come together at the interaction points. These beam pipes are contained within a vacuum of 10^{-10} to 10^{-11} mbar, which is the equivalent of 3 million molecules per cm^3.

The LHC uses a series of superconducting Niobium-Titanium (NbTi) magnets to focus the beams and direct them along the beam pipe. There are 1232 dipole and 392 quadrupole magnets in the LHC. The main dipoles are 14.3 m in length.

These magnets are cooled to 1.9 K using superfluid helium and operate at 8.33 T (7 TeV center-of-mass). While the beam pipes are separate, they share both the same mechanical structure and cryostat within the magnets, utilizing the "twin-bore" design.

Protons are injected into the LHC through the following injection chain: Linac2 which strips the hydrogen atoms of their electrons and accelerates them to 50 MeV, Proton Synchrotron Booster (PSB) which accelerates them to 1.4 GeV, Proton Synchrotron (PS) which accelerates them to 26 GeV, Super Proton Synchrotron (SPS) which accelerates them to 450 GeV. They are then injected into the LHC where the protons are accelerated to the desired center of mass energy before collisions begin. An image of the injection chain for the LHC is given in Fig. 2.1.

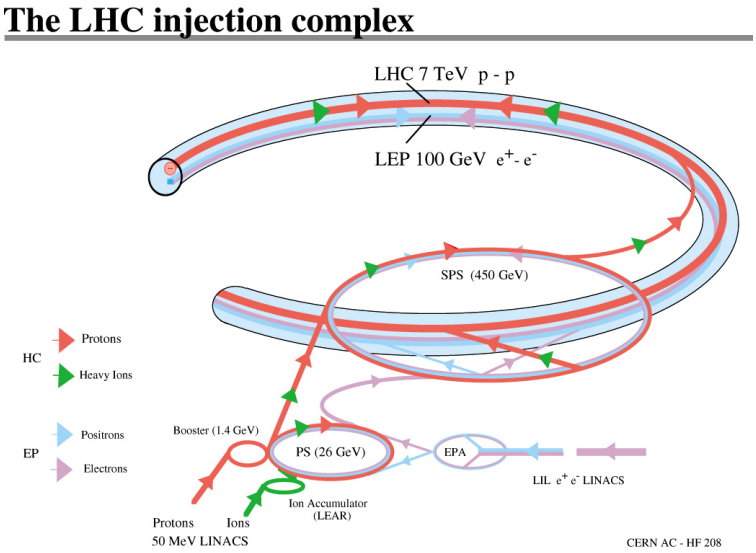

Figure 2.1: The LHC injection chain: Linac2, PSB, PS, SPS, LHC.

Protons are accelerated around the beam pipe using a series of superconducting RF cavities which operate at 400 MHz. The LHC operates with 1380 bunches with 50 ns spacing, where each bunch has 1.7×10^{11} protons. A 3 μs abort gap is left with unoccupied bunches to allow for beam dump. The LHC was designed to accommodate

25 ns spacing, allowing for 2808 bunches; however, it was operated with 50 ns for running so far.

There are four main detectors housed around the LHC ring.

- There are two high luminosity general purpose detectors, ATLAS (A Toroidal LHC ApparatuS) [36] and CMS (Compact Muon Solenoid) [37]. Both these experiments work towards precision measurements and searches for new physics.
- ALICE (A Large Ion Collider Experiment) [38] is a dedicated heavy ion detector, which focuses on QCD measurements.
- LHCb (Large Hadron Collider beauty) [39] is a lower luminosity experiment which is dedicated to studying B-physics.
- TOTEM (TOTal Elastic and diffractive cross section Measurement) [40] which measures the interaction cross section of the protons at the LHC and also probes the structure of the proton.

2.1.2 LHC Running

Construction was finished on the LHC in mid 2008, and the first injection test occurred in August 2008. On the 10th of August that same year, the first beams circled through the LHC. However, nine days later, a quench occurred in one of the busbars between magnets which went undetected at first. An arc occurred, heating the helium and causing it to boil. This released a large amount of pressure and caused the magnet stands to break. This delayed the LHC for over a year. Beams were running again in November of 2009, and the first LHC collisions at 3.5 TeV occurred in March of 2010 with a bunch spacing of 150 ns. In 2011, the LHC began running with a center-of-mass energy of 7 TeV with 50 ns bunch spacing, and in 2012, the

energy was increased to 8 TeV. The LHC reached a peak luminosity of 3.7×10^{33} $\text{cm}^{-2}\text{s}^{-1}$ in 2011, and in 2012, a luminosity of 7.7×10^{33} $\text{cm}^{-2}\text{s}^{-1}$ was reached. The integrated luminosity delivered by the LHC for 2011 was 5.46 fb^{-1} and in 2012 it was 22.8 fb^{-1}. Proton-proton collisions were ceased at the end of 2012, and a technical stop began in 2013 after heavy ion running. Work has been ongoing to consolidate the LHC and the detectors, and collisions are expected to begin in 2015 at a nominal center-of-mass energy of 13 TeV, possibly with 25 ns bunch spacing. The LHC is scheduled to continue running until a second technical stop beginning in 2018, after which the LHC will run again at twice the previous luminosity. A third long shutdown is scheduled for around 2022-2023 where large upgrades will be made to the LHC machine and detectors. After this shutdown, the LHC will be renamed the High-Luminosity LHC (HL-LHC) and is expected to provide 3000 fb^{-1} over a decade of running [41].

2.2 The ATLAS Detector

The ATLAS detector is one of the two high luminosity general purpose detectors located at the LHC. It is 44 m in length, 25 m in height, and weighs 7000 tonnes. Its layout and subsystems are shown in Fig. 2.2. The ATLAS detector has four main subsystems: the Inner Detector, the Electromagnetic Calorimeter, the Hadronic Calorimeter, and the Muon Spectrometer. A 2 T solenoidal magnetic field encloses the inner detector, which is used for particle identification, vertex measurements, and particle momentum measurements. The electromagnetic calorimeter is a liquid-argon (LAr) sampling calorimeter, and the hadronic calorimeter, or Tile calorimeter, is a sampling calorimeter composed of plastic scintillator tiles and steel plates. The outermost section of the detector is the muon spectrometer which, in conjunction with

three large toroidal magnets, provides very good muon momentum measurements through tracking. The subsystems directly used in the Higgs boson to diphotons analysis are discussed in greater detail in this chapter, namely the inner detector and the EM and Tile calorimeters.

The coordinate system used in ATLAS defines the origin as the interaction point within the detector and the z direction is along the beamline. Going around the beam axis is ϕ or the azimuthal angle. The polar angle, or θ is measured from the beamline; however it is rarely used within the experiment. Instead, the pseudorapidity, η, defined as

$$\eta = -\ln\left(\tan\left(\frac{\theta}{2}\right)\right) \tag{2.1}$$

is used. This quantity is not Lorentz-invariant, so for analyses which specialize in massive objects the rapidity, y, defined as

$$y = \frac{1}{2}\ln[(E + p_z)/(E - p_z)] \tag{2.2}$$

is used. For massless particles, the pseudorapidity is equal to the rapidity. Quantities measured transverse to the beamline, such as transverse momentum, p_T, transverse energy, E_T, and missing transverse energy, E_T^{miss}, are measured in the $x - y$ plane, where x is pointing radially towards the center of the collider ring. Oftentimes, it helps to define the distance between two different objects in the detector. For this, the distance ΔR is given in pseudorapidity and azimuthal angle space and defined as

$$\Delta R = \sqrt{\Delta\eta^2 + \Delta\phi^2} \tag{2.3}$$

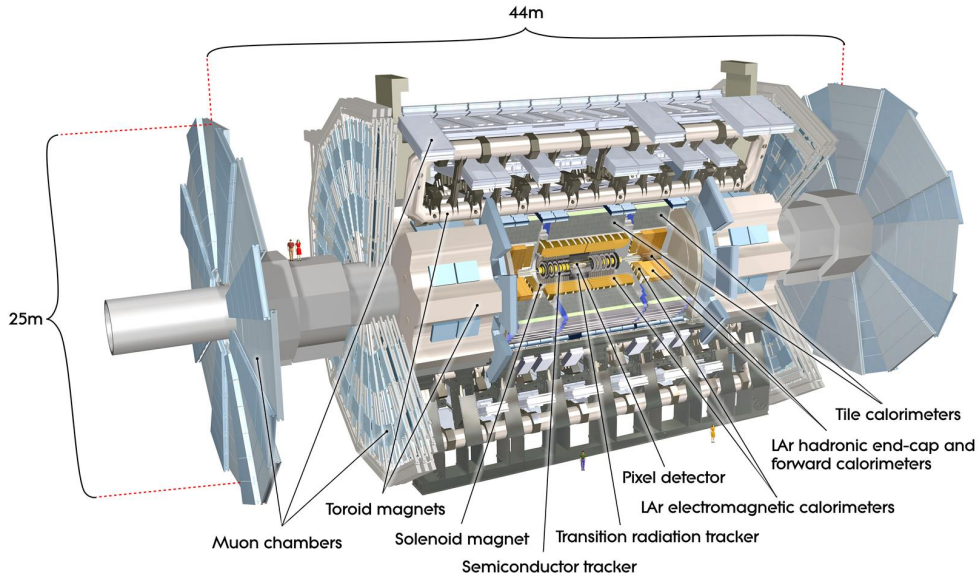

Figure 2.2: The ATLAS detector and its subsystems.

The ATLAS detector had very high data taking efficiencies (∼94%) in both 2011 and 2012, as can be shown in Fig. 2.3. In addition, the efficiency for runs to be considered 'good', meaning all detector subsystems were on and functioning correctly, was also very high (∼90% in 2011 and ∼95% in 2012).

2.2.1 Inner Detector

The Inner Detector is the closest component to the beam line and is entirely enclosed in a solenoid generating a 2 T magnetic field. This magnetic field bends the trajectory of charged particles allowing for particle identification and momentum measurements. In addition, the excellent tracking performance of the inner detector allows for very precise vertex measurements. Resolution within the inner detector is

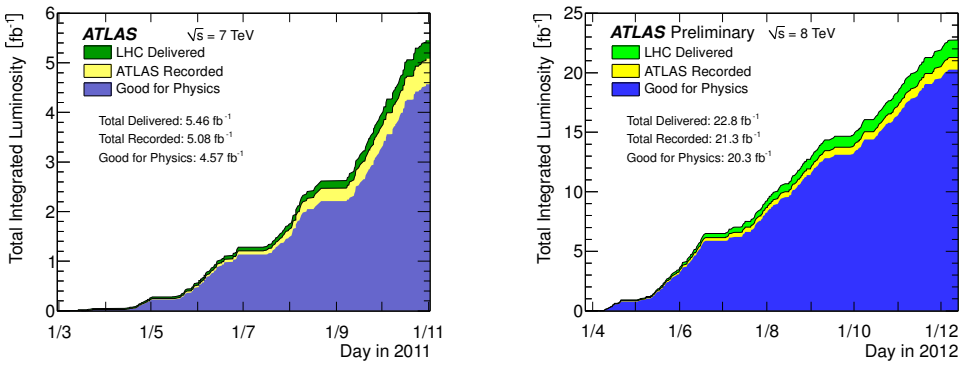

Figure 2.3: The cumulative delivered and recorded integrated luminosity by day for 7 TeV (2011) and 8 TeV (2012) collisions for the ATLAS experiment. In blue is the integrated luminosity deemed 'good' for physics analyses at ATLAS [42].

$$\frac{\sigma_{p_T}}{p_T} = 0.05\% \times p_T + 1\%. \tag{2.4}$$

The inner detector is comprised of three main components: the pixel detector, the silicon microstrip layer (SCT), and the transition radiation tracker (TRT). The layout of the inner detector and its three subdetector systems is shown in Fig. 2.4.

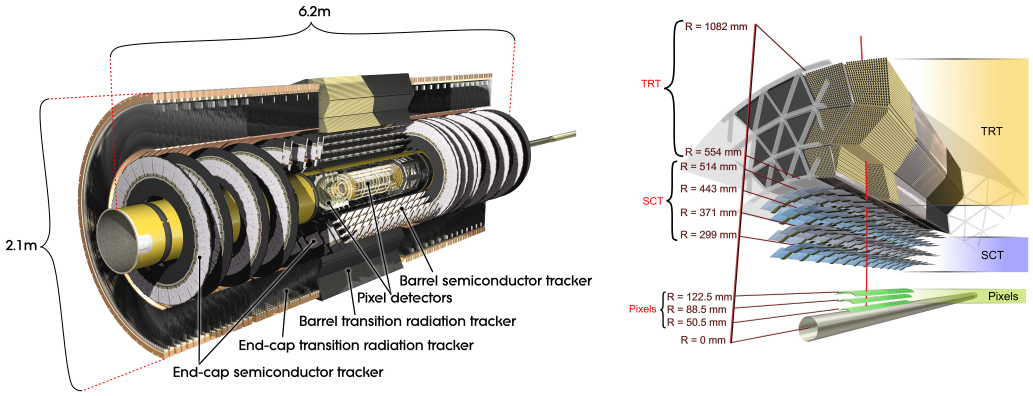

Figure 2.4: Diagrams of the ATLAS Inner Detector and its three components: Pixel, SCT, and TRT.

2.2.2 Pixel Detector

The innermost subsystem is the pixel detector, which covers the region $|\eta| < 2.5$. It is composed of 1744 silicon pixel sensors with dimensions 19 mm x 63 mm and a thickness of 250 μm. Each pixel sensor uses oxygenated n-type double sided wafers and contains 47232 pixels. The pixel sensors are arranged in three cylindrical layers in the barrel at radii of 50.5 mm, 88.5 mm, and 122.5 mm from the beamline. The innermost layer is called the 'B-layer', and it is particularly important for reconstructing secondary vertices and tagging b-quark jets. In each endcap, there is again three layers of pixel detectors; however, they are arranged in disks oriented perpendicular to the beamline. These are placed at 495 mm, 580 mm, and 650 mm from the interaction point.

2.2.3 SCT Detector

The second inner detector layer is the SCT detector, which is comprised of silicon microstrips. SCT sensors are one-sided, unlike the pixel detector, and are made with p-in-n strips. There are 15912 SCT sensors in ATLAS, which consist of 768 active strips each. Two sensors are daisy-chained together, while the strips have a pitch of 80μm. The sensors are in stereo with two sensors on the top and two sensors on the bottom of the barrel SCT modules. The SCT detector is arranged in four concentric cylinders in the barrel at radii of 299 mm, 371 mm, 443 mm, and 514 mm. Within each endcap region, the SCT detector has 9 disks oriented perpendicular to the beam line. These reach as far out as 2720.2 mm from the interaction point, covering the region $|\eta| < 2.5$.

2.2.4 TRT Detector

The last layer of the inner detector is the TRT detector, which is composed of polyimide drift tubes with diameters of 4 mm. The outer walls act as a cathode, while in the center of each tube are tungsten wires plated with gold which are kept at ground potential and act as the anode. Within the tube, a gas mixture of 70% Xe, 27% CO_2, and 3% O_2 is maintained. This gas mixture is ionized by charged particles passing through it, and the corresponding electrons will be gathered at the anode providing a signal current. The gas mixture is retained within the tubes by encasing them in CO_2. This envelope of CO_2 also helps with the dissipation of heat from the straw tubes.

The TRT also relies on transition radiation, where charged particles which pass between media with different dielectric constants will emit radiation. Therefore, the tubes are covered by a layer of polypropylene/polyethylene fibers. Because the energy of the transition radiation is dependent on the mass of the incident particle, the TRT detector can also be used to identify electrons.

In the barrel, the TRT is arranged into three rings with 32 modules each; the last layer extends to a radius of 1082 mm from the beam pipe. The straws in the barrel section run parallel to the beampipe. Each endcap has two sets of wheels; the layer closest to the interaction point has twelve wheels, each with eight layers, while the farther set has eight wheels, also each with eight layers. The TRT endcaps extend to 2710 mm in length along the beamline, and the straw tubes are oriented outward radially from the beampipe. There are a total of 298,304 straw tubes within the TRT detector.

The full amount of material a particle passes through from the inner detector and all its support material is shown in terms of radiation lengths in Fig. 2.5. Each track is expected on average to have 3 pixel hits, 8 SCT hits, and 36 TRT hits.

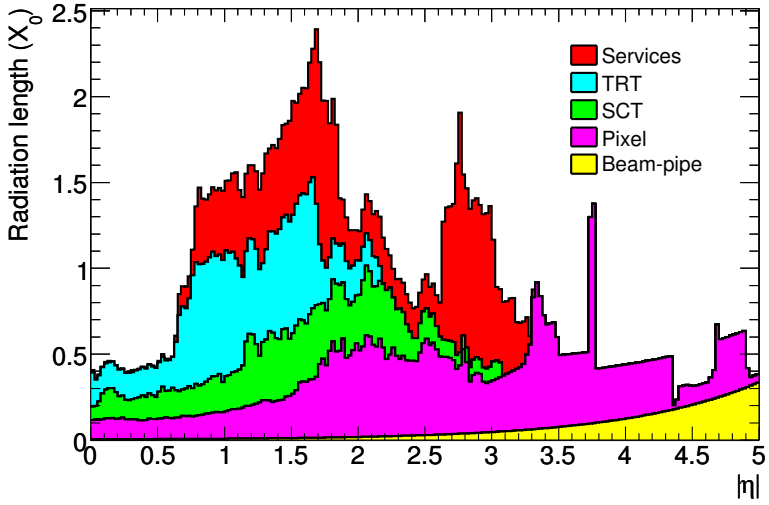

Figure 2.5: The radiation lengths of material comprised in the inner detector including all subsystems and support systems broken down by η and averaged over ϕ.

2.2.5 ElectroMagnetic Calorimeter

Outside the inner detector and its solenoid is the electromagnetic (EM) calorimeter, which is used to distinguish between electrons and photons and to measure their energies. The EM calorimeter is made of an active material (liquid Argon, or LAr), and an absorber material (lead). Within the LAr gap between absorbers is an electrode. The drift gap on each side of the electrode is 2.1 mm corresponding to a drift time of 450 ns. The barrel region is divided into two sections with a separation of 4 mm at the interaction point; each section is 3.2 m in length and extends from a radius of 2.8 m out to a radius of 4 m. This barrel region covers out to $|\eta|$ <1.475 and consists of 2048 absorbers. There are two endcap sections of the EM calorimeter, which are each separated into two wheels; the first covers the region 1.375< $|\eta|$ <2.5, and the second covers the region 2.5< $|\eta|$ <3.2. The EM calorimeter uses an accordion geometry to ensure full coverage through ϕ without any cracks and complete azimuthal symmetry. Each module of the EM calorimeter is divided by depth into three layers of varying

granularity. The innermost layer has the highest granularity ($\Delta\eta$ x $\Delta\phi$ =0.025 x 0.2). This "strip" layer provides excellent position resolution and allows for good photon-pion discrimination [43] by resolving the individual photon showers from pion decays. This strip layer only covers out to $|\eta|$ <2.37, so all analyses require photons to be within this pseudorapidity region. The second layer is where the largest fraction of energy is deposited within the EM calorimeter. Finally, the third layer is where the least fraction of energy is deposited, and as such, it has much more coarse granularity ($\Delta\eta$ x $\Delta\phi$ =0.050 x 0.025). This third layer is used to correct the tails of high energy showers in the EM calorimeter. These three layers and their proportions are shown in Fig. 2.6. Directly before the innermost EM layer is a presampler. The presampler is a thin 11mm thick separate layer of liquid-argon, which is used to correct for the energy a particle loses within the material before the EM calorimeter.

The resolution of the EM calorimeter is

$$\frac{\sigma_E}{E} = \frac{10\%}{\sqrt{E}} \oplus \frac{300MeV}{E} \oplus 0.7\%. \tag{2.5}$$

The first term is the stochastic term, which accounts for statistical fluctuations within the shower development, dead material in front of the calorimeter, and sampling fluctuations. The second term is the noise term, which accounts for pileup and electronic noise fluctuations. This term becomes especially important for low energy showers. The third term is the constant term, which describes effects coming from nonuniformities within the detector, things such as temperature differences, radiation damage, time stabilities, and material nonuniformity.

In total, the EM calorimeter spans from 22 radiation lengths (X_0) to 33 X_0 as shown in Fig. 2.7. Note the increased amount of material in front of the EM calorimeter around $|\eta|$ =1.5, the so-called 'crack region'. This is due to cabling, inner detector

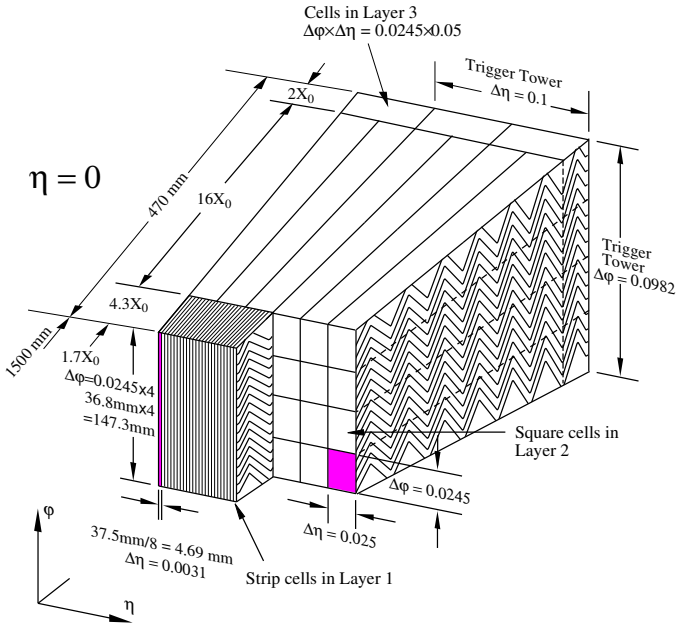

Figure 2.6: Diagram of one module in the EM calorimeter. The granularity gets more coarse with each layer.

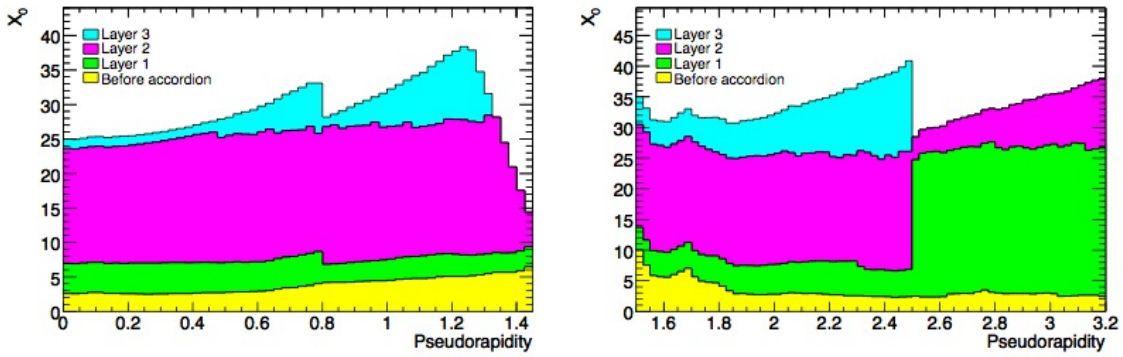

Figure 2.7: The radiation lengths before the EM calorimeter and for each layer of the calorimeter shown as a function of $|\eta|$.

services, and the end of the barrel cryostat. Photons in this region typically have much worse resolution and efficiencies, so the fiducial cut of $|\eta_\gamma|$ <1.37 OR $|\eta_\gamma|$ >1.56 is required.

2.2.6 Tile Calorimeter

Outside of the EM calorimeter is ATLAS's hadronic calorimeter, or Tile Calorimeter. The Tile calorimeter is also a sampling calorimeter, which uses plastic scintillator tiles as its active material, and steel plates as its absorber. The Tile calorimeter covers out to $|\eta|$ <1.7 and has an outer radius of 4.25 m. The Tile calorimeter is divided into four partitions: two long barrels and two extended barrels. The long barrels extend out to $|\eta|$ <1.0 and are 2.9 m in length, while the extended barrels are from 0.8< $|\eta|$ <1.7 and are 2.6 m in length. Each partition is further divided into 64 modules, which are arranged azimuthally around the beam line. Wavelength shifting fibers are attached to the side of each scintillator tile and are read out by photomultiplier tubes (PMTs) at the edge of each Tile module as shown in Fig. 2.8. Each module of the Tile calorimeter is divided in depth into cells with dimensions $\Delta\eta$ x $\Delta\phi$ =0.1 x 0.1 in the first two layers (cells A and B) and dimensions 0.2 x 0.1 in the third and final layer (the D cells). A drawing of the segmentation for one module is shown in Fig. 2.9.

The energy resolution for the Tile calorimeter is

$$\frac{\sigma_E}{E} = \frac{50\%}{\sqrt{E}} \oplus 3\%. \tag{2.6}$$

The total thickness of the Tile calorimeter is 7.4 λ. A schematic of the full ATLAS detector material by $|\eta|$ up to the beginning of the muon spectrometer is shown in Fig. 2.10. The material is divided by depth for the Tile calorimeter.

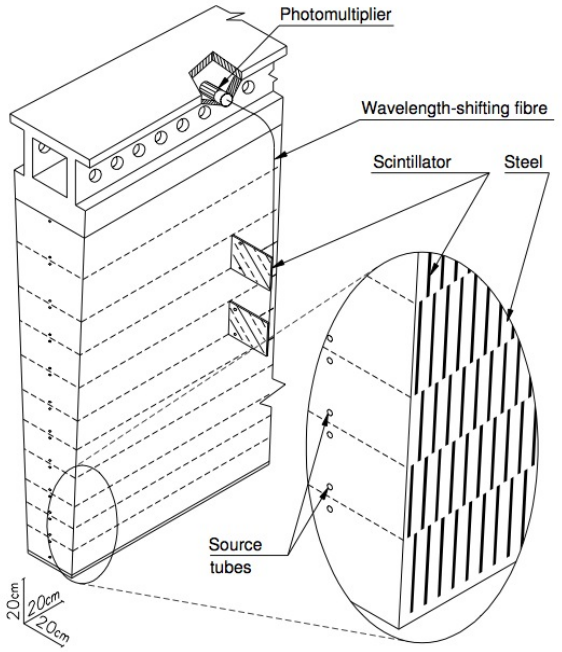

Figure 2.8: Drawing of a single Tile module and its array of alternating plastic scintillators and steel plates. Also pictured are the wavelength-shifting fibers and the PMTs which read them out.

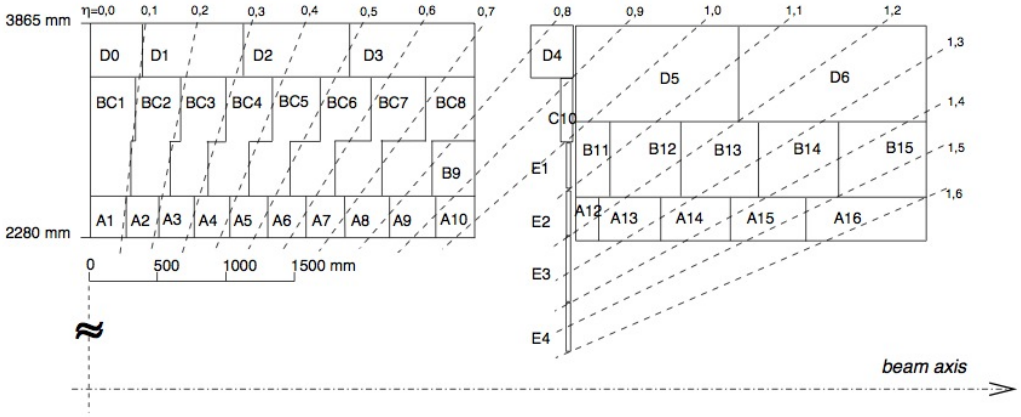

Figure 2.9: Drawing of the segmentation of a Tile module into A, B, C and D cells. The E cells shown correspond to the minimum-bias scintillators.

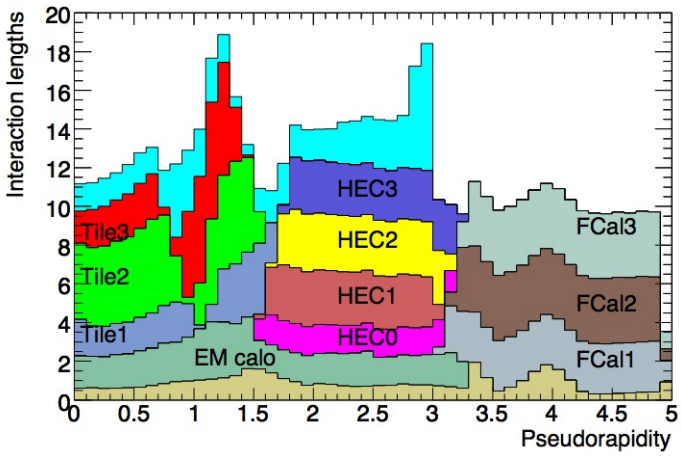

Figure 2.10: Plot of interaction lengths(λ) for the full amount of material up through the Tile calorimeter presented as a function of $|\eta|$. The light blue region at the top of the plot is the full amount of material up to right infront of the muon spectrometer.

2.2.7 Hadronic Endcap Calorimeter

The hadronic endcap calorimeter (HEC) is also a sampling calorimeter covering the pseudorapidity range of 1.5< $|\eta|$ <3.2. It is composed of liquid-argon acting as the active material, and the absorber material is copper. The HEC has two wheels in each endcap extending out to a radius of 2030 mm, and each wheel is further divided into 32 modules.

2.2.8 Forward Calorimeter

The forward calorimeters (FCal) in the ATLAS detector cover the region 3.1< $|\eta|$ <4.9, and sit about 4.7 m from the interaction point. The FCal is also made of liquid-argon; however, because of the expected high particle fluxes, the liquid-argon gaps are much smaller than those in the barrel EM calorimeter. There are three sections of the FCal: one EM module which sits closest to the interaction point, and two hadronic modules. The EM module utilizes copper as an absorber while the two hadronic modules use tungsten. A drawing of both the HEC and FCal is shown in Fig. 2.11.

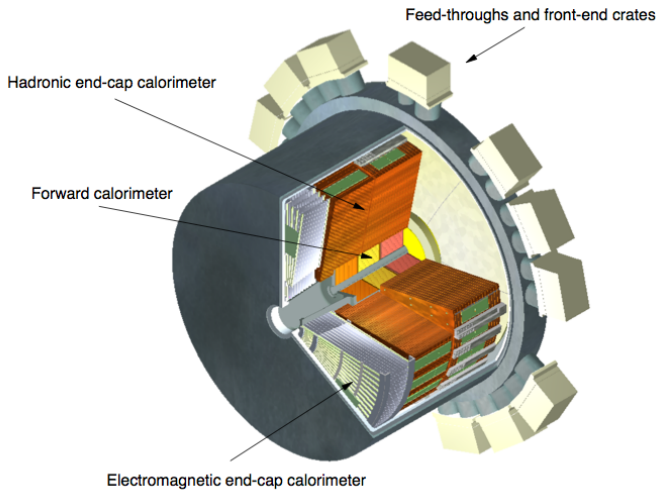

Figure 2.11: Drawing of the EM and Hadronic end-cap calorimeters and the three wheels of the Forward Calorimeter.

2.2.9 Muon Spectrometer

The ATLAS muon spectrometer is used for precision tracking and momentum measurement of muons. It is the part of the ATLAS detector which sits the farthest from the interaction point, and it covers the region out to $|\eta|$ <2.7. Much like all the other subsystems, the spectrometer is divided into a barrel region and two endcap regions. The barrel region is composed of three cylindrical layers centered around the beam pipe and extending to radii of 5 m, 7.5 m and 10 m. Here, muon tracks are bent using the superconducting toroid magnets generating a field of 0.5 T. The endcaps are composed of four wheels oriented perpendicular to the beam pipe. These extend to 7.4 m, 10.8 m, 14 m, and 12.5 m from the interaction point. Two smaller end-cap magnet wheels bend the muon tracks in the end-cap detectors with a magnetic field of 1 T. The majority of the muon spectrometer is composed of monitored drift tubes (MDTs) which contain a mixture of gas which is 93% Argon and 7% CO_2. The MDTs are maintained at a constant pressure of 3 bar. At the center of each tube is a gold-plated tungsten-rhenium wire which acts as the anode and collects the

ionized electrons from the gas. In the first layer of end-cap detectors, cathode strip chambers (CSCs) are used instead of MDTs. These cover the region $2< |\eta| <2.7$. CSCs are multiwire proportional chambers and are arranged into two disks each with eight chambers. They are designed to handle the higher particle fluxes. The design resolution for the muon spectrometer is 10% for a track p_T of 1 TeV.

2.2.10 ATLAS Trigger System

The ATLAS trigger system is divided into three levels: Level-1(L1), a hardware based trigger, and Level-2(L2) and the event filter(EF) which are both software based triggers and together form the High-Level Trigger(HLT). The L1 trigger first looks for hard objects or E_T^{miss} based on information from a subset of the detector; muons are identified just from the spectrometer, and calorimeter clusters are identified from the full set of calorimeters. Using these objects, the L1 trigger defines a Region-of-Interest (RoI), and sends along its coordinates to the L2 trigger. The L1 trigger's processing time is less than 2.5 μs, and it reduces the rate of information down to 75 kHz. While the L1 trigger uses very coarse information from the detectors, the L2 trigger uses the full capabilities of all detectors just within the RoI, including the inner detector. Here, the L2 trigger further reduces the rate of data to 3.5 kHz and has an average processing time of 40 ms. The EF uses offline analysis on the fully reconstructed events to reduce the rate to 200 Hz. Here, the processing time is about 4 s.

Chapter 3

Signal Reconstruction in the Tile Calorimeter

This chapter details the optimal filtering algorithm which is used to reconstruct signals in the Tile calorimeter. First, a brief overview of the electronics in the Tile calorimeter is given followed by a review of the optimal filtering algorithm. Finally, the studies which were carried out on the signal reconstruction behavior in the presence of pileup and the reconstruction of negative energies will be detailed.

3.1 Electronics of the Tile Calorimeter

The Tile calorimeter is composed of plastic scintillator plates (tiles) which produce light when particles from the interaction pass through them. This light is then read out by wavelength shifting fibers on either side of the modules and passed to the photomultiplier tubes (PMTs). Two PMTs read out the signals, one for each side of the module. Each PMT converts the light from the fibers to an analog signal where it is then passed to a 3-in-1 card which shapes the signals. This shaping gets rid of

fluctuations between signals so that every signal sent to the electronics has a uniform shape. Signals are then sent through two separate amplifiers after which they are sent to the digitizer. The digitizer then digitizes the signals every 25 ns, meaning it samples the signal shape seven times in intervals of 25 ns.

The electronics described above are front-end electronics meaning they are located directly on the detector. For the Tile calorimeter, these electronics are located in removable drawers at the outer edges of each calorimeter module. Signals are then transferred to the back-end electronics which are stored in a room which is separate from the detector and therefore is a much lower radiation environment. Signals from the front-end electronics are sent to the read-out driver (ROD) which has 8 input links from the front-end electronics. Each ROD has 2 processing units (PU) each of which has 2 digital signal processors (DSPs). The signal reconstruction using optimal filtering is carried out in these DSPs. Signal reconstruction is limited by the L1 Trigger, which outputs data at a rate of 100 kHz. Therefore, the signal reconstruction has an upper limit of 10 μs so as not to limit the rate of data taking. A schematic of the signal processing is shown in Fig. 3.1.

3.2 Optimal Filtering Alogrithm

The energy of a Tile calorimeter cell is reconstructed online in the DSPs using the optimal filtering algorithm. This algorithm relates the 7 samples from the digitizer in a linear way using precomputed weights [45]. The optimal filtering algorithm computes the amplitude (A) of the pulse, the phase (τ) of the pulse, and the pedestal (p). The amplitude is directly correlated with the energy deposited in the Tile cell and is the difference in ADC counts between the peak of the signal pulse and the pedestal. The pedestal is the noise level or baseline of the signal. Finally, the phase

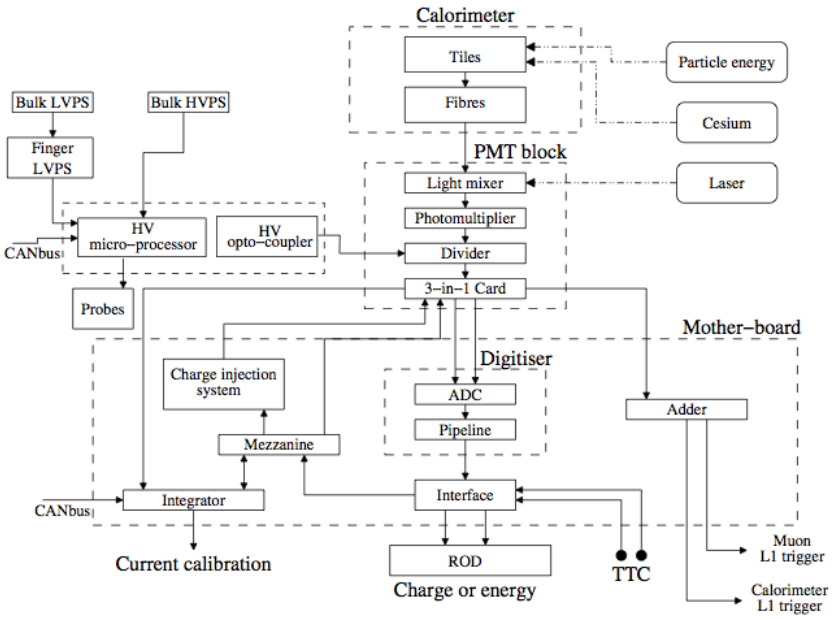

Figure 3.1: The Tile calorimeter electronics. Signals are read out by the optic fibers, converted to analog signals via the PMTs and then digitized on the Mother-board. They are then transferred to the RODs where signal reconstruction occurs [44].

is the timing difference between the peak of the signal pulse and the expected time of the peak. A signal's expected pulse time is taken from calibration runs and is dependent on the flight time of particles and the length of the readout fibers for each cell. The optimal filtering algorithm calculates these three values using the following three summations:

$$A = \sum_{i}^{7} a_i S_i \tag{3.1}$$

$$\tau = \frac{1}{A} \sum_{i}^{7} b_i S_i \tag{3.2}$$

$$p = \sum_{i}^{7} c_i S_i \tag{3.3}$$

where a_i, b_i, and c_i are the optimal filtering weights. A diagram of a signal pulse and these three computed values is shown in Fig. 3.2.

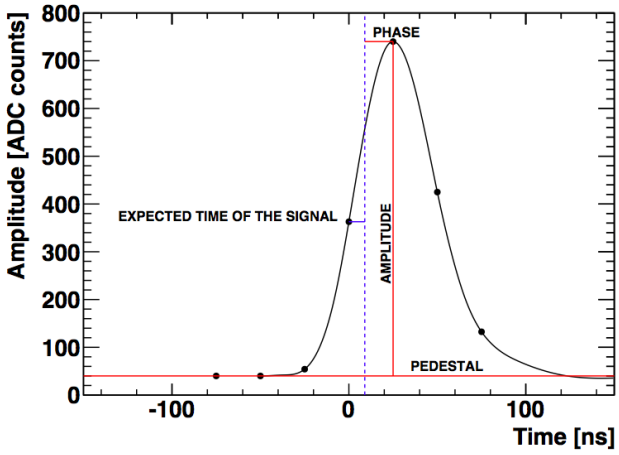

Figure 3.2: Signal pulse shape which is sampled 7 times (black dots) in the digitizer. These samples are combined linearly with precomputed weights in the optimal filtering algorithm to reconstruct the amplitude, phase, and pedestal [44].

The optimal filtering weights are computed using an auto-correlation matrix (ACM) which makes use of Lagrange multipliers. Weights are computed using the expected functional form of the signal, and are calculated by minimizing the variance of the signal amplitudes. Equation 3.4 is the matrix equation used for calculating the optimal filtering weights.

$$\begin{pmatrix} R_{1,1} & R_{1,2} & \dots & R_{1,7} & g_1 & g'_1 & 1 \\ R_{2,1} & R_{2,2} & \dots & R_{2,7} & g_2 & g'_2 & 1 \\ \vdots & \vdots & \ddots & \vdots & \vdots & \vdots & \vdots \\ R_{7,1} & R_{7,2} & \dots & R_{7,7} & g_7 & g'_7 & 1 \\ g_1 & g_2 & \dots & g_7 & 0 & 0 & 0 \\ g'_1 & g'_2 & \dots & g'_7 & 0 & 0 & 0 \\ 1 & 1 & \dots & 1 & 0 & 0 & 0 \end{pmatrix} \times \begin{pmatrix} a_1 \\ a_2 \\ \vdots \\ a_7 \\ \alpha \\ \beta \\ \gamma \end{pmatrix} = \begin{pmatrix} 0 \\ 0 \\ \vdots \\ 0 \\ 1 \\ 0 \\ 0 \end{pmatrix} \tag{3.4}$$

The elements $R_{i,j}$ are the ACM elements, g_i and g_i' are the functional form of the signal shape and its derivative, and α, β, γ are Lagrange multipliers.

These weights are computed for different expected pulse times in steps of 0.1 ns within the -75 ns to +75 ns timing window. Steps of 0.1 ns are used so that the timing resolution of the Tile calorimeter (1 ns) is not dependent on the steps used for the phase weights. In addition to these weight variations, three different versions of these weights also have to be stored in the DSP. The signal shape is different depending on whether the signals come from data runs, Laser calibration runs, or Charge Injection System (CIS) runs. Therefore different sets of weights need to be stored for each of these cases. These weights are stored in the ATLAS COOL conditions database [46].

The energy can then be calculated from the reconstructed amplitude by

$$E_{channel} = A \times C_{ADC \to pC} \times C_{pC \to GeV} \times C_{Cs} \times C_{Laser}. \tag{3.5}$$

Here $C_{ADC \to pC}$ is the conversion factor from ADC counts to charge in pC. This coefficient is determined using the CIS calibration runs where a known amount of charge is injected into the detector electronics and the corresponding amplitude in ADC counts for each channel is measured. $C_{pC \to GeV}$ is the conversion factor from charge to GeV which was measured using testbeams for a subset of modules. These coefficients are global but do have a layer dependence. The last two coefficients represent the non-uniformities of channels and the non-linearities of the PMTs respectively. The C_{Cs} coefficient is measured using a radioactive Cesium source, ^{137}Cs in the calorimeter, which calibrates the light yield from the scintillators and wavelength shifting fibers. Non-linearities in the PMTs are measured in Laser calibration runs where light is pointed at the PMTs and their responses are compared to their nominal response.

A measure of the goodness of the reconstruction is also done by the optimal filtering algorithm. This measure is called the Quality Factor (QF) and effectively measures the difference between an expected pulse and the actual signal pulse. The QF is defined as

$$QF = \sum_{i}^{7} (S_i - (Ag_i + A\tau g'_i + p))^2. \tag{3.6}$$

S_i are the digitized samples, A, τ, and p are the reconstructed amplitude, phase and pedestal, g_i are samplings determined from the normalized functional form of the pulse shape when it is at the same expected time, and g'_i are samplings from the derivative of that same functional form.

3.3 Negative Reconstructed Energies

It was noticed during 2011 data taking, that some Tile calorimeter cells had negative reconstructed energies. The spatial location of these negative signal cells was checked for the entire $\eta \times \phi$ region of the Tile calorimeter to ensure the negative signal cells are not localized and therefore an issue arising from the detector itself. While there is no isolated grouping of negative energy cells in the ϕ direction, as the energy threshold becomes more negative, the cells along $\eta \sim 1.2$ have the highest occupancy. This η region corresponds to the 'E' cells (Fig. 2.9) which are the most susceptible to pileup events. These spatial occupancy checks are shown in Fig. 3.3.

In addition to the $\eta \times \phi$ space, the negative energy occupancies for the various cell types was also checked. The fraction of times a cell-type is reconstructed with negative energy is shown in Fig. 3.4. Again, as the threshold cut on the negative energy

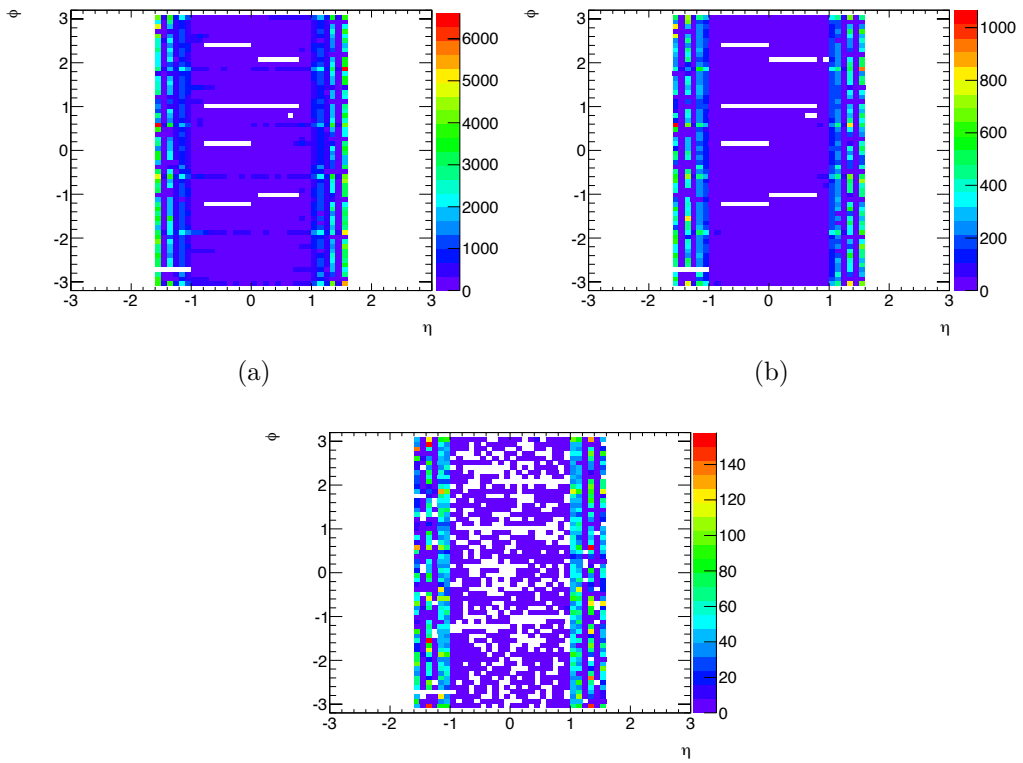

(a) (b)

(c)

Figure 3.3: $\eta \times \phi$ mapping of cells with negative reconstructed energies in the Tile calorimeter over time. Three negative energy thresholds are shown: (a) $E < -200$ MeV, (b) $E < -500$ MeV, (c) $E < -1000$ MeV.

becomes more negative, the cells begin to cluster in the 'E' cells, again suggesting pileup may be the cause.

A more in-depth look was taken into the 'A' cells, the Tile calorimeter cells closest to the beamline (Fig. 2.9), because the energy deposition in these cells is well understood. For these cells, a large energy threshold was applied, $|E| < -1.5$ GeV. Table 3.1 shows the results for one run in 2011. A total of 289 'A' cells were reconstructed with negative energy, most of which were channels set on the high-gain setting. The majority of negative energies were from 'A' cells in the extended barrels of the Tile calorimeter.

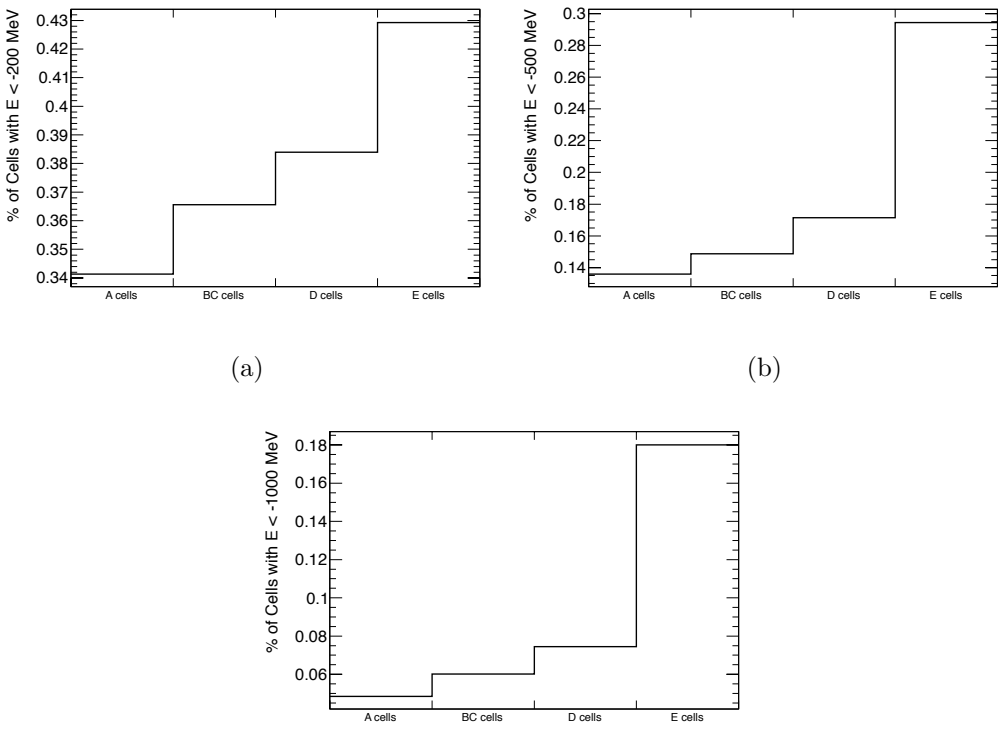

Figure 3.4: % of Tile calorimeter cell-types which are reconstructed with negative energies. Absolute energy thresholds are applied for three different thresholds: (a) $|E| < -200$ MeV, (b) $|E| < -500$ MeV, (c) $|E| < -1000$ MeV.

Tile Cell	HG Events	% of Total HG Events	LG Events	% of Total LG Events
A1	4	1.46	0	0
A2	10	3.65	0	0
A3	7	2.55	0	0
A4	6	2.19	0	0
A5	6	2.19	0	0
A6	7	2.55	0	0
A7	12	4.38	0	0
A8	11	4.01	0	0
A9	7	2.55	0	0
A10	13	4.74	1	6.67
A12	4	1.46	0	0
A13	36	13.14	0	0
A14	64	23.36	11	73.33
A15	59	21.53	3	20.00
A16	28	10.22	0	0

Table 3.1: Number of events with negative reconstructed energies $E < -1.5$ GeV for High-Gain (HG) and Low-Gain (LG) channels in the 'A' cells.

The concentration of negative energies in the 'E' cells and the extended barrel indicating that pileup may be the cause of reconstructed negative energies, suggested the cause may be in the signal reconstruction algorithm itself. Pileup signals are expected to have a larger reconstructed phase and a distorted signal shape leading to larger quality factor values. These assumptions were tested and Fig. 3.5 and 3.6 show the distributions for the timing and quality factor respectively for all Tile calorimeter signals and for just those cells with a negative reconstructed energy. As expected, the cells with negative reconstructed energy are those which also have a large difference in timing with respect to the expected signal time ($|t| >= 30$ ns) and have large quality factors. Figure 3.7 shows the breakdown of quality factors for high-gain and low-gain channels. It is clear for low-gain that one could define a quality factor cut above which almost all cells would have negative energies; however, the situation is not so clear for channels set on high-gain.

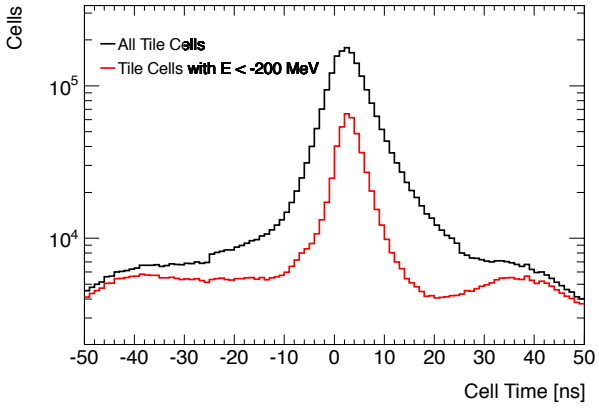

Figure 3.5: Signal timing distributons for all Tile calorimeter channels (black) and for those with negative reconstructed energies (red).

To investigate further the response of the optimal filtering, data from zero-bias runs was studied. Zero-bias runs are runs which randomly trigger, and therefore many events are expected to be out-of-time. The samplings of the waveforms for events with positive and negative reconstructed energies were divided based on which sampling

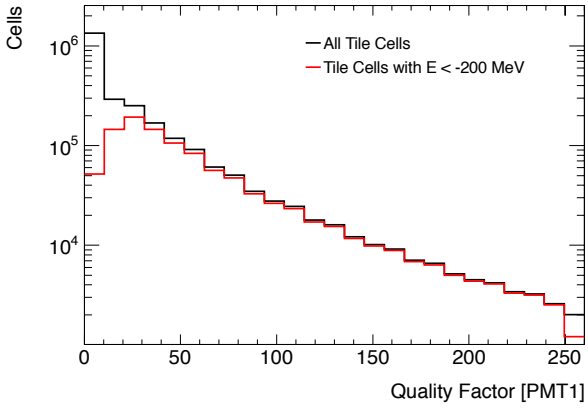

Figure 3.6: Quality factor distributions for all Tile calorimeter channels (black) and for those with negative reconstructed energies (red).

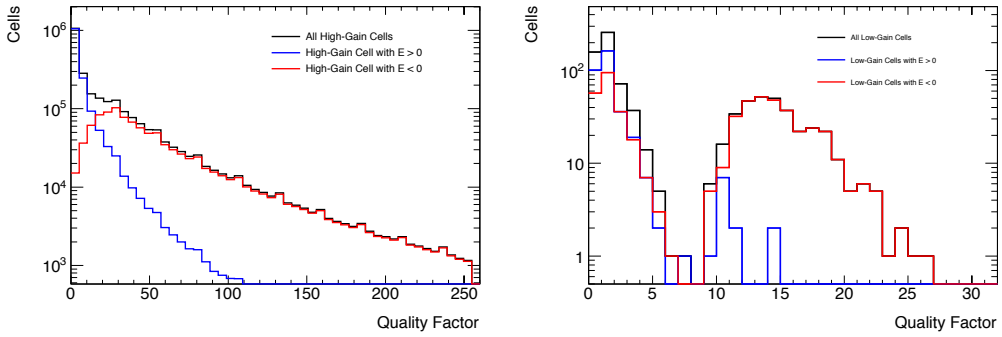

(a) (b)

Figure 3.7: Break down of quality factor distributions for channels set on (a) high-gain and (b) low gain.

(1-7) the signal peaked at. Figures 3.8 and 3.9 show the results for positive and negative energies respectively. The cells with positive reconstructed energy always had waveforms which peaked in the 4th or 5th samplings where the optimal filtering algorithm is designed to work. However, in cases where the signal arrived early or late, peaking in the first two or last two samplings, mimicking out-of-time pileup, the cells' energies were reconstructed as negative. This is due to the optimal filtering weights assigned to each sampling. The first and last two samplings are expected to contain the pedestal only, so these samplings receive negative weights in order to

properly subtract off the pedestal in the reconstruction of the signal amplitude. In cases where the signal peaks in these samplings, the peak is assigned these negative weights and the overall sum for the amplitude attains a negative value. In these cases the optimal filtering algorithm cannot properly account for the distorted shapes, and in higher-luminosity conditions even more cells are expected to be reconstructed with negative energies.

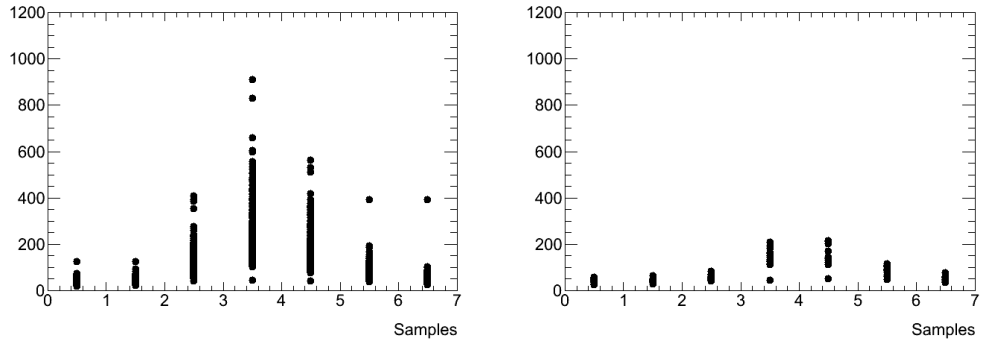

(a) (b)

Figure 3.8: Samplings of waveforms in cells with postive reconstructed energies. The waveforms peaked in the 4th (left) or 5th (right) samplings.

These results show that in the presence of out-of-time pileup, the current implementation of the optimal filtering cannot properly account for the change in signal shapes. This results in non-physical negative reconstructed energies in the Tile calorimeter cells. A short term solution is to apply a quality factor cut to eliminate many of the negative energy signals; however, this will not get rid of all or even the majority of the negative signals. Occupancy studies show these negative reconstructed energies occur in cells that are most susceptible to pileup conditions. Assuming only electronics noise (i.e. no pileup), the off-diagonal elements of the ACM are negligible. So far for LHC data taking, a unitary ACM has been used for online signal reconstruction in the Tile calorimeter, as it was assumed that the ACM would only be needed for higher luminosity data taking. In Ref. [47] it was shown that

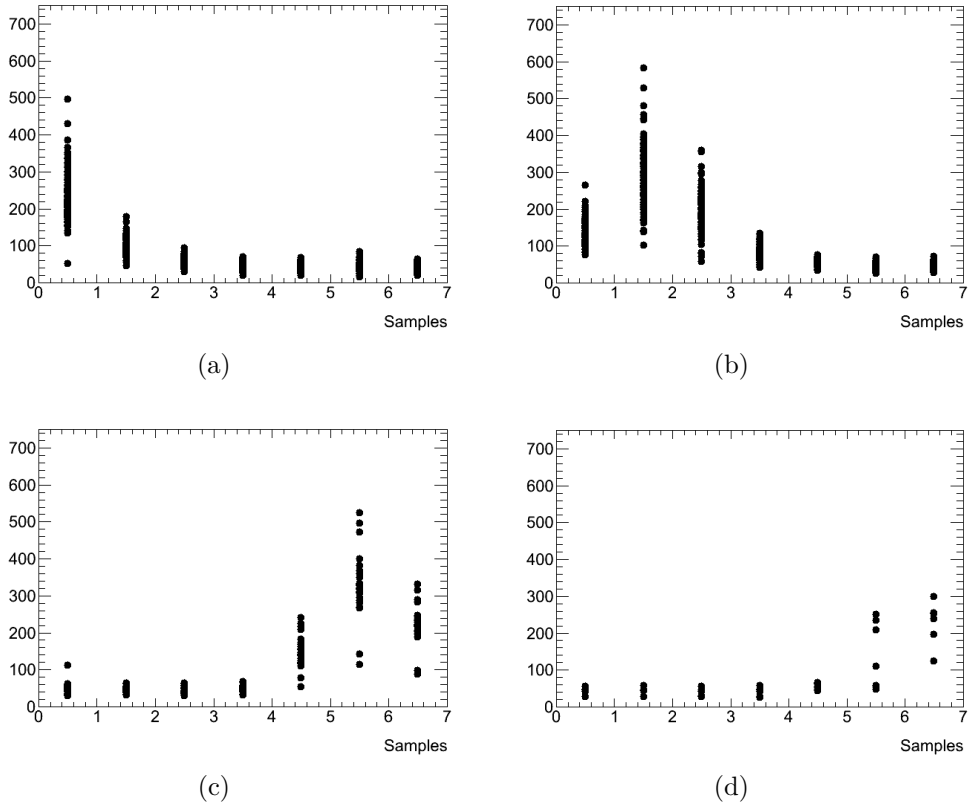

Figure 3.9: Samplings of waveforms in cells with negative reconstructed energies. The waveforms peaked in the first or last two samplings.

even the full ACM cannot distinguish between various levels of pileup. For future data-taking at the LHC, the method of signal reconstruction will have to be revisited in order to account for pileup and the resulting distortion of the signal shapes in the Tile calorimeter.

Chapter 4

Observation of the Higgs Boson With Diphoton Decay

This chapter describes the Higgs boson analyses for the diphoton decay channel. Two measurements are carried out: the mass of the Higgs boson and the coupling strengths. The overall strategies are similar for both. A narrow resonance on top of a continuous background distribution is fitted to data. Events are selected first based on the quality of the data, and further selection cuts are applied to ensure the identified photons are come from the primary interaction. Selected events are then divided into predefined categories, which differ between the mass and coupling analyses. The mass analysis defines categories based on the photons' locations in the EM calorimeter and the diphoton p_T in order to fully utilize the resolution of the calorimeter. For the coupling analysis, the strategy is to define categories with high purity for each of the five production processes: ggF, VBF, WH, ZH, and $t\bar{t}H$. The coupling categories for the associated production rely on the decay products of the W and Z bosons and top quarks produced with the Higgs boson. For the VBF process, the Higgs boson is produced in association with two forward/backward jets.

This production process, along with the VH process, provides a measure of the weak couplings of the Higgs boson. Unlike the ggF process, the VBF production process has very small theoretical errors. Two categories are defined for a high purity of VBF produced events, and a multivariate analysis is employed based on the kinematics of the diphoton and dijet systems. Details on the VBF categories are described in Sec. 4.4.2.

4.1 Datasets

4.1.1 Data Samples

For this analysis, the full 2012 dataset taken with the ATLAS detector at 8 TeV is used. The data was recorded using a trigger seeded by two clusters in the EM calorimeter (`EF_g35_loose_g25_loose`).

This corresponds to a recorded luminosity of 20.3 fb^{-1}. A good run list is then applied which removes 0.3% of events.

4.1.2 Signal Simulation Samples

The Higgs boson signal samples are produced for five productions modes: gluon-gluon fusion (ggF), vector boson fusion (VBF), WH, ZH, and $t\bar{t}H$. These samples are produced for masses from 100 GeV to 150 GeV at 5 GeV intervals. The simulation details of the different production modes is given below, and a summary of the process cross sections is given in Table 4.1.

The ggF samples are produced using POWHEG [48, 49] interfaced with PYTHIA8 [50] for Higgs boson decay, showering, hadronization, and underlying event. POWHEG produces events inclusively at next-to-leading order (NLO) in QCD tuned to next-to-

next-to-leading order (NNLO) order with soft-gluon resummations that are accurate at next-to-next-to-leading log (NNLL) [51, 52, 53]. These samples are then normalized to NNLO calculations [15, 14, 17, 18, 19, 20] in QCD with NLO electro-weak corrections applied [54, 55]. VBF samples are also produced with POWHEG [56] interfaced with PYTHIA8 and are normalized to NLO QCD and EW calculations [57, 58, 59] with approximate NNLO QCD corrections applied [60]. $t\bar{t}H$ samples are generated with POWHEG using the matrix elements generated from Helac-NLO [61]. Together, this generation is known as PowHel [62]. $t\bar{t}H$ events are then showered with PYTHIA8. These samples are only generated for mass points between 115 GeV and 135 GeV inclusively. All three of these samples, ggF, VBF, and $t\bar{t}H$, are produced with the CT10 [63] parton distribution function (PDF) and use the tune 11, or the ATLAS AU2-CT10 tune, in PYTHIA8 to simulate the underlying event.

The associated Higgs boson production with W and Z bosons are fully generated with PYTHIA8. PYTHIA8 was used also for the Higgs boson decay, showering, hadronization, and underlying event model. For these samples the internal PYTHIA tune 5, or 4C tune, described in Ref. [64] is used. The WH and ZH samples are normalized to NNLO calculations [65], and both samples include NLO EW radiative corrections [66]. Both the WH and ZH signal samples use the CTEQ6L1 [67] PDF.

Stable particles after showering and hadronization are defined as those with lifetimes longer than 10 ps. These are passed through GEANT4 [68], which simulates the ATLAS detector. Events are then digitized, which simulate the detector response. Then pile-up interactions are added to the events. These pile-up events are minimum bias events generated with PYTHIA8. The number of pile-up events added to the signal simulations is sampled from a Poisson distribution with a mean equal to the average number of interactions per bunch crossing, μ_{BCID}, at the LHC. The final step in simulation is reconstruction. Here, the simulated detector signals are passed

through ATLAS reconstruction exactly the same way data is.

In order to calculate the expected number of signal events in the dataset, the $H \to \gamma\gamma$ branching ratio must also be taken into account. The branching ratio has been calculated as described in Ref. [21] using the programs HDECAY [27, 69, 70] and PROPHECY4F [71, 72, 73]. First, all Standard Model allowed decay channels, as described in Sec 1.3.2, are calculated with HDECAY. The $H \to \gamma\gamma$ branching ratios are calculated at NLO in QCD [17, 74, 75, 76, 77, 78, 79], and the NLO electroweak corrections are interpolated from a grid of calculations presented in Ref. [55]. Then PROPHECY4F is used to calculate just the $H \to WW/ZZ \to 4f$ partial widths. The total Higgs boson width is then calculated as follow:

$$\Gamma_H = \Gamma_H^{HDECAY} - \Gamma_{ZZ}^{HDECAY} - \Gamma_{WW}^{HDECAY} + \Gamma_{4f}^{PROPHECY4F}, \tag{4.1}$$

and the corresponding branching ratio for $H \to \gamma\gamma$ is calculated from this full width,

$$BR_{H\to\gamma\gamma} = \frac{\Gamma_{\gamma\gamma}}{\Gamma_H}. \tag{4.2}$$

The higher order corrections for the $H \to \gamma\gamma$ branching ratio are estimated to be $<1\%$ [21]. Calculated partial widths for $H \to \gamma\gamma$ for different mass points are shown in Table 4.2.

M_H [GeV]	σ_{ggF} [pb]	σ_{VBF} [pb]	σ_{WH} [pb]	σ_{ZH} [pb]	$\sigma_{t\bar{t}H}$ [pb]
100	29.68	1.988	1.447	0.8102	0.2433
105	27.01	1.897	1.242	0.7022	0.2133
110	24.70	1.809	1.071	0.6125	0.1871
115	22.66	1.729	0.9266	0.5358	0.1651
120	20.86	1.649	0.8052	0.4710	0.1459
125	19.27	1.578	0.7046	0.4153	0.1293
130	17.85	1.511	0.6169	0.3671	0.1149
135	16.57	1.448	0.5416	0.3259	0.1024
140	15.42	1.389	0.4768	0.2898	0.09150
145	14.46	1.333	0.4216	0.2583	0.08199
150	13.55	1.280	0.3728	0.2308	0.07361

Table 4.1: Higgs boson production cross sections for 8 TeV as reported by the LHC Higgs Cross Section Working Group [21]. Values stated here are used to normalize the signal simulation samples.

M_H [GeV]	$H \to \gamma\gamma$ Branching Ratio
100	1.58E-03
105	1.77E-03
110	1.95E-03
115	2.11E-03
120	2.23E-03
125	2.28E-03
130	2.24E-03
135	2.12E-03
140	1.93E-03
145	1.67E-03
150	1.36E-03

Table 4.2: $H \to \gamma\gamma$ Standard Model branching ratios as reported by the LHC Higgs Cross Section Working Group [21].

4.2 Object Selection

4.2.1 Photons

Photons are first reconstructed from energetic clusters in the EM calorimeter. They are separated during reconstruction into converted and unconverted photons, where a converted photon is a photon which pair-produces before reaching the EM calorimeter. The converted photons are those for which at least one reconstructed track in the inner detector can be matched to the EM cluster in the calorimeter. Clusters with

no tracks matched to them are classified as unconverted photons. Identification of photons is done using variables which are built from the shower shapes within the EM calorimeter and the amount of leakage energy which enters into the Tile calorimeter. The shower shape variables are defined below:

R_{had1}: Ratio of transverse energy, E_T, deposited within the first sampling layer of the Tile calorimeter to the full transverse energy of the cluster. This is used in the region $|\eta|$ <0.8 and $|\eta|$ >1.37.

$$R_{had1} = \frac{E_T^{had1}}{E_T} \tag{4.3}$$

R_{had}: Ratio of E_T in the entire Tile calorimeter to the E_T of the cluster. This is used in the η regions where R_{had1} is not.

R_η: Ratio of cell energies in 3x7 cells to 7x7 cells, both centered on the cluster. This measures the spread of energy in η.

R_ϕ: Ratio of cell energies in 3x3 cells to 3x7 cells, both centered on the cluster. This measures the spread of energy in ϕ; however, this spread is expected to be wider for converted photons due to the magnetic field, and, thus, is less powerful in photon/electron discrimination than R_η.

$e277$: Cell energy in a block of 7x7 cells.

w_{eta2}: Lateral width of the shower in η using 3x5 blocks of cells.

$$w_{eta2} = \sqrt{\frac{\sum E_i \eta_i^2}{\sum E_i} - (\frac{\sum E_i \eta_i}{\sum E_i})^2} \tag{4.4}$$

f_{side}: Front side energy ratio is the fraction of shower energy outside the core of three strips but within seven strips.

w_{tot}: Total shower width in the first layer of the EM calorimeter.

ΔE: Difference in energy between the second maximum in the EM strip layer and the minimum value found between the first and second maxima.

E_{ratio}: Ratio of the difference in energies from the largest and second largest deposits in the EM calorimeter to the sum of these energies.

Photons must first pass a series of preselection cuts before they are considered photon candidates. Within this preselection are

- Fiducial Cuts. Photons candidates are required to have a p_T >25 GeV and to be within the region $|\eta|$ <2.37. Furthermore, due to deteriorated photon performance around the transition region between the barrel and endcap calorimeters, 1.37< $|\eta|$ <1.56 is also excluded.

- Quality Cuts. The photon must pass an object quality requirement ensuring the cells within a photon's EM cluster aren't bad, dead, or have high noise. Those photons receiving a majority of their energy from 'bad' calorimeter cells are removed.

- Ambiguity Removal. An ambiguity removal is required which removes any converted photons with reconstructed tracks within the Pixel layer where the first Pixel layer was not properly working.

- Photon ID Requirement. The photons must pass a 'loose' photon ID requirement based on shower shapes within the second layer of the EM calorimeter [80] as well as the amount of energy deposited in the Tile calorimeter. Converted and unconverted photons are treated the same.

At this point, only events with at least two 'good' photons are kept, meaning at least two photons have passes all the cuts listed above. Further selections are then applied to the Higgs boson diphoton candidates.

- The leading and subleading photons are required to have $p_T/m_{\gamma\gamma}$ >0.35 (0.25) respectively.

- Photons at this point must pass a 'tight' photon ID requirement [80]. Here the shower information from the strip layer in the EM calorimeter is also included and converted and unconverted photons are treated differently.

- Both photons must pass a calorimeter isolation E_{iso} <6 GeV. The calorimeter isolation energy is defined as the amount of energy within a cone of ΔR =0.4, excluding a central region of 0.125 x 0.175 in η x ϕ which accounts for the photon's energy [81]. This central region exclusion does not always account for the photon's full energy, so the calorimeter isolation is corrected for energy leakage outside of this region. Furthermore the isolation energy is corrected event by event for pileup and underlying event by using the same calorimeter cells to seed a k_t clustering algorithm [82, 83] with a size parameter of ΔR =0.5. This technique was first developed in Refs [84, 85].

- An additional track isolation is also imposed: E_{iso}^{track} <2.6 GeV, where E_{iso}^{track} is defined as the scalar p_T sum of tracks coming from within 15 mm of the diphoton vertex [86]. Tracks are required to have p_T >1 GeV and to be within ΔR <0.2 of the photons in order to be counted in the track isolation. If the photon is converted, the conversion tracks are subtracted before the isolation requirement.

4.2.2 Diphoton Primary Vertex

The diphoton primary vertex is identified using both the EM calorimeter's resolution and the inner detector tracking system. This selected primary vertex is important for the diphoton invariant mass calculation, the selection of jets by way of the jet vertex fraction (JVF) described in the next section, and the calculation of the track isolation as mentioned in the photon object selection. A common interaction point is found first by using a Neural Network algorithm (NN) based on the hybrid primary vertex variable which uses the position for each photon candidate using calorimetric pointing and any track hits in the inner detector if the photon was converted. Additionally, the NN depends on the sum of the squared p_T of tracks associated with each primary vertex: $\sum p_T^2$, as well as the scalar sum associated with each primary vertex: $\sum p_T$. Finally, the NN also depends on the $\Delta\phi$ angle between the primary vertex, calculated with the vector sum p_T of tracks, and the diphoton system. The η (and therefore the p_T) of the two Higgs candidate photons is then corrected using the selected primary vertex.

4.2.3 Jets

Jets are reconstructed using topological clusters [87, 88, 89] within the calorimeters. Jets are clustered according to the anti-k_t algorithm [90] with a distance parameter $R = 0.4$. p_T requirements are applied depending on the location of the jet; central jets with $|\eta|$ <2.4 are required to have p_T >25 GeV, while jets outside that region are required to have p_T >30 GeV. Jets are also required to be within $|\eta|$ <4.5. To reject pileup jets, a jet vertex fraction (JVF) [91] cut is applied. The JVF is defined as the sum of p_T of tracks matched to the jet and originating from the diphoton vertex divided by the sum of p_T of tracks matched to the jet coming from all primary vertices:

$$JVF(jet_i, PV_j) = \frac{\sum_k p_T(track_k^{jet_i}, PV_j)}{\sum_n \sum_l p_T(track_l^{jet_i}, PV_n)} \tag{4.5}$$

All jets within the tracking region of the inner detector, $|\eta|$ <2.4 must pass a JVF cut of |JVF| >0.50.

4.2.4 Electrons

Electrons are reconstructed using both EM calorimeter clusters and their associated tracks from the inner detector. They are required to pass the fiducial cuts $|\eta|$ <2.47 and p_T >15 GeV, where the electron energy is calibrated using the same method as the photon calibration. Electrons must pass the 'loose' ID criteria using a likelihood method [92] based on the electron's shower shapes in the EM calorimeter as well as its energy leakage into the Tile calorimeter. Both a calorimeter and a track isolation cut are imposed on electron candidates. The calorimeter isolation energy within ΔR <0.4 divided by the electron's p_T must be less than 0.2. For the track isolation, the sum

of track p_T within ΔR <0.2 of the electron's track divided by the electron's p_T must be less than 0.15.

4.2.5 Muons

Muons are required to be within $|\eta|$ <2.7 and to have p_T >10 GeV. In addition, muons must have an impact parameter ($|z_0|$) within 10 mm of the interaction point, and to have a transverse impact parameter of less than 1 mm. Muons are required to have at least one hit in the Pixel detector and at least 4 hits in the SCT detector within the inner detector. If the muon is within 0.1< $|\eta|$ <1.9, then the muon is also required to have at least 5 hits in the TRT detector. A 'loose' ID selection is applied to candidate muons. Muons are then required to be isolated using both a calorimetric and track isolation. The energy within a cone of ΔR <0.4 divided by the muon's p_T must be less than 0.2, and the sum p_T of tracks within ΔR <0.2 divided by the muon's p_T must be less than 0.15.

4.2.6 Overlap Removal Selection

During reconstruction, particles can be reconstructed as multiple different objects; for example, a photon can be reconstructed as an electron and/or a jet. To avoid double counting, an object overlap removal selection is done after the selection of 'good' objects as described above. The overlap removal is done in the following order:

- Electrons within ΔR <0.4 of selected photons are removed.
- Jets within ΔR <0.4 of a selected photon or within ΔR <0.2 of a selected electron are removed.
- Muons within ΔR <0.4 of a selected photon or within ΔR <0.4 of a selected jet are removed.

4.2.7 Missing Transverse Energy

In ATLAS, the missing transverse energy, or E_T^{miss}, is reconstructed by summing up all object p_T, and then applying the conservation of momentum in the transverse plane. In order to maintain a consistent treatment of photons, the object selection in building the E_T^{miss} must follow similar selections as the diphoton analysis. In the calculation, each object enters into the sum only once even if it is reconstructed as both a photon and an electron. Therefore, it is important in the context of $H \to \gamma\gamma$ that photons are given priority over electrons and enter into the sum first. Furthermore, the 'tight' photon ID requirement is applied to the photons before they enter into the sum. Finally, the calibration of photons for E_T^{miss} must match the calibration of photons in the $H \to \gamma\gamma$ analysis presented here.

It is well known that the resolution of E_T^{miss} goes as the square root of the total energy in the calorimeter, and significant degradation in the resolution has been observed in 2012. Therefore, for the categorization of events in this analysis, the E_T^{miss} significance is used. The E_T^{miss} significance is defined as the ratio E_T^{miss} over the resolution of the E_T^{miss}.

4.2.8 MC Corrections

The following corrections are applied to the MC signal samples:

- The pileup up simulation in the signal samples does not exactly match that measured in ATLAS data, so MC samples are reweighted according to the average number of interactions per bunch crossing (μ_{BCID}) seen in data. This is proportional to the instantaneous luminosity. Before the reweighting is done, a μ_{BCID} scaling factor of 1.09 is applied to again match the conditions observed in data. The distribution of μ_{BCID} measured in 2012 data and the distribution

for simulation before reweighting and scaling are shown in Fig. 4.1.

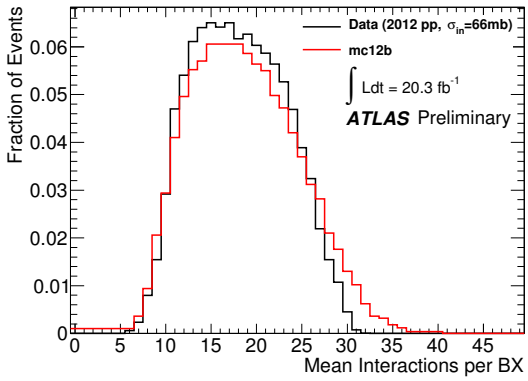

Figure 4.1: The luminosity-weighted distributions of the average number of interactions per bunch crossing in 2012 data and the MC simulation production before reweighting [93].

- A vertex reweighting is done to MC samples, as they were generated with a slightly wider beamspot. MC samples have a beam spot spread of 66 mm, while in data, the beam spot width is 48 mm as shown in Fig. 4.2.

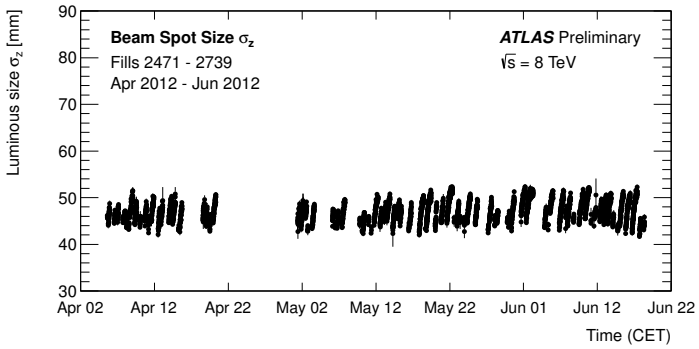

Figure 4.2: The offline beamspot reconstructed width in z in 2012. The reconstruction of the beamspot uses a likelihood fit to primary vertices, as describe in Ref. [94], where the primary vertices used had at least five or more tracks associated with them.

- The ggF signal samples have a p_T reweighting applied to them which reweights the p_T spectrum from POWHEG to that calculated by HRES2.1 [95]. HRES2.1 calculates the p_T spectrum to NNLO+NNLL precision and includes both the

effect of exact top and bottom masses and their interference [96]. Dynamic renormalization and factorization scales ($\mu = \sqrt{m_H^2 + p_{T,H}^2}$) are used in the calculation.

It was shown that reweighting to the inclusive p_T spectra from HRes2.1 affects the overall jet multiplicity in the sample, in particular, resulting in too few events with ≥2 jets. Therefore, two sets of p_T weights are used based on the number of truth jets with p_T >25 GeV (excluding jets that overlap with either of the photons from the Higgs boson decay). One set of weights is for events with 0 or 1 truth jets, and the other set is for events with ≥2 truth jets. It was checked that the resulting p_T distribution after reweighting for the case of ≥2 jets matches the p_T distribution from the HJJ [97] process in Powheg produced using the MiNLO (Multi-scale improved NLO) procedure [98, 99], which generates H+2 jet events at NLO. Furthermore, after the reweighting of all events using this two-binned HRes2.1 method, the jet multiplicities follow well the NNLO predictions from JetVHeto [100, 101, 102].

- The VBF, WH and ZH p_T spectra are reweighted to match the NLO p_T distribution from the MC program HAWK [103, 104].

- The decay of the Higgs boson is handled entirely by Pythia8, which by default includes Dalitz decays where $H \to \gamma\gamma^* \to \gamma f \bar{f}$ when set to decay the Higgs boson to two photons. It was found that about 5.74% of events at a Higgs boson mass of 125 GeV were decayed in this manner [105], which is relatively close to the calculated Dalitz decay width presented in Ref. [106]. These decays are not included in the branching fraction used for $H \to \gamma\gamma$, so they are removed from the initial number of events in the signal samples in order to correctly normalize the simulated signal to theoretical predictions. In data, however,

a small number of these Dalitz decays will pass the full event selection, and therefore, these Dalitz decay events are retained in the final signal samples for calculating the expected number of events and for the signal modeling described in Section 4.5.1. After selection, only 0.3% of simulated signal events are from Dalitz decays.

- The ggF signal sample is reweighted to include the effects of destructive interference between the ggF signal and the $gg \to \gamma\gamma$ background process. Interference effects are computed in bins of $\cos\theta^*$ and utilize both LO [107] and NLO [108] predictions. The NNLO effect is expected to be between the LO and NLO predictions, so the average of the two effects is applied to the ggF sample. One exception is for $\cos\theta^* > 0.7$, where, due to the applied analysis cuts, the LO weight is 0. In this region, only the NLO interference effect is applied to the signal sample. Interference effects result in a 2.5% reduction in expected ggF signal events.

- Correction factors are applied to the calorimeter shower shape variables before applying the photon identification cuts. These factors correct for shower shape differences between the simulated showers and those observed in inclusive photon samples in data.

- The energy of the photons is smeared in order to match the resolution of the simulated signal samples to the resolution seen in data.

4.3 Event Selection

A candidate Higgs boson event is selected first on the basis of the ATLAS trigger. Only events which triggered on two EM clusters passing loose photon ID require-

ments described in Sec. 4.2.1. and having $E_T > 35$ GeV for the leading cluster and $E_T > 25$ GeV for the subleading cluster. The corresponding ATLAS trigger is `EF_g35_loose_g25_loose`. The efficiency for this trigger is $99.4 \pm 0.2\%$ [109]. Then an event is required to have been recorded during a time when the full ATLAS detector was turned on and all components were functioning properly. To ensure this, a good-run-list is applied which removes data taken when at least one subsystem was not performing optimally. [1]

Flags for both the EM calorimeter and the Tile calorimeter are also stored which indicate the detector quality during each event. For example, if information from part of a detector is missing or the data is somehow corrupted, the event is flagged and then rejected. For a subset of runs, the Tile calorimeter had a hot cell, meaning it had a particularly high noise threshold. This cell was not masked in the Tile detector database, and therefore events which are affected by this hot cell must be removed by hand.

To apply the same reduction in the monte carlo (MC) samples, events are given a random run number, and if it equals the run numbers in data which had the unmasked noisy calorimeter cell, then the event is rejected from the MC events. This ensures a correct Higgs boson cross section measurement within data. During a portion of the runs in 2012, the Tile calorimeter had a channel with data corruption and an incorrect rejection threshold. This channel, channel 5 of LBC24, would create fake energy of 400 GeV in the cell. In some instances this was not masked, so any event in which this channel is saturated is rejected.

Following the photon object selection outlined in the previous section, events are required to have at least two selected photons, which are both isolated and both pass the 'tight' ID cuts. The invariant mass of the two selected photons, calculated by

[1] The good-run-list used here is the data12_8TeV.periodAllYear_DetStatus-v61-pro14-02_DQDefects-00-01-00_PHYS_StandardGRL_All_Good.xml.

$$m_{\gamma\gamma} = \sqrt{2E_{T1}E_{T2}(cosh\Delta\eta - cos\Delta\phi)} \tag{4.6}$$

is required to be within 105< $m_{\gamma\gamma}$ <160 GeV. This is to limit the mass range to a region where the background processes follow a continuous falling distribution. The mass is restricted specifically to be above 105 GeV to avoid any turn-on effects caused by the relative p_T requirements described in the photon object selection above.

4.4 Event Categorization

To utilize the full potential of the 2012 data, events are categorized based on sensitivity to different measurements. When measuring the mass of the Higgs boson, events are categorized into regions of good and worse mass resolutions, and into regions of higher and lower ratios of expected signal to background events. This categorization is based on the photons' locations in η within the EM calorimeter, the photons' conversion status, and on the orthogonal component of the diphoton p_T to the 'thrust-axis' calculated as

$$p_{Tt} = |\vec{p}_T^{\,\gamma\gamma} \times \hat{t}|, \text{ where } \hat{t} = \frac{\vec{p}_{T1} - \vec{p}_{T2}}{|\vec{p}_{T1} - \vec{p}_{T2}|} \text{ and } \vec{p}_T^{\,\gamma\gamma} = \vec{p}_{T1} + \vec{p}_{T2} \tag{4.7}$$

and shown in Fig. 4.3.

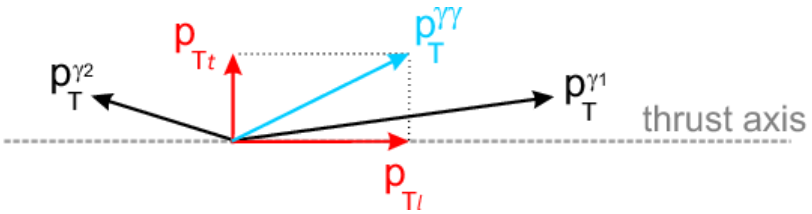

Figure 4.3: The transverse component, or p_{Tt} of the diphoton p_T.

4.4.1 Mass Categories

The mass measurement analysis has ten categories:

- **C1:** Both photons are unconverted, both are in the central region of the detector $|\eta_{S2}|$ <0.75, and the diphoton system has p_{Tt} <70 GeV.
- **C2:** Both photons are unconverted, both are in the central region of the detector $|\eta_{S2}|$ <0.75, and the diphoton system has p_{Tt} >70 GeV.
- **C3:** Both photons are unconverted, at least one photon is in the region $|\eta_{S2}|$ >0.75, and the diphoton system has p_{Tt} <70 GeV.
- **C4:** Both photons are unconverted, at least one photon is in the region $|\eta_{S2}|$ >0.75, and the diphoton system has p_{Tt} >70 GeV.
- **C5:** Both photons are unconverted and at least one photon is in the region 1.3< $|\eta_{S2}|$ <1.75
- **C6:** At least one photon is converted, both are in the central region of the detector $|\eta_{S2}|$ <0.75, and the diphoton system has p_{Tt} <70 GeV.
- **C7:** At least one photon is converted, both are in the central region of the detector $|\eta_{S2}|$ <0.75, and the diphoton system has p_{Tt} >70 GeV.
- **C8:** At least one photon is converted, at least one photon is in the region $|\eta_{S2}|$ >0.75, and the diphoton system has p_{Tt} <70 GeV.
- **C9:** At least one photon is converted, at least one photon is in the region $|\eta_{S2}|$ >0.75, and the diphoton system has p_{Tt} >70 GeV.
- **C10:** At least one photon is converted and at least one photon is in the region 1.3< $|\eta_{S2}|$ <1.75

4.4.2 Coupling Categories

The categories for the Higgs boson coupling measurement were chosen to isolate various Higgs boson production modes. Therefore, signal strengths measured in each category are essentially measurements of the Higgs boson coupling to particular objects. Categories are optimized for $t\bar{t}H$ production, associated Higgs boson production where the V boson decays leptonically or hadronically, associated Higgs boson production where the Z boson decays into neutrinos, and VBF production.

VBF Categories

The VBF process, described in Sec. 1.3.1, is characterized by two forward/backward jets, separated in η. The Higgs boson is produced in the rapidity gap between these two jets, and with little or no QCD activity from the hard scatter in the central region between the two jets. This is because in the VBF process, the Higgs boson is produced by interactions of the weak bosons, either two Ws or two Zs. This production mechanism for the Higgs boson provides a good measurement of the weak couplings to the Higgs boson.

For the categorization of VBF events, a Boosted Decision Tree (BDT) is used within the TMVA (Toolkit for Multivariate DATA Analysis with ROOT) [110] environment. Two categories are defined, a 'Tight' VBF category with a high purity of VBF events, and a 'Loose' VBF category with a slightly lower purity of VBF events.

A decision tree is the sequential application of cuts involving one variable at a time, which divide a given sample of events into nodes after each cut is applied. The set of cuts is defined by using the variable and cut values at each splitting which creates the best separation between signal and background events. This splitting continues until a specified minimum number of events in a node is reached. The nodes which the final cuts divide events into are called classifier nodes, where they

are assigned the label of 'signal' or 'background' based on whether the majority of events are from the input signal or background sample. In the end, the phase space is divided into N hypercubes defined as signal-like or background-like, where N is the number of input variables used in the BDT. A schematic of a decision tree is shown in Fig. 4.4. A single decision tree is subject to statistical fluctuations, which can cause a tree to be unstable. Therefore, a boosted technique is employed, where a 'forest' of decision trees is created. Events are boosted between decision trees, meaning events are reweighted based on their identified input sample, signal or background, and the classification of the node they ended up in, again signal or background. Events which are misclassified receive a higher weight for the training of the next decision tree. The weights of the misclassified events are multiplied by a boost weight α defined using the misclassification rate, ϵ_{mis} of the previous tree as

$$\alpha = \frac{1 - \epsilon_{mis}}{\epsilon_{mis}}. \tag{4.8}$$

All weights in the sample are subsequently renormalized so that the overall sum of event weights is constant throughout. The output of a BDT is a single variable called the discriminant, which quantifies the likelihood that an event is a signal event. A value of +1 means an event is very signal-like, while a value of -1 means an event is very background-like.

The following parameters are used for the BDT:

- NTrees = 850; The number of decision trees.
- nEventsMin = 50; The number of events in a node at which point the splitting stops.

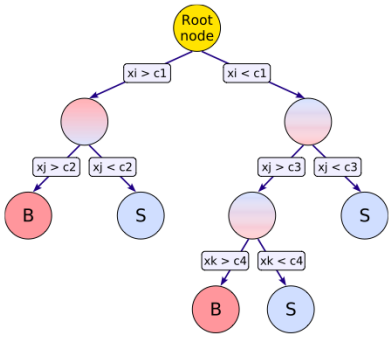

Figure 4.4: A schematic of the node splittings in a single decision tree [110].

- nCuts = 20; The number of scanned steps through each variable used during the cut optimization for each node.
- MaxDepth = 4; The maximum node depth allowed in a decision tree.

The BDT is first trained on signal and background samples using supervised learning. In supervised learning, two known input samples, one labeled as signal and the other as background, are given to the tool. Then a series of node splittings occur to separate the signal sample from the background sample, thus generating the BDT. A BDT is considered trained once the decision trees are created, and it can be used to classify events in other samples as signal or background like. Here, the signal samples are the VBF simulated samples described earlier, and the background sample is a mix of simulated $\gamma\gamma$ non-resonant events generated with Sherpa [111] and a control sample from data where the photon isolation cut was reversed, meaning one or both photons fails at least one of the calorimetric or track isolation requirements. This reverse isolation sample (RevISO) models the γ-*jet* and *jet*-*jet* background processes. Because the isolation cut is reversed, this control sample is completely orthogonal to the Higgs boson candidate events in data. The simulated sample is combined with the RevISO sample according to the fractions of γ-*jet* and *jet*-*jet* events observed in the data sidebands.

The goal of the BDT is to separate events produced by vector boson fusion from all other events. In particular, VBF events not only need to be separated from background events, but also from ggF events, which have the highest cross section of all Higgs boson production processes. However, it was shown that for most variables requiring two or more jets, that the ggF distributions follow the same shapes as that of the background processes. Therefore, the BDT can be trained using just non-resonant background samples, and the resulting BDT discriminant will also select out events from ggF, effectively providing a more pure VBF signal sample. The Sherpa+RevISO background sample is then reweighted to better match the background distribution in the data. The comparison is made with data in the sideband regions, meaning the signal region from $m_{\gamma\gamma} = 121$ GeV to $m_{\gamma\gamma} = 131$ GeV is excluded in the comparisons. The reweighting function is taken from a fit to the ratio of data sidebands to the Sherpa-RevISO sample in the distribution of the subleading jet's pseudorapidity. Reweighting to different variable distributions was investigated, and it was shown that reweighting to the subleading jet η produced the best expected signal significance as measured by

$$\sigma_{VBF} = \sqrt{2 \times (N_{VBF} + N_{ggF} + N_{Background} \times ln(1 + \frac{N_{VBF}}{N_{ggF} + N_{Background}}) - N_{VBF}} \qquad (4.9)$$

For training, only half of each simulated sample is used. The other half is then used as an independent sample to find the optimal BDT discriminant cuts for the VBF categories. The full RevISO sample is used for both training and optimization due to the small statistical size of the sample. If a BDT is trained with too many input variables, or parameters, on too few events, a situation called overtraining can occur. Overtraining does not allow the BDT the flexibility to properly separate signal and background events from any sample other than the exact samples it was trained on;

therefore the performance with the training samples will be a false estimator of the BDT's performance on any independent samples. Checks for overtraining are done using the Kolmogorov-Smirnov test (KS-test). The KS-test is a way to determine how similar two datasets are, and here the test is applied to the BDT discriminant distribution from the training samples and the BDT discriminant distribution from an independent validation sample. KS factors are calculated as the maximum difference in the cumulative fraction functions of a variable for two different samples. The KS-test is calculated for both the background and signal samples independently. In this case the signal validation sample is the other half of events that were not used in the training of the BDT. The background validation sample is the other half of the $\gamma\gamma$ events not used in the training combined with the RevIso sample. A KS-test value of close to 1 is considered good, while a very small KS-test value is evidence of overtraining.

Before events enter the BDT, they must first pass a set of preselection cuts. Events are required to have at least two selected jets with a sizeable rapidity separation, $\Delta\eta_{jj}$ >2.0, and a good balance between the dijets system and the diphoton system, $|\eta^*_{\gamma\gamma}|$ <5, where $|\eta^*_{\gamma\gamma}|$ is defined as

$$|\eta^*_{\gamma\gamma}| = |\eta_{\gamma\gamma} - \frac{1}{2} \times (\eta_{j1} + \eta_{j2})| \tag{4.10}$$

Six variables are used in the BDT:

- m_{jj}: The invariant mass of the two tagged jets
- $\Delta\eta_{jj}$: The difference in pseudorapidity between the two tagged jets
- p_{Tt}: The perpendicular component of the diphoton p_T with respect to the diphoton thrust axis

- $\Delta\phi_{\gamma\gamma,jj}$: The difference in azimuthal angle between the diphoton system and the dijet system
- $\Delta R^{min}_{\gamma,j}$: The minimum ΔR between the leading or subleading photon and the leading or subleading jet
- η^*: The difference in psuedorapidity between the diphoton system and the average of the jets

These variables are chosen for their discriminating power, and for their weak correlation with the final fitting parameter, the diphoton invariant mass. For most variables, the ggF distributions follow more closely the data sideband distributions.

The cuts on the BDT discriminant which define the 'Tight' and 'Loose' VBF categories are optimized based on the expected VBF significance as defined in Equation 4.9. The optimal cuts on the discriminant are BDT$>$ 0.83 for 'Tight' and $0.3< BDT <0.83$ for 'Loose'.

$t\bar{t}H$ Categories

While the ggF production proceeds through a top quark loop, and is therefore indirectly sensitive to the large top Yukawa coupling, the $t\bar{t}H$ production mechanism is directly sensitive to the coupling. The associated top quarks decay into W bosons and b-quarks, so two categories are defined based on the decay products of the W bosons: a leptonic category and a hadronic category.

In addition to the W bosons produced, b-quarks are also produced in the decay of the top quarks. As such, b-tagging jets are very important for these categories. In this analysis, the MV1c tagger at various working points is used. The MV1 tagger algorithm [112] is a neural network algorithm which relies on three different algorithms [113]: a likelihood ratio algorithm based on impact parameter, a secondary

vertex based algorithm, and a third algorithm called JetFitter, which reconstructs a common line between the primary vertex and the heavy-quark vertices. Working points are defined by the efficiencies of the tagger to correctly identify b-quark jets in $t\bar{t}$ events where jets satisfy p_T >20 GeV and $|\eta|$ <2.5.

The leptonic $t\bar{t}H$ category requires at least one selected lepton as defined in Section 4.2. In addition, either one b-tagged jet with E_T^{miss} >20 GeV, or two b-tagged jets are required. All b-tagged jets in this leptonic category use the MV1c tagger with 80% efficiency. In some cases, an electron from a Z/γ^* event is mis-identified as a photon. Therefore, if electrons are present in the event, the invariant mass of that electron and each of the photons individually ($m_{\gamma e}$) is checked. Any event with $m_{\gamma e}$ in the mass range of the Z boson, between 84 GeV and 94 GeV, is rejected.

The hadronic $t\bar{t}H$ category encompasses three subsets of $t\bar{t}H$ events:

- Six selected jets with at least two b-tagged jets at the 80% working point and a lepton veto
- Six selected jets with p_T >30 GeV with at least one b-tagged jet at the 60% working point and a lepton veto
- Five selected jets with p_T >30 GeV with at least two b-tagged jets at the 70% working point and a lepton veto

These three different selections are combined in order to increase the $t\bar{t}H$ signal yield while also restricting the contamination from the other Higgs boson production mechanisms, particularly that of ggF, which has a large theory uncertainty in selections with high jet multiplicity.

VH Categories

Four different VH categories are defined for the measurement of the weak couplings to the Higgs boson. Two categories, an E_T^{miss} category and a hadronic category, are aimed at both ZH and WH. A single lepton category is defined for WH events, and a dilepton category is defined to isolate ZH events.

The E_T^{miss} category requires an E_T^{miss} significance >5 and p_{Tt} >20 GeV. Additionally, a veto is applied if either selected photon passes the likelihood electron 'loose' ID requirements.

The hadronic category is defined for events in which the W or Z boson decays into jets. Therefore, the dijet invariant mass is expected to be consistent with the masses of the W and Z boson, 60< m_{jj} <110 GeV, and the jets are required to be close to each other with $\Delta\eta_{jj}$ <3.5. The following selections are also applied: p_{Tt} >70 GeV and $|\eta_{\gamma\gamma} - \eta_{jj}|$ <1.0.

The WH single lepton category requires the presence of at least one lepton, and an E_T^{miss} significance > 1.5. If an electron is present, a veto on the invariant mass of the leading electron and either of the selected photons must not be within the mass range of the Z: 84 GeV< $m_{e\gamma}$ <94 GeV. An event only enters the single lepton category if neither of the selected photons passes the likelihood electron 'loose' ID requirements.

The ZH dilepton category requires at least two leptons of the same flavor and opposite charge, and a dilepton mass consistent with the Z mass: 70 GeV< m_{ll} <110 GeV.

The twelve coupling categories are summarized below, and the expected signal events for a Higgs boson mass of 125 GeV divided by category and production process are presented in Table 4.3.

- **C1:** Both photons are within the region $|\eta_{S2}|$ <0.95 and the diphoton system has p_{Tt} <70 GeV.

- **C2:** Both photons are within the region $|\eta_{S2}|$ <0.95 and the diphoton system has p_{Tt} >70 GeV.

- **C3:** At least one photon is within the region $|\eta_{S2}|$ >0.95 and the diphoton system has p_{Tt} <70 GeV.

- **C4:** At least one photon is within the region $|\eta_{S2}|$ >0.95 and the diphoton system has p_{Tt} >70 GeV.

- **C5 (VBF Loose):** At least two jets with a 0.3<BDT<0.83, where a preselection is applied of $\Delta\eta_{jj}$ ≥2.0 and $|\eta^*|$ <5.0.

- **C6 (VBF Tight):** At least two jets with a BDT>0.83, where a preselection is applied of $\Delta\eta_{jj}$ ≥2.0 and $|\eta^*|$ <5.0.

- **C7 (VH hadronic):** At least two jets with 60 GeV< m_{jj} <110 GeV, p_{Tt} >70 GeV and $|\eta_{\gamma\gamma} - \eta_{jj}|$ <1.

- **C8 (VH E_T^{miss}):** E_T^{miss} significance >5 and p_{Tt} >20 GeV.

- **C9 (WH leptonic):** At least one selected lepton and E_T^{miss} significance > 1.5.

- **C10 (ZH leptonic):** Two leptons of the same flavor and opposite charge and invariant mass in the range 70 GeV< m_{ll} <100 GeV.

- **C11 ($t\bar{t}H$ hadronic):** A lepton veto and six jets with either, p_T >25 GeV where two jets are btagged with the 80% working point, or p_T >30 GeV where one jet is btagged with the 60% working point. Or a lepton veto and five jets with p_T >30 GeV where two jets are btagged with the 70% working point.

- **C12 ($t\bar{t}H$ leptonic):** At least one lepton, where, if the lepton is an electron, the invariant mass of the electron and either candidate photon is not within the range 84 GeV< $m_{e\gamma}$ <94 GeV (an effective Z-veto), and either, one b-tagged jet with E_T^{miss} >20 GeV, or two b-tagged jets.

Category	Total	ggF	VBF	WH	ZH	$t\bar{t}H$	$b\bar{b}H$	tH
Inclusive	401.58	349.25	29.00	10.96	6.57	1.83	3.85	0.07
C1	138.38	127.75	5.51	2.14	1.39	0.18	1.41	-
C2	11.42	8.31	1.83	0.64	0.40	0.15	0.09	-
C3	212.55	194.87	8.76	4.02	2.51	0.23	2.15	-
C4	16.54	11.88	2.67	1.06	0.64	0.15	0.13	-
C5	9.31	3.80	5.36	0.06	0.04	0.01	0.04	-
C6	5.89	1.10	4.76	0.01	0.00	0.00	0.01	-
C7	3.26	1.49	0.11	0.99	0.62	0.04	0.02	-
C8	1.13	0.01	0.00	0.42	0.58	0.11	0.00	-
C9	1.75	0.00	0.00	1.57	0.11	0.06	0.00	-
C10	0.26	0.00	0.00	0.00	0.26	0.00	0.00	-
C11	0.50	0.04	0.00	0.00	0.01	0.42	0.00	0.03
C12	0.59	0.00	0.00	0.05	0.01	0.48	0.00	0.04

Table 4.3: Expected events for a Higgs boson mass of 125.4 GeV for the coupling category analysis with 8 TeV data. Events are divided by category and production process. The tH process is only considered for the two $t\bar{t}H$ categories.

4.5 Signal Model

4.5.1 Signal Model

As mentioned previously, Higgs boson signal samples are generated for eleven mass points between 100 GeV and 150 GeV. All five production modes are summed according to their respective cross sections before fitting. Because some Dalitz decays in data will still pass the event selection, Dalitz decay events in the signal MC are included in the samples for the fits. All weights are also applied to the samples before fitting. Each mass point is fit with a Crystal Ball (CB) function [114], which is composed of a narrow Gaussian with a wider tail towards lower masses, and is defined as

$$\mathcal{C}(m_{\gamma\gamma};\mu_{\mathrm{CB}},\sigma_{\mathrm{CB}},\alpha_{\mathrm{CB}},n_{\mathrm{CB}}) = N\cdot\begin{cases}\exp\left(-t^2/2\right) & \text{if } t > -\alpha_{\mathrm{CB}}\\ \left(\frac{n_{\mathrm{CB}}}{\alpha_{\mathrm{CB}}}\right)^{n_{\mathrm{CB}}}\cdot e^{-\alpha_{\mathrm{CB}}^2/2}\cdot\left(\frac{n_{\mathrm{CB}}}{\alpha_{\mathrm{CB}}}-\alpha_{\mathrm{CB}}-t\right)^{-n_{\mathrm{CB}}} & \text{otherwise}\end{cases}$$

where $t = (m_{\gamma\gamma}-\mu_{CB})/\sigma_{CB}$, N is the overall normalization, μ_{CB} and σ_{CB} are the peak position and width of the core Gaussian component, n_{CB} and α_{CB} are the parameters of the tail function. For all fits, n_{CB} is fixed to 10. A Gaussian with a wider width is then added to the CB function for the fits in order to model the outliers in the mass spectrum. The Gaussian has a peak position of μ_{GA} and a width of σ_{GA} which is related to σ_{CB} by a constant parameter κ_{GA}. This forces the additional Gaussian to be wider, and therefore, only fit to the outliers of the distribution and not to the full set of events. One more parameter, f_{CB}, is used for the overall normalization fraction of the CB function, and the normalization fraction of the Gaussian component is 1-f_{CB}. The full signal model can then be parameterized as the sum of the Crystal Ball ($\mathcal{C}$) and the Gaussian ($\mathcal{G}$)

$$\mathcal{F} = f_{CB} \cdot \mathcal{C}(m_{\gamma\gamma}, \mu_{CB}, \sigma_{CB}, \alpha_{CB}) + (1 - f_{CB}) \cdot \mathcal{G}(m_{\gamma\gamma}, \mu_{GA}, \kappa_{GA} \cdot \sigma_{CB}). \quad (4.11)$$

4.5.2 Global Resolution Model

Instead of fitting six different parameters for each of the eleven mass points, it was decided instead to relate these parameters between the different mass points. It was shown that the relationships for many of them were linear across the different Higgs boson mass points. The global resolution, defined in the following equations, is fit simultaneously to all mass points.

$$\mu_{CB}(m_H) = \mu_{CB}(m_H = 125GeV) + s_{\mu,CB} \cdot (m_H - 125GeV) \quad (4.12)$$

$$\mu_{GA}(m_H) = \mu_{GA}(m_H = 125GeV) + s_{\mu,GA} \cdot (m_H - 125GeV) \quad (4.13)$$

$$\sigma_{CB}(m_H) = \sigma_{CB}(m_H = 125GeV) + s_{\sigma,CB} \cdot (m_H - 125GeV) \quad (4.14)$$

α_{CB}, κ_{CB}, and f_{CB} are kept constant across all masses. This lessens the number of total fit parameters across all masses to nine. An example global fit for all mass points is shown in Fig. 4.5.

4.5.3 Signal Yields

Because the relationship between the signal yields at different mass points is shown to not be linear, the signal yields between the simulated mass points are interpolated by fitting a third order polynomial to the yields from the eleven mass points. An example of a polynomial fit to the signal yields at each mass point is shown in Fig. 4.6. This signal yield parameterization is then taken into account in the normalization of the

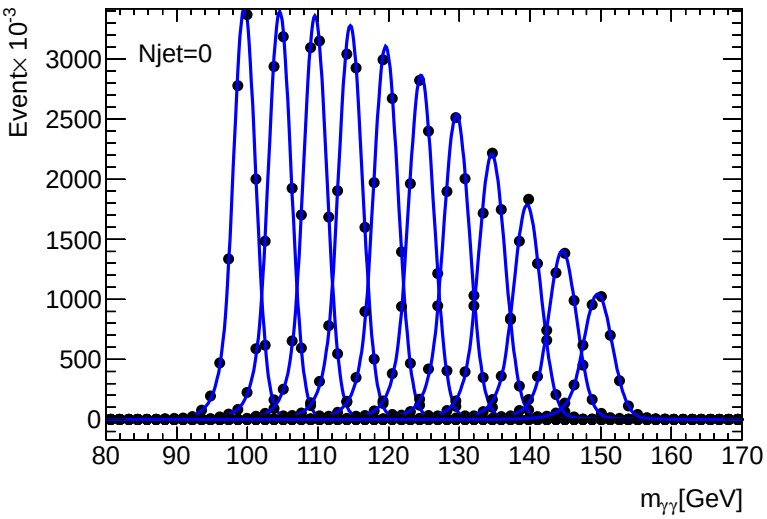

Figure 4.5: The simultaneous fit to each Higgs boson mass point. Parameters at each mass point follow a linear relationship.

global resolution fits. Once all parameters are fitted to the MC signal samples, they are then used in signal+background fits to the diphoton invariant mass distribution in data, where all signal shape parameters are kept constant. The expected signal yields are also kept constant, while the total fit yield in data is allowed to vary this expected yield by a factor μ. For the Standard Model, μ =1.

$b\bar{b}H$ Contribution

The $b\bar{b}H$ cross section for the inclusive case is on the order of the $t\bar{t}H$ cross section [115, 116]. Because the $b\bar{b}H$ cross section decreases rapidly as the b-jet p_T increases, it is not expected to have a large impact on the coupling analysis, and no MC samples are generated for this process. Nevertheless, $b\bar{b}H$ contributions are taken into account through the following prescription:

- The mass dependence is assumed to be similar to that of the $t\bar{t}H$ process.

- The signal efficiency is assumed to be the same as for ggF given the decrease in cross section with increasing jet p_T.

Therefore, the number of expected signal events from the $b\bar{b}H$ process is taken as

$$N_{b\bar{b}H}(m_H) = \frac{N_{t\bar{t}H}(m_H)}{N_{t\bar{t}H}(125.5)} \times \frac{N_{ggF}(125.5)}{\sigma_{ggF}(125.5)} \times \sigma_{b\bar{b}H}(125.5) \tag{4.15}$$

where $\sigma_{b\bar{b}H}$ and σ_{ggF} are taken from the LHC XS working group [21] and $\frac{\sigma_{b\bar{b}H}(125.5)}{\sigma_{ggF}(125.5)}$ =1.1%.

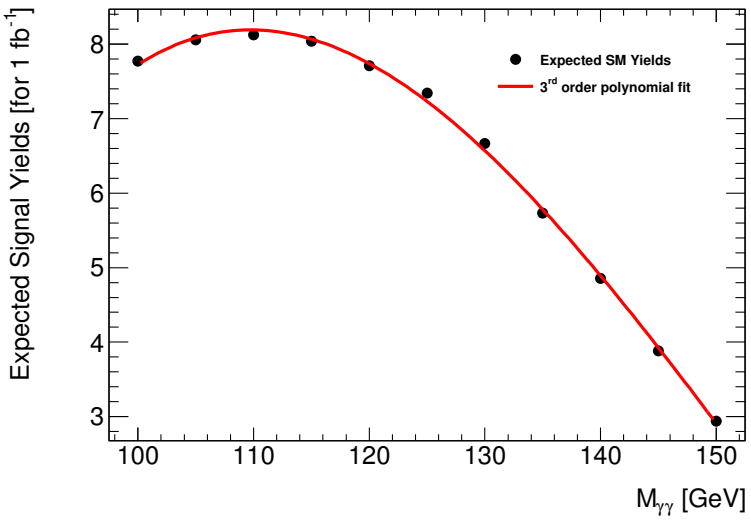

Figure 4.6: The expected signal yields at each mass point. A third order polynomial is fit to the values.

tH Contribution

The production of a Higgs boson in association with one top quark (tH) is expected to contribute up to 5% of the signal in the $t\bar{t}H$ categories. Two processes are included in the tH process: $tHjb$ and WtH.

4.6 Background Model

In order to reliably measure the number of signal events in data, both the shape and normalization of the background distribution must first be understood. This is done by fitting an analytical function to the background distribution in data. Multiple functions were tested on MC samples, and the final chosen background model is the function which introduces the least bias on the signal yield.

4.6.1 Background Monte Carlo Samples

Three background MC samples are used to simulate the main background processes: $\gamma\gamma$, γ-*jet*, *jet-jet*. The $\gamma\gamma$ and γ-*jet* samples are simulated with SHERPA with up to three QCD emissions modeled with the matrix element, while the *jet-jet* processes are simulated with PYTHIA. The three samples are combined based on the fractions measured within the data sidebands using a 2x2D technique: 77% $\gamma\gamma$, 20% γ-*jet*, 3% *jet-jet* [117].

A large number of statistics are needed for the background simulation so that the fitted functions aren't susceptible to statistical fluctuations. It is not reasonable to pass so many events through the full ATLAS reconstruction chain with detector effects, so background process simulation samples are used at the EVGEN (event generation) level, without any reconstruction applied. Instead, to simulate detector effects, a smearing is applied to all events. This smearing is based on a smaller sample of events which were passed through the full ATLAS reconstruction. The smearing was derived from the differences in these events before and after reconstruction and are calculated in bins of η and p_T to take into account the detector resolutions and reconstruction efficiencies of different regions. These large statistics samples are referred to as smeared MC samples.

In the case of the VH categories, these same smeared MC samples are used; however, the jets are used to represent leptons. This simulates the $W\gamma\gamma$ and $Z\gamma$ background contributions for the VH one-lepton and MET categories, and the $ll\gamma\gamma$ background for the dilepton category.

The backgrounds for the $t\bar{t}H$ categories are more complicated and utilize both a $Z \to ee$ Sherpa sample and three data control regions. The $Z \to ee$ sample is used only in the $t\bar{t}H$ leptonic category and is used to simulate the $e\gamma$ fakes. The three data control regions are from events where the photons pass the loose ID requirements but do not pass the tight ID or the isolation requirements. Table 4.4 summarizes the control regions and the $e\gamma$ background samples used for the $t\bar{t}H$ categories. More details can be found in Ref. [118].

Category	Photon Selection	Additional Objects	Sample Name
Leptonic	2 non-tight, non-isolated γs	1 lepton, 1 b-jet, MET>20 GeV OR 1 lepton, 2 b-jets	QCD::1
		1 lepton, 1 jet, MET>20 GeV OR 1 lepton, 2 jets	QCD::2
		2 jets, MET>20 GeV OR 3 jets	QCD::3
	1 tight isolated γ, 1 electron	1 lepton, 1 jet	$e\gamma$::1
		2-4 jets, 1 b-jet	$e\gamma$::2
Hadronic	2 non-tight, non-isolated γs	5 jets	QCD::1

Table 4.4: Samples used for the background modeling in $t\bar{t}H$ leptonic and hadronic categories in the coupling analysis.

4.6.2 Spurious Signal

To quantify the bias introduced by choosing to parameterize the background processes with a single function, the spurious signal (N_{spur}) is measured. The spurious signal is a measure of the flexibility of a background model to produce a signal-like peak around a specific diphoton mass. To measure the spurious signal, a signal+background model

is fit to the background-only distribution of smeared MC, and the number of fitted signal events is the spurious signal. For each tested background function, a mass scan is done in the range 119 GeV$< m_{\gamma\gamma} <$134 GeV where a signal+background fit is made with the mass fixed at each scan point and a corresponding spurious signal measurement is made for each point. The spurious signal is only tested in the range 119$< m_{\gamma\gamma} <$134 GeV because previous measurements show the Higgs boson has a mass around 126 GeV, and the signal model has a resolution of only 1-2 GeV depending on the category. Therefore, only fluctuations within this mass range will affect the final measured signal. The largest spurious signal in this mass range from each tested function is then used to choose which functional form should be used as the background parameterization when fitting to data. A background function is chosen if its spurious signal satisfies at least one of the following requirements:

- N_{spur} <10% of the expected signal events.
- N_{spur} <20% of the statistical uncertainty on the number of background events in data.

If more than one function passes one of these criteria, then the function with the least number of degrees of freedom is chosen.

The following functional forms were tested as background models:

- Single decaying exponential

$$e^{-\alpha \cdot m_{\gamma\gamma}} \tag{4.16}$$

- Exponential of a 2nd order polynomial

$$e^{\alpha_1 \cdot x + \alpha_2 \cdot x^2}, \text{ where } x = \frac{m_{\gamma\gamma} - 100}{100} \tag{4.17}$$

- Exponential of a 3rd order polynomial

$$e^{\alpha_1 \cdot x + \alpha_2 \cdot x^2 + \alpha_3 \cdot x^3}, \text{ where } x = \frac{m_{\gamma\gamma} - 100}{100} \tag{4.18}$$

- 2nd, 3rd, 4th, and 5th degree bernstein polynomials

This spurious signal test is done for each defined category above, so that each category has its own background function with its own parameter values. The chosen functional forms and the corresponding spurious signal for each set of categories are shown in Tables 4.5 and 4.6.

Category	Background Model	N_{spur}	N_{spur}/N_{SM}
C1	Expo. of 2nd order polynomial	3.5	5.8%
C2	Exponential	0.3	3.9%
C3	Expo. of 2nd order polynomial	4.4	4.5%
C4	Exponential	1.6	16.6%
C5	Expo. of 2nd order polynomial	1.7	9.1%
C6	Expo. of 2nd order polynomial	2.7	7.49%
C7	Exponential	0.2	5.4%
C8	Expo. of 2nd order polynomial	4.6	4.5%
C9	Exponential	2.6	20.3%
C10	Expo. of 2nd order polynomial	3.7	9.5%

Table 4.5: Chosen functional forms for each mass category and the corresponding spurious signal from the background fits to the smeared MC.

4.7 Analysis of 2011 Data

The mass and coupling analyses combine both the 2011 7 TeV and 2012 8 TeV datasets for the final results. Overall, the analysis is the same for both the 2011 and 2012 datasets. This section describes the few 2011 specific aspects of the analyses.

Category	Background Model	N_{spur}	N_{spur}/N_{SM}
C1	Expo. of 2nd order polynomial	6.7	5.0%
C2	Exponential	0.4	3.6%
C3	Expo. of 2nd order polynomial	7.0	3.4%
C4	Expo. of 2nd order polynomial	1.2	7.3%
C5	Exponential	1.3	14%
C6	Exponential	0.4	5.4%
C7	Exponential	0.5	14%
C8	Exponential	0.1	11%
C9	Exponential	0.1	6.4%
C10	Exponential	<0.1	8%
C11	Exponential	0.3	49%
C12	Exponential	0.2	28%

Table 4.6: Chosen functional forms for each coupling category and the corresponding spurious signal from the background fits to the smeared MC.

4.7.1 Datasets

The 7 TeV dataset was collected during 2011 corresponding to an integrated luminosity of 4.5 fb^{-1}. A good run list for 2011 is then applied to events, which require that all the detector systems were operating properly during the runs. The `EF_2g20_loose` trigger was used, which has an efficiency between $98.9^{+0.2}_{-0.3}$% and $98.8^{+0.3}_{-0.4}$% [119] depending on when in 2011 the data was collected. 7 TeV MC samples were generated with the exact same configurations as for 8 TeV MC described in Sec. 4.1. The samples were generated for Higgs boson masses between 100 and 150 GeV for each of the five production processes, and they are each normalized to the 7 TeV cross sections calculated by the LHC Higgs Cross Section Working Group [21] and listed in Tab. 4.7.

4.7.2 Object and Event Selection

Photons must first pass the same preselection and quality cuts as 2012 which are described in Sec. 4.2. The same p_T requirements of $p_T^\gamma/m_{\gamma\gamma}$ >0.35 (0.25) are then applied, but the 'tight' photon ID requirements are different for the 2011 dataset. While the 2012 tight ID selection is cut-based, the 2011 tight photon ID is based on a

M_H [GeV]	σ_{ggF} [pb]	σ_{VBF} [pb]	σ_{WH} [pb]	σ_{ZH} [pb]	$\sigma_{t\bar{t}H}$ [pb]
100	23.64	1.557	1.195	0.6616	0.1637
105	21.45	1.478	1.029	0.5724	0.1432
110	19.56	1.410	0.8845	0.4978	0.1240
115	17.89	1.344	0.7626	0.4345	0.1105
120	16.43	1.279	0.6617	0.3808	0.09758
125	15.13	1.222	0.5785	0.3351	0.08632
130	13.98	1.168	0.5059	0.2957	0.07660
135	12.95	1.117	0.4431	0.2616	0.06816
140	12.02	1.069	0.3896	0.2322	0.06079
145	11.24	1.023	0.3437	0.2068	0.05429
150	10.51	0.980	0.3034	0.1842	0.04867

Table 4.7: Higgs boson production cross sections for 7 TeV as reported by the LHC Higgs Cross Section Working Group [21]. Values stated here are used to normalize the signal simulation samples.

neural net, which is trained to separate prompt photons from π^0s. Both a calorimeter isolation and a track isolation are required for photons; however, the cut values are 5.5 GeV and 2.2 GeV respectively for 2011 data.

Jet selections are the same for 2011 as for 2012 with the exception of the jet vertex fraction. For 2011, a looser requirement of $|JVF| > 0.25$ is used.

Electron and muon selections are the same as for 2012, except for the electron tight ID requirement.

Dedicated 7 TeV samples for p_T reweighting were generated using HRes2.1 for the ggF process and using HAWK for the VBF and VH processes.

Events are then divided into the same categories as were defined in Sec. 4.4 for 2012 data.

4.7.3 Signal and Background Models

The signal shape is taken from a global fit to the signal MC for all mass points simultaneously; this is the same as is done for 2012. For the background models, the same functions which are chosen for 2012 using the spurious signal method (see

Category	Total	ggF	VBF	WH	ZH	$t\bar{t}H$	$b\bar{b}H$	tH
Inclusive	74.50	64.73	5.37	2.17	1.28	0.30	0.68	0.01
C1	25.97	23.93	1.07	0.42	0.27	0.03	0.25	-
C2	2.05	1.47	0.34	0.13	0.08	0.03	0.02	-
C3	39.53	36.16	1.66	0.80	0.49	0.04	0.38	-
C4	2.95	2.08	0.50	0.20	0.12	0.03	0.02	-
C5	1.64	0.63	0.99	0.01	0.01	0.00	0.01	-
C6	0.96	0.17	0.78	0.00	0.00	0.00	0.00	-
C7	0.59	0.26	0.02	0.19	0.12	0.01	0.00	-
C8	0.28	0.02	0.01	0.10	0.12	0.02	0.00	-
C9	0.32	0.00	0.00	0.30	0.02	0.01	0.00	-
C10	0.05	0.00	0.00	0.00	0.05	0.00	0.00	-
C11	0.06	0.01	0.00	0.00	0.00	0.05	0.00	0.00
C12	0.10	0.00	0.00	0.02	0.00	0.08	0.00	0.01

Table 4.8: Expected events for a Higgs boson mass of 125.4 GeV for the coupling category analysis for 7 TeV data. Events are divided by category and production process. The tH process is only considered for the two $t\bar{t}H$ categories.

Sec. 4.6.2) are used for the 7 TeV background functions. In the case of the low statistics categories, like VH E_T^{miss}, VH one and two leptons, and $t\bar{t}H$ categories, the background model parameters from the fit to the 2012 data are used for the 2011 analysis also. The signal is then extracted in the same way as for the 2012 analysis.

4.8 Systematics

In this analysis, there are six types of uncertainties. There are uncertainties on the total signal yield and the background estimation. There are also uncertainties on the breakdown of signal yields into each category; these are due to the migrations of events between categories. Due to the small MC statistics in certain regions of phase space, statistical uncertainties are included. Additionally, there are uncertainties on the modeling of the signal samples which are used to define the categories. Finally, there are two uncertainties associated with the signal shape, systematics on the signal resolution and systematics on the signal peak position. Each type of systematic is further broken down into its individual components and described in the following

sections.

Nuisance parameters for the signal yields and signal resolution are constrained using a lognormal function, $e^{\sigma\theta}$, where σ is the systematic and θ is its corresponding nuisance parameter. The nuisance parameters for all other systematics are constrained using a Gaussian function.

4.8.1 Experimental Systematics on the Signal Yield

- **Luminosity.** The amount of luminosity recorded by the ATLAS detector is extrapolated from measurements of the proton-proton elastic collisions measured in the forward direction using the LUCID and BCM detectors. These are placed on either side of the interaction point, and measure the proton-proton cross section using van der Meer scans. These scans are done by systematically separating the beams by varying widths and measuring the corresponding cross sections for each distance. Measurements with the van der Meer scans were found to have an uncertainty of $\pm 1.8\%$ for 2011 data taking [120] and $\pm 2.8\%$ in 2012 data taking [42]. The luminosity uncertainty is uncorrelated between the two years.

- **Trigger.** The efficiency of the triggers are evaluated for the relative p_T cuts used in this analysis. The relative p_T cuts allow the p_T of the photons to be much closer to the trigger thresholds than for previous absolute cuts; however, the efficiency for the relative p_T cuts was found to still be extremely good ($\sim$99.4%). The uncertainty on the trigger efficiency was calculated using photons from Z radiative decay. Selection cuts on the invariant mass of the three-body system, the dilepton mass, and the lepton p_T were varied independently to assess the uncertainty on the trigger efficiency. This uncertainty was found to be 0.2% for

both 2011 and 2012.

- **Photon Identification.** The uncertainty on the photon identification is from comparing the 'tight' photon ID efficiency in MC to the efficiency in data. This is then translated into an uncertainty on the signal yield by varying the photon ID efficiency up and down within its uncertainty and taking the average difference in signal yields as the final uncertainty. For the 'tight' photon ID, this amounts to an uncertainty of 1% inclusively for 2012 and 8.4% for 2011. This systematic was also computed separately for the $t\bar{t}H$ categories and the VH categories and was found to be 4.1% for 2012 and 9.3% for 2011.

- **Isolation.** For 2012, the isolation uncertainty was estimated using $Z \to ee\gamma$ events where one of the electrons radiates the photon. This process provides a good source of true photons with a very small contamination of fakes from Z+jet events. These events were compared between data and simulation, and the difference in isolation efficiency was found to be 0.13% per photon. An uncertainty of 0.3% is assigned due to the background contamination. The inclusive total uncertainty on the isolation is $2\times(0.13 \otimes 0.03)$ =0.3% for 2012 and 0.6% for 2011.

- **Photon Energy Scale.** The photon energy scale gives an uncertainty on the yield through the relative p_T requirements. The energy scale is varied within its uncertainties, and the differences in the final selection yields in each category are taken as the systematic. Inclusively, the impact of the photon energy scale is 0.04% and thus is neglected in this analysis.

- **Primary Vertex Systematic.** The uncertainty on the primary vertex selection was calculated in [121], and was found to be 0.03%. This was measured by comparing $Z \to ee$ peak positions between data and MC for different choices

of the primary vertex. The choices of primary vertex considered were using: the electron tracks from the Z to define the η direction, the pointing from clusters in the calorimeter only, the primary vertex in the inner detector with the highest sum p_T of tracks only, the interaction point (0,0,0), and the nominal primary vertex selection. The ratios between the peak positions in data and MC were compared, and the maximal deviation between these ratios was found to be 0.03% and are neglected in this coupling analysis.

4.8.2 Theoretical Systematics on the Signal Yield

- **Branching Ratio.** The branching ratio of the Standard Model Higgs boson decaying into two photons as calculated in [21] for a Higgs boson mass of 125.4 GeV has an uncertainty of +4.9%/-4.8%. This uncertainty varies with the Higgs boson mass from +6.20/-6.07 at m_H =100 GeV to +2.45/-2.43 at m_H =150 GeV.

- **QCD Scale.** The uncertainty on the Standard Model Higgs boson cross section due to missing higher-order terms can be evaluated by varying the renormalization and factorization scales up and down by a factor of 2. The largest of these uncertainties is from the ggF process. For a Higgs boson mass of 125.4 GeV, this scale uncertainty is +7.2%/-7.8%. As with the branching ratio, these uncertainties also vary with mass from +7.9%/-8.4% at m_H =100 GeV to +6.7%/-7.4% at m_H =150 GeV for the ggF process. QCD scale uncertainties for all production processes are listed in Tab. 4.9 and 4.10 for 8 and 7 TeV respectively.

- **PDF+α_s.** Uncertainties on the cross section also arise from the use of different PDFs. The calculation is done for three different PDF sets: CT10,

MSTW08 [122], and NNPDF2.3 [123]. Both the CT10 and MSTW08 PDFs are varied by their respective eigenvector sets, and the uncertainties are determined by the 'Master Equation' [124]

$$\begin{aligned} \Delta X^{+}_{max} &= \sqrt{\sum_{i} [max(X^{+}_{i} - X_0, X^{-}_{i} - X_0, 0)]^2} \\ \Delta X^{-}_{max} &= \sqrt{\sum_{i} [max(X_0 - X^{+}_{i}, X_0 - X^{-}_{i}, 0)]^2} \end{aligned} \tag{4.19}$$

where X_0 is the central value of the PDF, X^{+}_{i} is the value of the '+' direction of the eigenvector i of the PDF set, and X^{-}_{i} is the value of the '-' direction. For NNPDF2.3, the average value of all the PDF sets is used as the central PDF, and the 1σ variation around this value is taken as the uncertainty. The full uncertainty is then taken as the envelope of the uncertainties from the three PDF sets. Again, the largest PDF uncertainty comes from the ggF production process. At m_H =125.4 GeV the uncertainty is +7.5%/-6.9%. The PDF uncertainty also varies with mass but to a lesser degree. The uncertainties are +7.8%/-6.5% at m_H =100 GeV and +7.4%/-7.0% at m_H =150 GeV. PDF uncertainties for all production processes are listed in Tab. 4.9 and Tab. 4.10.

	ggF	VBF	WH	ZH	$t\bar{t}H$	$b\bar{b}H$
QCD Scale Up [%]	7.2	0.2	1.0	3.1	3.8	10.3
QCD Scale Down [%]	7.8	0.2	1.0	3.1	9.3	14.8
PDF+α_s Up [%]	7.5	2.6	2.4	2.5	8.1	6.1
PDF+α_s Down [%]	6.9	2.8	2.4	2.5	8.1	6.1

Table 4.9: QCD scale and PDF uncertainties for all production processes for a Standard Model Higgs boson with m_H =125.4 GeV [21] produced with a center of mass energy of 8 TeV.

- **ggF Higgs p_T Uncertainty.** The Higgs boson p_T has not been precisely measured, and this uncertainty in the shape can lead to migrations between the untagged high and low p_{Tt} categories. The p_T uncertainty is measured for

	ggF	VBF	WH	ZH	$t\bar{t}H$	$b\bar{b}H$
QCD Scale Up [%]	7.1	0.3	1.0	2.9	3.2	10.0
QCD Scale Down [%]	7.8	0.3	1.0	2.9	9.3	14.7
PDF+α_s Up [%]	7.6	2.5	2.6	2.6	8.4	6.2
PDF+α_s Down [%]	7.1	2.1	2.6	2.6	8.4	6.2

Table 4.10: QCD scale and PDF uncertainties for all production processes for a Standard Model Higgs boson with m_H =125.4 GeV [21] produced at a center of mass energy of 7 TeV.

the ggF production mode by reweighting to HRes2.0 p_T distributions calculated with different schemes. First, the renormalization (μ_R) and factorization (μ_F) scales are varied up and down by a factor of 2 (excluding the cases where the two scales differ by a factor of 4). Then the resummation scale for the top quark ($\frac{m_H}{2}$) is varied up and down by a factor of 2. Finally, the resummation scale associated with the bottom quark (m_b) is varied by a factor of 3. The envelope of all these variations is taken to be the uncertainty on the Higgs boson p_T distribution, and the uncertainties are then symmetrized. This symmetrized uncertainty is for the high p_{Tt} categories, while the uncertainty for the low p_{Tt} categories is calculated taking in the correlations between high and low p_{Tt} categories using the Stewart-Tackmann procedure [125].

$$\Delta\sigma_{low-p_{Tt}} = \Delta\sigma_{yield} \oplus \Delta\sigma_{high-p_{Tt}} \tag{4.20}$$

Table 4.11 shows the p_T uncertainties for the untagged categories.

8 TeV	C1	C2	C3	C4
$p_{T,H}$ mig, 7 TeV	-1.4	24.1	-1.4	23.8
$p_{T,H}$ mig, 8 TeV	-1.5	24.2	-1.5	23.9

Table 4.11: Uncertainty in % on the Higgs boson p_T from variations with HRes2.0 for the untagged coupling categories for both 7 and 8 TeV MC.

- **ggF Jet bin uncertainties.** For the Higgs boson coupling analysis, the categories involving jets contain a significant number of ggF events. These events are subject to large uncertainties due to the missing higher order perturbative terms when requiring two or more jets. Furthermore, the cut on the MVA discriminant effectively cuts on events that have exclusively two jets and those that have more than two jets. This exclusive binning of events is also associated with a large migration uncertainty between the jet bins. To determine these uncertainties, an extension of the Stewart-Tackmann (ST) method is applied to a fixed NLO H + 2jets calculation for the ggF process using MCFM [126, 127]. Details on this method are presented in Ref. [21]. The uncertainties for a scan of progressively looser cuts on $\pi - \Delta\phi_{H-jj}$ are shown in Fig. 4.7. The nominal prediction from MCFM is shown along with the uncertainties using the modified method. For comparison, the uncertainties obtained directly from varying the scales are also shown. It's clear from Fig. 4.7 that the direct scale uncertainties do not properly represent the migration uncertainties as the cut becomes tighter, meaning the binning becomes more of a 2-jet exclusive bin. The results are summarized in Table 4.12. Uncertainties for $\geq$3 jets are also calculated since the BDT discriminant for the tight VBF category relies heavily on the shape of the $\Delta\phi_{\gamma\gamma,jj}$ variable to distinguish between the VBF and ggF processes. This variable is sensitive to the presence of a third jet.

Category	VBF Loose	VBF Tight	VH hadronic
$\geq$2 jet uncertainty	20.4%	20.4%	20.4%
$\geq$3 jet uncertainty	25%	52%	0

Table 4.12: Systematics due to the modeling of gluon-fusion in phase spaces requiring at least two jets. Uncertainties are determined using MCFM.

- **Additional $t\bar{t}H$ category uncertainties.** Three additional uncertainties are

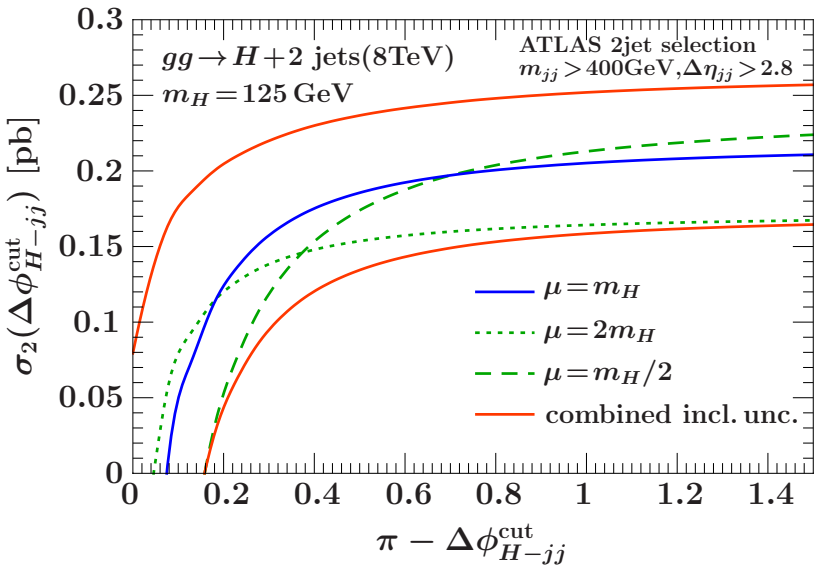

Figure 4.7: The cumulant distribution of the uncertainty on gluon-fusion for progressively looser cuts on the $\Delta\phi_{H-jj}$. The distribution is made with MCFM. [21].

applied to the $t\bar{t}H$ categories: $t\bar{t}H$ modeling uncertainty, uncertainties on ggF and WH yields, and heavy flavor uncertainties for ggF, VBF, and WH yields. For the $t\bar{t}H$ modeling uncertainty, two different reweightings are applied to the $t\bar{t}H$ samples. First, the sample is reweighted to match the truth distributions where the renormalization and factorization scales (m_t+$m_H/2$) have been varied up and down by a factor of two. A second, independent reweighting is also done, which reweights the samples to match distributions where a dynamic scale is used ($\mu = (m_T^t m_T^t m_T^H)^{1/3}$). An uncertainty is assigned for each case and is summarized in Table 4.13. The uncertainties from ggF and WH yields in the $t\bar{t}H$ categories are from varying the scales of the parton shower in Pythia8. The scales are varied up and down by a factor of 2 and result in an uncertainty of 50% for ggF and 5% for WH. The uncertainty measured for WH is also assigned to the ZH contribution. To account for the high uncertainty for heavy

flavors in the ggF, VBF, and WH production processes, a conservative 100% uncertainty is taken on each contribution to the $t\bar{t}H$ categories. Studies done in Ref. [128] show an MC/data agreement of within 30%; however, to cover the uncertainty conservatively, a 100% uncertainty for ggF was taken. Because VBF and WH proceed through qq interactions, their uncertainty was taken from $W + b - jets$ studies [129].

Category	Scale Variations	Dynamic Scale
Leptonic	+0.3	+2.2
Hadronic	-0.4	-1.2

Table 4.13: Systematics in % due to the modeling of $t\bar{t}H$ where the samples have been reweighted to match scale variations and a dynamic scale setting.

4.8.3 Limited MC Statistics

For some coupling categories, the phase space is so restricted, that the statistical uncertainty in the signal samples can be of the same order as the systematic uncertainties. Therefore, additional uncertainties are assigned for each production process, which accounts for the limited statistics of the samples. Tables 4.14 and 4.15 show the uncertainties per production mode for each coupling category for 7 TeV and 8 TeV samples respectively. These uncertainties are then pruned in order to simplify the nuisance parameters. Nuisance parameters are rejected if they affect the final μ_X (X =ggF,VBF,WH,ZH, or $t\bar{t}H$) more than 1%. It was decided to keep four of the nuisance parameters associated with the MC statistics regardless of effect on μ_X: ZH uncertainty in the VH dilepton category for 2011 and 2012, and the $t\bar{t}H$ uncertainty in the $t\bar{t}H$ categories for 2012. Following this, the rest of the MC statistical uncertainties are pruned.

Category	ggF	VBF	WH	ZH	$t\bar{t}H$
C1	0.19	0.37	0.55	0.53	1.01
C2	0.65	0.64	1.01	0.99	1.14
C3	0.15	0.29	0.40	0.39	0.90
C4	0.55	0.53	0.78	0.78	1.12
C5	1.12	0.38	3.51	3.51	4.27
C6	2.15	0.42	10.37	9.76	9.21
C7	1.72	2.68	0.81	0.79	2.07
C8	2.16	2.12	1.00	0.71	1.20
C9	12.60	10.00	0.64	1.79	2.08
C10	0.00	0.00	57.74	1.24	9.90
C11	11.62	12.91	12.13	8.84	0.77
C12	30.15	30.15	2.86	4.12	0.64

Table 4.14: Uncertainties in % accounting for the limited statistics of the 7 TeV signal MC samples in the 12 coupling categories.

Category	ggF	VBF	WH	ZH	$t\bar{t}H$
C1	0.19	0.37	0.57	0.54	1.08
C2	0.64	0.64	1.01	0.98	1.20
C3	0.16	0.30	0.41	0.40	0.95
C4	0.54	0.53	0.78	0.77	1.15
C5	1.09	0.39	3.31	3.21	4.43
C6	2.05	0.42	8.30	8.91	8.01
C7	1.70	2.74	0.82	0.80	2.14
C8	10.72	10.91	1.25	0.82	1.38
C9	13.48	12.91	0.66	1.91	1.89
C10	0.00	0.00	100.00	1.25	9.45
C11	12.13	13.61	14.00	8.28	0.70
C12	33.33	25.00	4.10	5.63	0.65

Table 4.15: Uncertainties in % accounting for the limited statistics of the 8 TeV signal MC samples in the 12 coupling categories.

4.8.4 Experimental Uncertainties due to Categorization

- **Material Mismodeling.** Migrations due to material mismodeling only have a significant effect on events defined by the conversion status of the photons, as the amount of material in the inner detector affects the probability that a photon will convert. The uncertainty due to the material mismodeling is calculated using an MC sample generated with additional detector material, and the uncertainty is the percent change in event yields per category between this additional material sample and the nominal sample. Because the coupling categories do not depend on the conversion status, the migration uncertainty from material mismodeling is only applied to the mass analysis.

- **Jet and E_T^{miss}.** There are two types of jet uncertainties: energy scale and energy resolution. The uncertainties on the jet energy scale can be categorized into five different subsets: statistical, detector, modeling/theory, mixed, and special, where mixed refers to mixed detector and modeling uncertainties and special refers to a few specific terms, for example pile up uncertainties. Uncertainties on the jet energy resolution are of three types: experimental, method, and modeling. The uncertainties on the E_T^{miss} are mainly due to the uncertainties on all objects in the event which enter into the sum. Because E_T^{miss} is calculated by taking the negative of the four vector sum of all objects in the event, the scale and resolution uncertainties on each of these objects is propagated through to the E_T^{miss} calculation. The other significant contribution to the E_T^{miss} uncertainty is the uncertainty on the soft terms. For the coupling analysis, a simplification procedure was adopted for both the jet and E_T^{miss} systematics, where only the largest systematics are quoted independently, and the rest are merged into one nuisance parameter by adding the uncertainties

in quadrature. First, production modes are combined where the uncertainties are of the same order of magnitude and the expected behavior of each process is expected to be similar. Then categories are merged using the same reasoning. Finally, the systematics are symmetrized by taking the average deviation of the up and down uncertainty components. The 7 TeV results for the E_T^{miss} uncertainties are shown in Tables 4.16 through 4.20, and the results for the jet uncertainties are shown in Tables 4.21 through 4.29.

Category	1-4	5	6	7	8	9	10	11	12
ggF+VBF	-0.01	-0.07	-0.06	-0.17	6.18	1.54	0	0	0.67
ttH	-0.29	-0.28	-0.30	-0.26	-0.45	-0.27	-0.76	-0.21	-0.25
WH	-0.13	-0.46	1.19	-0.19	1.53	0.13	0	0	0.43
ZH	-0.11	-0.21	1.65	-0.27	0.91	0.24	-0.01	0	-0.68

Table 4.16: MET uncertainties from PES (photon energy scale) for different production modes in each 2011 category [%].

Category	1-4	5	6	7	8	9	10	11	12
ggF+VBF	-0	-0.01	0.01	-0.09	0.70	2.96	0	0	0.67
ttH	-0.24	-0.32	-1.40	-0.36	1.34	0.18	1.90	0	-0.15
WH	0.01	-0.24	1.19	0.05	-0.09	-0.02	0	0	0.43
ZH	-0.02	-0.26	0	-0.06	0.22	0.11	0.01	0	-0.65

Table 4.17: MET uncertainties from PER (photon energy resolution) for different production modes in each 2011 category [%].

Category	1-4	5	6	7	8	9	10	11	12
ggF+VBF	-0.02	-0.04	-0.01	-0.24	9.88	7.64	0	0	2.72
ttH	-0.01	0.16	0	0.06	-0	0.05	0	0	0.15
WH	-0.16	-0.27	0.59	-0.16	1.61	0.24	0	0	0.36
ZH	-0.21	-0.09	0	-0.10	0.87	3.57	-0.03	0	1.71

Table 4.18: MET uncertainties from ScaleSoftTerms for different production modes in each 2011 category [%].

Category	1-4	5	6	7	8	9	10	11	12
ggF+VBF	-0	-0.01	-0.02	-0.05	1.46	-4.43	0	0	0.79
ttH	-0.14	-0.44	1.48	-0.34	0.79	0.26	0.08	0	0.15
WH	-0.03	-0.23	1.19	-0.03	0.23	0.09	0	0	0.36
ZH	-0.03	-0.19	0.73	-0.01	0.09	0.99	-0.01	0	-0.64

Table 4.19: MET uncertainties from ResoSoftTerms for different production modes in each 2011 category [%].

Category	1-4	5	6	7	8	9	10	11	12
ggF+VBF	0	0	0.01	0	0.21	0.80	0	0	0.32
ttH	0.03	0.35	0.45	0.12	0.06	0.09	1.35	0	0.34
WH	0.02	0.07	0	0.03	0.23	0.03	0	0	0.46
ZH	0.02	0	0	0.01	0.01	0.91	0.02	0	0.61

Table 4.20: MET uncertainties from the "merged" term for different production modes in each 2011 category [%].

Category	low ptt	high ptt	vbf loose	vbf tight	7	8	9	10	11	12
ggF	0	-0.42	2.85	0.04	-0.30	0.18	0	0	0	0
VBF	0.02	-0.41	0.34	-0.02	-0.22	0.26	0	0	0	0
ttH	0.04	-0.50	14.59	0.56	0.08	0.23	0.27	0	-0.15	-0.01
WH+ZH	-0.01	-0.41	11.40	0	-0.08	0.10	0.06	0.02	-0.92	-0.05

Table 4.21: JET uncertainties from JVF for different production modes in each 2011 category [%].

Category	low ptt	high ptt	vbf loose	vbf tight	7	8	9	10	11	12
ggF	0.01	0.06	0.01	0.07	-0.99	-0.51	-0.51	0.18	0	0
VBF	-0.02	-0.02	-0	-0.02	-0.01	0.05	-0.49	0.26	0	0
ttH	0.10	0.18	0.10	0.07	-0.46	0	-0.03	0.28	0.49	0
WH+ZH	-0	-0.02	-0.01	-0.05	-1.53	-0.99	-0	0.07	0.18	0.15

Table 4.22: JET uncertainties from PileUpRand for different production modes in each 2011 category [%].

Category	low ptt	high ptt	vbf loose	vbf tight	7	8	9	10	11	12
ggF	-0.02	-0.19	-0.01	-0.19	0.67	2.49	0.47	2.68	-3.80	0
VBF	0.53	0.83	0.46	0.67	-0.54	-1.70	-1.25	3.24	-0.68	0
ttH	-0.84	-1.42	-0.68	-1.06	-4.04	-3.92	1.03	0.16	0.47	-0.96
WH+ZH	-0.04	0.85	-0.02	0.57	2.25	4.88	-1.27	0.24	-0.17	-0.35

Table 4.23: JET uncertainties from JER (jet energy resolution) for different production modes in each 2011 category [%].

Category	low ptt	high ptt	vbf loose	vbf tight	7	8	9	10	11	12
ggF	-0	-0.44	3.14	0.69	0.40	-2.15	0	0	2.10	-0.27
VBF	-0.08	-0.38	0.33	0.33	-0.56	-1.14	-1.44	0	-1.25	5.76
ttH	-0.19	-0.57	10.61	1.12	-0.58	-0.37	0.29	0.09	0.55	-0.04
WH+ZH	-0.01	-0.42	11.51	-0.97	0.06	-0.10	0.07	-0.07	3.37	0.36

Table 4.24: JET uncertainties from JESMu for different production modes in each 2011 category [%].

Category	low ptt	high ptt	vbf loose	vbf tight	7	8	9	10	11	12
ggF	-0.04	-0.45	5.58	8.35	3.65	-11.47	-3.16	0	14.28	14.65
VBF	-1.42	-1.36	1.49	4.80	-1.71	-9.66	-5.90	0	17.98	5.75
ttH	-2.29	-1.01	-7.11	3.10	-3.39	-2.08	-0.96	0	6.29	-0.04
WH+ZH	-0.01	-0.38	3.45	6.45	1.72	-1.30	-0.41	-0.23	16.43	5.02

Table 4.25: JET uncertainties from JESFlavComp for different production modes in each 2011 category [%].

Category	low ptt	high ptt	vbf loose	vbf tight	7	8	9	10	11	12
ggF	-0.02	-0.43	3.05	4.32	1.64	-6.91	0.81	0	8.40	6.26
VBF	-0.71	-0.69	0.74	2.44	-1.37	-6.04	-2.43	0	12.41	0.05
ttH	-1.27	-0.57	-12.89	0.79	-1.88	-1.20	-0.52	0	3.34	-0.02
WH+ZH	0.01	-0.41	11.26	2.90	0.95	0.82	-0.24	-0.09	7.07	2.51

Table 4.26: JET uncertainties from JESFlavResp for different production modes in each 2011 category [%].

Category	low ptt	high ptt	vbf loose	vbf tight	7	8	9	10	11	12
ggF	-0.02	-0.43	2.93	2.70	1.51	-0.99	0.81	0	6.99	6.26
VBF	-0.54	-0.57	0.82	1.47	-0.90	-0.89	-1.32	0	12.39	0.05
ttH	-1.21	-0.58	-16.20	-0.60	-1.99	-0.73	-1.61	-0.90	3.17	0.13
WH+ZH	-0.01	-0.44	11.37	0.95	0.78	-0.09	-0.14	-0.09	6.98	2.08

Table 4.27: JET uncertainties from NPModelling1 for different production modes in each 2011 category [%].

Category	low ptt	high ptt	vbf loose	vbf tight	7	8	9	10	11	12
ggF	-0.06	-0.46	6.73	11.72	0.29	-0.99	-1.11	0	6.89	15.42
VBF	-1.91	-1.81	1.47	6.76	-1.38	-0.89	-1.32	0	11.97	0.05
ttH	-0.92	-0.57	11.54	4.46	-2.48	-0.54	-0.92	-0.90	2.20	0.10
WH+ZH	-0.03	-0.36	11.59	9.58	0.43	-0.01	-0.12	-0.05	6.38	1.73

Table 4.28: JET uncertainties from EtaInterCalib for different production modes in each 2011 category [%].

Category	low ptt	high ptt	vbf loose	vbf tight	7	8	9	10	11	12
ggF	0.02	1.44	10.01	2.96	1.05	3.28	0.29	0	6.80	6.87
VBF	0.43	1.40	1.21	1.49	1.15	2.90	4.24	0	10.11	0.12
ttH	0.87	1.85	4.42	3.04	2.44	1.01	1.90	0.90	2.33	0.23
WH+ZH	0.02	1.40	4.93	1.67	0.56	0.35	0.18	0.08	4.99	1.76

Table 4.29: JET uncertainties from the additional 1% uncertainty for jets in $\eta \in [1.5; 2.4]$ for different production modes in each 2011 category [%].

- **Electrons and Muons.** For the coupling categories, the electron and muon energy scale and smearing uncertainties were found to be negligible. Therefore, only the uncertainties on the lepton scale factors and the lepton isolation requirement are included in the systematics. Lepton uncertainties are only applied to those categories selecting leptons. Results for lepton scale factors are summarized in Tables 4.30 and 4.31, while for the lepton isolation a systematic of 0.3% is assigned in the WH leptonic category, 0.6% in the ZH leptonic category, and 0.4% in the $t\bar{t}H$ leptonic category.

Category	$t\bar{t}H$ leptonic	ZH leptonic	WH leptonic
ggF	1.91	0.00	0.62
VBF	0.86	0.00	1.00
WH	0.41	0.00	0.44
ZH	0.49	0.00	0.42
$t\bar{t}H$	0.41	0.00	0.39

Table 4.30: Uncertainty in [%] on the electron scale factors for the $t\bar{t}H$ leptonic, ZH leptonic, and WH leptonic categories.

Category	$t\bar{t}H$ leptonic	ZH leptonic	WH leptonic
ggF	0.05	0.00	0.27
VBF	0.15	0.00	0.16
WH	0.21	0.00	0.21
ZH	0.20	0.41	0.25
$t\bar{t}H$	0.28	0.29	0.23

Table 4.31: Uncertainty in [%] on the muon scale factors for the $t\bar{t}H$ leptonic, ZH leptonic, and WH leptonic categories.

- **B-tagging.** Migrations to and from the $t\bar{t}H$ categories can occur do to uncertainties associated with the b-tagging of jets. To assess the uncertainty, the scale factors for b-jets are varied according to their uncertainties. These scale factor uncertainties are dependent on the jet's truth label ($b/c/t$, *other*). The resulting migrations are then taken as the systematic for b-tagging jets in the $t\bar{t}H$ categories. In total, there are 96 eigenvectors, which are all evaluated.

However, because they are all quite small, only the largest 10 uncertainties are considered for this analysis. Table 4.32 shows the resulting 10 systematics from b-tagging.

	mistag48	btag14	btag23	btag24	ctag23	btag19	mistag32	ctag24	btag20	mistag47
Hadronic $t\bar{t}H$ Category										
ggF	1.200	0.158	0.202	0.012	0.439	8.530	1.540	14.200	1.090	2.270
VBF	0.452	0.366	0.053	0.499	0.807	2.000	1.920	0.109	1.440	3.750
WH	0.294	0.385	0.151	0.556	0.529	2.120	1.840	0.041	1.610	3.760
ZH	0.847	0.131	0.284	0.253	0.204	0.649	0.180	0.069	0.901	1.600
$t\bar{t}H$	0.743	0.493	0.246	0.882	0.675	0.281	0.032	0.008	0.216	0.471
Leptonic $t\bar{t}H$ Category										
ggF	0.375	0.147	0.864	0.033	0.362	7.140	0.408	9.540	0.466	2.480
VBF	0.684	0.383	0.180	0.614	0.466	4.540	4.340	4.560	1.750	4.920
WH	0.047	0.030	0.080	0.065	0.056	0.800	0.637	0.012	0.597	5.380
ZH	0.276	0.153	0.276	0.196	0.302	1.560	4.680	0.031	0.736	3.100
$t\bar{t}H$	0.440	0.266	0.180	0.425	0.420	0.104	0.047	0.004	0.076	0.212

Table 4.32: Systematics in [%] for the 10 leading uncertainties associated with the flavor tagging of jets.

4.8.5 Mis-modeling Uncertainties

- **VBF Selection.** The MVA VBF selection relies very much on the shapes of angular jet variables. These shapes are not well modeled by the nominal Powheg+Pythia sample, which is LO in Higgs + one jet. The second jet is always modeled by the parton shower in Pythia. Differences in the shapes of these variables can lead to migrations in and out of the VBF categories, so a systematic must be assigned to the ggF yields in the two VBF categories. To calculate the systematic, the nominal ggF sample was reweighted to a MiNLO HJJ sample, which is NLO for Higgs + two jets. This reweighting was done separately for two different variables used in the BDT, $\Delta\phi_{jj}$ and η^*; the resulting weights are shown in Fig. 4.8. The reweighted Powheg samples were then passed through the nominal BDT, and the resulting changes in yield in the two categories are taken as the uncertainties. These are summarized for the two

variable reweightings in Table 4.33, and the resulting BDT discriminant shapes are shown in Fig. 4.9.

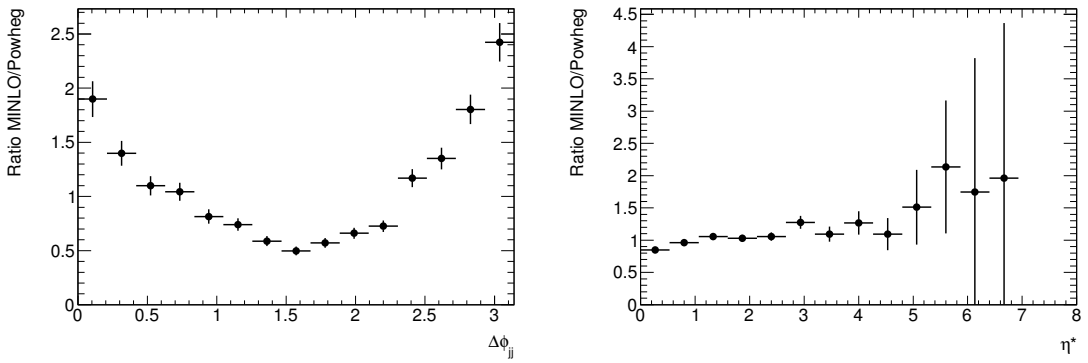

Figure 4.8: Weights derived by taking the ratio of the normalized MiNLO HJJ and Powheg ggH samples.

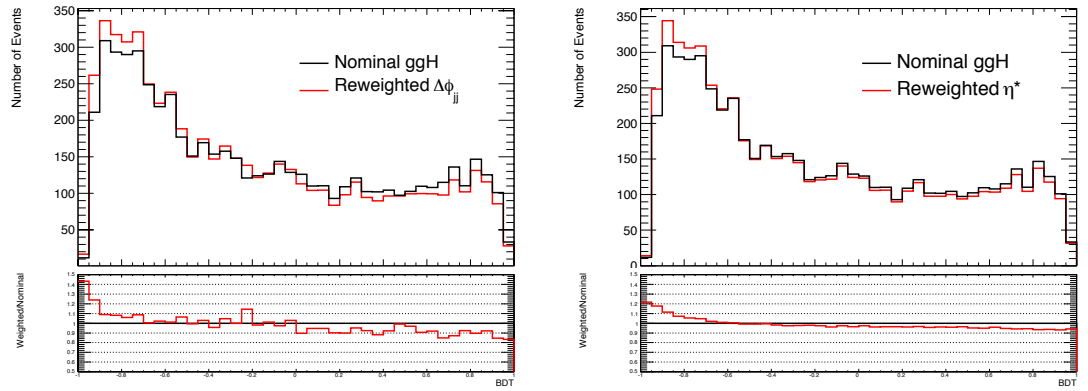

Figure 4.9: The resulting Powheg BDT distributions with (red) and without (black) reweighting.

Reweighted Sample	Tight VBF	Loose VBF
HJJ $\Delta\phi_{jj}$	-11.18	-8.93
HJJ η^*	-6.60	-4.82

Table 4.33: Uncertainty on the gluon-fusion yield in the two VBF BDT categories calculated from reweighting the $\Delta\phi_{jj}$ and η^* distributions to MiNLO HJJ.

- **Underlying Event.** The underlying event (UE), or multiple parton interactions, are the secondary interactions that happen in an event in addition to

the hardest scatter. These interactions are due to the composite nature of the protons that are colliding. To evaluate the uncertainty due to the modeling of the UE, ggF and VBF samples were produced without multiple parton interactions. The ratio of the sample with no UE to the nominal sample in the $\Delta\phi_{H,jj}$ distribution was fitted with a polynomial function. The $\Delta\phi_{H,jj}$ distribution was used because it was found to be quite sensitive to the UE due to the difference in balance when the second jet is produced from the UE versus when it is produced from the hard interaction producing the Higgs boson. This function was then used to reweight the nominal sample, and the yields in each category were compared to those without the reweighting. While the UE doesn't contribute much to the photon isolation cone, as the radiation is generally softer, it does impact the jet multiplicity of an event. Events in the sample without the UE tend to migrate towards the categories which do not require a selection on jets. The resulting uncertainties for each category are summarized in Table 4.34. Dashes show the cases where the systematic on the UE was less than or comparable to the statistical error. The effect of the underlying event was studied independently for the VH contributions in the $t\bar{t}H$ categories and were found to be 30% for the hadronic category and 13% for the leptonic $t\bar{t}H$ category. Underlying event studies with 7 TeV MC showed consistent results, so the same systematics values were used for both datasets.

Category	1	2	3	4	5	6	7	8	9	10	11	12
ggF UE sys	+0.1	+0.1	+0.1	+0.1	-6	-5	-6	-	-	-	-60	-5
VBF UE sys	+1.2	+1.2	+1.2	+1.2	-2.6	-1.7	-2.8	-2.2	-1.7	-	-4	-4

Table 4.34: Uncertainty [%] on the category migrations due to the modeling of the underlying event.

4.8.6 Diphoton Mass Scale Systematics

Systematic uncertainties on the photons' energy scale will affect the invariant mass of the diphoton system. 64 sources of uncertainty on the energy scale are propagated through the analysis in order to measure the bias on the diphoton invariant mass. These uncertainties come from many different sources, such as the difference between calibration using the EM strip layer versus the middle layer of the EM calorimeter, the effects of material mismodeling, the lateral leakage uncertainties, the shower shape variations when changing Geant4 versions, and the mismodeling of the electronic noise level or pedestal. Some uncertainties can be summed quadratically, which reduces the total number of independent systematics to 29. To calculate the systematics associated with the photon energy scale, the method known as 'm_H bias' is used. With this method, a ggF sample with m_H =125 GeV is created with one variation in the energy scale. This sample is then fitted with the signal model and the fitted mass, m'_H, is compared with the fitted mass from the nominal sample. The systematic is then taken as $\frac{m'_H - m_H}{m_H} - 1$. The full list of energy scale systematics for each category is given in Table 4.35 for the mass analaysis and in Table 4.36 for the coupling analysis.

4.8.7 Background Model Systematics

- **Spurious Signal.** The spurious signal is the systematic on the signal yield based on the choice of background parameterization. The method of calculating the spurious signal and the results per category are described in Section 4.6.2.

- **Background Mass Bias.** The impact on the mass scale due to the choice of background parameterization is also taken as a systematic. This is measured using an Asimov dataset generated from the smeared background MC as described in Section 4.6.1 and an injected signal (μ =1) using an Asimov dataset

	C1	C2	C3	C4	C5	C6	C7	C8	C9	C10
Zee	0.04	0.04	0.06	0.07	0.11	0.04	0.03	0.06	0.06	0.12
L2Gain	0.11	0.19	0.08	0.15	0.4	0.09	0.19	0.06	0.14	0.28
LatLeakUC	0.04	0.03	0.06	0.08	0.06	0.01	0.01	0.02	0.03	0.02
LatLeakCV	-	0.01	-	0.01	-	0.09	0.07	0.17	0.17	0.14
ConvInefficiency	0.03	0.02	0.02	0.04	0.04	0.01	-	0.01	0.01	0.01
ConvFakeRate	-	0.01	-	0.02	-	0.01	-	0.03	0.03	0.02
Geant4	0.02	0.01	0.01	0.03	-	0.01	-	0.01	0.02	-
Pedestal	0.01	0.03	-	0.02	0.01	0.01	0.03	0.02	0.01	-
ConvRadius	0.01	-	-	0.01	0.01	0.03	0.04	0.04	0.02	0.05
L1Gain	-	-	0.06	0.04	0.03	0.01	-	0.02	0.02	0.02
LArCalib_Barr	0.11	0.13	0.08	0.09	0.07	0.05	0.09	0.04	0.06	0.03
LArCalib_EC	-	-	0.03	0.03	0.03	-	-	0.02	0.02	0.03
LArUnconv_Barr	0.03	0.04	0.04	0.05	0.02	0.01	-	0.02	0.02	0.02
LArUnconv_EC	-	-	-	-	0.01	-	-	-	-	0.01
LArElUnc_Barr	0.05	0.06	0.13	0.13	0.13	0.03	0.03	0.06	0.08	0.06
LArElUnc_EC	-	-	0.01	0.01	0.2	-	-	0.01	0.01	0.12
LArCalibElec	0.01	-	0.01	0.02	0.01	0.01	-	-	0.01	0.01
MatID1	0.06	0.06	0.07	0.08	0.02	0.05	0.04	0.05	0.06	0.02
MatID2	-	-	0.02	0.03	0.08	-	-	0.02	0.02	0.05
MatID3	-	-	0.01	0.01	0.02	-	-	0.01	0.01	0.02
MatID4	-	-	0.01	0.01	-	-	-	0.01	-	-
Presampler_Barr	0.03	0.04	0.04	0.04	0.04	0.03	0.03	0.02	0.03	0.02
Presampler_EC	-	-	0.01	0.01	0.16	-	-	0.01	0.01	0.1
S12_Barr	0.03	0.03	0.02	0.02	0.03	0.01	0.03	-	0.01	0.01
S12_EC	-	-	0.01	0.01	0.01	-	-	0.01	0.01	0.01
MatCalo_Barr	0.03	0.02	0.02	0.02	0.01	0.01	0.01	0.01	0.01	0.01
MatCalo_EC	-	-	-	-	-	-	-	-	-	-
MatCryo_Barr	0.03	0.02	0.02	0.03	0.02	0.01	0.01	0.01	0.01	0.01
MatCryo_EC	-	-	0.01	0.01	0.16	-	-	0.01	0.01	0.09
Total	0.207	0.293	0.224	0.295	0.553	0.167	0.254	0.216	0.274	0.403

Table 4.35: Systematics from the photon energy scale using the m_H bias method for the 10 mass categories. The dashes indicate the systematic rounds to 0.

generated from the signal model. The injected signal is fixed at a particular mass value, and then the nominal signal+background model is fitted to the Asimov background+injected signal sample. The difference between the injected mass and the fitted mass is taken as the uncertainty. A scan of injected mass points is done in a mass region between 119 GeV$< m_{\gamma\gamma} <$135 GeV and the largest difference between the injected mass and the fitted mass is taken as the final uncertainty. This scan is performed independently for each category, and the results are shown in Table 4.37. The background mass bias is only taken into account in the mass analysis. For the coupling analysis, the Higgs boson mass is fixed to the combined $\gamma\gamma + ZZ$ measured mass.

	C1	C2	C3	C4	C5	C6	C7	C8	C9	C10	C11	C12
Zee	0.03	0.03	0.07	0.09	0.05	0.05	0.05	0.04	0.06	0.03	0.05	0.05
L2Gain	-0.10	-0.18	-0.11	-0.21	-0.15	-0.19	-0.22	-0.23	-0.16	-0.17	-0.18	-0.18
LatLeakUC	0.04	0.02	0.04	0.05	0.04	0.05	0.04	0.01	0.03	0.02	0.04	0.03
LatLeakCV	0.04	0.03	0.08	0.09	0.06	0.06	0.06	0.06	0.06	0.03	0.06	0.06
ConvInefficiency	0.02	-	0.02	0.03	0.02	0.02	0.01	-	0.02	-0.01	0.02	0.01
ConvFakeRate	0.01	-	0.01	0.03	0.01	0.01	-	-0.01	0.01	-0.02	0.01	0.01
Geant4	0.01	0.01	0.01	0.01	0.02	0.01	0.02	-0.01	0.02	-0.02	0.01	0.01
Pedestal	-0.01	-0.03	-0.01	-	-0.02	-0.01	-0.02	-0.05	-0.01	-0.03	-0.02	-0.03
ConvRadius	-0.01	-0.01	-0.02	-	-0.01	-	-	-0.03	-0.02	-0.04	-0.01	-0.02
L1Gain	-	-0.01	0.05	0.05	0.02	0.02	0.02	0.03	0.03	-	0.03	0.01
LArCalib_Barr	-0.10	-0.14	-0.05	-0.06	-0.08	-0.10	-0.09	-0.11	-0.08	-0.12	-0.09	-0.09
LArCalib_EC	-	-	-0.03	-0.03	-0.01	-0.02	-0.02	-0.01	-0.02	-0.03	-0.01	-0.02
LArUnconv_Barr	0.02	0.02	0.02	0.04	0.03	0.03	0.03	-0.01	0.02	-0.01	0.02	0.02
LArUnconv_EC	-	-	-	-	-	-	-	-	-	-	-	-0.01
LArElUnc_Barr	-0.05	-0.06	-0.09	-0.10	-0.08	-0.08	-0.09	-0.10	-0.08	-0.10	-0.08	-0.08
LArElUnc_EC	-	-	-0.06	-0.06	-0.03	-0.03	-0.04	-0.05	-0.04	-0.04	-0.03	-0.03
LArCalibElec	-	-0.01	0.01	0.02	0.01	0.01	-	-	-	-0.02	0.01	-0.02
MatID1	0.07	0.07	0.05	0.05	0.06	0.07	0.05	0.05	0.06	0.04	0.07	0.06
MatID2	-	-	0.03	0.04	0.02	0.02	0.02	-	0.02	-	0.02	0.01
MatID3	-	-	0.02	0.02	0.01	-	0.01	-	0.01	-	-	-
MatID4	-	-	0.01	0.01	-	-	-	-	0.01	-	-	-
Presampler_Barr	0.04	0.04	0.03	0.02	0.03	0.03	0.03	0.04	0.04	0.03	0.03	0.03
Presampler_EC	-	-	0.02	0.02	0.01	0.02	0.01	0.02	0.01	0.01	0.01	0.01
S12_Barr	0.02	0.03	0.01	0.01	0.01	0.02	0.02	0.03	0.01	0.03	0.02	0.02
S12_EC	-	-	0.01	0.01	0.01	-	0.01	0.01	0.01	0.02	-	-
MatCalo_Barr	0.02	0.02	0.02	0.02	0.02	0.02	0.02	0.02	0.02	0.01	0.02	0.02
MatCalo_EC	-	-	-	0.01	-	-	0.01	0.01	-	-	-	-
MatCryo_Barr	0.02	0.02	0.01	0.02	0.02	0.02	0.02	0.02	0.01	0.02	0.02	0.02
MatCryo_EC	-	-	0.04	0.04	0.02	0.01	0.02	0.03	0.02	0.02	0.01	0.01

Table 4.36: Systematics from the photon energy scale using the m_H bias method for the 12 coupling categories. The dashes indicate the systematic rounds to 0.

Category	Bkg Sys
C1	0.10%
C2	0.06%
C3	0.05%
C4	0.11%
C5	0.16%
C6	0.13%
C7	0.06%
C8	0.14%
C9	0.18%
C10	0.20%
Inclusive	0.18%

Table 4.37: Systematics from the choice of background parameterization as measured from the smeared background MC sample with an injected Asimov signal. Results are shown for each mass category and for the inclusive case.

4.9 Statistical Model

All aspects of the analysis are combined in one likelihood, which is then used to describe many different characteristics of the data. This likelihood encompasses the observable, $m_{\gamma\gamma}$, parameters of interest, m_H for the Higgs boson mass analysis, and the signal strength in relation to the expected SM signal ($\mu = (\frac{N_S}{N_S^{SM}})$) for the coupling analysis, and the nuisance parameters. These nuisance parameters describe the effect the different uncertainties in the analysis have on the final measured result. For the mass analysis, the signal strength μ is treated as a nuisance parameter without any constraints, meaning it's allowed to float freely in the fits. First, the likelihood for an individual event is constructed using the signal and background probability distributions (f_S and f_B) described in Sections 4.5.1 and 4.6.

$$\mathcal{L}(\mu, \boldsymbol{\theta}|m_{\gamma\gamma}) = \frac{\mu N_S(\boldsymbol{\theta})}{\mu N_S(\boldsymbol{\theta}) + N_B(\boldsymbol{\theta})} f_S(m_{\gamma\gamma}|\boldsymbol{\theta}) + \frac{N_B(\boldsymbol{\theta})}{\mu N_S(\boldsymbol{\theta}) + N_B(\boldsymbol{\theta})} f_B(m_{\gamma\gamma}|\boldsymbol{\theta}) \quad (4.21)$$

Here $\boldsymbol{\theta}$ represents the vector of nuisance parameters, N_S is the number of expected SM signal events, N_B is the number of background events, and f_S and f_B are from the pdfs for the signal and background events respectively.

The global likelihood is then the product of all the event likelihoods

$$\mathcal{L}(\mu, \boldsymbol{\theta}|\boldsymbol{m_{\gamma\gamma}}) = \frac{(\mu N_S + N_B)^{N'}}{N'!} e^{-\mu N_S + N_B} \prod_k^{N'} \mathcal{L}(\mu, \boldsymbol{\theta}|m_{\gamma\gamma,k}) \mathcal{G}(\boldsymbol{\theta}) \quad (4.22)$$

where $\boldsymbol{m_{\gamma\gamma}}$ is now the full set of measured $m_{\gamma\gamma}$ values from the N' events in the dataset. The first term in the global likelihood is the Poisson probability for the observed number of events (N'). The $\mathcal{G}(\boldsymbol{\theta})$ term is a unit Gaussian constraint for nuisance parameters.

Furthermore, if the dataset is broken into independent categories, then the global likelihood becomes the product of the above likelihood for each category:

$$\mathcal{L}(\mu, \boldsymbol{\theta}|\boldsymbol{m_{\gamma\gamma}}) = \prod_{c}^{N} \mathcal{L}_c(\mu, \boldsymbol{\theta_c}|\boldsymbol{m_{\gamma\gamma,c}}). \tag{4.23}$$

The vector of nuisance parameters ($\boldsymbol{\theta}$) contains the background model parameters and all the uncertainties within the analysis as described in Section 4.8. These nuisance parameters allow the signal yields and resolutions to vary in the model within their uncertainties (δ)

$$N_S \rightarrow N_S(1 + \delta_{syst}\theta_{syst}). \tag{4.24}$$

Most nuisance parameters are constrained by a Gaussian with unity width and vary within $\pm 5\sigma$ around the mean of 0. In some cases, a negative fluctuation is undesirable; for these cases, the nuisance parameters are modeled using a log-normal distribution

$$N_S \rightarrow N_S e^{(\sqrt{1+\delta^2})\theta}. \tag{4.25}$$

Systematics on the signal yield and the signal resolution are modeled with this log-normal function. In cases where uncertainties are correlated, they share the same nuisance parameter. The measured values are then those from maximizing the likelihood.

The profile likelihood for the parameter of interest is then defined as the ratio of the likelihood where the nuisance parameters are the values that maximize the likelihood for the parameter of interest hypothesis (m_H for the mass analysis; μ for

the coupling analysis) over the likelihood where all parameters are at their values which maximize the likelihood function

$$\lambda(m_H) = \frac{\mathcal{L}(m_H, \hat{\hat{\mu}}, \hat{\hat{\boldsymbol{\theta}}})}{\mathcal{L}(\hat{m_H}, \hat{\mu}, \hat{\boldsymbol{\theta}})}. \tag{4.26}$$

The profile likelihood ratio lies between 0 and 1, where a value of 1 means the tested value of m_H or μ matches well with the data.

In the case of the signal strength, a negative value is non-physical. Therefore, the modified profile likelihood is used

$$\lambda(\mu) = \begin{cases} \frac{\mathcal{L}(\mu, \hat{\hat{\boldsymbol{\theta}}}(\mu))}{\mathcal{L}(\hat{\mu}, \hat{\boldsymbol{\theta}})}, & \hat{\mu} \geq 0 \\ \frac{\mathcal{L}(\hat{\mu}, \hat{\hat{\boldsymbol{\theta}}}(\mu))}{\mathcal{L}(0, \hat{\hat{\boldsymbol{\theta}}}(0))}, & \hat{\mu} < 0 \end{cases} \tag{4.27}$$

The significance of an observation is quantified by calculating the compatibility of the observed data and a background-only hypothesis. The estimator for the statistical test is the test statistic ($\tilde{q_0}$) defined as

$$\tilde{q_0} = \begin{cases} 0, & \hat{\mu} < 0 \\ -2ln\lambda(0), & \hat{\mu} \geq 0 \end{cases} \tag{4.28}$$

The compatibility between the observed data and the background-only hypothesis is then quantified by the p-value given by integrating the distribution of test statistics from the observed value to infinity

$$p_0 = \int_{\tilde{q}_{0,obs}}^{+\infty} f(\tilde{q_0}|0, \hat{\hat{\boldsymbol{\theta}}}(0)) d\tilde{q_0}. \tag{4.29}$$

This gives the probability that a background-only process would yield the observed results. The probability is then turned into a significance using the quantile of a Gaussian with unit width

$$Z = \Phi^{-1}(1 - p_0) \tag{4.30}$$

where Φ is the inverted cumulative distribution of the gaussian. A discovery requires a significance greater than Z =5, and this was achieved in 2012. After the discovery, the focus turned to measurement of the new particle's properties. To do this, the test statistic

$$q_\mu = -2 \ln \lambda(\mu) \tag{4.31}$$

is built and the measured μ value is that which minimizes q_μ. Here asymptotics approximations are used which assume the behavior of $\lambda(\mu)$ follows a χ^2 distribution. As such, $\lambda(\mu)$ is taken as equivalent to a χ^2 change with respect to the minimum. In this way, confidence intervals are constructed around the measured μ values.

4.10 Results

The analysis presented here is an updated version of that which was used to discover the Higgs boson. For the previous analysis, nine categories were used, eight of which were defined solely on the photon characteristics and one tight VBF category [33]. Figure 4.10 shows the p_0 value for the diphoton channel at the time of discovery and with the current version of the $H \to \gamma\gamma$ coupling analysis. The significance at that

time for the combined decay channels was 5.9 σ. A comparison between the analysis without the VBF category and with the category is shown. As can be seen, the VBF category contributed a lot of sensitivity for the discovery. The analysis has been continually updated and reoptimized with the inclusion of the rest of the 2012 data, and the analysis presented in this paper is the final version of the Higgs decaying to diphoton analysis before the start of Run 2 of the LHC.

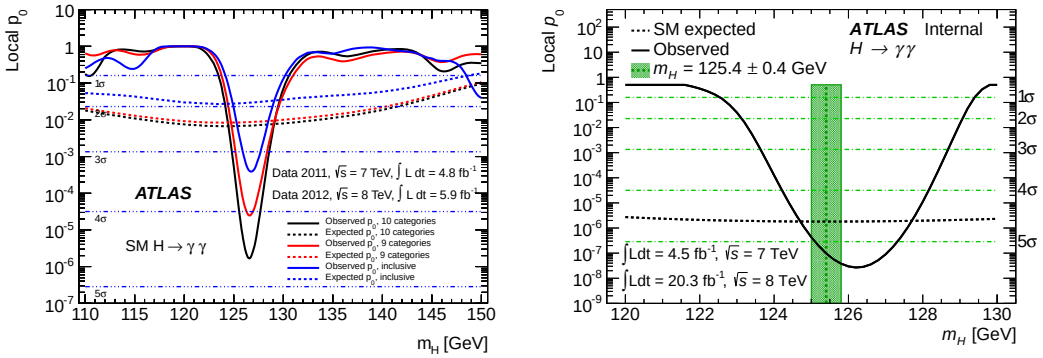

Figure 4.10: The p_0 value for the diphoton channel at the time of discovery [33] (left). Results are shown for a fully inclusive case, for only 9 categories defined by the photon kinematics, and for the full analysis including the 2-jet VBF category. On the right is the p_0 plot for the latest version of the diphoton Higgs analysis presented in this thesis.

The diphoton invariant mass distributions in data and the corresponding fits are shown in Fig. 4.11 and 4.12 for the inclusive and combined VBF categories respectively. Both 7 and 8 TeV are shown, and the data events are weighted by the corresponding signal-to-background ratio of the category it belongs to. For the fits, the Higgs boson mass was fixed to the combined $H \to \gamma\gamma$ and $H \to ZZ$ mass measurement 125.4 GeV.

The excess shown in Fig. 4.11 has a local observed significance of 5.2 σ while the expected significance is 4.7 σ. The measured μ value from the fits is

$$\mu = 1.17 \pm 0.23(\text{stat})^{+0.10}_{-0.08}(\text{syst})^{+0.12}_{-0.08}(\text{theory}). \tag{4.32}$$

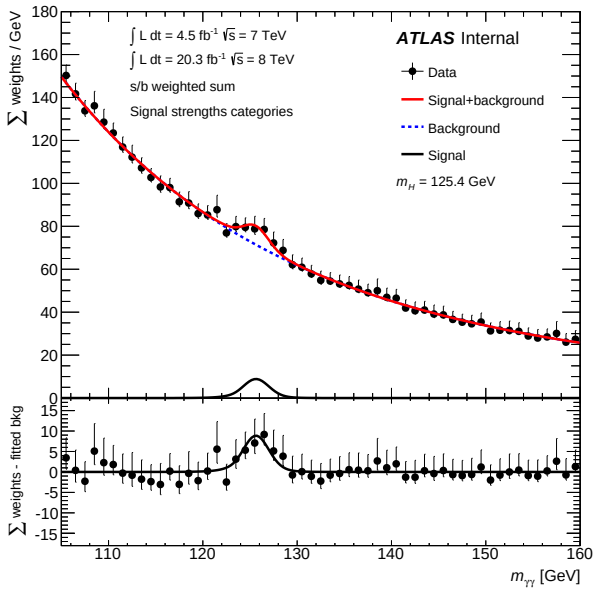

Figure 4.11: The inclusive diphoton invariant mass distribution. Events are weighted by the signal-to-background ratio in its category. Both 7 and 8 TeV data is shown here. The dotted line is the background-only model, while the solid curve is the signal plus background from the fit. Here, the curves are the sum of the fitted models in each category. The lower panel shows the difference between the data and the fitted background model.

When all the uncertainties are added in quadrature, the result is $\mu = 1.17^{+0.28}_{-0.26}$. This result has a 0.7 σ compatibility with the Standard Model. As shown in Fig. 4.13, the inclusion of the mass scale systematics broadens the μ dependence on the Higgs boson mass, so only a very small dependence on the mass exists in the $\pm$ 0.4 GeV range around the measured mass.

The measured signal strengths for each of the twelve defined categories is shown in Fig. 4.14. For this measurement, the μN_S terms in the likelihood were broken down into the individual production processes:

$$\mu N_S \rightarrow \sum_p \mu_p N_p, \tag{4.33}$$

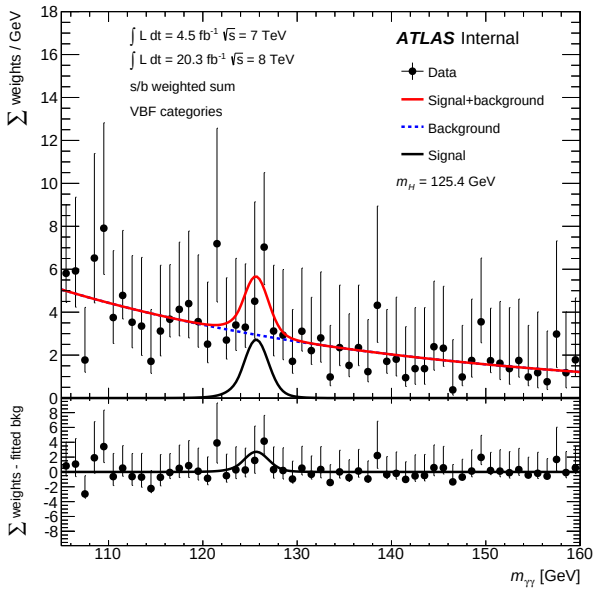

Figure 4.12: The diphoton invariant mass distribution for the combined VBF categories. Events are weighted by the signal-to-background ratio in its category. Both 7 and 8 TeV data is shown here. The dotted line is the background-only model, while the solid curve is the signal plus background from the fit. Here, the curves are the sum of the fitted models in each category. The lower panel shows the difference between the data and the fitted background model.

where p represents each production process, μ_p is the signal strengths of the individual production processes, and N_p is the corresponding expectation in the Standard Model.

Each is compatible with the combined μ value. Figure 4.15 shows the breakdown of the signal strengths into the combined categories for each production process type, and Fig. 4.16 shows the breakdown of the statistical and systematical errors. The measured signal strengths and their uncertainties are

$$
\begin{aligned}
\mu_{ggF} &= 1.32 \pm 0.32(\text{stat})^{+0.13}_{-0.09}(\text{syst})^{+0.19}_{-0.11}(\text{theory}) \\
\mu_{VBF} &= 0.8 \pm 0.7(\text{stat})^{+0.2}_{-0.1}(\text{syst})^{+0.2}_{-0.3}(\text{theory}) \\
\mu_{WH} &= 1.0 \pm 1.5(\text{stat})^{+0.3}_{-0.2}(\text{syst})^{+0.2}_{-0.1}(\text{theory}) \\
\mu_{ZH} &= 0.1^{+3.6}_{-0.1}(\text{stat})^{+0.7}_{-0.0}(\text{syst})^{+0.4}_{-0.0}(\text{theory}) \\
\mu_{t\bar{t}H} &= 1.6^{+2.6}_{-1.8}(\text{stat})^{+0.6}_{-0.4}(\text{syst})^{+0.5}_{-0.1}(\text{theory})
\end{aligned}
\tag{4.34}
$$

For the measurements, the tH and $b\bar{b}H$ production processes were assumed to be equal to the Standard Model prediction (μ_{tH} =1 and $\mu_{b\bar{b}H}$ =1).

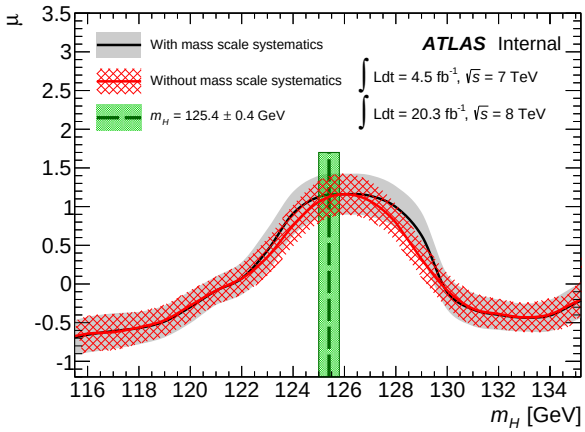

Figure 4.13: The combined measured signal strength (μ) versus the Higgs boson mass. A very small dependence is observed. The hatched band is excluding the systematics on the mass scale, while the shaded curve includes the mass scale systematic. The vertical dashed line is the combined measured mass of m_H =125.4 ± 0.4 Gev.

The correlations between the ggF and VBF production modes was studied by setting the tH and $b\bar{b}H$ contributions to the Standard Model expectations, and then profiling the signal strengths μ_{ZH}, μ_{WH}, $\mu_{t\bar{t}H}$. The best fit value for $\mu_{VBF} \times \mu_{ggF}$ and the 68% and 95% confidence level contours are shown in Fig. 4.17.

Ratios of the signal strengths for different production modes were also measured in order to have measurements independent of the diphoton branching ratio. Again

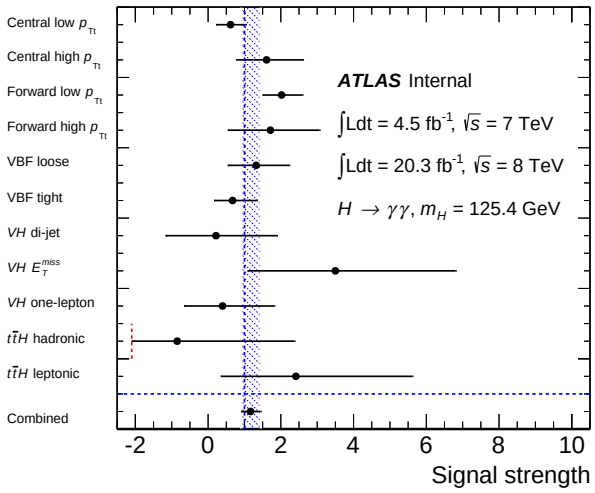

Figure 4.14: The measured signal strengths for each of the twelve coupling categories. The dashed vertical line at μ =1 shows the Standard Model expectation, and the hatched region shows the 68% confidence interval for the combined μ measurement. For $t\bar{t}H$ hadronic category, the dashed red line shows the limit at which the fitted signal strength becomes negative in the mass fit range.

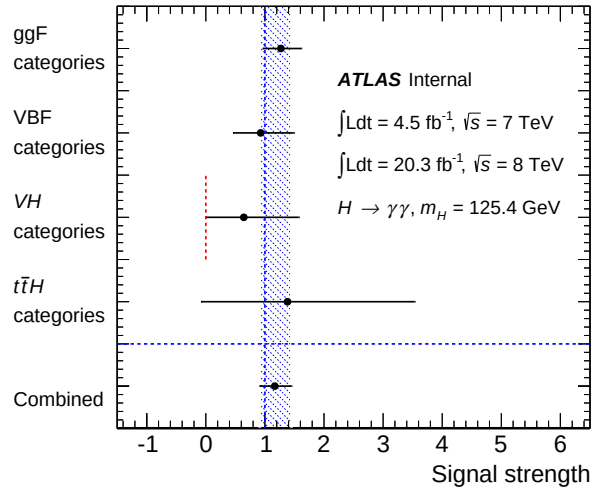

Figure 4.15: The measured signal strengths for categories defined for each production process type. The dashed vertical line at μ =1 shows the Standard Model expectation, and the hatched region shows the 68% confidence interval for the combined μ measurement. For VH categories, the dashed red line shows the limit at which the fitted signal strength becomes negative in the mass fit range.

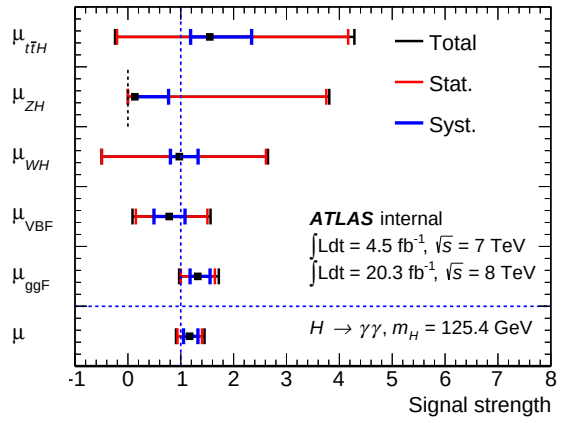

Figure 4.16: The measured signal strengths for categories defined for each production process and the combined μ. The Standard Model expectation is designated by the vertical dashed line.

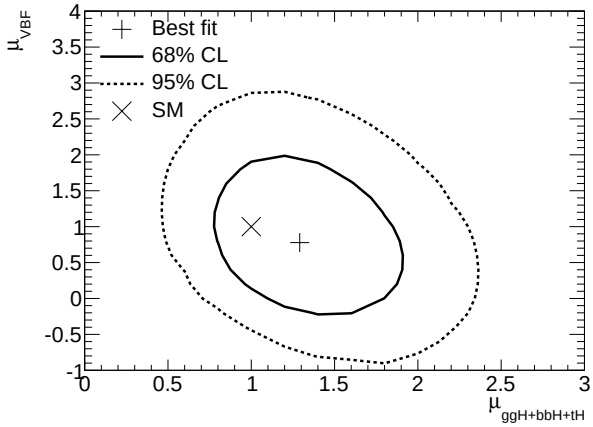

Figure 4.17: The 2D contours for μ_{ggF} and μ_{VBF}. The '+' indicates the best fit value, and the '×' indicates the Standard Model expectation. The solid (dashed) curve represents the 68% (95%) contour.

the μ_{tH} and $\mu_{b\bar{b}}H$ contributions were fixed to 1, and the other production process not being measured were profiled. The ratio results are

$$\begin{aligned} \mu_{VBF}/\mu_{ggF} &= 0.6^{+0.8}_{-0.5} \\ \mu_{VH}/\mu_{ggF} &= 0.6^{+1.1}_{-0.6} \\ \mu_{t\bar{t}H}/\mu_{ggF} &= 1.2^{+2.2}_{-1.4}. \end{aligned} \tag{4.35}$$

While these values are not measured to be exactly the Standard Model expectation, they are all consistent with it.

4.11 Summary

This chapter presented the signal strength measurements for the Higgs boson in the diphoton decay channel. Events were divided into twelve different categories defined to maximize production process purities for each of the five processes. The inclusive signal strength was measured to be μ =1.17$\pm$0.27 which is less than 1 σ from the Standard Model expectation. Additionally, the signal strength for each individual production process was measured. The signal strength for the VBF process was measured to be μ_{VBF} =0.7 $\pm$0.7. Signal strength ratios of each production process to the ggF production process were also measured and found to be compatible within 1 σ with the Standard Model expectation.

Chapter 5

Differential Cross Sections for the Higgs Boson

This chapter summarizes the fiducial and differential cross section measurements of the Higgs boson decaying into two photons with the 2012 data. The Higgs boson signal is extracted in a similar way to the mass and coupling measurements described in Sec. 4.5.1. The measured signal is at detector level, meaning it is measured after the particles hit the detector and are reconstructed. This detector level measurement is then unfolded to particle level using a bin-by-bin unfolding technique. Here, particle level is the truth-level distribution before any detector acceptance is applied. The unfolding factors account for the resolution effects of object reconstruction and the efficiencies associated with triggering and reconstruction. Care is taken to ensure the unfolding is as model independent as possible. The unfolded distributions are then compared to state-of-the-art theoretical predictions of the Standard Model Higgs boson. In addition, non-perturbative and fiducial acceptance factors are derived to allow comparison to theories which are at parton level and/or do not decay the Higgs boson. Variables probing the nature of the Higgs boson were selected for this

study, and in particular, distributions concerning the production of the Higgs boson in association with jets were a priority. The variables which are investigated are listed below.

Inclusive variables:

- The transverse momentum of the diphoton system, $p_T^{\gamma\gamma}$, is sensitive to the different production modes and any associated jets.
- The rapidity of the diphoton system, $|y_{\gamma\gamma}|$, is sensitive to the underlying PDFs.
- The angle between the diphoton system and the z-axis, $|\cos\theta^*|$, defined using the Collins-Soper rest frame [130], is sensitive to the spin of the Higgs boson.
- The orthogonal component of the diphoton p_T to the "thrust-axis" as defined in Eq. 4.7, $p_{Tt}^{\gamma\gamma}$. This variable is sensitive to the same physics as the diphoton p_T, but has better experimental resolution. As described in Sec. 4.4, $p_{Tt}^{\gamma\gamma}$ is used in the categorization for both the mass and coupling analyses.
- The difference in rapidity between the two photons, $|\Delta y_{\gamma\gamma}|$, is sensitive to the decay properties of the Higgs boson.
- The jet multiplicity, N_{jets}, in Higgs boson events is sensitive both to the different production mechanisms and to the QCD radiation. The N_{jets} spectrum is measured for two cases, once for jet p_T >30 GeV and once for jet p_T >50 GeV in order to probe different scales.
- The largest beam thrust, τ_1, of a jet is defined as [131]

$$\tau_1 = |\vec{p}_{T,jet}| e^{-|y_{jet} - y_{\gamma\gamma}|}. \tag{5.1}$$

  The beam thrust is important for understanding QCD radiation.

- The beam thrust of an event, $\sum_i \tau_i$, is also important for understanding QCD radiation, particularly in the case of jet-vetoes.

1-Jet inclusive variables:

- The p_T of the leading jet, $p_{T,jet1}$. This is also measured for ithe exclusive case, N_{jets} =1.
- The rapidity of the leading jet, $|y_{jet1}|$.
- The scalar sum of p_T for all jets, $H_{T,jets}$, is sensitive to the scale of the event.

2-Jet inclusive variables:

- The p_T of the subleading jet, $p_{T,jet2}$.
- The rapidity of the subleading jet, $|y_{jet2}|$.
- The p_T of the diphoton+dijet system, $p_{T,\gamma\gamma jj}$, which is also sensitive to the presence of a third jet.
- The invariant mass of the dijet system, m_{jj}, which is important for isolating the VBF and VH production processes.
- The azimuthal angle between the two leading jets, $\Delta\phi_{jj}$.
- The difference in rapidity between the two leading jets, Δy_{jj}, which is sensitive to the VBF production mode and the CP-quantum numbers.
- The azimuthal angle between the diphoton and dijet systems, $\Delta\phi_{\gamma\gamma,jj}$, which as described in Sec. 4.4 is used to categorize events in the coupling analysis.

3-Jet inclusive variables:

- The p_T of the jet with the third highest p_T, $p_{T,jet3}$.

2D distributions

- $p_T^{\gamma\gamma} \times N_{jets}$, the Higgs boson p_T spectrum in bins of jet multiplicity.
- $p_T^{\gamma\gamma} \times \cos\theta^*$, the Higgs boson p_T spectrum in bins of $\cos\theta^*$.

5.1 Data and MC Samples

The nominal reconstruction level datasets used in the differential cross section analysis are the same 2012 data and 8 TeV MC samples as used in the mass and coupling measurements described in Sec. 4.1 and are normalized in the same way.

For systematics studies ggF events were generated using different MC generators and one sample was generated using a different showering program. All samples are generated with the CT10 PDF and are normalized to the NNLO+NNLL QCD calculations with NLO electroweak corrections. To assess the impact of the showering, hadronization and underlying event models, the nominal POWHEG ggF events at parton level were passed through HERWIG [132, 133] and JIMMY [134]. For generator modeling systematics two ggF samples in association with jets were produced with POWHEG using the MiNLO procedure [99], and then showered using PYTHIA8. One sample is an H+1jet sample, which generates the Higgs boson in association with 1 jet at NLO and includes H+0jets at NLO. This sample is the MiNLO HJ sample. The second sample is H+2jets events at NLO and are referred to as MiNLO HJJ. This sample only includes H+0/1jet events at LO. More details on the POWHEG generation of the Higgs boson in association with jets is in Ref. [97].

Another ggF sample was generated with Sherpa using the CT10 PDF and the internal showering within Sherpa. The tune for the multiple parton interactions is the authors' default tune. This sample was generated with Sherpa v1.4.3 [111], which generates Higgs boson events with up to four partons in the final state at LO. The

CKKW procedure [135] is used to match the matrix element to the parton shower. This sample has been fully reconstructed with ATLAS software and is used to estimate the model dependence of the unfolding factors.

Extra samples were generated at truth level for a Higgs boson mass of 125.4 GeV, the measured mass from $H \to \gamma\gamma$ and $H \to ZZ$ in ATLAS [136], in order to compare the unfolded distributions to theory predictions.

The VH and $t\bar{t}H$ processes were generated and showered with Pythia8 using the CTEQ6L1 PDF. This is the same generation setup as is used for the reconstruction level MC. Similarly, the VBF process is also generated in the same way as the reconstruction level MC. Events are generated at parton level by Powheg using the CT10 PDF and then showered with Pythia8.

MiNLO HJ and MiNLO HJJ samples were also produced at particle level for a Higgs boson mass of 125.4 GeV. They were generated as before using the CT10 PDF and interfaced to Pythia8 for the showering, hadronization, and underlying event.

Parton level distributions for $p_T^{\gamma\gamma}$, $|y_{\gamma\gamma}|$, $\Delta y_{\gamma\gamma}$, and $|\cos\theta^*|$ variables were calculated with HRes2.2 [95], which is accurate to NNLO+NNLL in QCD but includes no electroweak corrections. The HRes predictions are then corrected in two ways: the calculation is corrected to particle level using derived non-perturbative correction factors, and a small correction is applied to account for the photon isolation requirement. Both of these corrections will be described in Sec. 5.8.

5.2 Reconstruction-Level Selections

5.2.1 Object Selection

The selection of reconstructed photons is the same as described in Sec. 4.2, where two photons are selected that both pass 'tight' ID requirements and isolation cuts.

Object selections are also similar to those described in Sec. 4.2, but with the following modifications:

- **Jets.** For all variables except the τ variables, a flat p_T >30 GeV requirement is applied to all jets. Instead of requiring $|\eta|$ <4.5 as in the coupling analysis 4.2.3, here, jets are required to have $|y|$ <4.4 as y is a Lorentz invariant quantity. All other selection cuts are the same as the coupling analysis. For the τ variables, the phase-space is opened up to match that of the diphoton coupling analysis: p_T >25 GeV for central jets $|y|$ <2.4.

- **Electrons.** Electron selection is exactly the same as described in Sec. 4.2.4: p_T >15 GeV and $|\eta|$ <2.47.

- **Muons.** The only use of muons in this analysis is the measurement of the production of the Higgs boson in association with at least one lepton. There is no distinction in the categorization between electrons and muons, so it was decided to unify the lepton selection. Therefore, the kinematic selections on muons are identical to those on electrons: p_T >15 GeV and $|\eta|$ <2.47. This unification of lepton selection also minimizes model dependence.

5.2.2 Event Selection

The event selection is identical to that described in Sec. 4.3, where various selections are applied to ensure the quality of the data, and the two leading photons are required to have $p_T/m_{\gamma\gamma} > 0.35$ (0.25) GeV with an invariant mass between 105 GeV and 160 GeV.

5.3 Truth-Level Object Selections

Truth objects are selected from the full event record in MC samples. Objects must be stable, final state particles, meaning they have a mean lifetime of at least 10 ps, and they do not come from the GEANT4 simulation. The remaining particles are then stored for jet clustering. Before photon and lepton selections, all particles originating from hadronization are rejected by checking the particle ID of all parent particles and rejecting those with ID>111 (π^0 and greater). In the case where a particle's parent is a τ or the same ID as the final-state particle, the ID of the grandparent particles is checked. Truth level particles are then selected using the criteria described below.

5.3.1 Truth Photons

Photons are first identified by their PDG ID (=22). The acceptance is similar to that for reconstructed photons where p_T >25 GeV and $|\eta|$ <2.37. For particle level, the transition region (1.37< $|\eta|$ <1.56), which is excluded at detector level, is included in the acceptance region. Because of the difference in hadronic activity between the different production modes, particularly in $t\bar{t}H$, a particle isolation is required in order to minimize the model dependence of the unfolding factors. The four-vectors of all stable particles withing $\Delta R < 0.4$ of the selected photon are summed. Muons, neutrinos and the selected photon are excluded from the summation. The resulting transverse energy, E_T^{iso}, is then required to be less than 14 GeV. This cut value of 14 GeV was chosen based on the reconstruction level isolation energy profiled as a function of truth isolation energy. The reconstruction isolation energy of 6 GeV used in this analysis corresponds to a truth level isolation energy of 14 GeV. This was checked for each production process independently, and all converged at roughly the same 14 GeV value.

5.3.2 Truth Leptons

Electrons and muons are also first identified by their PDG ID (=11 and =13 respectively). They are then dressed by truth photons within ΔR <0.1, where dressing means to add the photons' four-vectors to that of the lepton's. These photons have had no selection cuts applied, and they are matched only to the closest lepton, which ensures that each photon is only added to one lepton. Dressing the leptons in such a way recovers much of the final-state radiation, and the particle level lepton will more closely resemble what is measured in the EM calorimeter at reconstruction level. The resulting dressed leptons must then pass the same kinematic selection cuts as reconstructed leptons: p_T >15 GeV and $|\eta|$ <2.47. No isolation requirement is applied because it was unnecessary once particles originating from hadrons were rejected.

5.3.3 Truth Jets

Truth jets are clustered using the anti-k_t algorithm with distance parameter R = 0.4. All stable final state truth particles enter into the clustering except muons and neutrinos. This was done to mimic what is seen at detector level. Truth jets are then required to have p_T >30 GeV and $|y|$ <4.4.

5.3.4 Overlap Removal

An object overlap removal which mimics that at reconstruction level is then applied to all selected objects passing the above criteria. The overlap removal is as follows:

- Electrons within $\Delta R(e, \gamma)$ <0.4 are removed.
- Jets within $\Delta R(jet, e)$ <0.2 or within $\Delta R(jet, \gamma)$ <0.4 are removed.
- Muons within $\Delta R(\mu, \gamma)$ <0.4 are removed.

5.3.5 Higgs Candidate Selection

The final Higgs boson candidate photons are selected in the same way as at reconstruction level. The two isolated photons with the highest p_T are selected and must have $(p_T/m_{\gamma\gamma})$ <0.35 (0.25) for the leading (subleading) photon. The invariant mass must also be between 105 GeV and 160 GeV.

5.4 Binning of Variables

Binning for the differential distributions is based on a number of different criteria, and, where possible, without looking at the data in the signal region. Instead, the binning is based on the expected significance using $s/\sqrt{b}$. Each bin is required to have at least 1σ expected significance and all bins in a distribution to have approximately the same expected significance. A requirement for the unfolding is that each bin must have a high purity, where purity is defined as

$$P_i = \frac{n_i^{det,part}}{n_i^{det}}, \tag{5.2}$$

where n_i^{det} is the number of events in a bin at detector level, and $n_i^{det,part}$ is the number of events in a bin at both reconstruction level and particle (truth) level. The purity of a bin quantifies the migrations into and out of the bin when going from detector level to particle level. For unfolding, the purity of a bin must be high so as to avoid large uncertainties when correcting from detector level to particle level. This is especially important when using a bin-by-bin unfolding method as is used in this analysis.

Once a binning is chosen, it is possible that the number of events in a bin in data are not optimal. Bins with negative fit yields represent unphysical cross sections and cannot be unfolded using the bin-by-bin method. Also, if a bin is found to have too

few signal events due to a downward statistical fluctuation, the fits to the data will be very unstable. Therefore, in such cases, the binning of a variable will be revisited by simply merging the problem bin with neighboring bins, or readjusting the bin edges.

For many variables, there will be overflow events which are not included in the measurements. These events go into their own 'rest' category, which is only used for fitting purposes, as will be described in Sec. 5.5. For the leading jet p_T variable, the first bin, which is from 0-30 GeV, contains all events with exactly 0 jets. For the subleading and third jet p_T distributions, the first bins contain all events with exactly 1 jet and 2 jets respectively. A similar strategy is used for the τ_{jet} variables, where the first bin from 0-8 GeV includes events with 0 jets.

The binning for all differential variables is shown in Table 5.1.

Table 5.1: Variable bin edges for the differential cross section measurements. Some variables also have a 'rest', or overflow, bin that is considered as a separate category during signal extraction.

Variable	Binning	N_{bins}
$N_{\text{jets}}(p_T > 30$ GeV)	$\{0, 1, 2, \geq 3\}$	4
$p_{\text{T}}^{\gamma\gamma}$	$\{0, 20, 30, 40, 50, 60, 80, 100, 200\}$ GeV	8 + rest
$\lvert y_{\gamma\gamma}\rvert$	$\{0.0, 0.3, 0.6, 0.9, 1.2, 1.6, 2.4\}$	6
$\lvert\cos\theta^*\rvert$	$\{0, 0.1, 0.2, 0.3, 0.4, 0.5, 0.6, 0.7, 0.8, 0.9, 1.0\}$	10
$p_{\text{T,jet1}}$	$\{0, 30, 50, 70, 100, 140\}$	5 + rest
m_{jj}	$\{0, 200, 400, 650, 1000\}$	4 + rest
$H_{\text{T,jets}}$	$\{0, 30, 50, 70, 150, 250\}$	5 + rest
$N_{\text{jets}}(p_T > 50$ GeV)	$\{0, 1, 2, \geq 3\}$	4
$\lvert y_{\text{jet1}}\rvert$	$\{0.0, 1.0, 2.0, 3.0, 4.4\}$	4 + rest
$p_{\text{T,jet2}}$	$\{0, 30, 50, 70, 140\}$	4 + rest
$\Delta\phi_{\text{jj}}$	$\{0.0, \pi/3, 2\pi/3, 5\pi/6, \pi\}$	4 + rest
$\Delta\phi_{\gamma\gamma,\text{jj}}$	$\{0.0, 2.6, 2.9, 3.1, \pi\}$	4 + rest
$\Delta\phi_{\gamma\gamma,\text{jj}}$	$\{0.0, 2.6, 2.9, 3.1, \pi\}$	4 + rest
p_{Tt}	$\{0, 10, 20, 30, 40, 60, 80, 150]\}$	7 + rest
$\lvert y_{\gamma\gamma}\rvert$	$\{0.0, 0.3, 0.6, 0.9, 1.2, 1.5, 2.0, 2.55\}$	7 + rest
τ_1	$\{0, 8, 16, 30, 55\}$	4 + rest
$\sum_i \tau_i$	$\{0, 8, 16, 30, 55, 150\}$	5 + rest
$\lvert y_{\text{jet2}}\rvert$	$\{0.0, 1.0, 2.0, 3.0, 4.4\}$	4 + rest
$p_{\text{T,jet3}}$	$\{0, 30, 50, 150\}$	3 + rest
Δy_{jj}	$\{0.0, 2.0, 4.0, 5.5, 8.8\}$	4 + rest
$p_{\text{T}\gamma\gamma jj}$	$\{0, 30, 55, 80, 140\}$	4 + rest
$p_{\text{T}}^{\gamma\gamma} \times \lvert\cos\theta^*\rvert$	$\{0, 80, 200\} \times \{0.0, 0.25, 0.50, 0.75, 1.0\}$	8 + rest
$N_{\text{jets}} \times p_{\text{T}}^{\gamma\gamma}$	N_{jets}=0 $\times$ $\{0, 50, 200\}$ N_{jets}=1 $\times$ $\{0, 50, 100, 200\}$ $N_{\text{jets}}\geq$2 $\times$ $\{0, 50, 100, 200\}$	8 + rest

5.5 Signal and Background Models

5.5.1 Signal Model

The differential cross section uses the same signal model as the mass and coupling analyses. The signal is modeled by a Crystal Ball function with an added Gaussian to account for the wider tails of the distribution as defined in Sec. 4.5.1. Signal samples for each mass point are fitted with the global signal model defined in Sec. 4.5.2. A separate global fit is done for each bin of each variable, so for the $p_T^{\gamma\gamma}$ distribution, nine independent global signal fits are done.

It was noticed that a small fraction of events, $\sim$1%, in the high-mass tails of the signal distributions was greatly distorting the signal shapes. This was especially the case for variables involving jets. To avoid this, the signal shapes are only fit in the $m_{\gamma\gamma}$ range -20 GeV to +15 GeV around each mass point.

5.5.2 Background Model

The backgrounds are parameterized by a single smooth function, with each bin of each variable having its own background parameterization. As described in Sec. 4.6, the background function is chosen by fitting a signal+background function to a background-only distribution. The same smeared MC samples were used here, but with varying background process compositions. A 2x2D sideband technique is used to extract the background compositions from data control regions. Fifteen control regions are defined by each variation where at least one photon does not pass the 'tight' ID, at least one photon does not pass the isolation criteria, or at least one photon does not pass either the 'tight' ID or the isolation criteria. The background composition was derived for the inclusive case and for different jet multiplicities and are shown in Table 5.2. These compositions are then used to combine the different

smeared MC samples with the proper composition. H+1j variables use the derived composition for exactly 1 jet events, H+2j variables use the derived composition for exactly 2 jet events, and the $p_{T,jet3}$ variable uses the $\geq$3 jet composition. The background process compositions were found to vary slowly with respect to the jet multiplicity. The coupling analysis presented in Chapter 5 used a previous version of this 2x2D sideband background composition; however, only the composition of the inclusive case was used.

Table 5.2: The background compositions for the inclusive case and in bins of jet multiplicity.

	$\gamma\gamma$	γj	jj
Inclusive	78.3%	19.3%	2.4%
$N_{\text{jets}} = 0$	75.5%	21.6%	2.9%
$N_{\text{jets}} = 1$	81.9%	16.5%	1.6%
$N_{\text{jets}} = 2$	84.9%	14.3%	0.8%
$N_{\text{jets}} \geq 3$	85.0%	14.1 %	0.8%

The spurious signal, as defined in Sec. 4.6.2, is derived for each bin of each variable independently. As before, a background function is only considered if the spurious signal is either less than 10% of the expected Standard Model Higgs boson signal or less than 20% of the expected background statistical uncertainty. In the case where more than one function passes these criteria, the function with the fewer degrees of freedom is chosen.

The ratio of spurious signal to background is expected to have a smooth behavior when going from bin to bin in a single variable. However, this was shown not to be the case because the spurious signal can vary due to statistical fluctuations in the smeared MC. In order to account for these fluctuations, an averaging between bins is done. The spurious signal for each bin is averaged with its two neighboring bins; in

the case of the first or last bin, then the spurious signal is averaged with just the one neighboring bin. The formula for the averaging of bin i is

$$\langle b \rangle_i = \frac{B_i}{3} \sum_{j=i-1}^{i+1} \frac{b_j}{B_j}, \tag{5.3}$$

where b_j is the spurious signal for bin j and B_j is the number of background events in bin j taken from the fit. This averaging procedure aims to keep the ratio b/B constant since the spurious signal is expected to scale with the number of background events. A further refinement is done to take into account the mass dependence. The averaged spurious signal is evaluated for three different mass points: 120 GeV, 126.5 GeV, and 130 GeV. The final spurious signal is taken as the maximum of the three values in each bin.

The majority of background functions are a single decaying exponential or an exponential of a second-order polynomial (Eq. 4.17). The chosen background functions and the corresponding spurious signal for $p_T^{\gamma\gamma}$ and N_{jets} are shown in Tables 5.3 and 5.4.

5.5.3 Signal Extraction

The signal yields are extracted by making simultaneous signal+background fits for all bins of a variable in data. A first preliminary background-only fit is done. The fitted values for the background function parameters become the starting values for the s+b fit to data. The signal model is from the global fits, with all parameters held constant, and the expected yields are fixed to the Standard Model expectation, while the signal strength variable, μ, is allowed to float. Uncertainties on the mass scale, signal resolution, and mass bias are added to the mean of the Crystal Ball and

Table 5.3: The chosen background model functions and the corresponding spurious signal for bins of $p_{\mathrm{T}\gamma\gamma}$. The last column shows the ratio of the spurious signal to the expected Standard Model signal. Exp2 is an exponential of a second-order polynomial (Eq. 4.17) and exp3 is an exponential of a third-order polynomial (Eq. 4.18).

Cat.	Background Model	Spurious Signal	SS/Sig_SM
1	exp2	16.08	82.7%
2	exp3	9.45	5.4%
3	exp2	8.45	9.4%
4	exp3	5.49	5.3%
5	exp2	3.99	8.1%
6	exp2	4.49	6.8%
7	exp2	1.54	3.3%
8	exp2	1.89	7.3%

Table 5.4: The chosen background model functions and the corresponding spurious signal for bins of N_{jets}. The last column shows the ratio of the spurious signal to the expected Standard Model signal. Exp2 is an exponential of a second-order polynomial (Eq. 4.17).

Cat.	Background Model	Spurious Signal (SS)	SS/Sig_SM
1	exp2	11.42	4.2%
2	exp2	10.32	6.2%
3	exp2	5.03	6.6%
4	exp2	2.46	3.8%

Gaussian functions (μ_{CB} and μ_{GA} respectively) and to the width of the Crystal Ball function (σ_{CB}) in the signal PDF. The modified parameters become

$$\begin{aligned}
\mu_{\mathrm{CB}} &= (m_H + \mu_{\mathrm{CB\ offset}} + (m_H - 125)\,\mu_{\mathrm{CB\ slope}}) \cdot \Theta_{\mathrm{EnScale}} \cdot \Theta_{\mathrm{BkgBias}}\,, \\
\mu_{\mathrm{GA}} &= (m_H + \mu_{\mathrm{GA\ offset}} + (m_H - 125)\,\mu_{\mathrm{GA\ slope}}) \cdot \Theta_{\mathrm{EnScale}} \cdot \Theta_{\mathrm{BkgBias}}\,, \\
\sigma_{\mathrm{CB}} &= (\sigma_{\mathrm{offset}} + (m_H - 125)\,\sigma_{\mathrm{slope}}) \cdot \Theta_{\mathrm{EnRes}}\,,
\end{aligned} \tag{5.4}$$

where $\Theta_{\mathrm{EnScale}}$ is the uncertainty associated with the mass scale, $\Theta_{\mathrm{BkgBias}}$ is the mass

bias due to the choice of background function, and Θ_{EnRes} is the uncertainty associated with the mass resolution. The energy scale and resolution systematics are treated as correlated between all bins of a variable, while the mass bias systematic is treated as uncorrelated. Both the energy scale and mass bias systematics are modeled by a Gaussian constraint:

$$\Theta_{\text{EnScale/BkgBias}} = \left(1 + \boldsymbol{\delta}_{\text{EnScale/BkgBias}}\boldsymbol{\theta}_{\text{EnScale/BkgBias}}\right). \tag{5.5}$$

where $\theta_{\text{EnScale/BkgBias}}$ is the nuisance parameter and $\delta_{\text{EnScale/BkgBias}}$ is the uncertainty. The energy resolution is modeled by a log-normal constraint:

$$\Theta_{\text{EnRes}} = \exp\left(\boldsymbol{\theta}_{\text{EnRes}}\sqrt{\log\left(1 + \boldsymbol{\delta}^2_{\text{EnRes}}\right)}\right) \tag{5.6}$$

Details on the systematics are documented in Sec. 5.7.

For some variables, a 'rest' bin is defined. This bin is not included as part of the differential cross section measurement, but it is used in the simultaneous signal+background fits to data. With this method, the full statistics of the data is used to help constrain the the nuisance parameters and stabilize the fits. This is especially important for distributions with low statistics.

As the purpose of this analysis is to measure the differential cross sections of the Higgs boson and not its mass, the Higgs boson mass in all fits is fixed at the combined $H \to \gamma\gamma$,ZZ $ATLAS$ measured mass $m_H = 125.4$ GeV [136].

Table 5.5 shows the extracted signal yields for all bins of all variables, and Tab. 5.6 shows the total fitted signal yields for each variable.

Table 5.5: Extracted signal yields and uncertainties for all differential variables

Bin	1	2	3	4	5	6	7	8	9	10
Inclusive	569 ± 131									
VBF-enhanced	24.2 ± 8.7									
N_{jets}	274 ± 101	168 ± 68	76.3 ± 36.3	64.5 ± 21.7						
$p_{\text{T}}^{\gamma\gamma}$	19.4 ± 84.3	174 ± 55	89.8 ± 43.5	103 ± 36	49.4 ± 32.3	65.9 ± 33.3	46.9 ± 23.5	25.7 ± 21.4		
$\lvert y_{\gamma\gamma} \rvert$	110 ± 52	112 ± 51	53.7 ± 49.4	110 ± 53	127 ± 58	69.4 ± 50.0				
$\lvert \cos\theta^* \rvert$	45.2 ± 40.2	57.7 ± 38.6	120 ± 40	58.2 ± 41.7	11.2 ± 42.6	92.7 ± 47.7	33.7 ± 49.8	114 ± 48	24.8 ± 18.3	22.1 ± 15.0
p_{T}^{j1}	274 ± 100	113 ± 54	32.2 ± 36.6	56.9 ± 30.6	39.1 ± 19.6					
m_{jj}	47.9 ± 34.2	62.4 ± 20.7	22.9 ± 11.1	7.6 ± 6.0						
H_{T}	272 ± 100	99.0 ± 50.0	35.8 ± 31.7	47.3 ± 40.6	72.3 ± 21.9					
$N_{\text{jets}}^{50\text{ GeV}}$	397 ± 115	106 ± 46	54.8 ± 22.3	24.4 ± 10.6						
$\lvert y_{j_1} \rvert$	152 ± 51	82.6 ± 45.4	43.1 ± 29.3	18.1 ± 18.0						
p_{T}^{j2}	157 ± 67	61.2 ± 34.7	31.9 ± 18.7	44.0 ± 16.2						
$\Delta\phi_{jj}$	31.0 ± 17.2	19.3 ± 19.9	16.6 ± 19.7	79.1 ± 27.4						
$\Delta\phi_{\gamma\gamma,jj}$	54.0 ± 24.5	31.2 ± 21.0	23.2 ± 23.7	23.8 ± 12.0						
$p_{\text{Tt}\gamma\gamma}$	57.8 ± 89.3	210 ± 63	85.3 ± 46.5	74.7 ± 37.3	22.7 ± 35.7	92.1 ± 27.1	3.2 ± 17.0			
$\Delta y_{\gamma\gamma}$	84.6 ± 48.2	121 ± 48	64.2 ± 46.1	78.0 ± 50.4	46.6 ± 48.7	139 ± 60	46.9 ± 30.3			
$\lvert y_{j_2} \rvert$	54.0 ± 27.3	37.1 ± 24.7	28.1 ± 17.4	22.5 ± 11.4						
τ_{jet}	348 ± 105	62.1 ± 45.6	86.7 ± 42.7	6.1 ± 25.0						
$\sum \tau_{\text{jet}}$	350 ± 107	47.0 ± 44.7	68.0 ± 40.0	41.5 ± 31.4	56.5 ± 21.6					
p_{T}^{j3}	75.1 ± 35.8	29.5 ± 17.5	19.9 ± 9.8							
$\lvert \Delta y_{jj} \rvert$	85.4 ± 34.9	39.0 ± 21.5	15.1 ± 9.2	3.7 ± 3.8						
$p_{\text{T}\gamma\gamma jj}$	55.7 ± 30.3	25.8 ± 23.4	44.4 ± 15.2	7.9 ± 8.4						

Table 5.6: Sum of extracted signal yields and uncertainties for all differential variables

	Sum of yields	'Rest' yield	Total sum of yields
Inclusive	569.1 ± 130.7	0.0 ± 0.0	569.1 ± 130.7
VBF-enhanced	24.2 ± 8.7	546.9 ± 129.4	571.0 ± 129.7
N_{jets}	582.6 ± 128.5	0.0 ± 0.0	582.6 ± 128.5
$p_{\text{T}}^{\gamma\gamma}$	573.7 ± 128.3	6.3 ± 5.3	580.0 ± 128.4
$\lvert y_{\gamma\gamma}\rvert$	581.6 ± 128.1	0.0 ± 0.0	581.6 ± 128.1
$\lvert\cos\theta^*\rvert$	580.0 ± 126.2	0.0 ± 0.0	580.0 ± 126.2
$p_{\text{T}}^{j_1}$	515.1 ± 125.0	38.3 ± 14.4	553.4 ± 125.8
m_{jj}	140.8 ± 41.9	454.6 ± 122.5	595.4 ± 129.4
H_{T}	526.3 ± 125.1	25.2 ± 12.6	551.6 ± 125.7
$N_{\text{jets}}^{50\text{ GeV}}$	582.9 ± 126.0	0.0 ± 0.0	582.9 ± 126.0
$\lvert y_{j_1}\rvert$	296.1 ± 76.6	275.0 ± 101.1	571.0 ± 126.8
$p_{\text{T}}^{j_2}$	294.1 ± 79.0	282.2 ± 101.9	576.3 ± 128.9
$\Delta\phi_{jj}$	145.9 ± 42.8	453.2 ± 123.2	599.1 ± 130.4
$\Delta\phi_{\gamma\gamma,jj}$	132.2 ± 41.8	419.7 ± 121.9	551.9 ± 128.8
$p_{\text{Tt}\gamma\gamma}$	545.8 ± 133.5	12.7 ± 5.4	558.6 ± 133.6
$\Delta y_{\gamma\gamma}$	580.2 ± 127.4	0.0 ± 0.0	580.2 ± 127.4
$\lvert y_{j_2}\rvert$	141.7 ± 42.3	425.8 ± 121.6	567.6 ± 128.8
τ_{jet}	503.1 ± 124.8	40.3 ± 13.9	543.4 ± 125.6
$\sum \tau_{\text{jet}}$	563.3 ± 128.5	3.1 ± 5.0	566.4 ± 128.6
p_{T}^{j3}	124.5 ± 41.0	420.9 ± 121.7	545.4 ± 128.4
$\lvert\Delta y_{jj}\rvert$	143.2 ± 42.2	420.8 ± 122.7	564.0 ± 129.8
$p_{\text{T}\gamma\gamma jj}$	133.9 ± 42.0	423.6 ± 123.2	557.5 ± 130.2

5.6 Unfolding Procedure

The unfolding procedure used in this analysis is a bin-by-bin correction factor, where the correction factors are derived for each bin individually. These correction factors account for both the efficiency of object reconstruction and identification and the migrations to and from bins due to detector resolution and miscalibrations. The unfolding factor is defined as

$$c_i = \frac{n_i^{part}}{n_i^{det}}, \tag{5.7}$$

where n_i^{part} is the number of events in bin i at particle level and n_i^{det} is the number of events in bin i at detector level. The correction factors are derived using the signal MC normalized to the Standard Model expectation and are calculated for all production processes combined. These correction factors are then applied to the extracted signal in data to unfold the distributions to particle level:

$$n_i^{data,part} = c_i n_i^{data}, \tag{5.8}$$

where $n_i^{data,part}$ is the number of events in bin i in the unfolded data distribution and n_i^{data} is the number of extracted signal events in data. The full differential distributions, n_i^{diff}, are calculated by

$$n_i^{diff} = \frac{n_i^{data,part}}{\mathscr{L} \cdot w_i}, \tag{5.9}$$

where $\mathscr{L}$ is the integrated luminosity of the dataset and w_i is the width of bin i.

Two quantities are of importance when doing a bin-by-bin unfolding: the purity and efficiency within a bin. The purity, defined as

$$P_i = \frac{n_i^{det,part}}{n_i^{det}}, \tag{5.10}$$

is the fraction of events in bin i at detector level that are also in bin i at particle level. This is a measure of the migrations in and out of each bin caused by detector resolution and fake events which are reconstructed at detector level but do not exist at particle level. As low values of purity indicate large fake contributions, it is important for bins to have a high purity in order to be model independent, and for this analysis, bins are required to have a purity greater than 0.50. The efficiency of a bin also takes into account the migrations, but also includes the efficiencies of object reconstruction and identification. Efficiency is defined as

$$\epsilon_i = \frac{n_i^{det,part}}{n_i^{part}}. \tag{5.11}$$

The correction factors and their uncertainties are presented in Sec. 5.7.7.

5.7 Systematics

5.7.1 Luminosity

This analysis uses only 2012 data collected at a center of mass energy of 8 TeV. The full dataset corresponds to an integrated luminosity of 20.2769 fb^{-1}. As described in Sec. 4.8.1, the luminosity is measured with the LUCID and BCM detectors, and the uncertainty on the measurement for 2012 data is 2.8%.

5.7.2 Photon Selection

There are three sources of uncertainty on the selection of photons: the uncertainty on the trigger efficiency, the uncertainty on the photon identification efficiency, and the uncertainty on the isolation selection efficiency. These uncertainties are documented in Sec. 4.8.1 and the trigger efficiency uncertainty and the photon identification efficiency are measured to be 0.5% and 1% respectively. The effect on the photon identification efficiency as a function of jet multiplicity was shown to be negligible, so the uncertainty of 1% is used for all categorizations.

The uncertainty on the isolation selection was rederived for this analysis taking into account the efficiencies for different jet multiplicities. Efficiencies between data and MC are compared for bins of 0, 1, 2, and $\geq$3 jets and are presented in Table 5.7. The corresponding uncertainties are taken as 1% for the 0 and 1 jet bins, 2% for the 2 jet bin, and 4% for the $\geq$3 jet bin.

	$N_{jets} = 0$	$N_{jets} = 1$	$N_{jets} = 2$	$N_{jets} \geq 3$
$\epsilon_{Data}/\epsilon_{MC}$	1.004 $\pm$ 0.002	0.999 $\pm$ 0.004	0.999 $\pm$ 0.010	0.992 $\pm$ 0.021

Table 5.7: Efficiency ratio between data and MC for the photon selection in bins of jet multiplicity.

5.7.3 Signal Extraction

Mass Energy Resolution.

The full systematics on the mass energy resolution are calculated in the same way as described in Sec. 4.8; however, a simplification procedure is adopted here. The four systematics on the energy resolution are summed quadratically, and only one nuisance parameter is used for the fits. This combined resolution uncertainty is 8.49% for the inclusive case.

Mass Energy Scale.

The mass energy scale systematic is calculated using the m_H bias method described in Sec. 4.8. A simplification procedure is adopted here as well. The largest four uncertainties are kept separate: L2Gain, LArElecUnconv_Barrel, LArCalib_Barrel, LeakageConv, while the rest of the 25 uncertainties are merged by summing them quadratically. This results in a total of five nuisance parameters associated with the diphoton mass scale.

Background Modeling.

The function chosen to parameterize the background distribution can have enough flexibility to affect the scale of the fitted mass. Therefore, an uncertainty is assigned to the mass scale using the MC method described in Sec: 4.8. This is done for each individual bin since each bin can have a different background parameterization, and therefore the nuisance parameters are treated as uncorrelated across bins. An Asimov dataset is created from the background distribution of the smeared MC. The signal is injected into this distribution by first creating an Asimov dataset from the signal model and then adding it to the background Asimov dataset. The signal+background model is then fit to this combined dataset with the signal strength parameter μ fixed at 1 and all the signal shape parameters held constant. The fitted mass is then compared to the injected mass, and this is taken as the bias on the mass scale. A scan is done where signal is injected for masses between 119 GeV and 137 GeV in steps of 0.2 GeV, and the largest bias in this mass range is taken as the bias. The signal+background fits to the combined Asimov dataset are shown in Fig. 5.1 for a scan mass of 125 GeV in bins of $p_{T,\gamma\gamma}$. Scans of the bias in each bin of $p_{T,\gamma\gamma}$ are shown in Fig. 5.2, and the resulting mass bias for all variables is shown in Table 5.8.

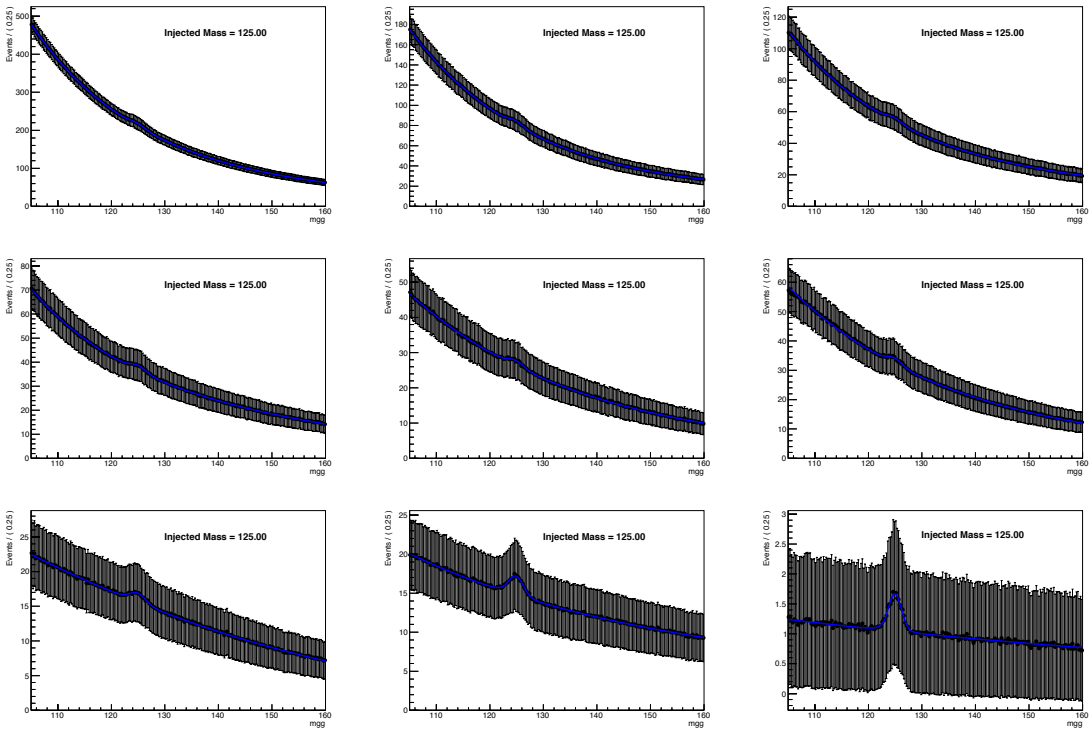

Figure 5.1: Signal+background fits to the asimov dataset with injected signal at m_H =125 GeV in bins of $p_{T,\gamma\gamma}$.

5.7.4 Detector Modeling

The unfolding method for this analysis is the bin-by-bin unfolding, where distributions at reconstruction level are unfolded to particle level by the multiplication of unfolding factors, defined in Sec. 5.6. These unfolding factors are simply the ratio of particle level events over reconstruction-level events in a particular bin. Therefore, any uncertainties on the reconstruction of events will affect the unfolding factors by changing the number of events in the denominator. To evaluate detector modeling uncertainties, the reconstruction level events are varied by the detector uncertainties, and new unfolding factors are derived. The variation in these unfolding factors from the nominal ones are the uncertainty on the unfolding factors themselves. There are four main sources of experimental uncertainty associated with the reconstruction of

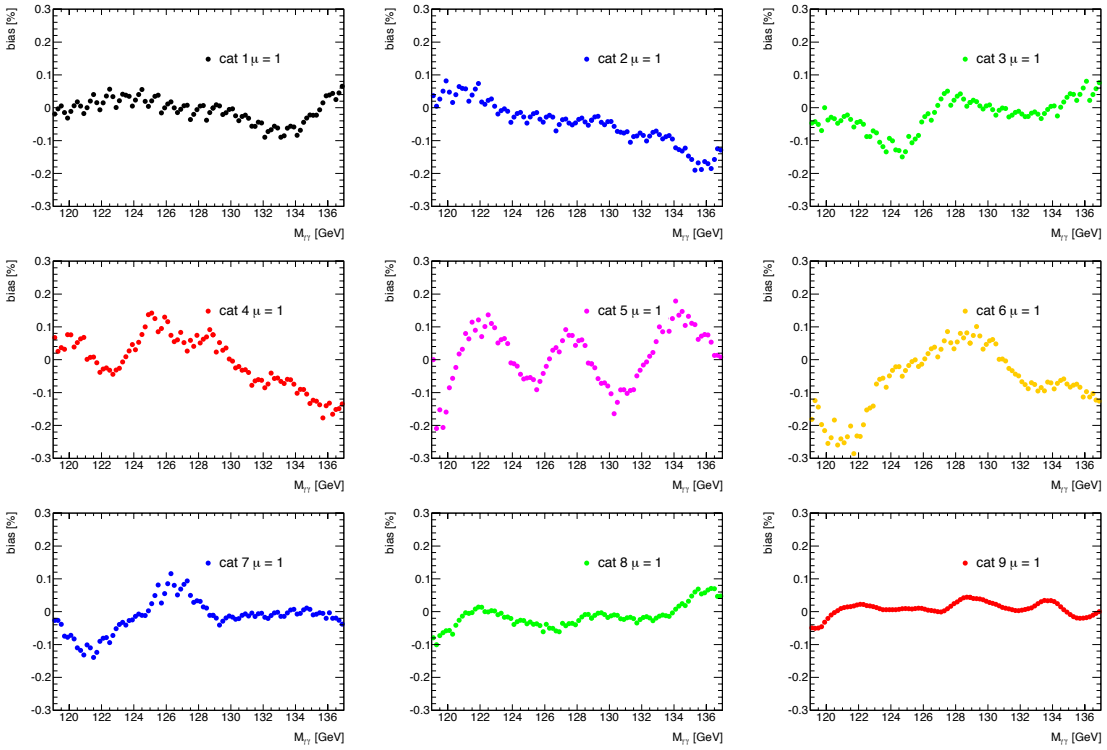

Figure 5.2: The percent bias on the mass scale for the injected signal scan between 119 GeV and 137 GeV in bins of $p_{T,\gamma\gamma}$.

events: jet energy scale and resolution, jet vertex fraction and pileup, E_T^{miss}, and photon and electron energy scale and resolution. The evaluation of the jet energy scale, jet resolution, jet vertex fraction, and E_T^{miss} uncertainties are evaluated in the same way as described in the mass and coupling analysis chapter in Sec. 4.8. For the evaluation of the pileup uncertainty, a fraction of pileup jets is removed from the MC, and the unfolding factors recalculated. Pileup jets are identified by matching the reconstruction level jets to jets at truth level using a cone of ΔR =0.4. The fraction of pileup jets removed, 35%, is taken from the ratio of pileup jets with a jet vertex fraction less than 0.1 to the number of pileup jets with a jet vertex fraction less than 0.5, and the final uncertainties are $\leq$6.6%. Uncertainties from the photon and electron energies are evaluated as described in Sec. 4.8, and are found to be less

Table 5.8: Mass bias from choice of background parameterization. Results are the difference in % between the fitted and the injected masses, and represent the largest bias in the scan region 119-136 GeV.

Bin	1	2	3	4	5	6	7	8	9	10
N_{jets}	0.25	0.23	0.30	0.45						
$p_{\text{T}}^{\gamma\gamma}$	0.09	0.19	0.15	0.18	0.21	0.29	0.14	0.10	0.05	
$\lvert y_{\gamma\gamma}\rvert$	0.07	0.09	0.07	0.10	0.09	0.11				
$\lvert\cos\theta^*\rvert$	0.15	0.10	0.14	0.14	0.15	0.22	0.19	0.03	0.12	0.23
$p_{\text{T}}^{j_1}$	0.09	0.10	0.11	0.18	0.20	0.14				
m_{jj}	0.11	0.13	0.24	0.12	0.33					
H_{T}	0.09	0.10	0.12	0.09	0.13	0.26				
$N_{\text{jets}}^{50\text{ GeV}}$	0.65	0.69	0.66	0.93						
$\lvert y_{j_1}\rvert$	0.12	0.08	0.11	0.13	0.09					
$p_{\text{T}}^{j_2}$	0.09	0.09	0.18	0.33	0.08					
$\Delta\phi_{jj}$	0.09	0.08	0.25	0.23	0.34					
$\Delta\phi_{\gamma\gamma,jj}$	0.31	0.13	0.19	0.11	0.08					
$p_{\text{Tt}\gamma\gamma}$	0.14	0.07	0.11	0.11	0.15	0.13	0.06	0.06		
$\Delta y_{\gamma\gamma}$	0.06	0.08	0.10	0.09	0.12	0.19	0.06			
$\lvert y_{j_2}\rvert$	0.23	0.15	0.15	0.24	0.07					
τ_{jet}	0.14	0.40	0.13	0.20	0.23					
$\sum\tau_{\text{jet}}$	0.17	0.31	0.11	0.14	0.21	0.21				
p_{T}^{j3}	0.11	0.12	0.07							
$\lvert\Delta y_{jj}\rvert$	0.12	0.11	0.15	0.10	0.07					
$p_{\text{T}\gamma\gamma jj}$	0.12	0.17	0.39	0.19	0.07					

than 0.2% for photons and less than 0.01% for electrons. Thus, these uncertainties are neglected in this analysis.

5.7.5 Theory Modelling

The goal of this analysis is to unfold distributions with as little bias from the underlying theoretical model used to derive the unfolding factors as possible. In practice, it is not possible to be completely unbiased, so systematics are assigned in order to reduce this dependence. This is done using three types of variations: the signal model composition of the different production processes are varied, MC samples using different generators are used to calculate unfolding factors, and the MC distributions

are reweighted according to the unfolded distributions in data.

Using the Standard Model Higgs boson signal composition makes assumptions on the Higgs boson couplings which can bias the distributions, particularly those involving jet variables. Therefore, the effect of varying the composition of the signal is taken as a modeling uncertainty on the unfolding factors. The signal composition is varied in two ways. First, the $t\bar{t}H$ contribution is varied up and down from $\sigma_{t\bar{t}H}\times 0$ to $\sigma_{t\bar{t}H}\times 5$, and the resulting unfolding factors are calculated. Then, the contributions from VBF and VH are varied simultaneously from $\sigma_{VBF+VH}\times 0.5$ to $\sigma_{VBF+VH}\times 2$.

The nominal unfolding factors are calculated using POWHEG+PYTHIA8 for the ggF and VBF production process and PYTHIA8 for the VH and $t\bar{t}H$ processes; however, these are not the only available generators for these processes, and in some cases, the differences between generators can be quite large, particularly for the ggF component. Therefore, the unfolding factors are also calculated using different ggF generators: Sherpa, MiNLO HJ+PYTHIA8, and MiNLO HJJ+PYTHIA8. The effect of the parton showering was also varied: the Sherpa sample has its own parton shower model built in, and a second sample where the POWHEG samples were showered with JIMMY was used.

Finally, the effect of the underlying event was taken into account by calculating the unfolding factors with POWHEG+PYTHIA8 samples which have the multiple parton interactions (MPI) in PYTHIA8 switched off. Inclusively, this sample with the MPI turned off gave the largest modeling uncertainty of 1.03%. The total modeling uncertainty on the unfolding factors is taken as the envelope from all these samples.

In order to take into account differences between the spectra in data and that in MC, the truth distributions in MC are reweighted according to the unfolded distributions in data. Smooth functions are fit to the data/MC ratios in the $p_{T,\gamma\gamma}$ and $y_{\gamma\gamma}$ distributions. Then, the truth level distributions in MC are reweighted simul-

taneously by both of these functions and the corresponding unfolding factors are calculated. This results in an inclusive uncertainty of 3.25%.

For the total theory modeling uncertainty, first the uncertainties from the signal composition and the generator modeling are added in quadrature. Then the envelope is taken of this combined uncertainty and the data reweighting uncertainty. No symmetrizing is done, so the final uncertainties can be asymmetric.

5.7.6 Dalitz Decays

As mentioned in Sec. 4.2.8, a small fraction of events in PYTHIA8 come from Dalitz decays, $H \to \gamma\gamma^* \to \gamma f \bar{f}$. These are not included in the particle level distributions, but because they can enter into our selection in data, they are included in the reconstruction level distributions. The branching ratio of these events is not well known, so for this analysis a 100% uncertainty is assigned to the Dalitz contributions resulting in up to 0.50% uncertainty on the signal.

5.7.7 Systematics Summary

Figures 5.3 through 5.6 summarize the fractional uncertainties on the unfolded distributions from data. Despite the many systematics described above, the uncertainties are still statistics dominated. Summaries of all the uncertainty contributions are shown in Tab. 5.9 through 5.30.

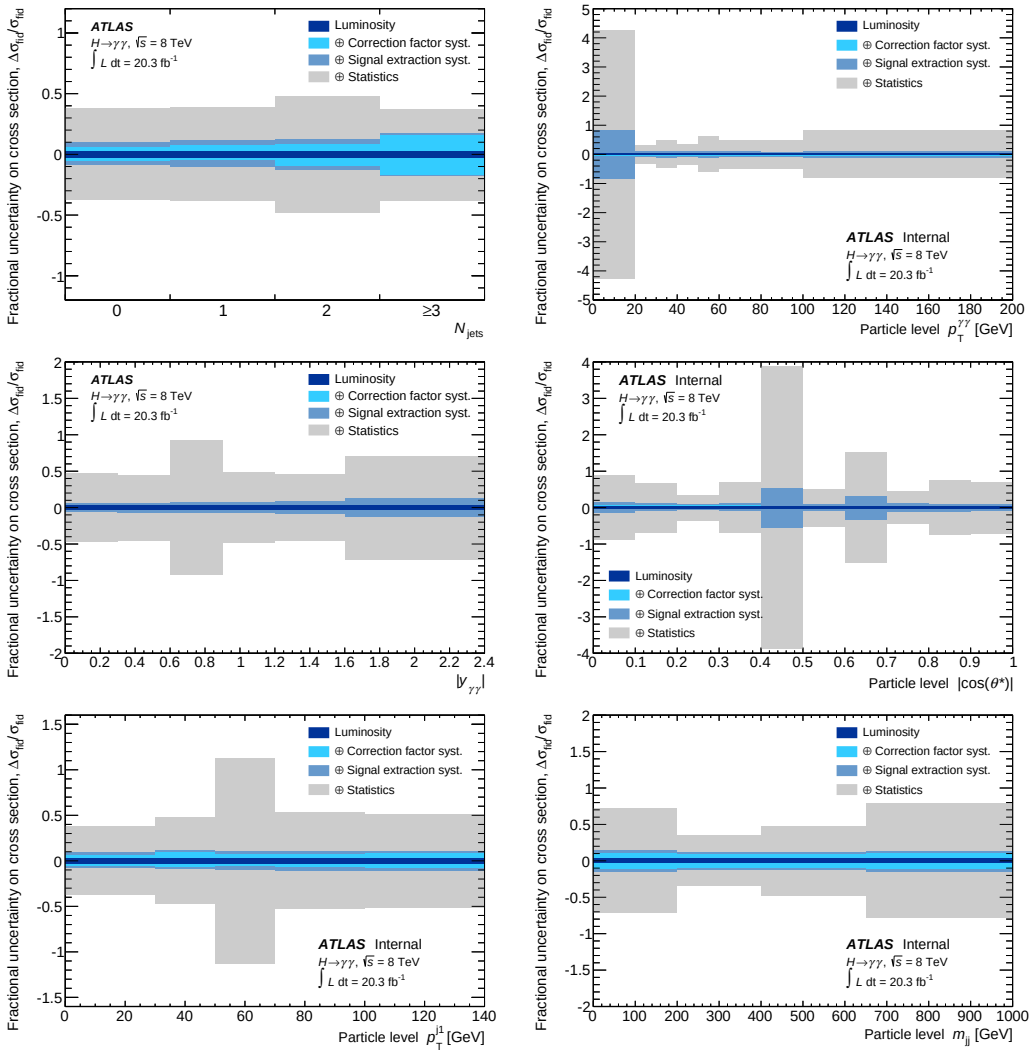

Figure 5.3: Summary of the fractional uncertainties on the particle level differential cross sections for the different variables.

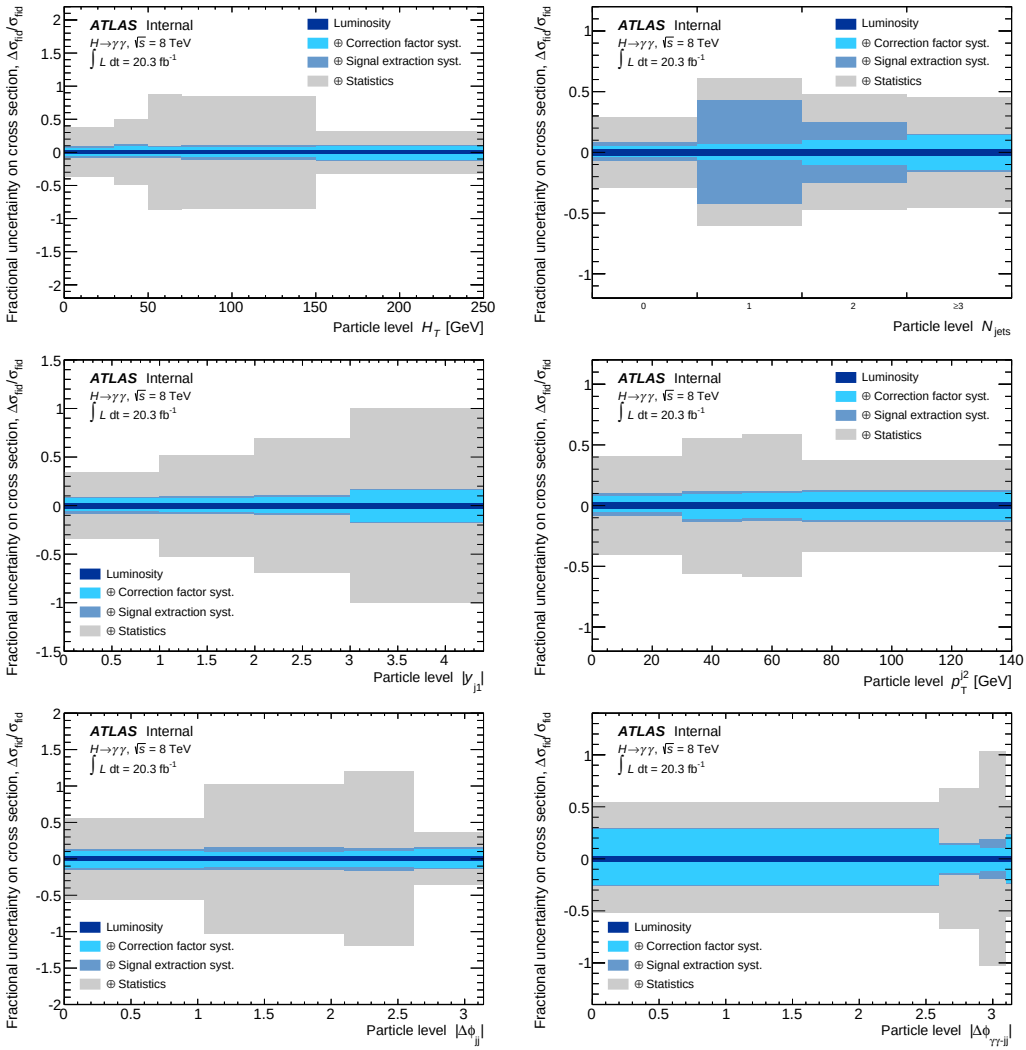

Figure 5.4: Summary of the fractional uncertainties on the particle level differential cross sections for the different variables.

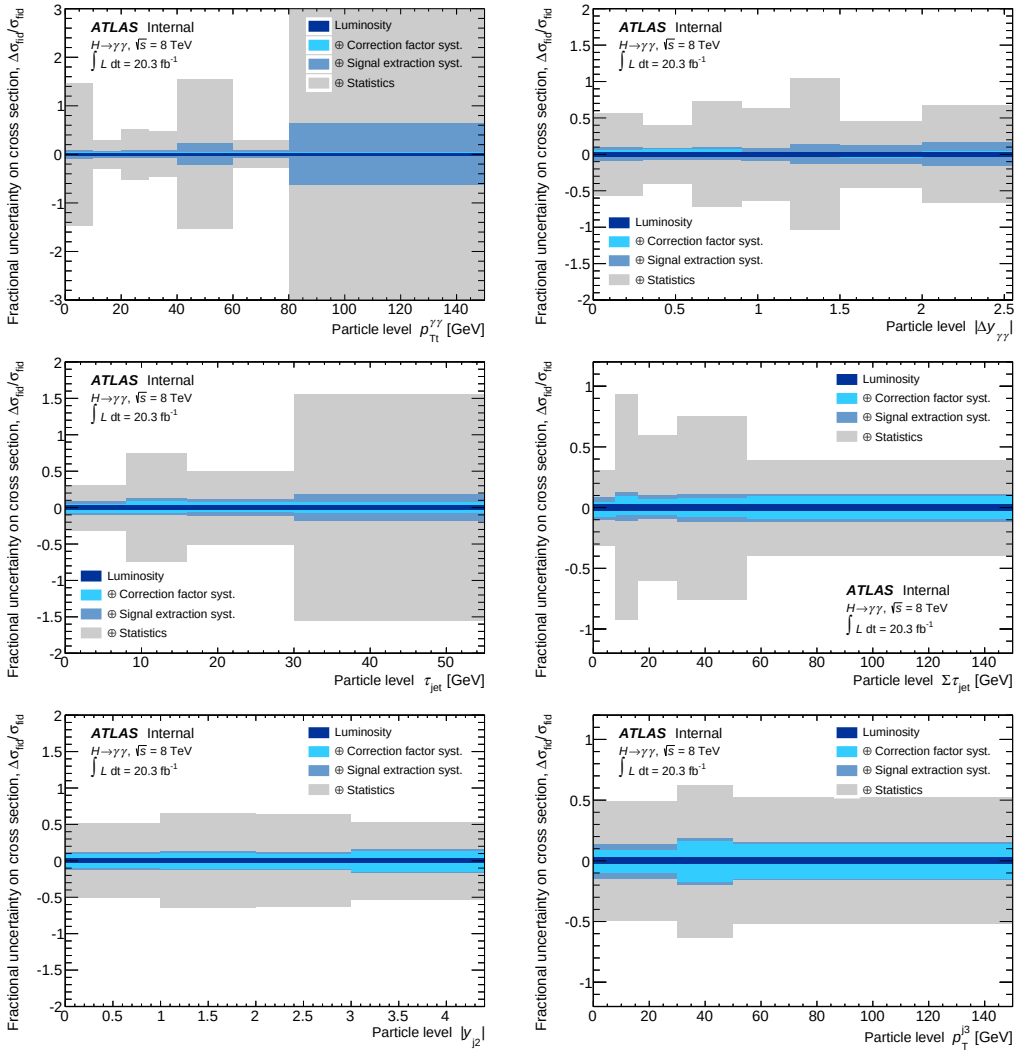

Figure 5.5: Summary of the fractional uncertainties on the particle level differential cross sections for the different variables.

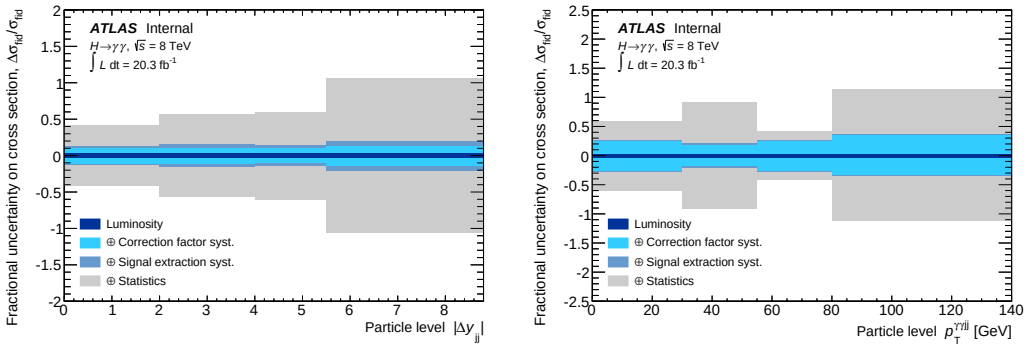

Figure 5.6: Summary of the fractional uncertainties on the particle level differential cross sections for the different variables.

Table 5.9: Summary of results and uncertainties on the particle level fiducial cross-sections for the Inclusive category.

Bin	1
Signal yield	569.09
Background PDF	exp2
Fit: total uncert.	23.0%
Fit statistical	21.8%
Fit systematics	6.2%
Spurious signal	1.7%
σ_{fid} [fb]	42.74
Correction factors	1.52
Purity	0.99
Luminosity	2.8%
PID	1.0%
Isolation	1.0%
Generator modelling	$^{+3.2\%}_{-1.0\%}$

Table 5.10: Summary of results and uncertainties on the particle level fiducial cross-sections for the VBF-enhanced category.

Bin	1
Signal yield	24.17
Background PDF	expo
Fit: total uncert.	35.9%
Fit statistical	34.3%
Fit systematics	4.7%
Spurious signal	7.7%
σ_{fid} [fb]	1.67
Correction factors	1.40
Purity	0.81
Luminosity	2.8%
PID	1.0%
Isolation	2.0%
Pileup	-0.5%
Jet energy scale + resolution	11.3%
Generator modelling	$^{+2.2\%}_{-3.2\%}$

Table 5.11: Summary of results and uncertainties on the particle level differential cross-sections for N_{jets}

Bin	1	2	3	4
Signal yield/bin width	274.13	167.74	76.28	64.49
Background PDF	exp2	exp2	exp2	exp2
Fit: total uncert.	36.7%	40.4%	47.6%	33.6%
Fit statistical	36.5%	36.9%	46.5%	33.3%
Fit systematics	5.8%	6.5%	6.3%	5.2%
Spurious signal	4.2%	6.2%	6.6%	3.8%
$\mathrm{d}\sigma_{\text{fid}}/\mathrm{d}X$ [fb]	21.63	12.20	5.15	3.96
Correction factors	1.60	1.48	1.37	1.24
Purity	0.95	0.78	0.71	0.70
Luminosity	2.8%	2.8%	2.8%	2.8%
PID	1.0%	1.0%	1.0%	1.0%
Isolation	1.0%	1.0%	2.0%	4.0%
Pileup	0.8%	-0.7%	-1.3%	-3.3%
Jet energy scale + resolution	4.1%	3.1%	7.3%	13.9%
Generator modelling	$^{+3.5\%}_{-0.7\%}$	$^{+5.6\%}_{-1.5\%}$	$^{+2.5\%}_{-3.4\%}$	$^{+6.3\%}_{-4.9\%}$

Table 5.12: Summary of results and uncertainties on the particle level differential cross-sections for $p_{\text{T}}^{\gamma\gamma}$

Bin	1	2	3	4	5	6	7	8
Signal yield/bin width	0.97	17.36	8.98	10.29	4.94	3.30	2.34	0.26
Background PDF	exp2	exp3	exp2	exp3	exp2	exp2	exp2	exp2
Fit: total uncert.	433.3%	31.5%	48.5%	35.2%	65.4%	50.4%	50.2%	83.2%
Fit statistical	418.3%	30.0%	46.4%	34.1%	59.3%	48.4%	47.6%	80.4%
Fit systematics	9.5%	5.5%	5.6%	5.6%	6.1%	6.3%	6.2%	6.3%
Spurious signal	82.7%	5.4%	9.4%	5.3%	8.1%	6.8%	3.3%	7.3%
$\mathrm{d}\sigma_{\text{fid}}/\mathrm{d}X$ [fb]	0.07	1.30	0.67	0.78	0.38	0.25	0.18	0.02
Correction factors	1.52	1.52	1.52	1.54	1.54	1.54	1.54	1.51
Purity	0.97	0.90	0.90	0.90	0.89	0.93	0.93	0.97
Luminosity	2.8%	2.8%	2.8%	2.8%	2.8%	2.8%	2.8%	2.8%
PID	1.0%	1.0%	1.0%	1.0%	1.0%	1.0%	1.0%	1.0%
Isolation	1.0%	1.0%	1.0%	1.0%	1.0%	1.0%	1.0%	1.0%
Generator modelling	$^{+2.2\%}_{-1.4\%}$	$^{+2.8\%}_{-1.5\%}$	$^{+3.0\%}_{-0.6\%}$	$^{+3.4\%}_{-1.2\%}$	$^{+3.6\%}_{-0.4\%}$	$^{+3.6\%}_{-0.6\%}$	$^{+3.4\%}_{-0.4\%}$	$^{+3.3\%}_{-0.7\%}$

Table 5.13: Summary of results and uncertainties on the particle level differential cross-sections for $|y_{\gamma\gamma}|$

Bin	1	2	3	4	5	6
Signal yield/bin width	366.41	373.50	179.14	366.38	316.29	86.78
Background PDF	exp2	exp2	exp2	exp2	exp2	exp2
Fit: total uncert.	47.1%	45.9%	91.9%	48.2%	45.7%	72.1%
Fit statistical	46.5%	44.6%	92.3%	48.0%	44.6%	69.9%
Fit systematics	4.6%	5.2%	5.4%	6.5%	7.3%	11.2%
Spurious signal	2.2%	1.5%	2.9%	1.4%	2.6%	4.7%
$d\sigma_{fid}/dX$ [fb]	23.46	25.16	13.26	30.18	28.23	7.74
Correction factors	1.30	1.37	1.50	1.67	1.81	1.81
Purity	0.98	0.98	0.97	0.97	0.98	0.98
Luminosity	2.8%	2.8%	2.8%	2.8%	2.8%	2.8%
PID	1.0%	1.0%	1.0%	1.0%	1.0%	1.0%
Isolation	1.0%	1.0%	1.0%	1.0%	1.0%	1.0%
Generator modelling	$^{+0.5\%}_{-1.0\%}$	$^{+0.3\%}_{-1.3\%}$	$^{+0.7\%}_{-1.0\%}$	$^{+0.9\%}_{-0.9\%}$	$^{+1.2\%}_{-1.0\%}$	$^{+0.8\%}_{-0.9\%}$

Table 5.14: Summary of results and uncertainties on the particle level differential cross-sections for $|\cos\theta^*|$

Bin	1	2	3	4	5	6	7	8	9	10
Signal yield/bin width	452.47	577.29	1204.68	582.09	112.09	926.51	337.32	1138.35	248.48	220.76
Background PDF	exp2	exp2	exp2	exp2	exp2	exp2	exp2	bern3rd	exp2	exp2
Fit: total uncert.	88.8%	66.8%	33.5%	71.7%	380.0%	51.5%	147.6%	42.4%	73.7%	67.9%
Fit statistical	86.8%	67.3%	33.6%	69.1%	384.3%	50.9%	147.9%	42.8%	74.7%	69.8%
Fit systematics	5.8%	4.8%	5.1%	5.5%	7.7%	6.0%	5.4%	6.9%	7.2%	6.5%
Spurious signal	13.0%	7.3%	3.1%	6.6%	53.4%	6.4%	32.1%	7.9%	6.0%	5.0%
$d\sigma_{fid}/dX$ [fb]	32.74	43.58	91.10	44.25	8.30	68.61	25.72	89.66	19.28	16.83
Correction factors	1.47	1.53	1.53	1.54	1.50	1.50	1.55	1.60	1.57	1.55
Purity	0.99	0.99	0.98	0.98	0.98	0.98	0.98	0.95	0.96	0.97
Luminosity	2.8%	2.8%	2.8%	2.8%	2.8%	2.8%	2.8%	2.8%	2.8%	2.8%
PID	1.0%	1.0%	1.0%	1.0%	1.0%	1.0%	1.0%	1.0%	1.0%	1.0%
Isolation	1.0%	1.0%	1.0%	1.0%	1.0%	1.0%	1.0%	1.0%	1.0%	1.0%
Generator modelling	$^{+5.0\%}_{-0.9\%}$	$^{+6.2\%}_{-0.1\%}$	$^{+5.8\%}_{-1.2\%}$	$^{+5.8\%}_{-0.9\%}$	$^{+2.0\%}_{-1.1\%}$	$^{+0.4\%}_{-1.5\%}$	$^{+0.5\%}_{-1.9\%}$	$^{+1.3\%}_{-1.9\%}$	$^{+1.1\%}_{-1.8\%}$	$^{+1.1\%}_{-2.4\%}$

Table 5.15: Summary of results and uncertainties on the particle level differential cross-sections for $p_{\mathrm{T}}^{j_1}$

Bin	1	2	3	4	5
Signal yield/bin width	9.12	5.66	1.61	1.90	0.98
Background PDF	exp2	exp2	exp2	exp2	expo
Fit: total uncert.	36.6%	47.7%	113.8%	53.7%	50.3%
Fit statistical	36.5%	46.3%	112.3%	51.9%	50.2%
Fit systematics	5.9%	6.0%	5.9%	5.7%	5.7%
Spurious signal	2.2%	2.3%	5.1%	6.2%	5.1%
$\mathrm{d}\sigma_{\mathrm{fid}}/\mathrm{d}X$ [fb]	0.72	0.39	0.11	0.14	0.07
Correction factors	1.60	1.39	1.44	1.46	1.46
Purity	0.95	0.67	0.65	0.72	0.74
Luminosity	2.8%	2.8%	2.8%	2.8%	2.8%
PID	1.0%	1.0%	1.0%	1.0%	1.0%
Isolation	1.0%	1.0%	1.0%	1.0%	1.0%
Pileup	0.8%	-1.9%	-0.8%	-0.3%	-0.1%
Jet energy scale + resolution	4.1%	4.6%	4.5%	5.4%	6.9%
Generator modelling	$^{+3.5\%}_{-0.7\%}$	$^{+7.0\%}_{-1.9\%}$	$^{+4.5\%}_{-2.2\%}$	$^{+2.6\%}_{-3.2\%}$	$^{+2.0\%}_{-1.7\%}$

Table 5.16: Summary of results and uncertainties on the particle level differential cross-sections for m_{jj}

Bin	1	2	3	4
Signal yield/bin width	0.24	0.31	0.09	0.02
Background PDF	exp2	exp2	expo	expo
Fit: total uncert.	71.5%	33.1%	48.4%	79.1%
Fit statistical	70.1%	32.8%	46.5%	77.6%
Fit systematics	8.6%	5.9%	6.1%	7.9%
Spurious signal	5.7%	4.5%	4.9%	6.0%
$\mathrm{d}\sigma_{\mathrm{fid}}/\mathrm{d}X$ [fb]	0.02	0.02	0.01	0.00
Correction factors	1.30	1.39	1.39	1.35
Purity	0.70	0.71	0.70	0.71
Luminosity	2.8%	2.8%	2.8%	2.8%
PID	1.0%	1.0%	1.0%	1.0%
Isolation	2.0%	2.0%	2.0%	2.0%
Pileup	-2.3%	-1.7%	-1.2%	-1.1%
Jet energy scale + resolution	9.3%	8.3%	8.2%	8.9%
Generator modelling	$^{+3.5\%}_{-3.6\%}$	$^{+2.6\%}_{-2.8\%}$	$^{+2.0\%}_{-2.9\%}$	$^{+2.9\%}_{-4.5\%}$

Table 5.17: Summary of results and uncertainties on the particle level differential cross-sections for H_{T}

Bin	1	2	3	4	5
Signal yield/bin width	9.06	4.95	1.79	0.59	0.72
Background PDF	exp2	exp2	exp2	exp2	exp2
Fit: total uncert.	36.8%	50.4%	88.5%	85.9%	30.3%
Fit statistical	36.7%	48.6%	86.7%	84.5%	29.7%
Fit systematics	6.0%	6.1%	6.0%	6.2%	6.2%
Spurious signal	2.6%	1.8%	2.5%	5.8%	1.5%
$\mathrm{d}\sigma_{\mathrm{fid}}/\mathrm{d}X$ [fb]	0.72	0.35	0.13	0.04	0.05
Correction factors	1.60	1.43	1.48	1.42	1.38
Purity	0.95	0.62	0.57	0.76	0.76
Luminosity	2.8%	2.8%	2.8%	2.8%	2.8%
PID	1.0%	1.0%	1.0%	1.0%	1.0%
Isolation	1.0%	2.0%	2.0%	2.0%	2.0%
Pileup	0.8%	-1.5%	-0.4%	-1.2%	-1.0%
Jet energy scale + resolution	4.1%	3.6%	2.7%	5.8%	9.0%
Generator modelling	$^{+3.5\%}_{-0.7\%}$	$^{+7.5\%}_{-1.8\%}$	$^{+5.1\%}_{-2.8\%}$	$^{+2.4\%}_{-2.1\%}$	$^{+2.0\%}_{-3.1\%}$

Table 5.18: Summary of results and uncertainties on the particle level differential cross-sections for $N_{\mathrm{jets}}^{50\ \mathrm{GeV}}$

Bin	1	2	3	4
Signal yield/bin width	397.30	106.40	54.79	24.42
Background PDF	exp2	exp2	exp2	exp2
Fit: total uncert.	28.8%	43.6%	40.7%	43.2%
Fit statistical	28.1%	43.2%	40.4%	42.7%
Fit systematics	5.8%	41.9%	22.3%	5.6%
Spurious signal	1.8%	5.2%	4.6%	3.8%
$\mathrm{d}\sigma_{\mathrm{fid}}/\mathrm{d}X$ [fb]	30.32	7.71	3.74	1.64
Correction factors	1.55	1.47	1.38	1.36
Purity	0.97	0.84	0.76	0.75
Luminosity	2.8%	2.8%	2.8%	2.8%
PID	1.0%	1.0%	1.0%	1.0%
Isolation	1.0%	1.0%	2.0%	4.0%
Pileup	0.1%	-0.2%	-0.9%	-1.8%
Jet energy scale + resolution	1.9%	4.6%	9.1%	12.2%
Generator modelling	$^{+3.5\%}_{-0.7\%}$	$^{+3.3\%}_{-2.2\%}$	$^{+2.7\%}_{-2.5\%}$	$^{+3.8\%}_{-5.0\%}$

Table 5.19: Summary of results and uncertainties on the particle level differential cross-sections for $|y_{j_1}|$

Bin	1	2	3	4
Signal yield/bin width	152.29	82.62	43.06	12.94
Background PDF	exp2	exp2	exp2	exp2
Fit: total uncert.	33.6%	54.9%	68.1%	99.3%
Fit statistical	32.9%	51.5%	68.2%	98.7%
Fit systematics	4.9%	4.9%	4.8%	4.8%
Spurious signal	2.8%	2.8%	4.7%	4.7%
$\mathrm{d}\sigma_{\mathrm{fid}}/\mathrm{d}X$ [fb]	10.94	5.87	3.00	0.83
Correction factors	1.46	1.44	1.41	1.29
Purity	0.85	0.84	0.82	0.73
Luminosity	2.8%	2.8%	2.8%	2.8%
PID	1.0%	1.0%	1.0%	1.0%
Isolation	1.0%	1.0%	1.0%	1.0%
Pileup	-0.7%	-0.7%	-1.5%	-2.8%
Jet energy scale + resolution	4.2%	5.1%	5.7%	14.2%
Generator modelling	$^{+4.4\%}_{-1.3\%}$	$^{+4.5\%}_{-1.9\%}$	$^{+5.3\%}_{-2.6\%}$	$^{+7.1\%}_{-5.0\%}$

Table 5.20: Summary of results and uncertainties on the particle level differential cross-sections for $p_{\mathrm{T}}^{j_2}$

Bin	1	2	3	4
Signal yield/bin width	5.24	3.06	1.59	0.63
Background PDF	exp2	exp2	exp2	exp2
Fit: total uncert.	42.4%	56.8%	58.7%	36.8%
Fit statistical	39.4%	54.6%	57.4%	35.5%
Fit systematics	6.1%	6.5%	5.9%	5.5%
Spurious signal	3.4%	3.1%	2.8%	2.0%
$\mathrm{d}\sigma_{\mathrm{fid}}/\mathrm{d}X$ [fb]	0.38	0.20	0.11	0.04
Correction factors	1.48	1.31	1.36	1.40
Purity	0.78	0.64	0.63	0.79
Luminosity	2.8%	2.8%	2.8%	2.8%
PID	1.0%	1.0%	1.0%	1.0%
Isolation	2.0%	2.0%	2.0%	2.0%
Pileup	-0.0%	-1.2%	-0.6%	-0.2%
Jet energy scale + resolution	3.1%	8.7%	8.9%	10.5%
Generator modelling	$^{+5.6\%}_{-1.5\%}$	$^{+2.9\%}_{-4.1\%}$	$^{+2.9\%}_{-3.2\%}$	$^{+2.7\%}_{-2.6\%}$

Table 5.21: Summary of results and uncertainties on the particle level differential cross-sections for $\Delta\phi_{jj}$

Bin	1	2	3	4
Signal yield/bin width	29.61	18.39	31.62	151.02
Background PDF	expo	exp2	exp2	exp2
Fit: total uncert.	55.4%	103.6%	119.0%	34.6%
Fit statistical	54.1%	101.4%	118.6%	32.9%
Fit systematics	6.8%	8.2%	9.1%	7.5%
Spurious signal	5.9%	8.6%	7.1%	2.2%
$d\sigma_{fid}/dX$ [fb]	1.92	1.24	2.14	9.49
Correction factors	1.31	1.37	1.38	1.27
Purity	0.73	0.75	0.71	0.68
Luminosity	2.8%	2.8%	2.8%	2.8%
PID	1.0%	1.0%	1.0%	1.0%
Isolation	2.0%	2.0%	2.0%	2.0%
Pileup	-1.0%	-0.9%	-1.5%	-5.0%
Jet energy scale + resolution	9.6%	8.7%	8.8%	9.0%
Generator modelling	$^{+2.7\%}_{-4.8\%}$	$^{+2.3\%}_{-2.6\%}$	$^{+3.8\%}_{-3.9\%}$	$^{+8.2\%}_{-5.0\%}$

Table 5.22: Summary of results and uncertainties on the particle level differential cross-sections for $\Delta\phi_{\gamma\gamma,jj}$

Bin	1	2	3	4
Signal yield/bin width	20.76	104.07	115.80	571.70
Background PDF	exp2	exp2	exp2	expo
Fit: total uncert.	45.5%	67.3%	102.2%	50.4%
Fit statistical	45.3%	66.0%	101.4%	50.4%
Fit systematics	5.7%	5.8%	7.0%	5.4%
Spurious signal	1.7%	3.5%	14.0%	5.2%
$d\sigma_{fid}/dX$ [fb]	1.08	6.54	7.94	45.09
Correction factors	1.06	1.27	1.39	1.60
Purity	0.50	0.51	0.60	0.54
Luminosity	2.8%	2.8%	2.8%	2.8%
PID	1.0%	1.0%	1.0%	1.0%
Isolation	2.0%	2.0%	2.0%	2.0%
Pileup	-6.6%	-1.5%	-0.5%	-0.2%
Jet energy scale + resolution	22.9%	12.3%	9.4%	22.0%
Generator modelling	$^{+15.6\%}_{-6.6\%}$	$^{+2.5\%}_{-4.9\%}$	$^{+2.7\%}_{-5.4\%}$	$^{+4.8\%}_{-3.0\%}$

Table 5.23: Summary of results and uncertainties on the particle level differential cross-sections for $p_{\mathrm{Tt}\gamma\gamma}$

Bin	1	2	3	4	5	6	7
Signal yield/bin width	5.78	21.00	8.53	7.47	1.14	4.60	0.05
Background PDF	exp2	exp2	exp2	exp2	exp2	exp2	expo
Fit: total uncert.	154.4%	30.1%	54.5%	50.0%	157.1%	29.5%	530.7%
Fit statistical	146.7%	28.9%	51.4%	46.2%	151.9%	27.8%	512.0%
Fit systematics	7.0%	5.9%	5.8%	6.2%	7.9%	5.9%	12.6%
Spurious signal	3.1%	0.9%	2.4%	2.2%	20.6%	3.0%	62.1%
$\mathrm{d}\sigma_{\mathrm{fid}}/\mathrm{d}X$ [fb]	0.44	1.58	0.64	0.56	0.09	0.35	0.00
Correction factors	1.53	1.52	1.53	1.53	1.53	1.53	1.49
Purity	0.98	0.97	0.96	0.94	0.95	0.94	0.97
Luminosity	2.8%	2.8%	2.8%	2.8%	2.8%	2.8%	2.8%
PID	1.0%	1.0%	1.0%	1.0%	1.0%	1.0%	1.0%
Isolation	1.0%	1.0%	1.0%	1.0%	1.0%	1.0%	1.0%
Generator modelling	$^{+3.5\%}_{-1.0\%}$	$^{+3.3\%}_{-1.6\%}$	$^{+3.3\%}_{-0.8\%}$	$^{+3.2\%}_{-1.4\%}$	$^{+2.9\%}_{-0.8\%}$	$^{+2.5\%}_{-1.1\%}$	$^{+3.1\%}_{-0.9\%}$

Table 5.24: Summary of results and uncertainties on the particle level differential cross-sections for $\Delta y_{\gamma\gamma}$

Bin	1	2	3	4	5	6	7
Signal yield/bin width	282.12	404.75	214.00	259.91	155.43	277.06	85.19
Background PDF	exp2	exp2	exp2	exp2	exp2	exp2	exp3
Fit: total uncert.	57.0%	39.8%	71.8%	64.7%	104.4%	43.3%	64.7%
Fit statistical	56.0%	39.2%	72.0%	62.7%	103.5%	43.7%	65.1%
Fit systematics	6.1%	6.0%	5.7%	6.6%	5.9%	6.2%	13.8%
Spurious signal	5.0%	2.3%	4.3%	4.5%	11.7%	10.4%	7.5%
$\mathrm{d}\sigma_{\mathrm{fid}}/\mathrm{d}X$ [fb]	20.69	30.53	16.22	19.09	11.61	21.75	7.09
Correction factors	1.49	1.53	1.54	1.49	1.51	1.59	1.69
Purity	0.99	0.99	0.99	0.99	0.99	0.98	0.91
Luminosity	2.8%	2.8%	2.8%	2.8%	2.8%	2.8%	2.8%
PID	1.0%	1.0%	1.0%	1.0%	1.0%	1.0%	1.0%
Isolation	1.0%	1.0%	1.0%	1.0%	1.0%	1.0%	1.0%
Generator modelling	$^{+5.4\%}_{-0.8\%}$	$^{+5.8\%}_{-0.8\%}$	$^{+5.5\%}_{-0.7\%}$	$^{+0.6\%}_{-1.5\%}$	$^{+0.9\%}_{-0.7\%}$	$^{+1.0\%}_{-2.1\%}$	$^{+2.9\%}_{-1.5\%}$

Table 5.25: Summary of results and uncertainties on the particle level differential cross-sections for τ_{jet}

Bin	1	2	3	4
Signal yield/bin width	43.60	7.80	6.21	0.70
Background PDF	exp2	exp2	exp2	exp2
Fit: total uncert.	30.2%	73.2%	49.3%	155.4%
Fit statistical	29.6%	73.6%	49.3%	154.1%
Fit systematics	6.3%	7.8%	6.8%	9.6%
Spurious signal	2.1%	2.3%	5.5%	14.0%
$\mathrm{d}\sigma_{\text{fid}}/\mathrm{d}X$ [fb]	3.39	0.52	0.45	0.05
Correction factors	1.57	1.36	1.48	1.47
Purity	0.96	0.65	0.77	0.81
Luminosity	2.8%	2.8%	2.8%	2.8%
PID	1.0%	1.0%	1.0%	1.0%
Isolation	2.0%	2.0%	2.0%	2.0%
Pileup	0.5%	-1.1%	-0.3%	-0.1%
Jet energy scale + resolution	2.6%	4.5%	4.5%	5.8%
Generator modelling	$^{+1.0\%}_{-6.0\%}$	$^{+6.9\%}_{-1.7\%}$	$^{+4.5\%}_{-1.7\%}$	$^{+2.9\%}_{-2.2\%}$

Table 5.26: Summary of results and uncertainties on the particle level differential cross-sections for $\sum \tau_{\text{jet}}$

Bin	1	2	3	4	5
Signal yield/bin width	43.78	5.88	4.86	1.66	0.59
Background PDF	exp2	exp2	exp2	exp2	exp2
Fit: total uncert.	30.6%	95.1%	58.8%	75.7%	38.2%
Fit statistical	29.5%	91.9%	58.9%	74.7%	37.5%
Fit systematics	6.5%	8.8%	6.7%	7.6%	5.6%
Spurious signal	2.1%	2.2%	3.1%	3.3%	3.7%
$\mathrm{d}\sigma_{\text{fid}}/\mathrm{d}X$ [fb]	3.40	0.40	0.35	0.12	0.04
Correction factors	1.57	1.38	1.48	1.44	1.41
Purity	0.96	0.61	0.71	0.75	0.84
Luminosity	2.8%	2.8%	2.8%	2.8%	2.8%
PID	1.0%	1.0%	1.0%	1.0%	1.0%
Isolation	2.0%	2.0%	2.0%	2.0%	2.0%
Pileup	0.5%	-0.9%	-0.3%	-0.4%	-0.3%
Jet energy scale + resolution	2.6%	3.8%	4.0%	6.1%	8.2%
Generator modelling	$^{+1.0\%}_{-6.0\%}$	$^{+7.5\%}_{-1.7\%}$	$^{+4.9\%}_{-1.3\%}$	$^{+2.6\%}_{-3.1\%}$	$^{+2.6\%}_{-1.9\%}$

Table 5.27: Summary of results and uncertainties on the particle level differential cross-sections for $|y_{j_2}|$

Bin	1	2	3	4
Signal yield/bin width	54.02	37.09	28.14	16.06
Background PDF	exp2	exp2	exp2	exp2
Fit: total uncert.	50.6%	66.6%	61.8%	50.6%
Fit statistical	49.7%	63.4%	62.0%	50.8%
Fit systematics	5.9%	5.8%	5.8%	6.5%
Spurious signal	4.7%	4.9%	3.2%	1.5%
$\mathrm{d}\sigma_{\mathrm{fid}}/\mathrm{d}X$ [fb]	3.67	2.46	1.85	0.98
Correction factors	1.38	1.34	1.33	1.24
Purity	0.71	0.68	0.70	0.64
Luminosity	2.8%	2.8%	2.8%	2.8%
PID	1.0%	1.0%	1.0%	1.0%
Isolation	1.0%	1.0%	1.0%	1.0%
Pileup	-1.3%	-1.3%	-2.3%	-3.3%
Jet energy scale + resolution	8.3%	9.3%	8.4%	12.8%
Generator modelling	$^{+2.6\%}_{-4.0\%}$	$^{+3.4\%}_{-1.7\%}$	$^{+2.4\%}_{-5.0\%}$	$^{+3.4\%}_{-5.3\%}$

Table 5.28: Summary of results and uncertainties on the particle level differential cross-sections for p_{T}^{j3}

Bin	1	2	3
Signal yield/bin width	2.50	1.47	0.20
Background PDF	exp2	expo	expo
Fit: total uncert.	47.7%	59.3%	49.1%
Fit statistical	47.0%	59.8%	49.6%
Fit systematics	5.6%	5.0%	5.0%
Spurious signal	9.0%	7.9%	4.7%
$\mathrm{d}\sigma_{\mathrm{fid}}/\mathrm{d}X$ [fb]	0.17	0.09	0.01
Correction factors	1.37	1.21	1.36
Purity	0.71	0.58	0.75
Luminosity	2.8%	2.8%	2.8%
PID	1.0%	1.0%	1.0%
Isolation	4.0%	4.0%	4.0%
Pileup	-1.3%	-3.8%	-1.8%
Jet energy scale + resolution	7.3%	14.5%	12.2%
Generator modelling	$^{+2.5\%}_{-3.4\%}$	$^{+5.2\%}_{-4.4\%}$	$^{+3.8\%}_{-5.0\%}$

Table 5.29: Summary of results and uncertainties on the particle level differential cross-sections for $|\Delta y_{jj}|$

Bin	1	2	3	4
Signal yield/bin width	42.71	19.50	10.07	1.12
Background PDF	exp2	exp2	expo	expo
Fit: total uncert.	40.9%	55.1%	60.9%	103.3%
Fit statistical	39.7%	54.7%	58.4%	104.1%
Fit systematics	5.7%	6.2%	5.5%	12.1%
Spurious signal	3.4%	9.9%	8.5%	8.2%
$d\sigma_{fid}/dX$ [fb]	2.81	1.30	0.67	0.07
Correction factors	1.33	1.35	1.34	1.27
Purity	0.75	0.75	0.77	0.74
Luminosity	2.8%	2.8%	2.8%	2.8%
PID	1.0%	1.0%	1.0%	1.0%
Isolation	2.0%	2.0%	2.0%	2.0%
Pileup	-1.9%	-1.9%	-1.5%	-2.0%
Jet energy scale + resolution	9.3%	8.8%	8.7%	12.1%
Generator modelling	$^{+3.6\%}_{-2.7\%}$	$^{+2.5\%}_{-4.7\%}$	$^{+2.3\%}_{-4.1\%}$	$^{+4.3\%}_{-5.1\%}$

Table 5.30: Summary of results and uncertainties on the particle level differential cross-sections for $p_{T\gamma\gamma jj}$

Bin	1	2	3	4
Signal yield/bin width	1.86	1.03	1.78	0.13
Background PDF	exp2	exp2	expo	expo
Fit: total uncert.	54.4%	90.7%	34.2%	106.0%
Fit statistical	53.5%	88.5%	31.4%	106.5%
Fit systematics	6.3%	6.5%	8.2%	7.2%
Spurious signal	3.5%	10.1%	2.9%	10.4%
$d\sigma_{fid}/dX$ [fb]	0.13	0.06	0.10	0.01
Correction factors	1.43	1.23	1.19	1.22
Purity	0.71	0.51	0.48	0.60
Luminosity	2.8%	2.8%	2.8%	2.8%
PID	1.0%	1.0%	1.0%	1.0%
Isolation	2.0%	2.0%	2.0%	2.0%
Pileup	-1.2%	-2.6%	-3.0%	-2.0%
Jet energy scale + resolution	25.1%	16.6%	24.2%	32.5%
Generator modelling	$^{+2.8\%}_{-4.4\%}$	$^{+2.1\%}_{-4.9\%}$	$^{+7.7\%}_{-7.2\%}$	$^{+10.0\%}_{-5.2\%}$

5.8 Non-Perturbative and Fiducial Acceptance Correction Factors

In some cases, theory predictions and calculations are only done at the parton level. In order to allow for comparisons to the measurements made in this analysis, non-perturbative correction factors are supplied. Also calculated, are the kinematic acceptance factors to allow comparisons to calculations which do not decay the Higgs boson.

5.8.1 Non-perturbative Correction Factors

The non-perturbative effects to be included in these correction factors are the hadronization process and the multiple parton interactions. Because these cannot be calculated, different showering programs have adopted different methods of implementing them.

The correction factors are defined as the ratio of events in each bin at the particle level to the events at the parton level

$$c_{i,NP} = \frac{N_i^{MPI+Had}}{N_i^{noMPI+noHad}}. \tag{5.12}$$

To evaluate the non-perturbative correction factors and their uncertainties, the nominal Powheg ggF samples were interfaced with different showering programs with different underlying event tunes. The nominal Pythia8 with the AU2 tune [137] was used, Herwig++ using the UE-EE-4-LO tune [138], Pythia6 using the AUET2B-LO tune, and Pythia6 using the AMBT2B-LO tune [139] were all also used. The envelope of all non-perturbative correction factors is taken as the full uncertainty, and the central point is taken as the final correction factor.

5.8.2 Fiducial Acceptance Factors

The fiducial acceptance factors correct an undecayed Higgs boson, or the full phase space of the diphoton decay, to the fiducial diphoton phase space used in this analysis. They are divided into two separate parts,

$$c_{i,Fid} = \frac{N_i^{fid}}{N_i^{full}} \tag{5.13}$$

to account for the kinematic cuts on the photons: $p_T/m_{\gamma\gamma}$ >0.35 (0.25) and $|\eta_\gamma|$ <2.37, and

$$c_{i,Iso} = \frac{N_i^{fid+iso}}{N_i^{fid}} \tag{5.14}$$

to account for the truth level isolation requirement on the photons: E_T^{iso} <14 GeV.

The fiducial factors are calculated at parton level with no underlying event. Kinematic correction factor uncertainties are calculated by reweighting the nominal POWHEG ggF sample to different PDFs. The MSTW08 and NNPDF2.3 PDFs are used as variations, and the envelope of all PDFs and their uncertainties are taken as the final uncertainty on the fiducial factors. The MSTW08 variations are taken from the 42 eigenvector sets using the symmetrized 'Master Equation' of Equation 4.19. NNPDF2.3 has 100 eigenvector sets. The central value for NNPDF2.3 is taken as the average of all 100 sets, and the uncertainties are the +/- 1σ around the central value. As shown in Fig. 5.7, the cross section for CT10 is consistently smaller than the cross section when using MSTW08 or NNPDF2.3. Also shown is the impact the PDF set can have on the shape of the rapidity distribution. HeraPDF was only used as a cross-check and is not used in any uncertainty calculations. The effect of varying

the QCD scales was also checked, and the results were negligible compared to the PDF uncertainties. Uncertainties on the isolation efficiencies are calculated in the same way as for the non-perturbative correction factors described in Sec. 5.8.1. Table 5.31 summarizes the kinematic acceptance factors, and Tab. 5.32 summarizes the isolation efficiencies. Example plots of the kinematic acceptance factors and isolation efficiencies are shown in Fig. 5.8.

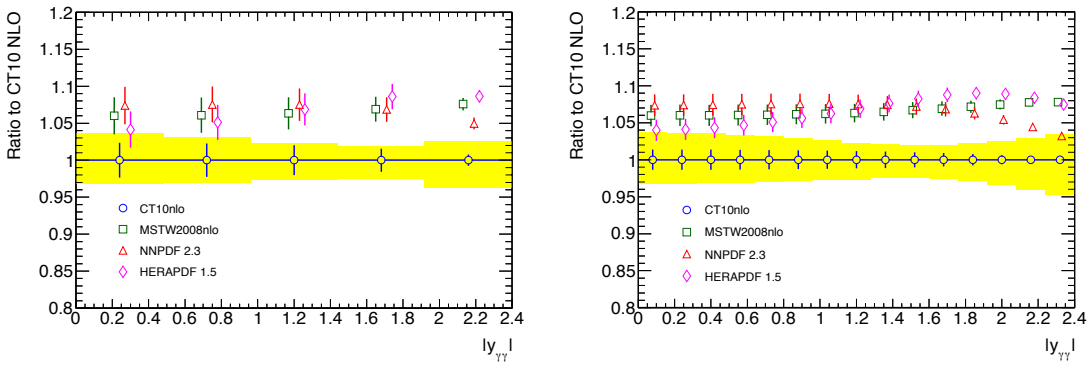

Figure 5.7: Checks on the cross section in Higgs rapidity bins for four PDF sets. A coarse binning is used on the left, while a finer binning to show more details is on the right.

Table 5.31: Diphoton kinematic acceptances in percent for gluon-gluon fusion for each fiducial region/variable bin studied in this paper, defined as the probability to fulfil the diphoton kinematic criteria: $p_{\mathrm{T}}/m_{\gamma\gamma} < 0.35$ (0.25) for the leading (subleading) photon and $|\eta_{\gamma}| < 2.37$. The factors are evaluated using the POWHEG event generator with MPI modelling and hadronization turned off. Consistent results for the diphoton variables are obtained by HRes 2.2. Uncertainties are taken from PDF variations. QCD scale varaitions have a negligable impact on these factors.

Bin	1	2	3	4	5	6	7	8
Inclusive	62.6 ± 0.9							
≥ 1 jet	61.1 ± 0.7							
≥ 2 jet	61.9 ± 0.6							
≥ 3 jet	63.8 ± 0.6							
$p_{\mathrm{T}}^{\gamma\gamma}$ [GeV]	62.1 ± 1.1	64.9 ± 1.0	64.1 ± 0.9	62.8 ± 0.8	61.7 ± 0.7	60.1 ± 0.7	60.2 ± 0.7	59.9 ± 0.5
$\lvert y_{\gamma\gamma}\rvert$	73.9 ± 0.7	74.0 ± 0.7	74.2 ± 0.6	73.9 ± 0.6	69.9 ± 0.6	38.8 ± 0.5		
N_{jets}	63.6 ± 1.0	60.8 ± 0.7	61.2 ± 0.6	63.8 ± 0.6				
$N_{\mathrm{jets}}^{50\ \mathrm{GeV}}$	62.9 ± 0.9	60.7 ± 0.6	64.3 ± 0.6	67.8 ± 0.6				
H_{T} [GeV]	63.6 ± 1.0	60.9 ± 0.8	60.1 ± 0.7	59.3 ± 0.6	63.8 ± 0.6			
$p_{\mathrm{T}}^{j_1}$ [GeV]	63.6 ± 1.0	60.7 ± 0.8	59.8 ± 0.7	59.6 ± 0.6	60.5 ± 0.5			
$\lvert y_{j_1}\rvert$	61.5 ± 0.6	61.5 ± 0.7	60.2 ± 0.7	60.1 ± 0.7				
$p_{\mathrm{T}}^{j_2}$ [GeV]	60.8 ± 0.7	60.1 ± 0.6	62.9 ± 0.6	67.5 ± 0.6				
$\lvert y_{j_2}\rvert$	61.1 ± 0.5	61.6 ± 0.6	63.1 ± 0.6	63.4 ± 0.6				
p_{T}^{j3} [GeV]	61.2 ± 0.6	62.2 ± 0.6	68.9 ± 0.6					
m_{jj} [GeV]	61.0 ± 0.6	62.7 ± 0.6	64.2 ± 0.6	62.6 ± 0.6				
$\lvert\Delta y_{jj}\rvert$	62.1 ± 0.6	62.0 ± 0.6	60.1 ± 0.6	60.9 ± 0.5				
$\Delta\phi_{jj}$	54.4 ± 0.5	79.6 ± 0.8	66.7 ± 0.7	42.5 ± 0.4				
$p_{\mathrm{T}\gamma\gamma jj}$ [GeV]	60.3 ± 0.6	62.3 ± 0.6	63.3 ± 0.6	67.4 ± 0.6				
$\Delta\phi_{\gamma\gamma,jj}$	57.5 ± 0.6	65.7 ± 0.7	61.5 ± 0.6	60.8 ± 0.5				
τ_{jet} [GeV]	59.5 ± 1.0	61.5 ± 0.7	59.7 ± 0.6	61.8 ± 0.6				
$\sum \tau_{\mathrm{jet}}$ [GeV]	63.0 ± 1.0	61.3 ± 0.7	59.8 ± 0.6	60.5 ± 0.5	67.3 ± 0.6			
$p_{\mathrm{T}}^{j_1}$, $N_{\mathrm{jets}} = 1$ [GeV]	60.9 ± 0.8	59.7 ± 0.7						

Table 5.32: Isolation efficiency factors in percent for gluon-gluon fusion $H \to \gamma\gamma$ for each fiducial region/variable bin measured in this analysis defined as the probaility for both photons being isolated ($E_{\mathrm{T}}^{\mathrm{iso}} < 14$ GeV as desribed in the text) for events that fulfil the diphoton kinematic criteria. Uncertainties are assined in the same way as for the non-perturbative correction factors: by varying the fragementation and underlying event modelling. These factors can be multiplied by the kinematic acceptance factors (see Table 5.31) to extrapolate an inclusive ggF Higgs prediction to the fiducial volume used in this analysis.

Bin	1	2	3	4	5	6	7	8	9	10
Inclusive	98.1 ± 0.5									
≥ 1 jet	97.5 ± 0.6									
≥ 2 jet	96.4 ± 1.0									
≥ 3 jet	95.1 ± 1.9									
$p_{\mathrm{T}}^{\gamma\gamma}$ [GeV]	99.5 ± 0.5	98.4 ± 0.9	97.6 ± 1.1	97.1 ± 1.1	96.7 ± 1.2	96.5 ± 1.0	96.6 ± 1.3	97.4 ± 1.0		
$\lvert y_{\gamma\gamma} \rvert$	98.0 ± 0.7	98.1 ± 0.7	98.0 ± 0.7	98.2 ± 0.7	98.2 ± 0.7	98.0 ± 0.9				
$\lvert \cos\theta^* \rvert$	97.8 ± 0.7	97.8 ± 0.8	97.9 ± 0.8	98.0 ± 0.8	98.2 ± 0.8	98.4 ± 0.9	98.7 ± 0.9	98.9 ± 1.1	97.9 ± 2.0	97.9 ± 2.3
N_{jets}	98.5 ± 0.6	97.9 ± 0.7	96.7 ± 1.1	94.9 ± 1.9						
$N_{\mathrm{jets}}^{50\ \mathrm{GeV}}$	98.4 ± 0.6	97.3 ± 0.7	95.7 ± 1.7	94.6 ± 3.7						
H_{T} [GeV]	98.5 ± 0.6	98.2 ± 0.9	97.9 ± 1.1	97.3 ± 0.9	96.4 ± 1.4					
$p_{\mathrm{T}}^{j_1}$ [GeV]	98.5 ± 0.6	98.1 ± 0.8	97.6 ± 1.0	97.3 ± 1.2	96.8 ± 1.4					
$\lvert y_{j_1} \rvert$	97.1 ± 0.7	97.4 ± 0.8	97.7 ± 1.2	97.9 ± 1.8						
$p_{\mathrm{T}}^{j_2}$ [GeV]	97.9 ± 0.7	96.7 ± 1.2	96.0 ± 2.0	95.1 ± 2.6						
$\lvert y_{j_2} \rvert$	95.9 ± 1.5	96.1 ± 1.6	96.5 ± 2.1	97.1 ± 3.2						
p_{T}^{j3} [GeV]	96.7 ± 1.1	95.3 ± 2.1	93.8 ± 3.8							
m_{jj} [GeV]	96.5 ± 1.2	95.8 ± 1.8	95.7 ± 3.2	95.6 ± 4.8						
$\lvert \Delta y_{jj} \rvert$	96.0 ± 1.2	96.4 ± 1.7	97.1 ± 3.6	97.7 ± 7.8						
$\Delta\phi_{jj}$	96.1 ± 1.6	96.3 ± 1.6	96.5 ± 2.2	95.5 ± 2.4						
$p_{\mathrm{T}\gamma\gamma jj}$ [GeV]	97.4 ± 1.5	96.1 ± 1.8	94.6 ± 3.0	92.4 ± 3.8						
$\Delta\phi_{\gamma\gamma,jj}$	93.9 ± 3.2	95.9 ± 2.0	96.7 ± 1.4	96.9 ± 2.2						
$p_{\mathrm{T}t\gamma\gamma}$ [GeV]	98.2 ± 0.5	98.2 ± 0.6	98.4 ± 0.9	98.3 ± 1.0	98.3 ± 0.9	98.0 ± 1.1	97.4 ± 1.0			
$\Delta y_{\gamma\gamma}$	97.8 ± 0.6	97.8 ± 0.7	98.0 ± 0.7	98.2 ± 0.7	98.5 ± 0.8	98.9 ± 0.9	99.2 ± 2.3			
τ_{jet} [GeV]	98.1 ± 0.6	97.9 ± 0.9	97.3 ± 0.8	96.9 ± 1.3						
$\sum \tau_{\mathrm{jet}}$ [GeV]	98.4 ± 0.6	98.1 ± 1.0	97.5 ± 0.9	97.0 ± 1.2	95.8 ± 1.4					
$p_{\mathrm{T}}^{j_1}$, $N_{\mathrm{jets}} = 1$ [GeV]	98.2 ± 0.9	97.8 ± 0.8								

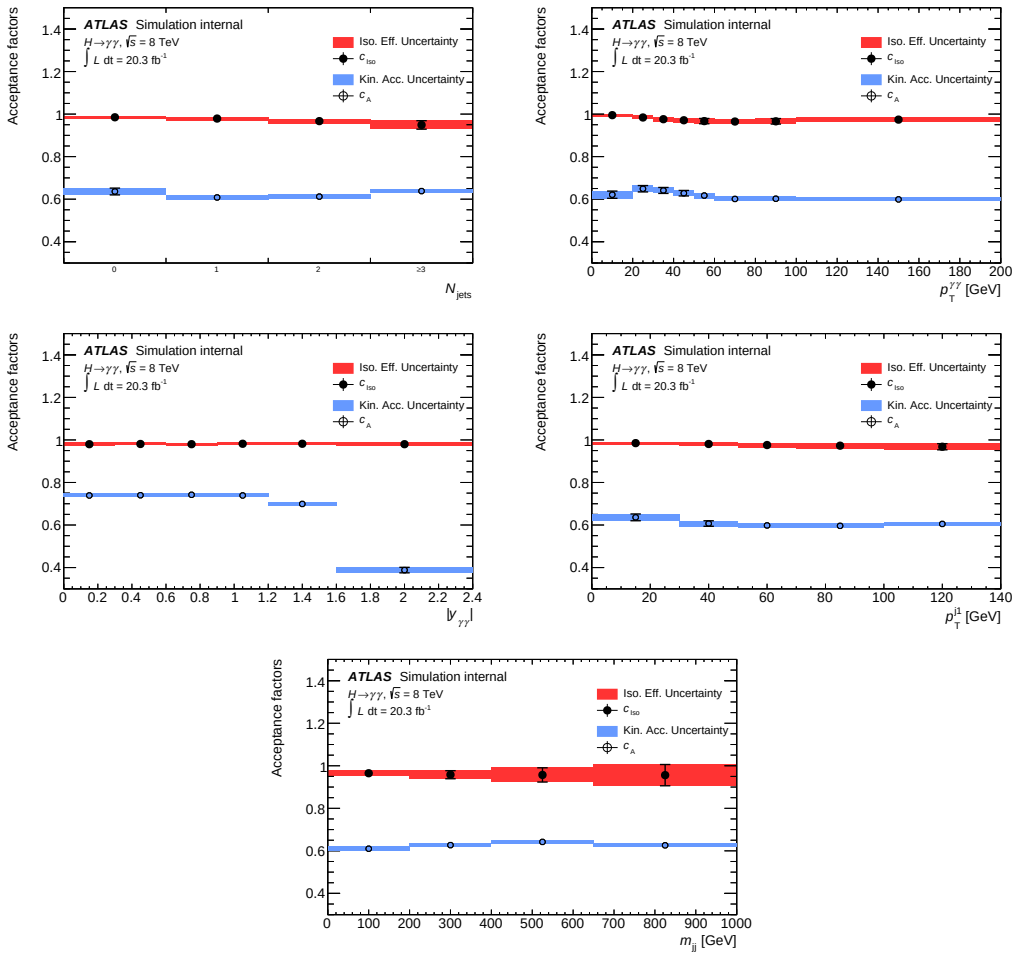

Figure 5.8: The fiducial kinematic acceptance factors (open circles) and the isolation efficiencies calculated at parton level. The full fiducial acceptance is calculated by multiplying the two factors shown. Uncertainty bands for the kinematic acceptance and isolation are from PDF variations and showering tunes respectively.

5.9 Results

The unfolded differential cross sections as measured in data are presented here. The differential cross sections are defined as

$$d\sigma_i/dp_{T,i} = \frac{n_i^{data,part}}{\mathcal{L} \cdot w_i} \tag{5.15}$$

where $n_i^{data,part}$ is the number of unfolded events from data in bin i, $\mathcal{L}$ is the integrated luminosity for the 2012 dataset, 20.3fb^{-1}, and w_i is the width of bin i. Figures 5.10 through 5.13 show the final unfolded results for all variables. Results are compared to MC Standard Model predictions, where the dashed line is the combined contribution from VBF+$WH + ZH + t\bar{t}H$, and the bands are the sum of the VBF+$WH + ZH + t\bar{t}H$ contribution and the ggF component. All cross sections have been normalized according to the LHC Higgs Cross Section Working Group [21] cross sections. The theory band around the MC prediction is calculated from the quadratic sum of scale variations, PDF variations, branching ratio uncertainty, and non-perturbative modeling. Three ggF predictions are used for the comparisons to unfolded distributions. HRes2.2 is used to calculate the inclusive Higgs boson production from ggF, and it is compared to the data for the $p_T^{\gamma\gamma}$, $y_{\gamma\gamma}$, $cos\theta^*$, $p_{T,t}$, and $\Delta y_{\gamma\gamma}$ distributions. For distributions involving two or more jets, MiNLO HJJ, which generates the Higgs boson in association with two jets at NLO, is chosen for the theory comparison. All other distributions are compared to MiNLO HJ, which generates the Higgs boson in association with 0 and 1 jets at NLO. Uncertainty bands for the theoretical predictions are the quadratic sum of the scale uncertainties, PDF uncertainties, and non-perturbative uncertainties. The scale uncertainties were estimated with the variation of the renormalization and factorization scales by factors

of 2. PDF uncertainties were taken from the envelope of the CT10 PDF uncertainty and the central values of the MSTW08 and NNPDF2.3 PDFs. Uncertainty from the non-perturbative modeling is taken from the non-perturbative correction factor uncertainties described in Sec. 5.8.1. For the unfolded data, the black vertical error bars represent the total uncertainty on the measurement, and the grey band is the systematic component of the uncertainty. As seen in the plots, errors on the cross section measurement are dominated by the statistical uncertainty.

All distributions measured in data show good agreement with the Standard Model theory predictions. Slight excesses are seen in the jet multiplicity distributions for both $p_{T,jet}$ >30 GeV and $p_{T,jet}$ >50 GeV shown in Fig. 5.10 and 5.11. These excesses are not statistically significant. Another deviation from the predictions is seen in the measured distribution of the azimuthal angle difference between the two highest p_T jets shown in Fig. 5.11. The excess is in the bin $\Delta\phi_{jj} > \frac{5}{6\pi}$ and has a significance of 2.3σ. This distribution was cross checked by using only central jets and requiring a tighter JVF cut; the excess is still present in this distribution suggesting that the discrepancy is not a result of mismodeled pileup jets.

In addition to the differential distributions, fiducial cross sections were measured for the inclusive case, the VBF topology case, and the jet multiplicities. Limits were set for Higgs boson production in association with at least one lepton and in association with missing transverse energy. Results for these measurements are shown in Fig. 5.9 and summarized in Table 5.33.

Fiducial region	Measured cross section (fb)
Baseline	$43.2 \pm 9.4\,(\text{stat.})\,^{+3.2}_{-2.9}\,(\text{syst.}) \pm 1.2\,(\text{lumi})$
$N_{\text{jets}} \geq 1$	$21.5 \pm 5.3\,(\text{stat.})\,^{+2.4}_{-2.2}\,(\text{syst.}) \pm 0.6\,(\text{lumi})$
$N_{\text{jets}} \geq 2$	$9.2 \pm 2.8\,(\text{stat.})^{+1.3}_{-1.2}\,(\text{syst.}) \pm 0.3\,(\text{lumi})$
$N_{\text{jets}} \geq 3$	$4.0 \pm 1.3\,(\text{stat.}) \pm 0.7\,(\text{syst.}) \pm 0.1\,(\text{lumi})$
VBF-enhanced	$1.68 \pm 0.58\,(\text{stat.})^{+0.24}_{-0.25}\,(\text{syst.}) \pm 0.05\,(\text{lumi})$
$N_{\text{leptons}} \geq 1$	< 0.80
$E_T^{miss} > 80$ GeV	< 0.74

Table 5.33: Measured cross sections in the baseline, $N_{\text{jets}} \geq 1$, $N_{\text{jets}} \geq 2$, $N_{\text{jets}} \geq 3$ and VBF-enhanced fiducial regions, and cross-section limits at 95% confidence level in the single-lepton and high-E_T^{miss} fiducial regions.

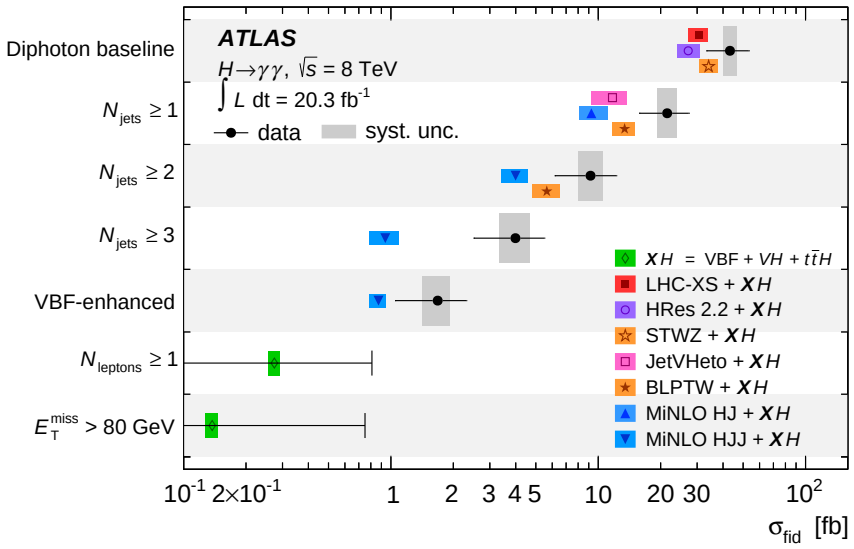

Figure 5.9: The measured cross sections and cross-section limits for $pp \to H \to \gamma\gamma$ in seven fiducial regions. The intervals on the vertical axis each represent one of these fiducial regions. The data are shown as filled (black) circles. The error bar on each measured cross section represents the total uncertainty in the measurement, with the systematic uncertainty shown as dark grey rectangles. The error bar on each cross-section limit is shown at the 95% confidence level. The data are compared to state-of-the-art theoretical predictions (see text for details). The width of each theoretical prediction represents the total uncertainty in that prediction. All regions include the SM prediction arising from VBF, VH and $t\bar{t}H$, which are collectively labeled as XH.

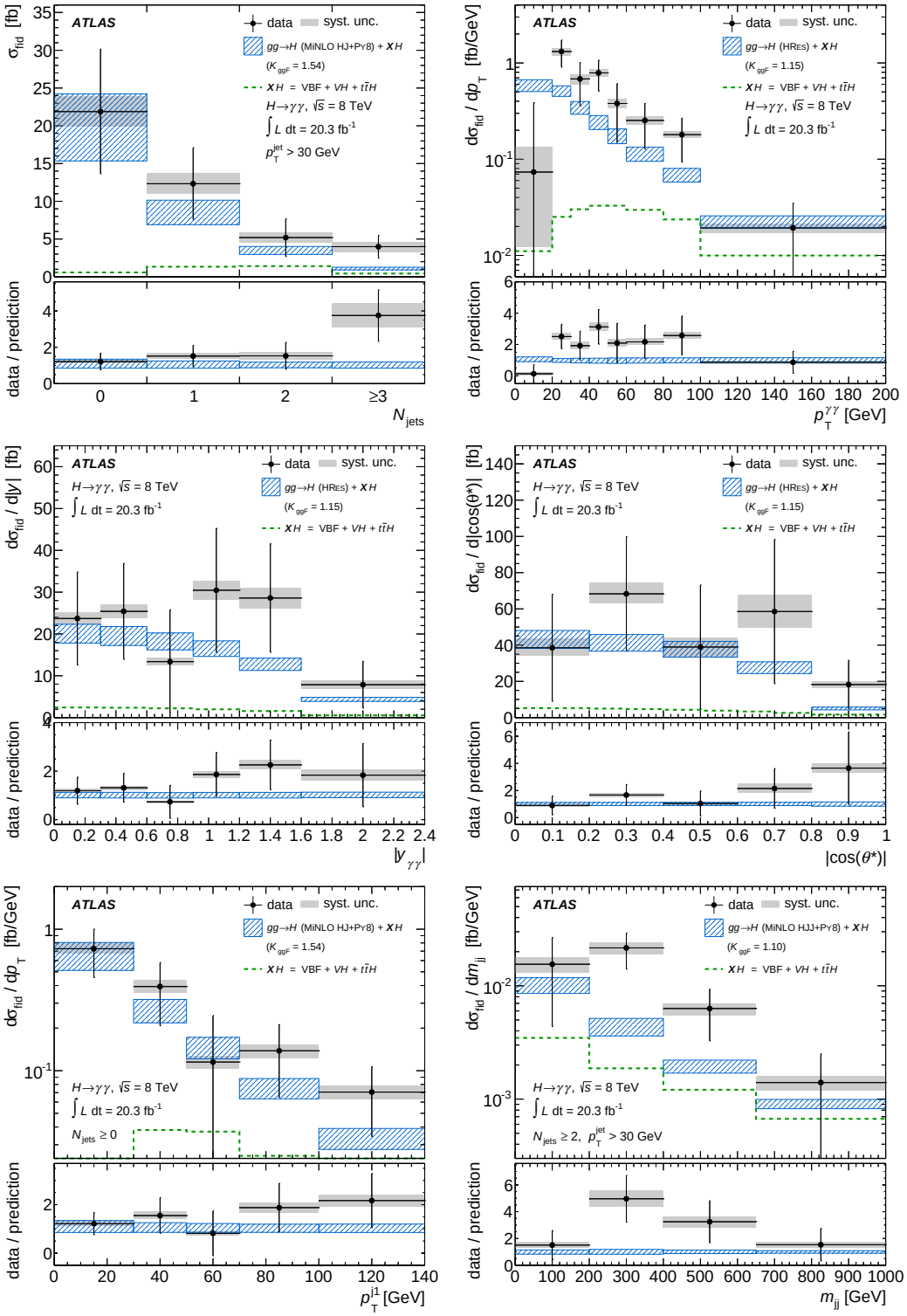

Figure 5.10: Particle level differential cross-sections for each variable.

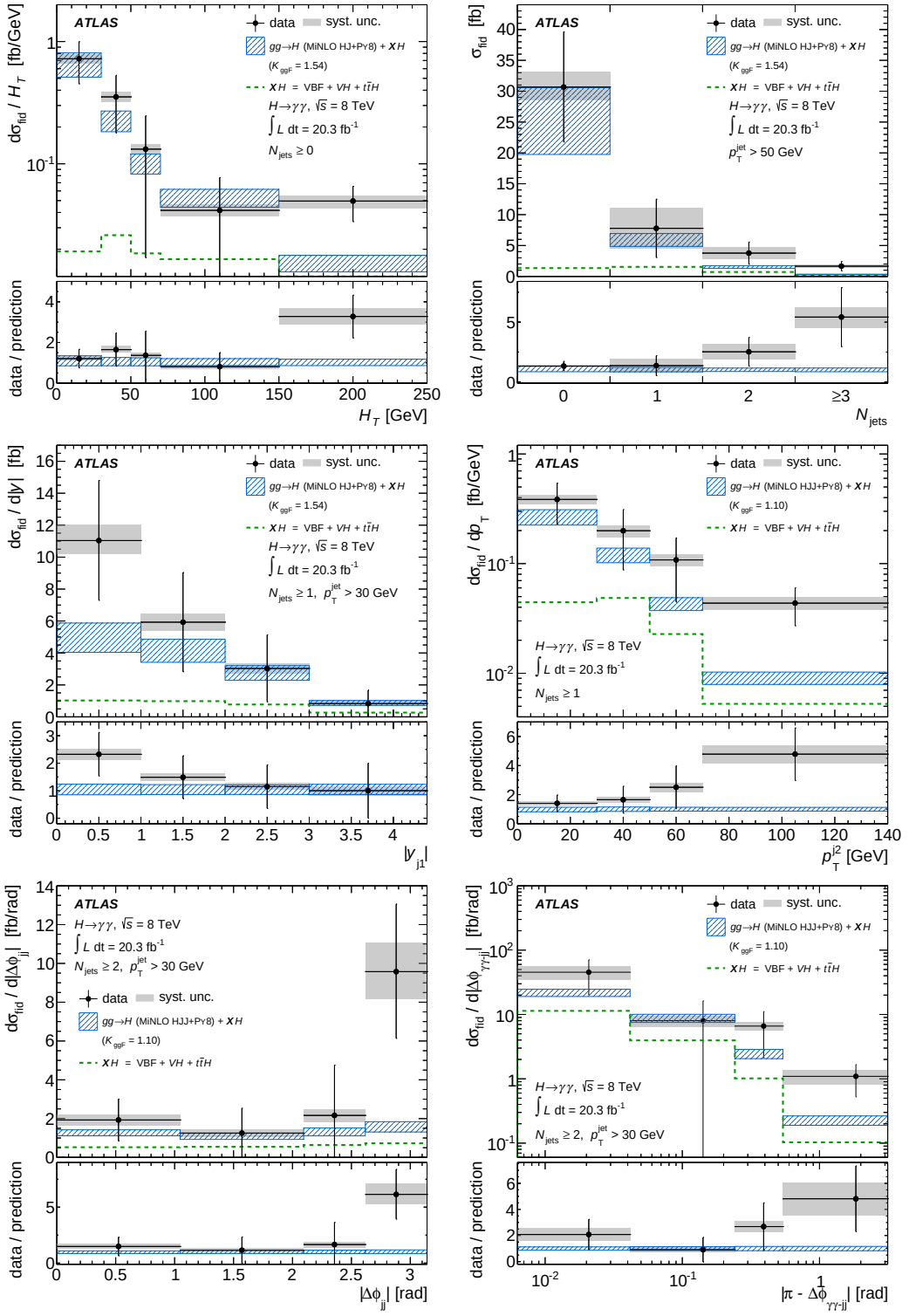

Figure 5.11: Particle level differential cross-sections for each variable.

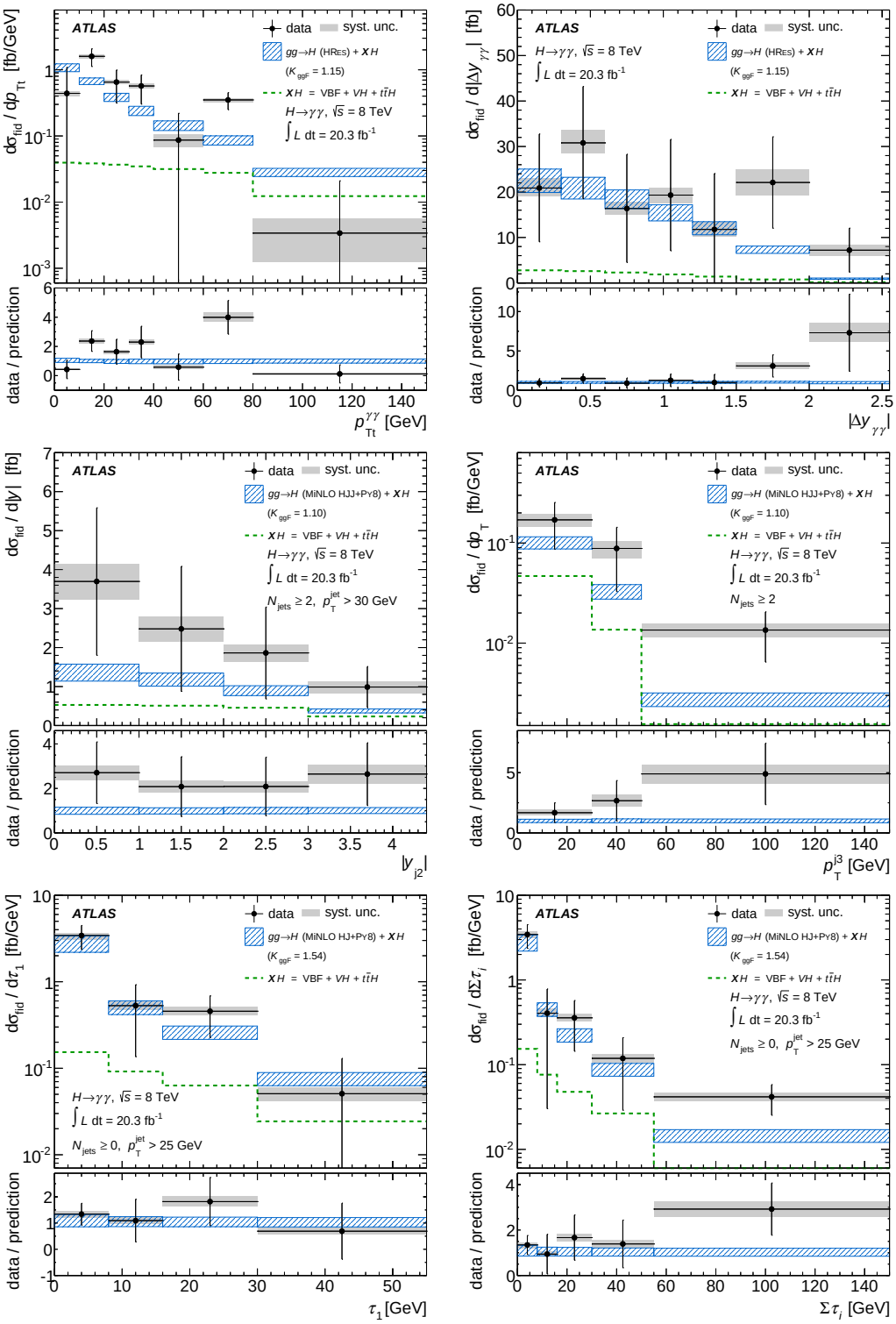

Figure 5.12: Particle level differential cross-sections for each variable.

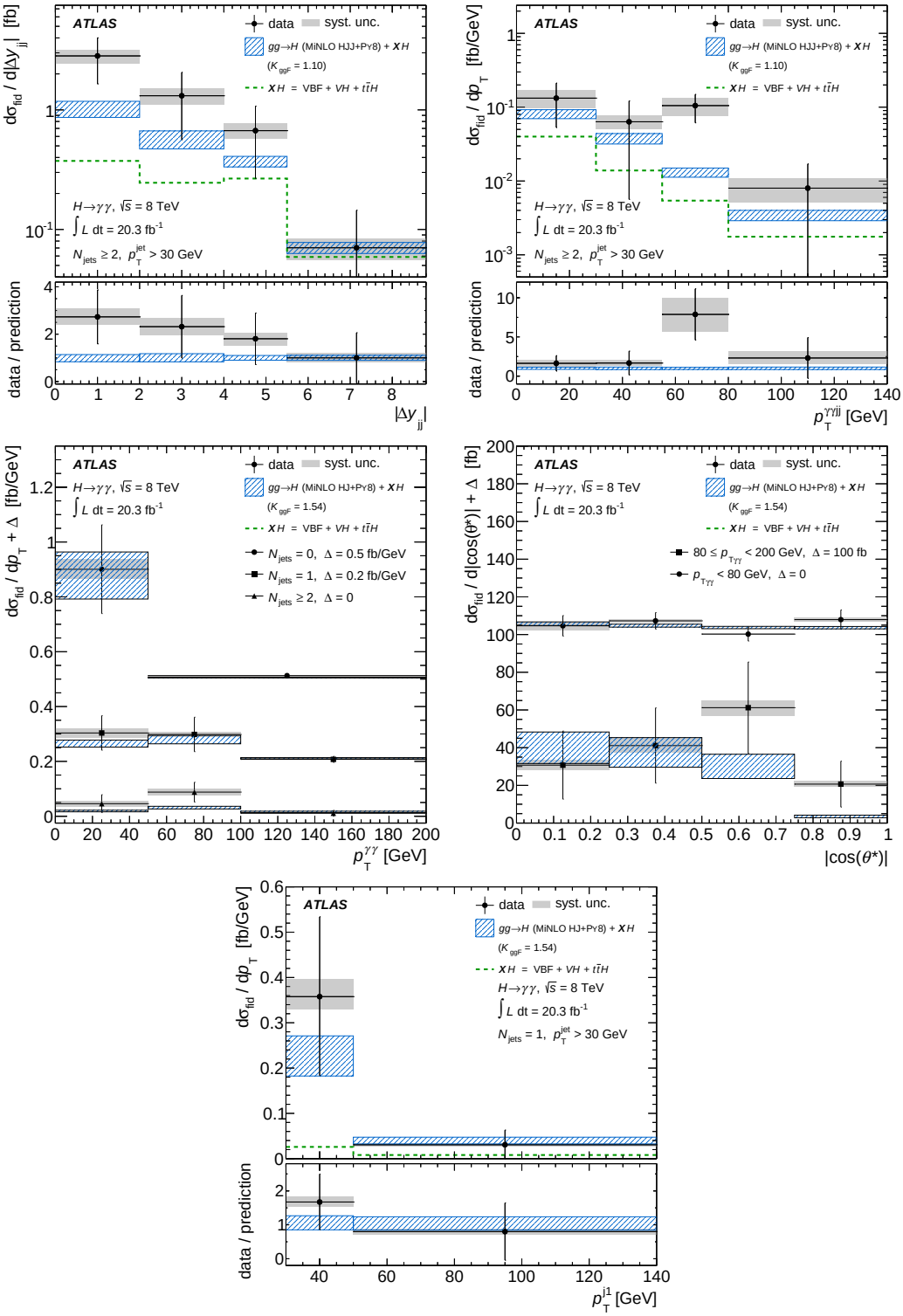

Figure 5.13: Particle level differential cross-sections for each variable.

5.10 Monte-Carlo Comparisons for Gluon-Gluon Fusion

As described in Sec. 5.1, there are many different theoretical predictions for the ggF production process. The ones compared here are HRes2.2, POWHEG ggF, MiNLO HJ, and MiNLO HJJ though many more exist. Figs. 5.14 through 5.16 show the ratios of the data and theory predictions to the reference MiNLO HJ prediction. Theory bands are calculated using the same prescription as in Sec. 5.9. Quantitative comparisons between the measured data and the different ggF theoretical predictions are done using a χ^2 comparison. Table 5.34 shows the χ^2 for each available prediction normalized to the LHC-HXWG cross sections. There is agreement between all the theoretical predictions and the unfolded data distributions; however, the dataset is too statistically limited to make any more definitive statements, and this dataset is unable to distinguish between the many ggF predictions at this time.

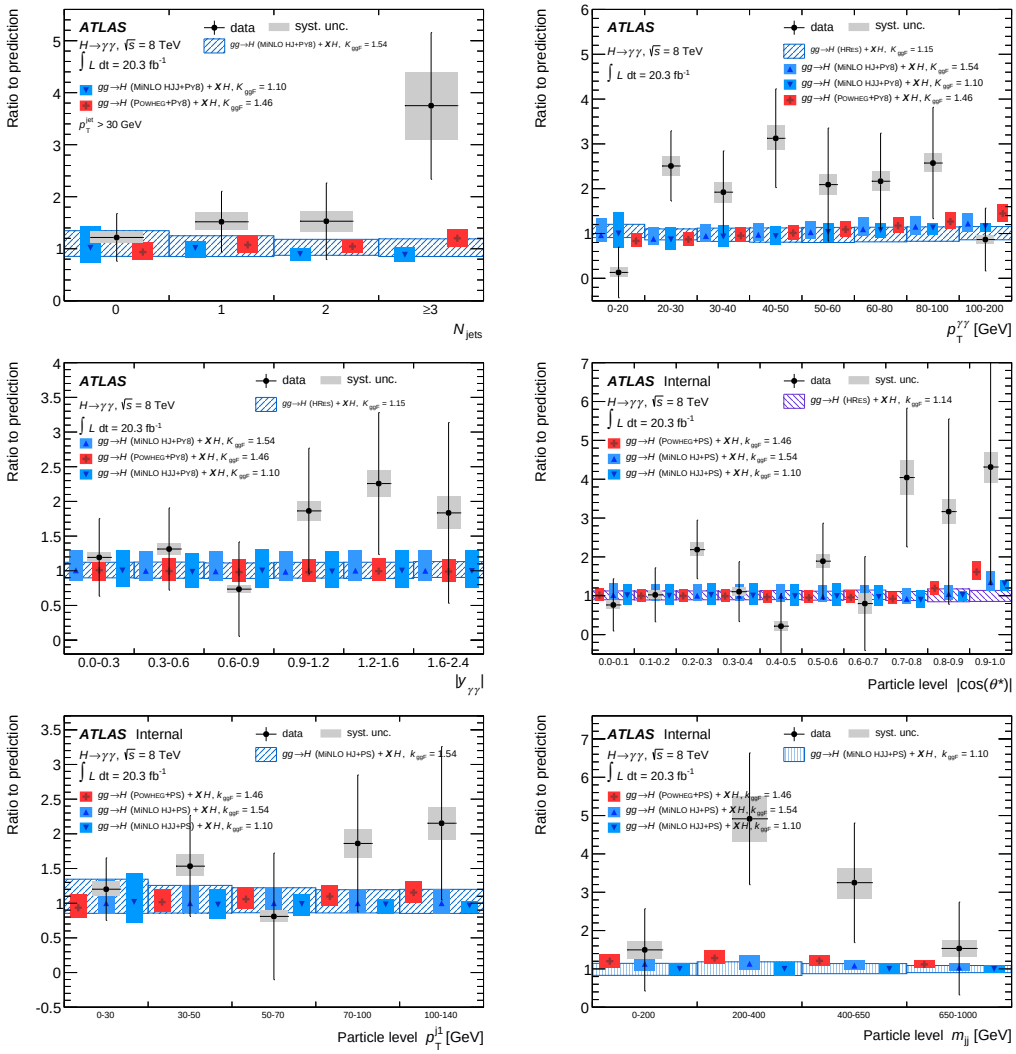

Figure 5.14: Particle level differential cross-sections for each variable compared to a selection of theoretical predictions of the Standard Model.

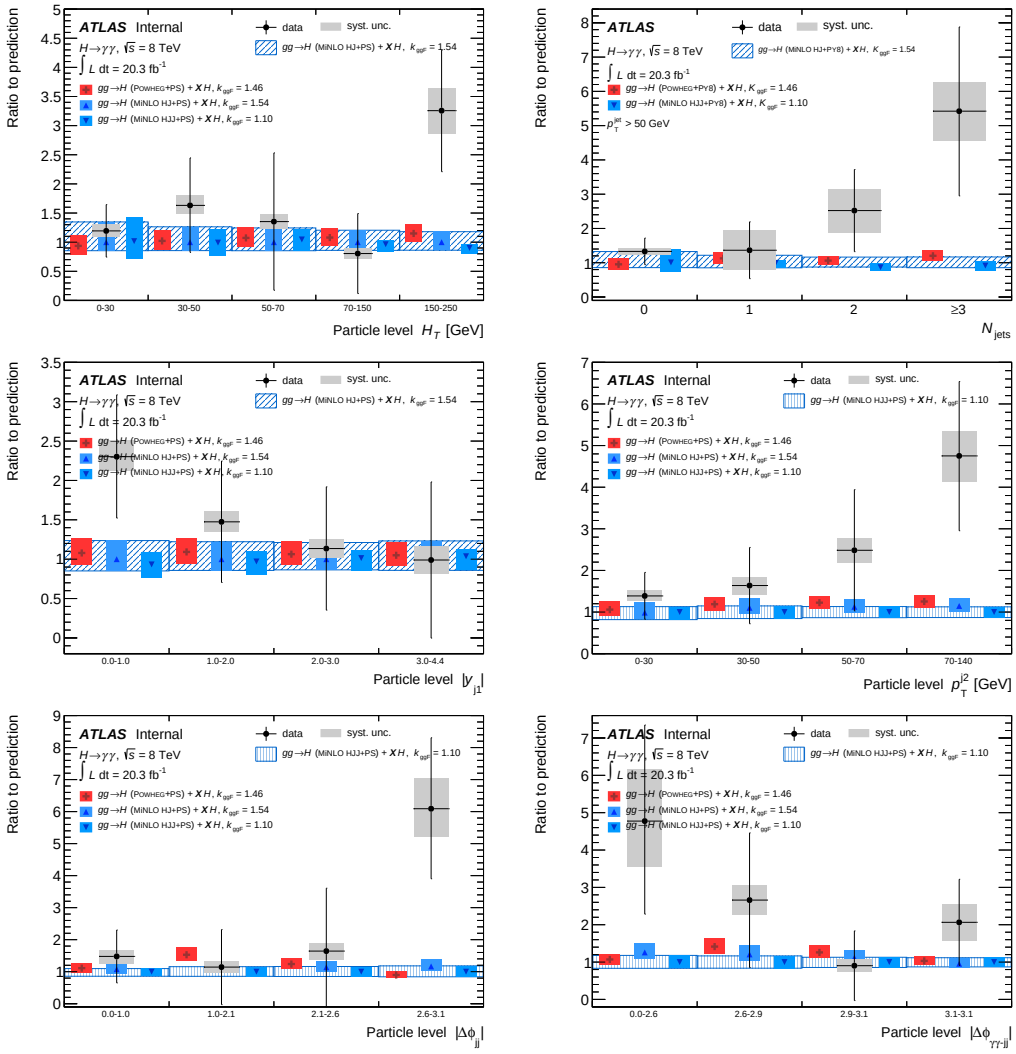

Figure 5.15: Particle level differential cross-sections for each variable compared to a selection of theoretical predictions of the Standard Model.

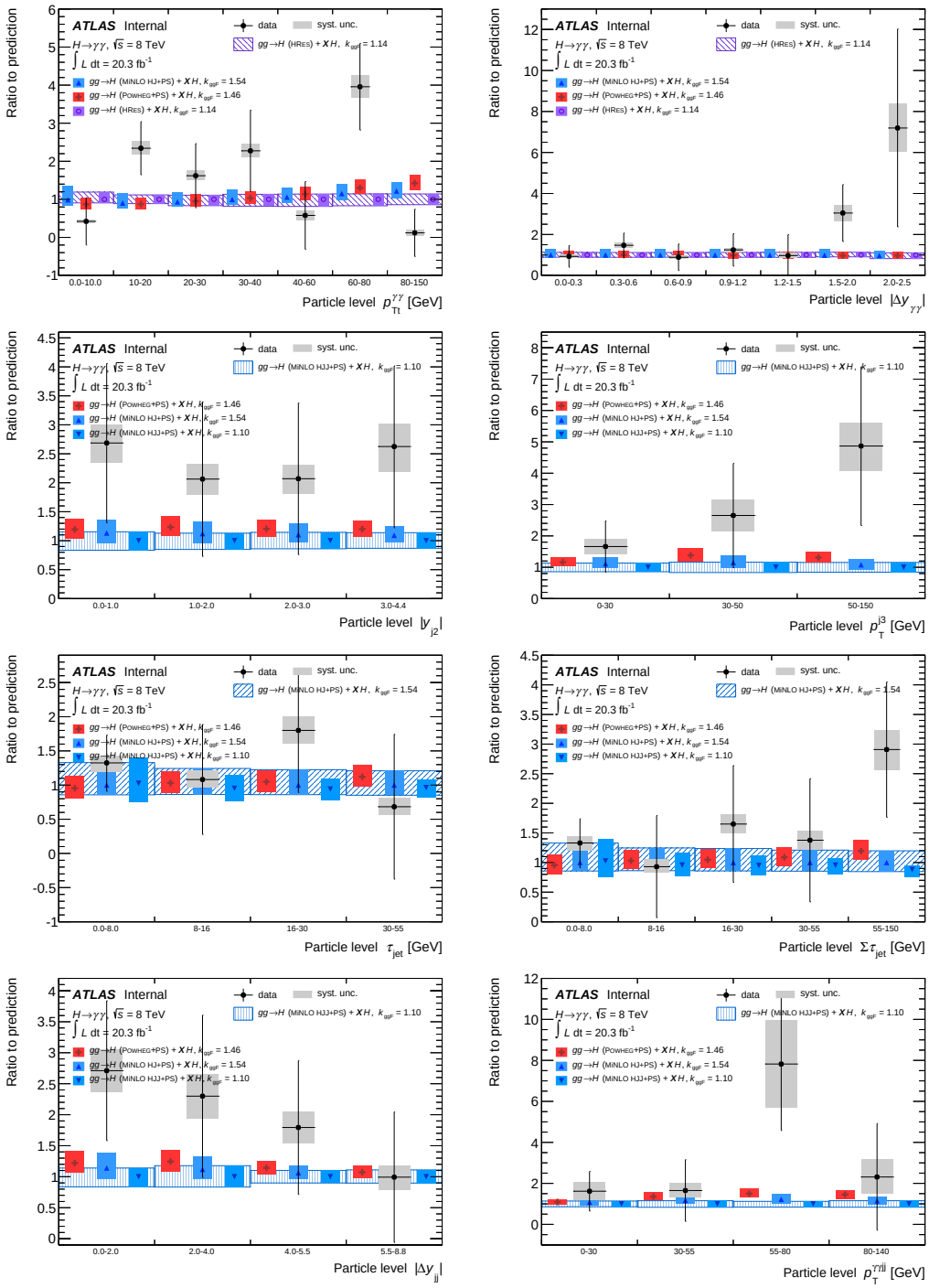

Figure 5.16: Particle level differential cross-sections for each variable compared to a selection of theoretical predictions of the Standard Model.

Variable	POWHEG	MiNLO HJ	MiNLO HJJ	HRes2.2
Inclusive	0.25	0.29	0.32	-
VBF-enhanced	0.29	0.22	0.20	-
N_{jets}	0.42	0.36	0.30	-
$p_{\text{T}}^{\gamma\gamma}$ [GeV]	0.12	0.10	0.09	0.12
$\lvert y_{\gamma\gamma}\rvert$	0.81	0.83	0.83	0.80
$\lvert\cos\theta^*\rvert$	0.59	0.57	0.58	0.56
$p_{\text{T}}^{j_1}$ [GeV]	0.84	0.82	0.79	-
m_{jj} [GeV]	0.22	0.18	0.14	-
H_{T} [GeV]	0.43	0.39	0.34	-
$N_{\text{jets}}^{50\text{ GeV}}$	0.33	0.33	0.30	-
$\lvert y_{j_1}\rvert$	0.64	0.58	0.51	-
$p_{\text{T}}^{j_2}$ [GeV]	0.34	0.29	0.23	-
$\Delta\phi_{jj}$[rad]	0.21	0.28	0.24	-
$\Delta\phi_{\gamma\gamma,jj}$[rad]	0.45	0.46	0.42	-
$p_{\text{Tt}\gamma\gamma}$ [GeV]	0.02	0.03	0.03	0.04
$\Delta y_{\gamma\gamma}$	0.73	0.74	0.74	0.73
$\lvert y_{j_2}\rvert$	0.62	0.56	0.46	-
τ_1 [GeV]	0.82	0.86	0.87	-
$\sum\tau_i$ [GeV]	0.68	0.64	0.58	-
p_{T}^{j3} [GeV]	0.45	0.38	0.32	-
$\lvert\Delta y_{jj}\rvert$	0.64	0.58	0.49	-
$p_{\text{T}\gamma\gamma jj}$ [GeV]	0.34	0.30	0.25	-

Table 5.34: Probabilities from χ^2 tests for the agreement between the diffential cross section measurements and the theoretical predictions. Each prediction is normalised to the LHC-XS cross section before selection.

5.11 Summary

Measurements of the fiducial and differential cross sections for the Higgs boson decaying into diphotons were presented. Results were unfolded to particle level and compared to Standard Model predictions. The inclusive cross section was measured to be

$$\sigma = 43.2 \pm 9.4(\text{stat})^{+3.2}_{-2.9}(\text{syst.}) \pm 1.2(\text{lumi})\text{ fb}. \tag{5.16}$$

This result is within 1.2 σ of the signal strength measured in Chapter 5 where the events were divided into twelve different categories targeted at the individual production processes. Many differential distributions were measured for various diphoton kinematics and jet production in association with the Higgs boson. The measured differential cross section distributions were compared to theory predictions and the resulting χ^2 values show acceptable agreement. Multiple ggF predictions were checked; however, the results are extremely limited statistically and do not have the power to distinguish between different theoretical predictions. All measurements show agreement with Standard Model predictions.

Chapter 6

Higgs Plus 1 Jet VBF Studies for High Luminosity LHC

As luminosity increases at the LHC, higher pileup is expected. This was the case when increasing the center-of-mass energy from 7 TeV to 8 TeV, and as a consequence, the jet p_T thresholds had to be revisited. Increasing jet p_T thresholds can have a large impact on the VBF production process where two forward/backward jets are produced with very low transverse momentum.

A study was done using a specially produced 8 TeV VBF MC sample with an average number of vertices of 40 ($< \mu >$=40). The nominal jet selection cuts were applied, which during 2011 data taking had a p_T threshold of 25 GeV. Selected jets were then matched back to truth jets using a cone of $\Delta R = 0.4$, and the fraction of jets where at least one of the leading two selected jets was a fake jet (from pileup) was checked. The dependence of this fraction on the number of vertices in the sample shows the effect of pileup; an increase in the fake rate with increasing number of vertices shows the jet selection is sensitive to the amount of pileup in an event. In the current VBF coupling analysis described in Sec. 4.4.2, the dijet kinematics are heavily

relied on to distinguish between VBF events and background events. Selecting on pileup jets destroys the correlations between the jets and the shapes that enter into the BDT will no longer look like VBF events. Figure 6.1 shows the fake rate fractions for increasing number of simulated vertices. Also shown are the rates for increasing jet p_T thresholds for the leading jet/subleading jet divided into central ($|\eta|$ <2.5) and forward jets. The original p_T threshold of 25 GeV for both central and forward jets shows a clear increasing fake rate with increasing number of vertices meaning it is susceptible to pileup jets. When increasing the p_T threshold to 30 GeV just for forward jets, the fake rate is decreases by roughly half the rate. Further increasing the jet p_T thresholds has a small impact on the pileup dependence. It was decided during 2012 data-taking to increasing the jet p_T threshold for forward jets to p_T >30 GeV.

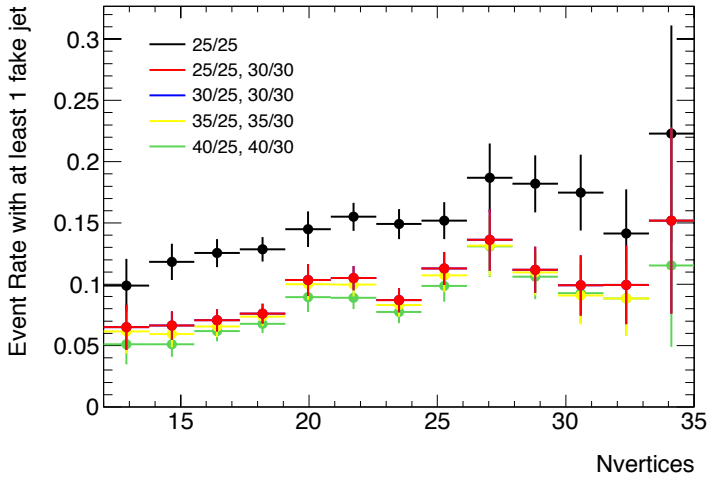

Figure 6.1: The dependence on the fake rates of jets on the number of vertices for VBF MC. The first (second) set of numbers is for central (forward) jets. The two numbers separated by a '/' indicate the p_T thresholds for the leading/subleading jets.

What is not obvious from Fig. 6.1 is the overall loss in VBF signal when raising the jet p_T threshold. Figure 6.2 shows the leading jet p_T thresholds for three different sets of events: those events with at least two jets which pass VBF topology cuts

($\Delta\eta_{jj} > 2.8$, m_{jj} >520 GeV, $(\eta_H - 0.5(\eta_{j1} + \eta_{j2}))$ <= 2.4, $\Delta\phi_{H,jj}$ >= 2.6), those events with at least two jets which fail the VBF topology cuts, and events with only one jet with p_T >30 GeV. This distribution is for the leading jet p_T, so the subleading jet p_T will always be less than these distributions. As the jet p_T cut is raised, as it will need to be for higher pileup situations, many of these 2-jet events will become 1-jet events. A VBF category defined using only one tagged jet is proposed to recover these VBF events which no longer pass 2-jet VBF topology cuts and to exploit diphoton+jet kinematics to create a 1-jet VBF category with high VBF purity.

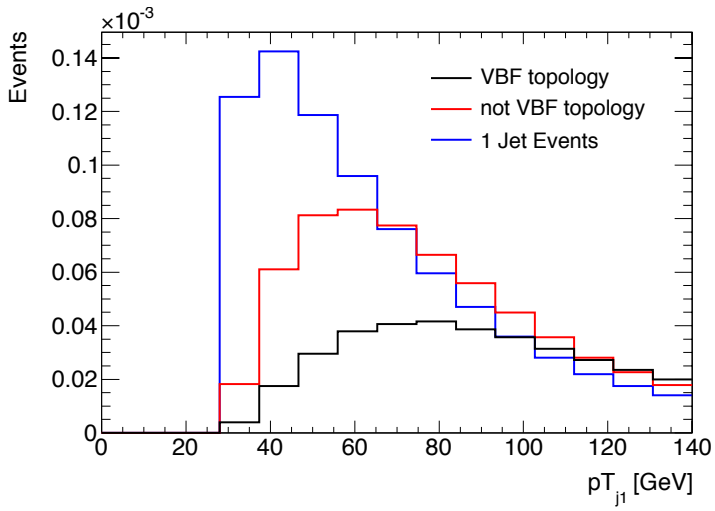

Figure 6.2: The leading jet p_T distribution for VBF events. The black distribution is for 2-jet events which pass VBF topology cuts, the red distribution is for 2-jet events which fail the VBF topology cuts, and the blue distributions is for 1-jet events.

6.1 MC Samples

MC samples are generated at truth particle level using POWHEG interfaced with PYTHIA8 for the parton shower, hadronization, and underlying event. Three samples were generated: VBF, HJ (H+1jet ggF process), and HJJ (H+2jet ggF process). HJ and HJJ were generated using the MiNLO procedure [99]. All three process were

generated with the CT10 PDF. Scale uncertainties were calculated by varying the renormalization and factorization scales up and down by factors of 2. The HJ and HJJ ggF processes show a very small difference in rapidity between the diphoton and leading jet system while the VBF process shows a larger separation. Therefore, the VBF 1-jet category will be defined by placing a cut at larger Δy_{Hj} separation.

6.2 1-Jet VBF Category

An H+1jet VBF category is proposed using the rapidity difference between the diphoton and leading jet (Δy_{Hj}) as the discriminating variable. Figure 6.3 shows the normalized Δy_{Hj} distributions for the VBF, HJ, and HJJ samples and their corresponding scale uncertainties. The uncertainties for the VBF process are well behaved and relatively small. The proposed 1-jet category will minimize the theory uncertainties on the ggF contribution. ggF theoretical uncertainties are typically large when applying dijet kinematic cuts to isolate the VBF process in a 2-jet category. With the 1-jet category, the extraction of the VBF process relies on the ratio of ggF events with high Δy_{Hj} separation to ggF events with low separation. This ratio ensures the cancellation of large theoretical uncertainties. First, the ratio of high separation to low separation is defined as

$$R_{low}^{high} = \frac{N_{g,H} + N_{V,H}}{N_{g,L} + N_{V,L}}. \tag{6.1}$$

Here the subscript g (V) denotes the ggF (VBF) contribution, and the subscript H (L) denotes the region of high (low) Δy_{Hj} separation. This can be rewritten by defining the ratio of ggF events in the region of large separation to ggF events in the low separation region: $\xi^g = \frac{N_{g,H}}{N_{g,L}}$. Then with the assumption that the VBF process

contributes very little in the region with low Δy_{Hj} separation Eq. 6.1 becomes

$$R_{low}^{high} \approx \xi^g + \frac{N_{V,H}}{N_{g,L}}. \tag{6.2}$$

Here, $N_{g,L}$ is the number of events in the low Δy_{Hj} region which is extracted experimentally, and ξ^g and $N_{V,H}$ are from the theoretical expectations. The uncertainties on the VBF signal extraction in the 1-jet category (the high Δy_{Hj} region) is expressed as

$$\left(\sqrt{N_{g,H} + N_{V,H}} \oplus \sqrt{N_{g,L}\xi^g} \oplus \delta\xi^g N_{g,L}\right) / N_{V,H}, \tag{6.3}$$

where $\delta\xi^g$ is the theoretical uncertainty on the ratio ξ^g. As shown in Fig. 6.3, the theoretical uncertainties on $N_{V,H}$ are relatively small. The scale uncertainties for ggF were calculated for both high and low regions of Δy_{Hj} and then propagated to the ratio ξ^g. The resulting uncertainty on ξ^g was found to be 6.5%. This is significantly less than the 20% ggF theoretical uncertainty associated with the 2-jet VBF categories listed in Tab: 4.12.

It is important to ensure that the difference in Δy_{Hj} shape between the VBF and HJJ process is maintained as the jet p_T threshold is increased. Otherwise the H+1j VBF category will not be viable for higher pileup scenarios. $\Delta y_{Hj} \times p_{T,2jcut}$ 2D distributions were checked for both VBF and HJJ events. These distributions are shown in Fig. 6.4, and it can be seen that as the jet p_T threshold is increased, the HJJ events become more evenly spread over the lower Δy_{Hj} values, but the VBF events maintain a concentration at Δy_{Hj} values around $\sim$1.5.

The cut on Δy_{Hj} was optimized for the different jet p_T thresholds and the results for an integrated luminosity of 300 fb^{-1} are shown in Tab. 6.1. Expected signal events

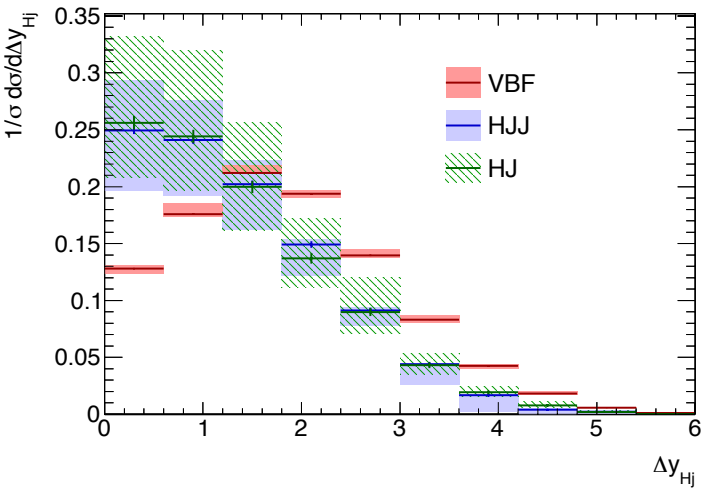

Figure 6.3: The normalized Δy_{Hj} distributions for the VBF, HJ, and HJJ samples. Shaded regions are the scale uncertainties calculated by varying the renormalization and factorization scales up and down by factors of 2.

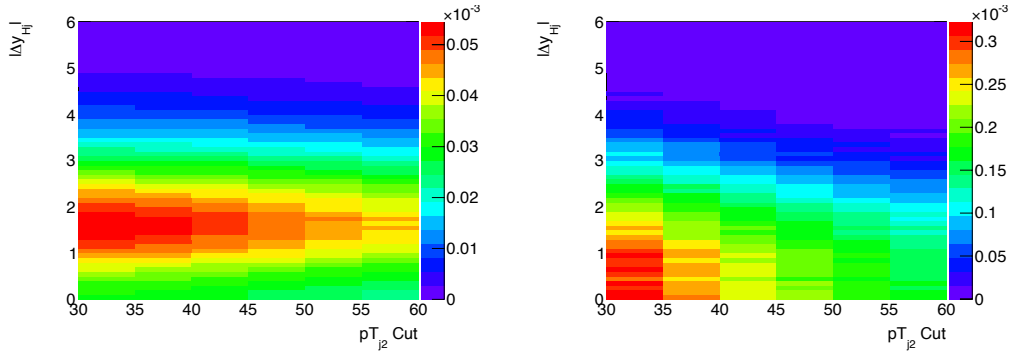

Figure 6.4: Effective cross section [fb] of VBF (left) and ggF (right) processes as a function of jet p_T and Δy_{Hj} thresholds.

for VBF and ggF are listed along with the corresponding signal-to-background ratio and error on the μ_{VBF} measurement. An assumed 5% error is included for the ggF production process. The cut on Δy_{Hj} was stable across all jet p_T thresholds. Combining both a VBF 2-jet category with the proposed VBF 1-jet category lowers the error on the VBF signal strength measurement. For jet p_T thresholds above 50 GeV, the sensitivity in the VBF 1-jet category dominates.

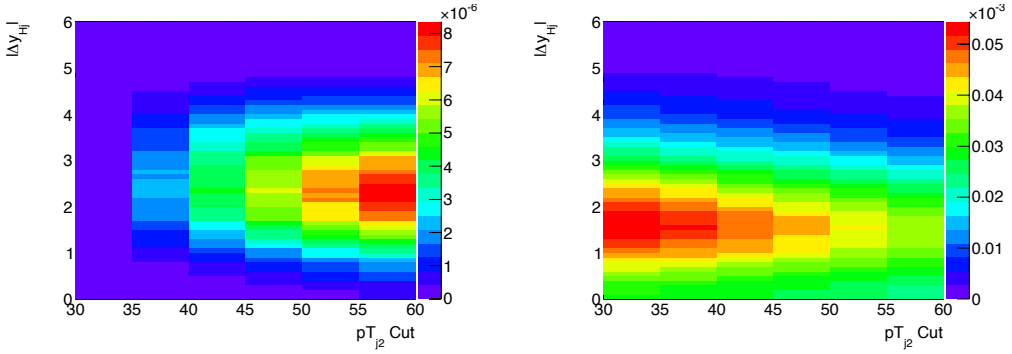

Figure 6.5: Effective cross section [fb] of VBF events which pass standard VBF topology cuts (left) and those which do no (right) as a function of jet p_T and Δy_{Hj} thresholds.

		VBF category				$1j$ category				
p_{Tj}	Δy_{Hj}	S	ggF	S/ggF	$\Delta\mu$	S	ggF	S/ggF	$\Delta\mu$	$\Delta\mu^{Tot}$
30	1.4	137.321	30.668	4.478	0.095	261.526	1203.739	0.217	0.146	0.080
35	1.4	120.202	25.320	4.747	0.101	255.874	988.994	0.259	0.138	0.081
40	1.4	103.333	20.985	4.924	0.108	247.336	814.661	0.304	0.132	0.084
45	1.4	87.569	17.285	5.066	0.117	235.912	681.020	0.346	0.128	0.087
50	1.4	73.577	14.827	4.962	0.128	222.203	573.959	0.387	0.127	0.090
55	1.4	61.162	12.139	5.039	0.140	207.925	482.780	0.431	0.126	0.094

Table 6.1: VBF Signal and ggF background rates for 300 fb^{-1} integrated luminosity. Thresholds on the the jet p_T are given in GeV. Results are given for different values of the threshold on p_{Tj2} and the resulting optimal value of the cut on Δy_{Hj} . Results are shown for the expected accuracy of the signal strength measurement for the individual categories and ther combination, $\Delta\mu^{Tot}$.

6.3 Sensitivity to New Physics

It was shown in Ref. [140], that a general form of the beyond-the-Standard Model (BSM) HVV vertex can be written as

$$\Gamma_{\mu\nu}^{BSM}(p,q) = \frac{g}{M_V}[\lambda(p\cdot q g_{\mu\nu} - p_\nu q_\mu) + \lambda^{'}\epsilon_{\mu\nu\rho\sigma}p^\rho q^\sigma], \tag{6.4}$$

where λ and $\lambda^{'}$ are the coupling strengths for CP-even and CP-odd interactions. The Δy_{Hj} distribution will be affected by any BSM couplings in the HVV vertex. A λ value of zero corresponds to the Standard Model couplings. As can be seen from

Eq. 6.4, the CP-even BSM coupling is dependent on the momentum of the gauge bosons, causing the rapidity of the jets to be much smaller. This in turn causes a lower separation between the leading jet and the diphoton system as shown in Fig. 6.6.

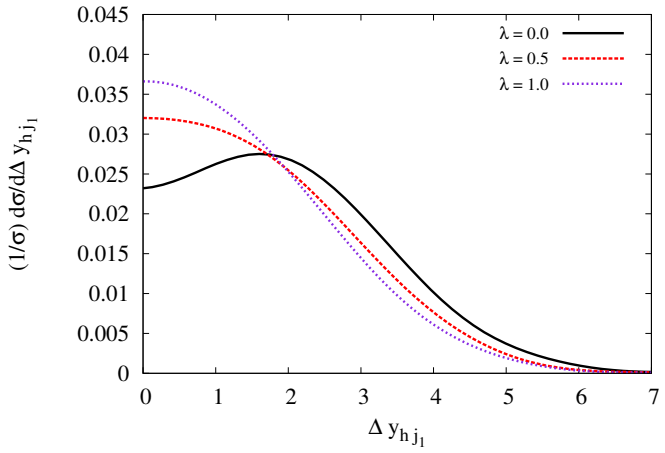

Figure 6.6: Δy_{Hj} distribution dependence on the tensor structure of the HVV coupling.

6.4 Conclusion

A 1-jet VBF category defined by the separation of the tagged jet from the diphoton system is proposed for high-luminosity LHC running. This category isolates the VBF production process while minimizing the ggF theoretical errors that typical 2-jet VBF categories suffer from. Studies were done for varying jet p_T thresholds, which are expected to rise with increasing pileup. The optimized Δy_{Hj} cuts were shown to be stable with respect to the p_T thresholds, and by relying on ratios of observables, the ggF theory uncertainty is $\sim$6.5%.

In addition to lowering the error on the VBF signal strength measurement, this 1-jet VBF category is sensitive to BSM couplings of the Higgs boson. Because the

BSM couplings have a p_T dependence, the shape of Δy_{Hj} becomes more central with stronger the BSM coupling.

Chapter 7

Conclusions

Both experiments at the LHC, ATLAS and CMS, announced the discovery of the Higgs boson in 2012, with sensitivity from mainly the diphoton and ZZ decay channels. While the discovery required a significance greater than 5 σ from the combined decay channels, the ATLAS significance of the diphoton decay channel was already greater than 4 σ by itself. This was achieved by breaking down events into predefined categories, taking advantage of the signal to background ratios in each category in order to increase the overall significance. At the time of discovery, the diphoton analysis included one coupling category: a VBF category defined based on the kinematics of the dijet system. The category was optimized using a cut-based analysis which discriminated between VBF and both ggF and diphoton background processes. This VBF category had the largest signal to background ratio of all the categories, and the addition of the VBF category to the overall analysis increased the sensitivity from around 4 σ to the final 4.6 σ in the diphoton channel. With its higher production rate and small theoretical errors, with enough luminosity, the VBF signal rate will be able to very precisely measured.

After the discovery of the Higgs boson, the analysis shifted from a search to a

measurement philosophy. Instead of optimizing on increased sensitivity, the goal became lessening the errors on the signal strength measurements. More coupling categories like the VBF category were added for the different production processes. The VBF category was further optimized using a multivariate analysis which takes into account the shapes of the kinematic distributions. The category was optimized on background events but shown to also discriminate against ggF events as well. With the improvement of the BDT VBF analysis, a second looser VBF category was added to the analysis. A VBF signal strength of 0.8 was measured which is lower than the expected Standard Model rate, but still consistent with it.

In addition to the measurement of the individual signal strengths, it is important to understand the kinematic shapes associated with the production of a Higgs boson. The first differential cross section measurements of the Higgs boson were presented in this thesis, where data was unfolded to particle level. Particular focus was on diphoton kinematics and the production of jets in association with the Higgs boson. The measured jet multiplicities show clear jet production in association with the production of a Higgs boson, and a slight but not significant excess was observed for N_{jets} >3. With the current luminosity of the LHC Run I, the differential cross section measurements were dominated by statistical uncertainties. Distributions were compared to various theoretical prediction generated for the combined measured Higgs boson mass, but with the limited statistics, there was no discriminating power between predictions.

With the end of Run I, attention was focused on conditions in Run II and beyond. The energy of the LHC is to be increased, and a higher luminosity is expected. With higher luminosity, more pileup is also expected, which can greatly affect the jet acceptance for VBF categories. The jet p_T threshold will mostly likely need to increased, which greatly reduces the VBF acceptance in a 2-jet category. Therefore, a 1-jet VBF category was proposed which was optimized to discriminate between VBF

events and 2-jet ggF events. The addition of this 1-jet category greatly reduced the error on the signal strength measurement, and when the jet p_T threshold is raised to around 50 GeV, the 1-jet category shows greater sensitivity for the VBF process than the standard 2-jet category. It was also shown that this 1-jet category has the potential to discriminate between different spin and CP quantum numbers of the Higgs boson, which will grant insight into any beyond the Standard Model couplings.

Bibliography

[1] C.-N. Yang and R. L. Mills, *Conservation of Isotopic Spin and Isotopic Gauge Invariance*, Phys.Rev. **96** (1954) 191–195.

[2] P. W. Anderson, *Plasmons, Gauge Invariance, and Mass*, Phys.Rev. **130** (1963) 439–442.

[3] Y. Nambu, *Quasiparticles and Gauge Invariance in the Theory of Superconductivity*, Phys.Rev. **117** (1960) 648–663.

[4] Y. Nambu, *Axial vector current conservation in weak interactions*, Phys.Rev.Lett. **4** (1960) 380–382.

[5] J. Goldstone, *Field Theories with Superconductor Solutions*, Nuovo Cim. **19** (1961) 154–164.

[6] A. Djouadi, *The Anatomy of electro-weak symmetry breaking. I: The Higgs boson in the standard model*, Phys.Rept. **457** (2008) 1–216, arXiv:hep-ph/0503172 [hep-ph].

[7] Y. Nambu and G. Jona-Lasinio, *Dynamical Model of Elementary Particles Based on an Analogy with Superconductivity. 1.*, Phys.Rev. **122** (1961) 345–358.

[8] Y. Nambu and G. Jona-Lasinio, *DYNAMICAL MODEL OF ELEMENTARY PARTICLES BASED ON AN ANALOGY WITH SUPERCONDUCTIVITY. II*, Phys.Rev. **124** (1961) 246–254.

[9] J. Goldstone, A. Salam, and S. Weinberg, *Broken Symmetries*, Phys.Rev. **127** (1962) 965–970.

[10] F. Englert and R. Brout, *Broken Symmetry and the Mass of Gauge Vector Mesons*, Phys.Rev.Lett. **13** (1964) 321–323.

[11] P. W. Higgs, *Broken symmetries, massless particles and gauge fields*, Phys.Lett. **12** (1964) 132–133.

[12] P. W. Higgs, *Broken Symmetries and the Masses of Gauge Bosons*, Phys.Rev.Lett. **13** (1964) 508–509.

[13] G. Guralnik, C. Hagen, and T. Kibble, *Global Conservation Laws and Massless Particles*, Phys.Rev.Lett. **13** (1964) 585–587.

[14] S. Dawson, *Radiative corrections to Higgs boson production*, Nucl.Phys. **B359** (1991) 283–300.

[15] A. Djouadi, M. Spira, and P. Zerwas, *Production of Higgs bosons in proton colliders: QCD corrections*, Phys.Lett. **B264** (1991) 440–446.

[16] D. Graudenz, M. Spira, and P. Zerwas, *QCD corrections to Higgs boson production at proton proton colliders*, Phys.Rev.Lett. **70** (1993) 1372–1375.

[17] M. Spira, A. Djouadi, D. Graudenz, and P. Zerwas, *Higgs boson production at the LHC*, Nucl.Phys. **B453** (1995) 17–82, arXiv:hep-ph/9504378 [hep-ph].

[18] R. V. Harlander and W. B. Kilgore, *Next-to-next-to-leading order Higgs production at hadron colliders*, Phys.Rev.Lett. **88** (2002) 201801, arXiv:hep-ph/0201206 [hep-ph].

[19] C. Anastasiou and K. Melnikov, *Higgs boson production at hadron colliders in NNLO QCD*, Nucl.Phys. **B646** (2002) 220–256, arXiv:hep-ph/0207004 [hep-ph].

[20] V. Ravindran, J. Smith, and W. L. van Neerven, *NNLO corrections to the total cross-section for Higgs boson production in hadron hadron collisions*, Nucl.Phys. **B665** (2003) 325–366, arXiv:hep-ph/0302135 [hep-ph].

[21] LHC Higgs Cross Section Working Group Collaboration, S. Heinemeyer et al., *Handbook of LHC Higgs Cross Sections: 3. Higgs Properties*, arXiv:1307.1347 [hep-ph].

[22] R. N. Cahn, *The Higgs Boson*, Rept.Prog.Phys. **52** (1989) 389.

[23] J. F. Gunion, H. E. Haber, G. L. Kane, and S. Dawson, *The Higgs Hunter's Guide*, Front.Phys. **80** (2000) 1–448.

[24] W. J. Stirling, *Why we should search for the Higgs boson*, .

[25] L. Resnick, M. Sundaresan, and P. Watson, *Is there a light scalar boson?*, Phys.Rev. **D8** (1973) 172–178.

[26] J. R. Ellis, M. K. Gaillard, and D. V. Nanopoulos, *A Phenomenological Profile of the Higgs Boson*, Nucl.Phys. **B106** (1976) 292.

[27] M. Spira, *QCD effects in Higgs physics*, Fortsch.Phys. **46** (1998) 203–284, arXiv:hep-ph/9705337 [hep-ph].

[28] The ALEPH, DELPHI, L3, OPAL Collaborations, the LEP Electroweak Working Group, *Electroweak Measurements in Electron-Positron Collisions at W-Boson-Pair Energies at LEP*, Phys. Rept. **532** (2013) 119, arXiv:1302.3415 [hep-ex].

[29] LEP Working Group for Higgs boson searches, ALEPH Collaboration, DELPHI Collaboration, L3 Collaboration, OPAL Collaboration Collaboration, R. Barate et al., *Search for the standard model Higgs boson at LEP*, Phys.Lett. **B565** (2003) 61–75, arXiv:hep-ex/0306033 [hep-ex].

[30] M. Kado and C. Tully, *The searches for Higgs bosons at LEP*, Ann.Rev.Nucl.Part.Sci. **52** (2002) 65–113.

[31] Tevatron New Physics Higgs Working Group, CDF Collaboration, D0 Collaboration Collaboration, *Updated Combination of CDF and D0 Searches for Standard Model Higgs Boson Production with up to 10.0 fb^{-1} of Data*, arXiv:1207.0449 [hep-ex].

[32] CDF Collaboration, D0 Collaboration Collaboration, T. Aaltonen et al., *Combination of Tevatron searches for the standard model Higgs boson in the W+W- decay mode*, Phys.Rev.Lett. **104** (2010) 061802, arXiv:1001.4162 [hep-ex].

[33] ATLAS Collaboration Collaboration, G. Aad et al., *Observation of a new particle in the search for the Standard Model Higgs boson with the ATLAS detector at the LHC*, Phys.Lett. **B716** (2012) 1–29, arXiv:1207.7214 [hep-ex].

[34] CMS Collaboration Collaboration, S. Chatrchyan et al., *Observation of a new boson at a mass of 125 GeV with the CMS experiment at the LHC*, Phys.Lett. **B716** (2012) 30–61, arXiv:1207.7235 [hep-ex].

[35] L. R. Evans and P. Bryant, *LHC Machine*, J. Instrum. **3** (2008) S08001. 164 p.

[36] ATLAS Collaboration, *The ATLAS Experiment at the CERN Large Hadron Collider*, JINST **3** (2008) S08003.

[37] CMS Collaboration, *The CMS experiment at the CERN LHC*, JINST **3** (2008) S08004.

[38] ALICE Collaboration, *The ALICE experiment at the CERN LHC*, JINST **3** (2008) S08002.

[39] LHCb Collaboration, *The LHCb Detector at the LHC*, JINST **3** (2008) S08005.

[40] TOTEM Collaboration, *The TOTEM experiment at the CERN Large Hadron Collider*, JINST **3** (2008) S08007.

[41] *The HL-LHC Project*, Jan., 2014. http://hilumilhc.web.cern.ch/hilumilhc/index.html.

[42] *ATLAS Experiment - Public Results: Luminosity Public Results*, Sept., 2013. https://twiki.cern.ch/twiki/bin/view/AtlasPublic/LuminosityPublicResults.

[43] ATLAS Collaboration Collaboration, *Electron and photon reconstruction and identification in ATLAS: expected performance at high energy and results at 900 GeV*, ATLAS-CONF-2010-005, CERN, Geneva, Jun, 2010.

[44] C. A. Solans Snchez, J. A. Valls Ferrer, and E. Hign Rodrguez, *Implementation of the ROD Crate DAQ Software for the ATLAS Tile*

Calorimeter and a Search for a MSSM Higgs Boson decaying into Tau pairs. PhD thesis, Valencia, Universitat de Valencia, Valencia, 2010. Presented on 26 Nov 2010.

[45] E. Fullana, J. Castelo, V. Castillo, C. Cuenca, A. Ferrer, E. Hign, C. Iglesias, A. Munar, J. Poveda, A. Ruiz-Martinez, B. Salvacha, C. Solans, R. Teuscher, and J. Valls, *Optimal Filtering in the ATLAS Hadronic Tile Calorimeter*, ATL-TILECAL-2005-001. ATL-COM-TILECAL-2005-001. CERN-ATL-TILECAL-2005-001, CERN, Geneva, 2005.

[46] *ATLAS Tile Calorimeter Group. Tile conditions cool layout.*, .

[47] A. K. Kruse, J. G. Lima, and J. Proudfoot, *On the Toeplitz nature of the Auto-Correlation Matrices to improve the performance of signal reconstruction in the Atlas TileCal in the presence of pileup*, ATL-COM-TILECAL-2013-011, CERN, Geneva, Mar, 2013.

[48] S. Alioli, P. Nason, C. Oleari, and E. Re, *A general framework for implementing NLO calculations in shower Monte Carlo programs: the POWHEG BOX*, JHEP **1006** (2010) 043, arXiv:1002.2581 [hep-ph].

[49] S. Alioli, P. Nason, C. Oleari, and E. Re, *NLO Higgs boson production via gluon fusion matched with shower in POWHEG*, JHEP **0904** (2009) 002, arXiv:0812.0578 [hep-ph].

[50] T. Sjostrand, S. Mrenna, and P. Z. Skands, *A Brief Introduction to PYTHIA 8.1*, Comput.Phys.Commun. **178** (2008) 852–867, arXiv:0710.3820 [hep-ph].

[51] S. Catani, D. de Florian, M. Grazzini, and P. Nason, *Soft gluon resummation for Higgs boson production at hadron colliders*, JHEP **0307** (2003) 028, arXiv:hep-ph/0306211 [hep-ph].

[52] D. de Florian, G. Ferrera, M. Grazzini, and D. Tommasini, *Transverse-momentum resummation: Higgs boson production at the Tevatron and the LHC*, JHEP **1111** (2011) 064, arXiv:1109.2109 [hep-ph].

[53] S. Dittmaier, S. Dittmaier, C. Mariotti, G. Passarino, R. Tanaka, et al., *Handbook of LHC Higgs Cross Sections: 2. Differential Distributions*, arXiv:1201.3084 [hep-ph].

[54] U. Aglietti, R. Bonciani, G. Degrassi, and A. Vicini, *Two loop light fermion contribution to Higgs production and decays*, Phys.Lett. **B595** (2004) 432–441, arXiv:hep-ph/0404071 [hep-ph].

[55] S. Actis, G. Passarino, C. Sturm, and S. Uccirati, *NLO Electroweak Corrections to Higgs Boson Production at Hadron Colliders*, Phys.Lett. **B670** (2008) 12–17, arXiv:0809.1301 [hep-ph].

[56] P. Nason and C. Oleari, *NLO Higgs boson production via vector-boson fusion matched with shower in POWHEG*, JHEP **1002** (2010) 037, arXiv:0911.5299 [hep-ph].

[57] M. Ciccolini, A. Denner, and S. Dittmaier, *Strong and electroweak corrections to the production of Higgs + 2jets via weak interactions at the LHC*, Phys.Rev.Lett. **99** (2007) 161803, arXiv:0707.0381 [hep-ph].

[58] M. Ciccolini, A. Denner, and S. Dittmaier, *Electroweak and QCD corrections to Higgs production via vector-boson fusion at the LHC*, Phys.Rev. **D77** (2008) 013002, arXiv:0710.4749 [hep-ph].

[59] K. Arnold, M. Bahr, G. Bozzi, F. Campanario, C. Englert, et al., *VBFNLO: A Parton level Monte Carlo for processes with electroweak bosons*, Comput.Phys.Commun. **180** (2009) 1661–1670, arXiv:0811.4559 [hep-ph].

[60] P. Bolzoni, F. Maltoni, S.-O. Moch, and M. Zaro, *Higgs production via vector-boson fusion at NNLO in QCD*, Phys.Rev.Lett. **105** (2010) 011801, arXiv:1003.4451 [hep-ph].

[61] G. Bevilacqua, M. Czakon, M. Garzelli, A. van Hameren, A. Kardos, et al., *HELAC-NLO*, Comput.Phys.Commun. **184** (2013) 986–997, arXiv:1110.1499 [hep-ph].

[62] M. Garzelli, A. Kardos, C. Papadopoulos, and Z. Trocsanyi, *Standard Model Higgs boson production in association with a top anti-top pair at NLO with parton showering*, Europhys.Lett. **96** (2011) 11001, arXiv:1108.0387 [hep-ph].

[63] H.-L. Lai, M. Guzzi, J. Huston, Z. Li, P. M. Nadolsky, et al., *New parton distributions for collider physics*, Phys.Rev. **D82** (2010) 074024, arXiv:1007.2241 [hep-ph].

[64] R. Corke and T. Sjostrand, *Interleaved Parton Showers and Tuning Prospects*, JHEP **1103** (2011) 032, arXiv:1011.1759 [hep-ph].

[65] O. Brein, A. Djouadi, and R. Harlander, *NNLO QCD corrections to the Higgs-strahlung processes at hadron colliders*, Phys.Lett. **B579** (2004) 149–156, arXiv:hep-ph/0307206 [hep-ph].

[66] M. Ciccolini, S. Dittmaier, and M. Kramer, *Electroweak radiative corrections to associated WH and ZH production at hadron colliders*, Phys.Rev. **D68** (2003) 073003, arXiv:hep-ph/0306234 [hep-ph].

[67] P. M. Nadolsky, H.-L. Lai, Q.-H. Cao, J. Huston, J. Pumplin, et al., *Implications of CTEQ global analysis for collider observables*, Phys.Rev. **D78** (2008) 013004, arXiv:0802.0007 [hep-ph].

[68] GEANT4 Collaboration, S. Agostinelli et al., *GEANT4: A Simulation toolkit*, Nucl.Instrum.Meth. **A506** (2003) 250–303.

[69] A. Djouadi, J. Kalinowski, and M. Spira, *HDECAY: A Program for Higgs boson decays in the standard model and its supersymmetric extension*, Comput.Phys.Commun. **108** (1998) 56–74, arXiv:hep-ph/9704448 [hep-ph].

[70] J. Butterworth, A. Arbey, L. Basso, S. Belov, A. Bharucha, et al., *The Tools and Monte Carlo working group Summary Report*, arXiv:1003.1643 [hep-ph].

[71] A. Bredenstein, A. Denner, S. Dittmaier, and M. Weber, *Precise predictions for the Higgs-boson decay $H \to WW/ZZ \to 4leptons$*, Phys.Rev. **D74** (2006) 013004, arXiv:hep-ph/0604011 [hep-ph].

[72] A. Bredenstein, A. Denner, S. Dittmaier, and M. Weber, *Radiative corrections to the semileptonic and hadronic Higgs-boson decays $H \to WW/ZZ \to 4fermions$*, JHEP **0702** (2007) 080, arXiv:hep-ph/0611234 [hep-ph].

[73] S. D. A. M. A. Bredenstein, A. Denner and M. M. Weber, *A Monte Carlo generator for a Proper description of the Higgs decay into 4 fermions*, 2011. http://omnibus.uni-freiburg.de/~sd565/programs/prophecy4f/prophecy4f.html.

[74] H.-Q. Zheng and D.-D. Wu, *First order QCD corrections to the decay of the Higgs boson into two photons*, Phys.Rev. **D42** (1990) 3760–3763.

[75] A. Djouadi, M. Spira, J. van der Bij, and P. Zerwas, *QCD corrections to gamma gamma decays of Higgs particles in the intermediate mass range*, Phys.Lett. **B257** (1991) 187–190.

[76] S. Dawson and R. Kauffman, *QCD corrections to $H \to \gamma\gamma$*, Phys.Rev. **D47** (1993) 1264–1267.

[77] A. Djouadi, M. Spira, and P. Zerwas, *Two photon decay widths of Higgs particles*, Phys.Lett. **B311** (1993) 255–260, arXiv:hep-ph/9305335 [hep-ph].

[78] K. Melnikov and O. I. Yakovlev, *Higgs $\to$ two photon decay: QCD radiative correction*, Phys.Lett. **B312** (1993) 179–183, arXiv:hep-ph/9302281 [hep-ph].

[79] M. Inoue, R. Najima, T. Oka, and J. Saito, *QCD corrections to two photon decay of the Higgs boson and its reverse process*, Mod.Phys.Lett. **A9** (1994) 1189–1194.

[80] ATLAS Collaboration Collaboration, *Measurements of the photon identification efficiency with the ATLAS detector using 4.9 fb1 of pp collision data collected in 2011*, ATLAS-CONF-2012-123, CERN, Geneva, Aug, 2012.

[81] S. Laplace and J. de Vivie, *Calorimeter isolation and pile-up*, ATL-COM-PHYS-2012-467, CERN, Geneva, May, 2012.

[82] S. D. Ellis and D. E. Soper, *Successive combination jet algorithm for hadron collisions*, Phys.Rev. **D48** (1993) 3160–3166, arXiv:hep-ph/9305266 [hep-ph].

[83] S. Catani, Y. L. Dokshitzer, M. Seymour, and B. Webber, *Longitudinally invariant K_t clustering algorithms for hadron hadron collisions*, Nucl.Phys. **B406** (1993) 187–224.

[84] M. Cacciari and G. P. Salam, *Pileup subtraction using jet areas*, Phys.Lett. **B659** (2008) 119–126, arXiv:0707.1378 [hep-ph].

[85] M. Cacciari, G. P. Salam, and S. Sapeta, *On the characterisation of the underlying event*, JHEP **1004** (2010) 065, arXiv:0912.4926 [hep-ph].

[86] T. HSG1 Group, *Selection for H→gammagamma analysis supporting note, for Moriond 2013*, ATL-COM-PHYS-2013-093, CERN, Geneva, Jan, 2013.

[87] ATLAS Liquid Argon EMEC/HEC Collaboration Collaboration, C. Cojocaru et al., *Hadronic calibration of the ATLAS liquid argon end-cap calorimeter in the pseudorapidity region $1.6 < |\eta| < 1.8$ in beam tests*, Nucl.Instrum.Meth. **A531** (2004) 481–514, arXiv:physics/0407009 [physics].

[88] W. Lampl, S. Laplace, D. Lelas, P. Loch, H. Ma, S. Menke, S. Rajagopalan, D. Rousseau, S. Snyder, and G. Unal, *Calorimeter Clustering Algorithms: Description and Performance*, ATL-LARG-PUB-2008-002. ATL-COM-LARG-2008-003, CERN, Geneva, Apr, 2008.

[89] ATLAS Collaboration Collaboration, G. Aad et al., *Jet energy measurement with the ATLAS detector in proton-proton collisions at $\sqrt{s} = 7$ TeV*, Eur.Phys.J. **C73** (2013) 2304, arXiv:1112.6426 [hep-ex].

[90] M. Cacciari, G. P. Salam, and G. Soyez, *The Anti-k(t) jet clustering algorithm*, JHEP **0804** (2008) 063, arXiv:0802.1189 [hep-ph].

[91] S. Argyropoulos, J. A. Backus Mayes, L. Bryngemark, R. C. Camacho Toro, J. Katzy, J. Lacey, C. Sawyer, A. Schwartzman, and P. Starovoitov, *Pile-up subtraction and suppression for jets in ATLAS*, ATL-COM-PHYS-2013-251, CERN, Geneva, Mar, 2013.

[92] J. Alison, K. Brendlinger, S. Heim, J. Kroll, and C. M. Lester, *Description and Performance of the Electron Likelihood Tool at ATLAS using 2012 LHC Data*, ATL-COM-PHYS-2013-378, CERN, Geneva, Apr, 2013.

[93] *Profiles used for 2012 Monte Carlo production*, Nov., 2013. https://twiki.cern.ch/twiki/bin/view/AtlasPublic/DataPrepGenPublicResults.

[94] ATLAS Collaboration Collaboration, *Characterization of Interaction-Point Beam Parameters Using the pp Event-Vertex Distribution Reconstructed in the ATLAS Detector at the LHC*, ATLAS-CONF-2010-027, CERN, Geneva, May, 2010.

[95] D. de Florian, G. Ferrera, M. Grazzini, and D. Tommasini, *Higgs boson production at the LHC: transverse momentum resummation effects in the $H \to 2gamma$, $H \to WW \to lnulnu$ and $H \to ZZ \to 4l$ decay modes*, JHEP **1206** (2012) 132, arXiv:1203.6321 [hep-ph].

[96] M. Grazzini and H. Sargsyan, *Heavy-quark mass effects in Higgs boson production at the LHC*, JHEP **1309** (2013) 129, arXiv:1306.4581 [hep-ph].

[97] J. M. Campbell, R. K. Ellis, R. Frederix, P. Nason, C. Oleari, et al., *NLO Higgs Boson Production Plus One and Two Jets Using the POWHEG BOX, MadGraph4 and MCFM*, JHEP **1207** (2012) 092, arXiv:1202.5475 [hep-ph].

[98] Keith Hamilton, Paolo Nason, Carlo Oleari, Giulia Zanderighi, *Merging H/W/Z + 0 and 1 jet at NLO with no merging scale: a path to parton shower + NNLO matching*, arXiv:1212.4504 [hep-ph]. http://arxiv.org/abs/1212.4504.

[99] K. Hamilton, P. Nason, and G. Zanderighi, *MINLO: Multi-Scale Improved NLO*, JHEP **1210** (2012) 155, arXiv:1206.3572 [hep-ph].

[100] A. Banfi, P. F. Monni, and G. Zanderighi, *Quark masses in Higgs production with a jet veto*, JHEP **1401** (2014) 097, arXiv:1308.4634 [hep-ph].

[101] A. Banfi, G. P. Salam, and G. Zanderighi, *NLL+NNLO predictions for jet-veto efficiencies in Higgs-boson and Drell-Yan production*, JHEP **1206** (2012) 159, arXiv:1203.5773 [hep-ph].

[102] A. Banfi, P. F. Monni, G. P. Salam, and G. Zanderighi, *Higgs and Z-boson production with a jet veto*, Phys.Rev.Lett. **109** (2012) 202001, arXiv:1206.4998 [hep-ph].

[103] M. Ciccolini, A. Denner, and S. Dittmaier, *Electroweak and QCD corrections to Higgs production via vector-boson fusion at the LHC*, Phys.Rev. **D77** (2008) 013002, arXiv:0710.4749 [hep-ph].

[104] A. Denner, S. Dittmaier, S. Kallweit, and A. Muck, *Electroweak corrections to Higgs-strahlung off W/Z bosons at the Tevatron and the LHC with HAWK*, JHEP **1203** (2012) 075, arXiv:1112.5142 [hep-ph].

[105] T. HSG1 Group, *Measurement of differential cross sections of the Higgs boson in the diphoton decay channel using 8 TeV pp data: Supporting documentation*, ATL-COM-PHYS-2013-714, CERN, Geneva, Jun, 2013.

[106] D. A. Dicus and W. W. Repko, *Dalitz Decay $H \to f\bar{f}\gamma$ as a Background for $H \to \gamma\,\gamma$*, arXiv:1402.5317 [hep-ph].

[107] L. J. Dixon and M. S. Siu, *Resonance continuum interference in the diphoton Higgs signal at the LHC*, Phys.Rev.Lett. **90** (2003) 252001, arXiv:hep-ph/0302233 [hep-ph].

[108] L. J. Dixon and Y. Li, *Bounding the Higgs Boson Width Through Interferometry*, Phys.Rev.Lett. **111** (2013) 111802, arXiv:1305.3854 [hep-ph].

[109] H. W. Group, *Signal studies in $H \to \gamma\gamma$ search with 8 TeV data*, ATL-COM-PHYS-2012-755, CERN, Geneva, Jun, 2012.

[110] A. Hoecker, P. Speckmayer, J. Stelzer, J. Therhaag, E. von Toerne, and H. Voss, *TMVA: Toolkit for Multivariate Data Analysis*, PoS **ACAT** (2007) 040, arXiv:physics/0703039.

[111] T. Gleisberg, S. Hoeche, F. Krauss, M. Schonherr, S. Schumann, et al., *Event generation with SHERPA 1.1*, JHEP **0902** (2009) 007, arXiv:0811.4622 [hep-ph].

[112] I. Burmeister, I. Connelly, A. Ferretto, F. Filthaut, R. Goncalo, R. Hawkings, H. Esch, F. Parodi, D. Sidorov, C. Schiavi, J. Thomas-Wilsker, J. Yu, and M. Zur Nedden, *Measurement of the b-tagging performance in the 2012 ATLAS data*, ATLAS-COM-CONF-2013-087, CERN, Geneva, Jul, 2013.

[113] ATLAS Collaboration Collaboration, *Commissioning of the ATLAS high-performance b-tagging algorithms in the 7 TeV collision data*, ATLAS-CONF-2011-102, CERN, Geneva, Jul, 2011.

[114] J. Gaiser, *Charmonium Spectroscopy From Radiative Decays of the J/ψ and ψ'*, .

[115] J. M. Campbell, R. K. Ellis, F. Maltoni, and S. Willenbrock, *Higgs-Boson production in association with a single bottom quark*, Phys.Rev. **D67** (2003) 095002, arXiv:hep-ph/0204093 [hep-ph].

[116] S. Dawson, C. Jackson, L. Reina, and D. Wackeroth, *Exclusive Higgs boson production with bottom quarks at hadron colliders*, Phys.Rev. **D69** (2004) 074027, arXiv:hep-ph/0311067 [hep-ph].

[117] *Differential cross sections of the Higgs boson measured in the diphoton decay channel using 8 TeV pp collisions*, ATLAS-CONF-2013-072, CERN, Geneva, Jul, 2013.

[118] J. Adelman, J. Erdmann, A. Hard, A. Loginov, P. Tipton, J. Vasquez, F. Wang, H. Wang, S. L. Wu, and H. Yang, *Search for $t\bar{t}H$ production in the diphoton channel with 20.3 fb^{-1} of data at 8 TeV and 4.5 fb^{-1} data at 7 TeV*, ATL-COM-PHYS-2014-011, CERN, Geneva, Jan, 2014. Supporting note for the ttH, H-¿gamgam publication.

[119] H. W. Group, *Signal studies in $H \to \gamma\gamma$ search with 4.9 fb^{-1} of 7 TeV data.*, ATL-COM-PHYS-2012-501, CERN, Geneva, May, 2012.

[120] ATLAS Collaboration, G. Aad et al., *Improved luminosity determination in pp collisions at $\sqrt{s}$ = 7 TeV using the ATLAS detector at the LHC*, Eur.Phys.J. **C73** (2013) 2518, arXiv:1302.4393 [hep-ex].

[121] G. Unal and D. Froidevaux, *Higgs mass measurements and uncertainties in 2011 and 2012 data*, ATL-COM-PHYS-2012-1774, CERN, Geneva, Dec, 2012.

[122] A. Martin, W. Stirling, R. Thorne, and G. Watt, *Parton distributions for the LHC*, Eur.Phys.J. **C63** (2009) 189–285, arXiv:0901.0002 [hep-ph].

[123] R. D. Ball, V. Bertone, S. Carrazza, C. S. Deans, L. Del Debbio, et al., *Parton distributions with LHC data*, Nucl.Phys. **B867** (2013) 244–289, arXiv:1207.1303 [hep-ph].

[124] J. M. Campbell, J. Huston, and W. Stirling, *Hard Interactions of Quarks and Gluons: A Primer for LHC Physics*, Rept.Prog.Phys. **70** (2007) 89, arXiv:hep-ph/0611148 [hep-ph].

[125] I. W. Stewart and F. J. Tackmann, *Theory Uncertainties for Higgs and Other Searches Using Jet Bins*, Phys.Rev. **D85** (2012) 034011, arXiv:1107.2117 [hep-ph].

[126] J. M. Campbell, R. K. Ellis, and G. Zanderighi, *Next-to-Leading order Higgs + 2 jet production via gluon fusion*, JHEP **0610** (2006) 028, arXiv:hep-ph/0608194 [hep-ph].

[127] J. M. Campbell, R. K. Ellis, and C. Williams, *Hadronic production of a Higgs boson and two jets at next-to-leading order*, Phys.Rev. **D81** (2010) 074023, arXiv:1001.4495 [hep-ph].

[128] S. Guindon, E. Shabalina, J. Adelman, M. Alhroob, S. Amor dos Santos, A. Basye, J. Bouffard, M. Casolino, I. Connelly, A. Cortes Gonzalez, V. Dao, S. D'Auria, A. Doyle, P. Ferrari, F. Filthaut, R. Goncalo, N. de Groot, S. Henkelmann, V. Jain, A. Juste, G. Kirby, D. Kar, A. Knue, K. Kroeninger, T. Liss, E. Le Menedeu, J. Montejo Berlingen, M. Moreno Llacer, O. Nackenhorst, T. Neep, A. Onofre, M. Owen, M. Pinamonti, Y. Qin, A. Quadt, D. Quilty, C. Schwanenberger, L. Serkin, R. St Denis, J. Thomas-Wilsker, and T. Vazquez-Schroeder, *Search for the Standard Model Higgs boson produced in association with top quarks and decaying to $b\bar{b}$ in pp collisions at $\sqrt{s}$= 8 TeV with the ATLAS detector at the LHC*, ATL-COM-PHYS-2013-1659, CERN, Geneva, Dec, 2013. The note contains internal documentation of the ttH(bb) analysis approved as a preliminary result (ATLAS-CONF-2014-011).

[129] ATLAS Collaboration Collaboration, G. Aad et al., *Measurement of the cross-section for W boson production in association with b-jets in pp collisions at $\sqrt{s}$ = 7 TeV with the ATLAS detector*, JHEP **1306** (2013) 084, arXiv:1302.2929 [hep-ex].

[130] J. C. Collins and D. E. Soper, *Angular Distribution of Dileptons in High-Energy Hadron Collisions*, Phys.Rev. **D16** (1977) 2219.

[131] F. J. Tackmann, J. R. Walsh, and S. Zuberi, *Resummation Properties of Jet Vetoes at the LHC*, Phys.Rev. **D86** (2012) 053011, arXiv:1206.4312 [hep-ph].

[132] G. Corcella, I. Knowles, G. Marchesini, S. Moretti, K. Odagiri, et al., *HERWIG 6: An Event generator for hadron emission reactions with*

interfering gluons (including supersymmetric processes), JHEP **0101** (2001) 010, arXiv:hep-ph/0011363 [hep-ph].

[133] G. Corcella, I. Knowles, G. Marchesini, S. Moretti, K. Odagiri, et al., *HERWIG 6.5 release note*, arXiv:hep-ph/0210213 [hep-ph].

[134] J. Butterworth, J. R. Forshaw, and M. Seymour, *Multiparton interactions in photoproduction at HERA*, Z.Phys. **C72** (1996) 637–646, arXiv:hep-ph/9601371 [hep-ph].

[135] S. Catani, F. Krauss, R. Kuhn, and B. Webber, *QCD matrix elements + parton showers*, JHEP **0111** (2001) 063, arXiv:hep-ph/0109231 [hep-ph].

[136] ATLAS Collaboration Collaboration, *Measurement of the Higgs boson mass from the $H \to \gamma\gamma$ and $H \to ZZ^* \to 4\ell$ channels with the ATLAS detector using 25 fb^{-1} of pp collision data*, arXiv:1406.3827 [hep-ex].

[137] *Further ATLAS tunes of PYTHIA6 and Pythia 8*, ATL-PHYS-PUB-2011-014, CERN, Geneva, Nov, 2011.

[138] *New ATLAS event generator tunes to 2010 data*, ATL-PHYS-PUB-2011-008, CERN, Geneva, Apr, 2011.

[139] *ATLAS tunes of PYTHIA 6 and Pythia 8 for MC11*, ATL-PHYS-PUB-2011-009, CERN, Geneva, Jul, 2011.

[140] A. Djouadi, R. Godbole, B. Mellado, and K. Mohan, *Probing the spin-parity of the Higgs boson via jet kinematics in vector boson fusion*, Phys.Lett. **B723** (2013) 307–313, arXiv:1301.4965 [hep-ph].